technische universität
dortmund

With Bottom-Up to the Top and Beyond

Differential Measurement of the Production Cross-Section of a Pair of Top Quarks at the ATLAS Experiment and Search for Beyond the Standard Model Effects in the Framework of Effective Field Theories

Kevin Sedlaczek

2022

A document submitted in partial fulfillment of the requirements for the degree of
Doctor rerum naturalium
at
Fakultät Physik, Technische Universität Dortmund

Supervised by
Prof. Dr. Kevin Kröninger and Prof. Dr. Johannes Albrecht

Erstgutachter:	Prof. Dr. Kevin Alexander Kröninger
Zweitgutachter:	Prof. Dr. Johannes Albrecht
Vorsitz der Prüfungskommission:	Prof. Dr. Carsten Westphal
Vertretung der wiss. Mitarbeiter:	Prof. Dr. Herre Jelger Risselada

Datum des Einreichens der Arbeit:	3. Juni 2022
Datum der mündlichen Prüfung:	19. August 2022

This thesis is set in Latin Modern (Serif, Sans and Math) and Fira Code,
typeset using LaTeX with LuaTeX from TeX-Live 2021.

Abstract

In this thesis, the measurement of the inclusive and differential production cross-sections of a top quark in association with an anti-top quark at large transverse momenta in proton-proton collisions, as well as one of the first direct interpretations of such a measurement in the framework of effective field theories (EFT) are presented. The measurement is based on data collected with the ATLAS detector at the Large Hadron Collider at CERN and corresponds to an integrated luminosity of $139\,\mathrm{fb}^{-1}$. Events of the process $t\bar{t} \to WbWb \to \ell\nu bqq'b$ in the region of large transverse momenta are analyzed. After unfolding the data to particle level, the cross-section is presented as function of several kinematic variables relevant to this process. In order to validate the predictions based on the Standard Model of particle physics, the data is compared to several predictions and effects of higher order contributions in quantum chromodynamics are investigated. In this measurement, the impact of systematic uncertainties on the energy reconstruction of jets is reduced by employing a novel method. It introduces a scaling of the energies of the jets in order to decrease discrepancies in the reconstruction of jet energies in data and the different predictions. Using this precision measurement, an indirect and model-independent search for physics beyond the Standard Model (BSM) in the framework of EFT is performed. In particular, the effects of two EFT operators on the coupling of the top quark to gluons and other quarks are investigated. A model based on the two operators O_{tG} and $O_{tq}^{(8)}$ in the top-quark sector of the EFT framework is employed to interpret the measurement in the context of BSM physics. Bayesian statistics is used in order to set limits on the effects of these operators via their respective Wilson coefficients C_{tG} and $C_{tq}^{(8)}$. This analysis is among the very first direct EFT interpretations of a differential cross-section measurement in the top-quark sector. The determined limits on $C_{tq}^{(8)}$ are competitive with recent global combinations, while soundly treating all parameters of the interpretation and without employing any of the assumptions, typical in global combinations. Both Wilson coefficients are found to be compatible with the SM.

Zusammenfassung

In dieser Arbeit wird die Messung der inklusiven und differentiellen Produktionswirkungsquerschnitte eines Top-Quarks in Verbindung mit einem Anti-Top-Quark bei großen Transversalimpulsen in Proton-Proton-Kollisionen vorgestellt. Des Weiteren wird eine der ersten direkten Interpretationen einer solchen Messung im Rahmen der effektiven Feldtheorien (EFT) vorgestellt. Die Messung basiert auf Daten, die mit dem ATLAS-Detektor am Large Hadron Collider am CERN aufgenommen wurden und einer integrierten Luminosität von $139\,\mathrm{fb}^{-1}$ entsprechen. Es werden Ereignisse des Prozesses $t\bar{t} \to WbWb \to \ell\nu bqq'b$ im Bereich großer Transversalimpulse analysiert. Nach der Entfaltung der Daten auf Teilchenebene wird der Wirkungsquerschnitt als Funktion mehrerer, für diesen Prozess relevanter, kinematischer Variablen untersucht. Um die Vorhersagen auf der Grundlage des Standardmodells der Teilchenphysik zu überprüfen, werden die Messungen mit verschiedenen Vorhersagen verglichen und die Auswirkungen von Korrekturen höherer Ordnung in der Quantenchromodynamik untersucht. Bei dieser Messung werden die Auswirkungen systematischer Unsicherheiten auf die Energierekonstruktion von Jets durch den Einsatz einer neuartigen Methode verringert. Dazu wird eine Skalierung der Energien der Jets eingeführt, um die Diskrepanzen bei der Rekonstruktion der Jet-Energien in den Daten und den verschiedenen Vorhersagen zu verringern. Mit dieser Präzisionsmessung wird eine indirekte und modellunabhängige Suche nach Physik jenseits des Standardmodells (BSM) im Rahmen der EFT durchgeführt. Insbesondere werden die Auswirkungen von zwei EFT-Operatoren auf die Kopplung des Top-Quarks an Gluonen und andere Quarks untersucht. Ein Modell, das auf den beiden Operatoren O_{tG} und $O_{tq}^{(8)}$ im Top-Quark-Sektor der EFT basiert, wird zur Interpretation der Messung im Kontext von Suchen nach BSM-Physik konstruiert und verwendet. Mit Hilfe der Bayes'schen Statistik werden die Auswirkungen dieser Operatoren über ihre jeweiligen Wilson-Koeffizienten C_{tG} und $C_{tq}^{(8)}$ begrenzt. Diese Analyse ist eine der ersten direkten EFT-Interpretationen einer differentiellen Wirkungsquerschnittsmessung im Top-Quark-Sektor. Die ermittelten erlaubten Parameterbereiche für $C_{tq}^{(8)}$ sind konkurrenzfähig mit den jüngsten globalen Kombinationen, wobei alle Parameter der Interpretation konsistent behandelt werden und keine der für globale Kombinationen typischen Annahmen getroffen werden. Beide Wilson-Koeffizienten erweisen sich als kompatibel mit dem SM.

Contents

1 Introduction

Fundamental research in particle physics aims to improve the understanding of the processes and forces that govern our universe. This goal reflects the inherent curiosity of humans in general and started with the tangible surroundings humans can perceive. Over time, it progressed to more sophisticated parts and concepts realized in our universe, becoming increasingly abstract and fundamental. Understanding and describing the most fundamental laws and dynamics of the universe, which lie far beyond what humans can perceive, is at the core of particle physics. These aspects reach as far as the beginning of the universe and its earliest history, involving the most fundamental concepts and objects there are. Despite the abstract nature of this research, data can be used to obtain observation-based knowledge in this field. This data is, e.g., created at laboratories like CERN with machines like the Large Hadron Collider (LHC) and collected with detectors like the ATLAS detector. By analyzing the provided data, physicists are able to deepen their understanding of the fundamental processes and objects.

Mathematical theories provide a framework for describing physical laws and objects such that testable predictions can be made. Depending on the recorded observation, those theories are then updated and modified to provide the most inclusive description of the current knowledge. Only the combination of mathematical theories and observation-based measurements allows for deepening the understanding of the universe. This is important to leave room for observations that are not described by a theory yet, and, therefore, hint at missing pieces or flaws within a theory.

In particle physics, the current most accurate theoretical description of the universe is called the Standard Model of particle physics (SM). The various aspects of the SM were developed during the last century and showed unprecedented potential in describing and predicting physical phenomena. Several of the fundamental particles described in the SM were observed after their prediction, while others shaped the structure of the theory through observations. However, there are multiple observations either in tension to the SM or without a corresponding concept or prediction in the SM. These discrepancies hint at the necessity of extensions or a replacement of the SM, albeit no clear path for such is obvious. Thus, the search for a more fundamental and complete theory is the superior goal of the field of particle physics. The ATLAS detector at the LHC (which is described in Section 5) was built to generate data to address this challenge.

The most massive particle in the SM is the top quark, which has only been discovered in 1995 [1, 2]. Many proposals for extensions to the SM are strongly connected to the top quark due to its unique high mass [3–6]. During the last years, the ATLAS detector has collected an unprecedented dataset of top quark interactions, generated by the proton-proton collisions at the LHC. From 2015 to 2018 (Run 2), a dataset corresponding to

$139\,\mathrm{fb}^{-1}$ of proton-proton collisions at a centre-of-mass energy of $\sqrt{s} = 13\,\mathrm{TeV}$ has been collected. The search for non-resonant deviations from the SM is one possible approach to find hints for a more fundamental and complete theory. These are especially likely to appear in particularly high-energy interactions, or in high transverse momentum (boosted) top-quark events [7–10]. Therefore, such data represent the ideal context to search for new physics phenomena in the framework of non-resonant descriptions of such.
The measurement presented in this thesis is among the first measurements of the production of a top quark in association with an anti-top quark using the entire Run 2 dataset. The production cross-section of this process is measured using events corresponding to the semileptonic decay channel ($t\bar{t} \to WbWb \to \ell\nu bqq'b$, allowing both charges for the lepton ℓ), both inclusively and as a function of various kinematic variables (differential cross-section measurements) after correcting for detector effects. The variables chosen in this measurement characterize the kinematics of the top quarks, as well as additional radiation in the selected dataset. The measured distributions are compared to the most precise current SM predictions, which are calculated at *next-to-leading-order* (NLO) precision in the perturbative description of quantum chromodynamics (QCD), as well as predictions reweighted to match NNLO predictions in QCD at parton level. This way, important input to test and improve the SM predictions, as well as the implementations of the numerical calculations are generated. Such measurements have been performed by the ATLAS and CMS collaborations using different datasets at different center-of-mass energies before [11–14], however not at this statistical precision. This measurement directly follows the previous ATLAS measurement using a smaller dataset at a center-of-mass energy of $\sqrt{s} = 13\,\mathrm{TeV}$ [15]. The precision is improved significantly due to the larger dataset, as well as a novel method reducing systematic uncertainties related to the reconstruction of jets in the measurement.
The unprecedented statistical and systematic precision of this measurement is then used to test for the presence of physics beyond the SM. For such tests, the non-resonant description of new physics is employed in the framework of effective field theories. This framework allows for systematic tests for effects of new physics even in the absence of a hypothetical new fundamental theory by extending the SM via an infinite series of higher-dimensional terms in the Lagrange description. Using this model-independent framework, such effects are quantified in order to make statistical statements about potential hints of new physics based on the data presented in this measurement. This work is among the first differential measurements in the top-quark sector to include a direct interpretation of this kind. The interpretation is performed by constructing a numerical model of the EFT framework and applying the Bayesian approach to knowledge inference. The potential of this measurement to make such statements is shown for an expansion of the SM via two EFT operators: O_{tG} and $O_{tq}^{(8)}$. These operators are defined in the Warsaw basis [16] of EFT operators.

The work, described in this thesis, has been published in two publications, performed within the ATLAS collaboration, with the second publication superseding the first partial result.

1. ATLAS Collaboration. *Measurements of differential cross-sections in top-quark pair events with a high transverse momentum top quark and limits on beyond the Standard Model contributions to top quark pair production with the ATLAS detector.* Geneva, 2021. https://cds.cern.ch/record/2777237

2. ATLAS Collaboration. "Measurements of differential cross-sections in top-quark pair events with a high transverse momentum top quark and limits on beyond the Standard Model contributions to top-quark pair production with the ATLAS detector at $\sqrt{s} = 13\,\text{TeV}$", JHEP 63, 2022. arxiv: 2202.12134. doi: 10.1007/JHEP06(2022)063

The work presented in this document has been carried out in close collaboration with Mark Owen, Federica Fabbri, and Jonathan Jamieson, who also describes this measurement in his Ph.D. thesis. The measurement described in Sections 6-8 has largely been performed by the collaborators. Among their contributions are the code base used in the measurement as well as the implementation and execution of the measurement steps. In this context, I contributed to the development of the measurement, particularly with respect to the EFT interpretation, as well as explicitly to the selection of the signal events and the dedicated studies on its extension described in Section 6.5. Furthermore, I planned the EFT interpretation of this measurement and executed the set-up, implementation, validation and final interpretation of this measurement, as described in Sections 4, 9, 10, 11 and 12.

This document presents a brief introduction to the SM and the extensions via effective field theories in Section 2. The larger context of EFT interpretations, particularly at the LHC, is given in Section 3, while the specifics of the approach in this work are described in Section 4. The ATLAS detector at the LHC is described in Section 5, followed by a description of the various datasets, used in this measurement in Section 6. The various steps of the differential measurement are outlined in Section 7, and the results of the measurement are discussed in Section 8. The implementation of the EFT model used in the interpretation of the measurement is outlined in Section 9. The expected limits on the EFT effects, as well as the model validation are presented in Section 10 and Section 11, respectively. The observed limits based on the measurement are shown and discussed in Section 12, including a comparison in the global context of EFT in the top sector. Finally, Section 13 presents the conclusions of this work as well as an outlook on future prospects.

Brief Introduction to the Standard Model of Particle Physics and Beyond

2

The field of particle physics focuses on understanding and describing the properties and interactions of fundamental particles. The theoretical basis that makes this possible is the Standard Model of particle physics (SM), which is a combination of relativistic quantum field theories that describe elementary particles and how they interact. Although it is assumed to be incomplete, it has successfully been used to describe and predict experimental measurements for multiple decades and in multiple contexts. Furthermore, experimental observations have significantly contributed to shaping the SM and extending it to the theory it is today. Thus, testing and advancing this theory is paramount to developing the field of particle physics further.
This chapter briefly introduces the SM with particular focus on the top quark and discusses the shortcomings of this theory, which motivate further searches for a fundamental description of the universe.

2.1 The Top Quark in the Standard Model of Particle Physics

The dynamics of the particle content of the SM are described using the Lagrange formalism. This formalism is employed using the inherent symmetries of the theory. In the case of the SM, the overall theory is invariant under a gauge symmetry following a group of the structure $\mathrm{SU(3)_C} \times \mathrm{SU(2)_L} \times \mathrm{U(1)_Y}$. In this order, the three gauge groups correspond to the strong interactions, the weak interactions, and the electromagnetic (EM) interactions. These symmetries of the SM create certain conservation laws. In particular, the $\mathrm{SU(3)_C}$ symmetry introduces color charge conservation, the $\mathrm{SU(2)_L}$ symmetry the conservation of the weak isospin and the $\mathrm{U(1)_Y}$ symmetry the conservation of hyper charge Y. To describe the dynamics of the particle content of the SM under these interactions, they are encoded in a Lagrangian $\mathcal{L}_{\mathrm{SM}}$. The SM Lagrangian containing all the interactions and dynamics of the SM particles can be written as

$$\begin{aligned}\mathcal{L}_{\mathrm{SM}} = &-\frac{1}{4}B_{\mu\nu}B^{\mu\nu} - \frac{1}{4}G^A_{\mu\nu}G^{A\mu\nu} - \frac{1}{4}W^I_{\mu\nu}W^{I\mu\nu} \\ &+ (D_\mu\phi)^\dagger(D^\mu\phi) + \mu^2\phi^\dagger\phi - \lambda(\phi^\dagger\phi)^2 \\ &+ i(\bar{u}_{\mathrm{R}}\not{D}u_{\mathrm{R}} + \bar{d}_{\mathrm{R}}\not{D}d_{\mathrm{R}}) \\ &+ i(\bar{l}_{\mathrm{L}}\not{D}l_{\mathrm{L}} + \bar{e}_{\mathrm{R}}\not{D}e_{\mathrm{R}} + \bar{q}_{\mathrm{L}}\not{D}q_{\mathrm{L}}) \\ &- (Y^u\bar{q}_{\mathrm{L}}\tilde{\phi}u_{\mathrm{R}} + Y^d\bar{q}_{\mathrm{L}}\phi d_{\mathrm{R}} + Y^e\bar{l}_{\mathrm{L}}\phi e_{\mathrm{R}} + \mathrm{h.c.})\,.\end{aligned} \tag{2.1}$$

Here, the field strength tensors of the SM gauge group $\mathrm{SU(3)_C} \times \mathrm{SU(2)_L} \times \mathrm{U(1)_Y}$ are represented by $B_{\mu\nu}$, $W^I_{\mu\nu}$ and $G^A_{\mu\nu}$. The Higgs field is denoted as ϕ and the covariant derivative is D_μ. The quark doublets of the $\mathrm{SU(2)_L}$ are represented by q_L while the lepton doublets are represented by l_L. The singlets for the up- and down-type quarks are represented by u_R and d_R respectively, while the charged lepton singlet is represented by e_R. Finally, the Yukawa matrices are encoded in Y^i. In this notation, the summation over the various generations of particles is implied.

The strong interaction, described in the framework of quantum chromodynamics (QCD), is described by the $\mathrm{SU(3)_C}$ symmetry. It describes interactions of color-charged particles, which can take three different color charges, and its mediator bosons are the eight massless gluons g. The color-charged fermionic particles in the SM are called quarks. Since the mediator bosons in QCD also carry color, gluons self-interact. In nature, only color-neutral states exist. This phenomenon, called *confinement*, therefore does not allow for free quarks. While the quarks carry a single color-charge, the gluons represent states carrying combinations of color and anti-color. There are 6 types (*flavors*) of quarks in the SM, divided into the 3 generations $\binom{u}{d}$, $\binom{c}{s}$ and $\binom{t}{b}$. The particles in the generations are increasing in mass, starting with the u quark and increasing to the top quark t, which is the most massive particle in the SM with a mass of $m_\mathrm{top} = (172.69 \pm 0.48)\,\mathrm{GeV}$ [17]. Furthermore, there exist anti-particles with opposite additive quantum numbers for each one of the quarks, denoted by a bar (e.g. $\bar{t}$). The up-type quarks (u, c and t) carry an electric charge of $+2/3e$ while the down-type quarks (d, s, b) carry an electric charge of $-1/3e$.

The interactions among electrically charged particles, like quarks, are described by the EM interactions. The electric charge describes the corresponding quantum number, with the massless photon γ as the mediator boson. The electrically charged particles in the SM also contain leptons and the $W^\pm$ bosons, which mediate charged weak currents. Similar to the generations of quarks, there are three generations of leptons in the SM: $\binom{\nu_e}{e}$, $\binom{\nu_\mu}{\mu}$ and $\binom{\nu_\tau}{\tau}$, with the electron e, muon μ and tau lepton τ increasing in mass and the neutrinos ν predicted to be massless in the SM. However, neutrinos have been found to show mixing and therefore be massive as well [18–20]. In contrast to the neutrinos, the electron, muon and tau lepton carry electric charge.
All fermionic particles participate in the weak interaction, mediated by the charged $W^\pm$ bosons and the neutral Z boson. The corresponding quantum number of the weak interactions is called the weak isospin. For electrically charged particles, the Z boson interacts differently with right- and left-handed particles, while the $W^\pm$ bosons only couple to left-handed particles. Unlike the leptons, which only mix within the respective generations and therefore display lepton family number conservation, the quarks do not show this behavior in the context of the weak interactions. Instead, there is inter-generational mixing between the quark flavors. This phenomenon arises from the distinction between the mass eigenstates of quarks (shown above) and the interaction eigenstates within the weak force. Here, the interaction states of the quarks represent mixtures of the mass eigenstates encoded in mathematical rotations. These rotations are described by the unitary Cabibbo-Kobayashi-Maskawa (CKM) matrix. With the mass eigenstates of the

down-type quarks $\begin{pmatrix} d \\ s \\ b \end{pmatrix}$ and the interaction eigenstates $\begin{pmatrix} d' \\ s' \\ b' \end{pmatrix}$ this rotation can be written as

$$\begin{pmatrix} d' \\ s' \\ b' \end{pmatrix} = \begin{pmatrix} V_{ud} & V_{us} & V_{ub} \\ V_{cd} & V_{cs} & V_{cb} \\ V_{td} & V_{ts} & V_{tb} \end{pmatrix} \begin{pmatrix} d \\ s \\ b \end{pmatrix} . \tag{2.2}$$

The description of this rotation based on the down-type quarks is purely conventional and leads to the up-type quarks' mass- and interaction-eigenstates being equal. In this description, for example, the complex number V_{tb} describes the mixing of t to b, e.g., in the process $t \to b + W^+$. Its absolute value can take any value between zero and one and is measured to be $|V_{tb}| = 1.013 \pm 0.030$ [21]. Since the matrix is unitary by construction in the SM, this indicates that the probability of the mixing within the third quark generation is huge and that mixing with the other generations for the top quark is very rare. A similar - although not as strong - picture emerges for the other two generations, because the entries on the diagonal of the CKM matrix are much larger than the off-diagonal entries. Due to the unitarity, it can be described by four parameters. One of these is a phase parameter, which leads to a CP-asymmetry.

Since the massive mediators of the weak interaction distinguish between the fermion chiralities, they do not allow for direct mass terms in $\mathcal{L}_{\mathrm{SM}}$, obeying local $\mathrm{SU(2)_L}$ gauge-invariance. Thus, there has to be a different mechanism to create the masses for the fermions. This is facilitated by the Brout-Englert-Higgs mechanism [22, 23], which spontaneously breaks the $\mathrm{SU(2)_L} \times \mathrm{U(1)_Y}$ symmetry. This way, the three massive gauge bosons Z and $W^\pm$ acquire their masses, while still conserving local gauge invariance, and the EM and weak interactions are unified as the electroweak (EW) interactions. As a result, the initial independent conservation of the weak isospin and hypercharge are combined as the conservation of the electric charge.

This mechanism introduces a massive scalar particle, the Higgs boson H, as the excitation of the scalar Higgs field ϕ. While all gauge bosons in the SM are vector bosons, the Higgs boson is a scalar boson with its spin being zero. Electrically charged fermions in the SM acquire their masses through Yukawa couplings to the Higgs boson. The strength of these couplings determines the fermions' masses. However, the couplings are not explained by the SM, but rather free parameters of the theory, determined through measurements. The top quark is the only particle with a Yukawa coupling of ≈ 1, giving it a strong connection to the EW symmetry breaking and, therefore, the Higgs sector. The validity of the Higgs mechanism is supported by the discovery of the Higgs boson, its predicted resonance [24–30].

The respective coupling constants α_i describe the strength of each interaction depending on the energy scale and vary largely among the interactions. The scale dependence of each individual coupling strength can lead to vastly different behavior at a given energy. The strong coupling constant α_s, e.g., diverges at small energies so that color-charged particles can only exist in color-neutral bound states - called hadrons - at this scale. This characteristic of the strong interaction is called color confinement. All quarks beside the top quark create hadrons in a process called hadronization. The top quark decays on such a small time scale that it generally decays before forming a hadron bound state, allowing for an interesting phenomenology of a quasi-free particle. In order to study the properties

of the top quark, it has to be created, for example in particle collisions, that provide enough energy. Since it is not abundantly accessible, like the much lighter u or d quark, which comprise the stable matter in our universe, this is facilitated, e.g., by proton-proton (pp) collisions.

2.2 Production of a Pair of Top Quarks at the LHC

The production of two top quarks (here and later implying a pair of t and $\bar{t}$) in proton-proton collisions happens via different production modes, called channels. Firstly, the initial particles creating the particular final state can vary. Additionally, there are multiple versions of possible final states originating from a pair of top quarks. For a given energy scale in pp collisions (e.g., the collision of protons at twice the top mass in the production of a pair of top quarks), the probability for any elementary particle to carry enough momentum and, therefore, produce the desired final state, depends on the centre-of-mass energy of the proton. The probabilities for certain combinations of initial particles additionally depend, among other things, on the substructure of the proton. Since it is not an elementary object and thus has a non-trivial structure, the energy and, therefore, the momentum are distributed among the constituents, called partons. The corresponding probability distribution for the momentum fraction of a given parton is described by the respective *parton distribution functions* (PDFs). These are determined from dedicated measurements and globally modeled, since they universally apply to all pp interactions. Thus, these PDFs are essential in order to describe collisions involving a proton in the relativistic regime and therefore to predict the production of a top-quark pair. The PDFs of all, but the three valence quarks of the proton, show diverging probabilities at low momentum fractions. The PDF for the gluon shows a much stronger form of this behavior. Due to this large difference of the PDFs of the proton's constituents and the very high centre-of-mass energy of the LHC compared to the energy scale of the process, a pair of top quarks is dominantly produced via the fusion of two gluons, as shown in Figures 2.1a and 2.1b. Following from the PDFs, larger momentum fractions for quarks are favored, which in turn lead to a higher probability of generating high-energy collision products. These collision products appear as large-momentum particles, so that a kinematic region of interest tailored to such products would be characterized by a large initial-quark luminosity, relative to the gluon one in this process. This way, the production of a pair of top quarks via a process with initial quarks - as shown in Figure 2.1c - becomes more likely. As mentioned in the context of the CKM matrix, the top quark almost exclusively decays into a b quark and W boson (with the respective quantum numbers depending on the charge of the top quark). This W boson can then subsequently decay hadronically, meaning into a quark and antiquark, or leptonically, into a pair of leptons ($\ell\nu$). The decay of a pair of top quarks with one decaying leptonically and one decaying hadronically is denoted as the semileptonic decay, in this work.

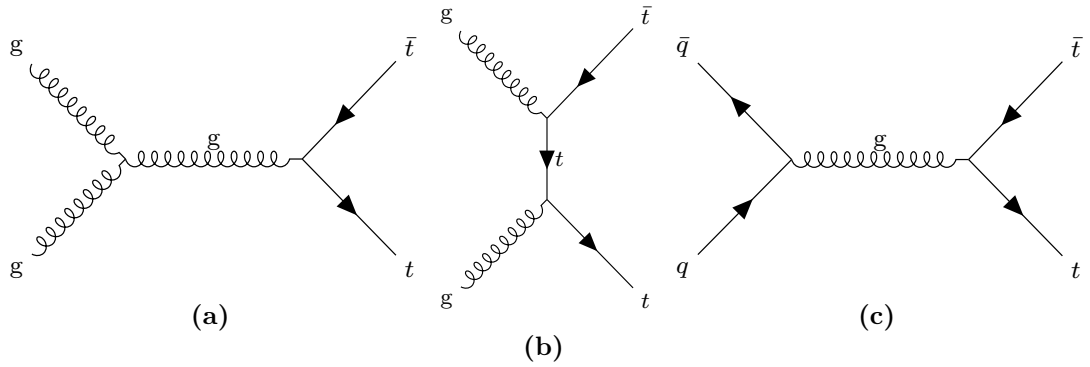

Figure 2.1: Feynman diagrams of the production of a pair of top quarks via the fusion of two gluons (a), the splitting of two gluons (b) and the annihilation of a pair of quarks (c). Due to the PDFs of the partons in the proton-proton collisions, diagrams (a) and (b) yield the dominant contributions to the production of a pair of top quarks at the LHC.

2.3 Motivation for the Search for BSM Physics

Despite the outstanding success of the SM as the theoretical description of a large number of experimental observations of the fundamental processes in the universe, it still lacks proper theoretical description in several cases. There are multiple observed phenomena that cannot be described within the SM, as well as multiple theoretical shortcomings and input parameters to the theory not specified within the SM framework. A non-exhaustive list of these phenomena, which motivate searches for physics beyond the SM, follows below.

Cosmological interpretation of observations [31] of the dynamics of galaxies and other objects in the universe are found to vary from predictions in a way that suggests the existence of non-luminous matter. This matter is called *Dark Matter* [32] and is estimated to make up a majority of the matter content of the universe, with about 85 % of the total matter content of the universe [21]. Dark matter does not interact via the electromagnetic force, which motivated the choice for the name. However, none of the elementary particles within the SM is well-suited as a candidate to describe this matter. Several theoretical models beyond the SM yield such candidates (see, for example, Ref. [33]), which motivate the search for such.

Furthermore, the SM lacks a mechanism to describe the observed matter-anti-matter asymmetry [34]. The existence of a universe filled with baryonic matter with the absence of similar amounts of anti-matter shows a fundamental asymmetry in our universe. For this asymmetry to exist, several criteria are necessary [35]. Among these criteria is the necessity for certain interactions of elementary particles to violate baryon number symmetry, as well as, violation of the charge symmetry (C) and charge-parity symmetry (CP) in certain processes. Despite the existence of the CP-violating phase in the weak interactions, its size does not lead to an asymmetry of the observed magnitude, hinting at the need for extensions of the SM. This is however intertwined with cosmological considerations.

Deviations observed in recent measurements to predictions of the SM concern the description of its leptons. The observation of the aforementioned neutrino oscillations falls into this region. Additionally, there are multiple measurements with leptons in the final states, which show tensions of 3 to 4 standard deviations with respect to the SM predictions. While not providing direct proof, these are strong hints towards BSM physics. The measurements in question include recent measurements of $b \to s\ell\ell$ transitions by the LHCb collaboration [36–41] as well as the measurement of the muon anomalous magnetic moment, commonly referred to as $(g-2)$ by FNAL and BNL [42, 43]. Additionally, the recently published measurement of the W boson mass by the CDF collaboration presents very strong tensions to the SM prediction [44]. The measured mass is only compatible with the SM prediction at a significance of seven standard deviations and presents strong tensions with other measurements e.g., by the ATLAS and LHCb collaborations [45, 46]. While this discrepancy needs further investigations – primarily due to the tension with other measurements – it may hint at the existence of physics beyond the SM.

Finally, the symmetry breaking in the EW sector of the SM is still an area of many input parameters to the theory, which generally should be avoided. The masses of the fermions follow a hierarchical structure described by the underlying Yukawa mechanism, with its corresponding couplings as input parameters to the theory. The origin of this structure is still an unknown territory. The area of the symmetry breaking in the EW sector and the strong connection of the Higgs mechanism to the top quark, due to the strong coupling of the two particles, make searches involving top quarks particularly interesting.

Despite these multiple areas of discrepancies and, therefore, possibilities for BSM physics, there is no direct evidence for BSM physics at this point. Especially the observed discrepancies, mentioned above, motivate several BSM models focusing on the top quark (see, for example, Ref. [47–49]). The top quark is a particularly interesting candidate due to its large mass and the strong connection to the EW symmetry breaking. Since no evidence of BSM physics at low energy scales has emerged so far, it is generally assumed to lie at large energy scales. Therefore, the large mass of the top quark makes it an interesting candidate. The absence of direct evidence in measurements based on the LHC data, even at the highest energies, could imply that potential resonances or other manifestations of BSM physics lie at much larger energy scales than the current reach of collider experiments. This is one of the reasons for plans for future colliders that will exceed the current energy reach [50, 51]. BSM physics of this kind would generally be more prominent in data at higher energies. Other models imply potential BSM physics to be characterized by very small couplings, which in turn could render the current amounts of data too small to make significant measurements. A way to extend the potential reach of searches for BSM physics at currently accessible energy scales to much larger energy scales in a model-independent way is presented in the next section.

2.4 Effective Field Theories in Top-Quark Physics

The search for BSM physics at the LHC can be categorized into two approaches: direct and indirect searches. In general, the direct searches test for a particular prediction, like a resonance of a specific new extension to the SM in the observed data. These *top-down* approaches yield very clear topologies and predictions for possible discoveries since they are based on a specific theory. However, each search can only shed light on narrow regions of potential BSM physics, namely the model of choice and the energy range within direct reach. Especially in the absence of clear indicators of probable potential BSM models, the way to a BSM discovery can be particularly hard.
Indirect searches, on the other hand, offer approaches to search for BSM effects in data taken at low centre-of-mass energies when compared to the natural BSM energy scale by looking for the low-energy effects of BSM processes which directly manifest themselves at much higher energy scales. Here, the SM is assumed to be the approximation of a more fundamental theory at low energy scales. This way, both, the energy reach of the search as well as potential precision can be increased. However, indirect searches like this can also be constructed from a specific model. In this case, still only a specific model or group of models is tested.
A way to extend the energy reach of sensitivity to BSM effects and make searches much more independent of specific models is provided in the framework of effective field theories (EFT). The EFT framework adapted to the top quark is called SMEFT, differing in the energy scale from, for example, the weak effective theory framework in b physics. In the context of EFT, the possible contributions from BSM physics at high-energy scales are described in a *bottom-up* approach by expanding the SM Lagrangian with higher dimensional operators according to:

$$\mathcal{L}_{\text{SMEFT}} = \mathcal{L}_{\text{SM}} + \sum_{i,D\geq 5} \frac{C_i^{(D)}}{\Lambda^{D-4}} O_i^{(D)}, \tag{2.3}$$

where each operator $O_i^{(D)}$ of mass dimension D has a corresponding Wilson coefficient C_i and Λ is the energy scale associated with the new physics. The scaling by this energy scale reduces the additional terms in the Lagrangian to mass-dimension four. Under the SM assumption, all operators of higher mass dimension than four are forbidden in order to keep the theory renormalizable. A SM Lagrangian containing such terms would not be renormalizable, and the theory would contain divergencies that cannot be removed by introducing a finite number of counterterm parameters. Therefore, allowing for higher-dimensional terms renders the SM an effective description rather than a fundamental theory. The EFT approach parametrizes BSM physics via such particular operators. The operators $O_i^{(D)}$ consist of SM fields and are built so that they obey certain SM symmetries. Lorentz invariance, Poincare symmetry and local gauge symmetry under the SM group are necessities here, while, for example, CP-violating contributions can be allowed if chosen. In the EFT scenario, no fundamental model at high energy scales is assumed. The *bottom-up* approach rather parametrizes all possible ways in which such a theory could manifest at low energy scales through the construction of all possible EFT operators at

higher mass-dimension. Possible observations parametrized this way can then be matched to a given specific fundamental theory, or *vice versa*. Therefore, a single interpretation of a measurement in this framework can be related to a large number of fundamental BSM theories. Generally, the Wilson coefficients describe the strength of EFT contributions through the respective operator. The observation of non-zero values for such would thus not only show the existence of BSM physics, but connect it to a particular coupling, represented by the corresponding operator's mathematical structure.
Assuming that the energy scale Λ lies at such large energies that no resonances are predicted within direct reach of the data, an effective description like this is valid, and the sum can be truncated at dimension six, which is the first term that gives non-zero contributions under the assumption of lepton- and baryon-number conservation. This way, a large number of EFT operators can be constructed at the different mass dimensions.
At dimension six, assuming baryon number conservation and minimal flavour violation [52], there are 2499 different operators [53]. The SM is recovered by setting all the Wilson coefficients to zero.
In general, these EFT operators will only affect very specific processes or observables depending on their quantum field content and the coupling structure. When looking at couplings involving top quarks, there are 59 independent operators that can potentially contribute [8]. When interpreting a single measurement, this number will be even smaller depending on the process that is observed and the specifics of that particular measurement.
Extending the Lagrangian in Equation (2.1) in the framework of EFT introduces new Feynman rules and may increase the number of Feynman diagrams for a given process. Therefore, these operators translate into a modified matrix element $\mathcal{M}$ as a function of the Wilson coefficients of the given EFT operators. In this work, only single insertions of EFT couplings at dimension six are considered. Thus, the EFT-modified matrix element takes the form

$$\mathcal{M} = \mathcal{M}_{\text{SM}} + \frac{1}{\Lambda^2} \sum_i C_i \mathcal{M}_i^{\text{EFT}} + \mathcal{O}\left(\frac{1}{\Lambda^4}\right) , \tag{2.4}$$

with the Wilson coefficients C_i. Here, terms of the order Λ^{-4} arising from multiple operator insertions are not considered. The dynamics of the modified couplings are encoded in $\mathcal{M}_i^{\text{EFT}}$. Any physics observable, like a cross-section σ is then derived from $|\mathcal{M}|^2$, giving a functional description of the kind shown in Equation (2.5).

$$\sigma = \sigma_{\text{SM}} + \frac{1}{\Lambda^2} \sum_i C_i \sigma_i^{\text{SM-EFT-interference}} + \frac{1}{\Lambda^4} \sum_{i,j} C_i C_j \sigma_{i,j}^{\text{EFT}} \tag{2.5}$$

The source for this functional description can be displayed in a schematic way, as is done in Figure 2.2. It shows the different insertions of additional Feynman diagrams for non-zero EFT contributions in the calculation of $|\mathcal{M}|^2$ and how the terms in Equation (2.5) arise. This description represents a quadratic function in the Wilson coefficients C_i. It contains the SM contribution as a constant σ_{SM}, while the EFT contributions yield terms both linear and quadratic in the Wilson coefficients C_i. The linear terms $\sigma_i^{\text{SM-EFT-interference}}$ of the order Λ^{-2} arise from interferences of the EFT terms in $\mathcal{M}$ with the SM, whereas the quadratic terms at $\mathcal{O}(\Lambda^{-4})$ are the result of products of two EFT terms of different or the

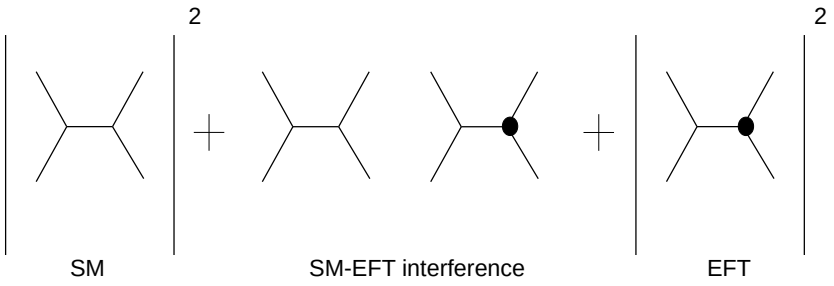

Figure 2.2: Schematic calculation of $|\mathcal{M}|^2$ for non-zero EFT contributions (black blobs) showing how the EFT contributions enter the calculation, creating the terms in Equation (2.5), inspired by Ref. [54].

same operators. Thus, the latter can also contain interferences between different EFT operators, if possible.
The functional description in Equation (2.5) is the basis for the description of EFT effects in the observables measured in this work. The different orders in the BSM energy scale Λ are furthermore examined in two setups:

linear including terms up to $\mathcal{O}(\Lambda^{-2})$

quadratic including terms up to $\mathcal{O}(\Lambda^{-4})$

In this work, only dimension six operators are considered. However, terms of the order $\mathcal{O}(\Lambda^{-4})$ in the observables can also include potential interference terms of the SM with dimension-eight operators. This work focuses on dimension-six operators.
Generally, the number of EFT operators of interest determines the minimum number of observables, necessary to constrain the EFT effects. Therefore, measurements of the total cross-section of a given process with more than one potential EFT operator will not be able to break the degeneracy introduced by the EFT model. In the presence of a sufficient number of measurements, however, the degeneracy is only broken if these measurements are sufficiently orthogonal, meaning they contain information that can be used to disentangle the effects of multiple operators.

3 Context of EFT Interpretations

Describing new physics phenomena in particle physics in the framework of EFT is a commonly used tool. EFTs can be used to describe the dynamics of certain processes and make predictions in the absence of a fundamental theory. As pointed out in Section 2.4, the effective description only holds if the natural energy scale of the interaction is much larger than that of the observations to be described in an effective way. A famous example of a successful application of this approach is Enrico Fermi's theory of the beta decay [55]. In this approach, the decay of a neutron into a proton, an electron, and an electron anti-neutrino via the weak interaction is described in an effective theory with a direct coupling of the three decay products to the initial particle. Through this approach, a description of the weak charged currents was possible, albeit the more fundamental EW theory only being formulated years later [56–58]. Within the EW theory, the interaction is described by the W^- boson changing the d quark to a u quark and subsequently decaying into the lepton pair. However, since the W boson's mass with $m_W \approx 100\,\text{GeV}$ is two orders of magnitude larger than the overall maximum energy scale of this process with $m_{\text{Neutron}} \approx 1\,\text{GeV}$, the effective description works very well. This was later confirmed by measurements. Analogously, many EW processes that fulfill this criterion can be described in an effective way, like, for example, the decay of the muon.
Similar to these descriptions, the EFT framework allows to quantitatively describe BSM physics effects in data, without strong assumptions[1] on the underlying theory. On the one hand, one of the caveats is the limited precision of the approach in ruling out or yielding evidence for certain predictions. On the other hand, significant deviations of EFT interpretations from the SM prediction can yield direct evidence for the presence of BSM physics. Especially in the absence of clear evidence for potential BSM scenarios and lacking even well-motivated directions forward, this allows for much broader searches. Thus, EFT interpretations are useful as a complementary method to direct searches for BSM physics.

3.1 EFT Interpretation of Measurements at the LHC

The data collected at the different experiments at the LHC allows for measurements of the physics of proton-proton collisions at the highest energies ever recorded at a particle collider. With the abundance of data after two data taking periods, the data allows an ever increasing precision in large numbers of measurements. However, because of the lack

[1] However, specific EFT approaches also contain certain basic model assumptions like the choice of flavor structure or whether or not CP-violating operators are allowed.

of clear evidence for any potential BSM model so far, the indirect search for BSM physics as a complementary approach is vital to make more efficient use of this data. The benefit of indirect searches lies not only in the complementarity to direct searches, but also in the natural way to combine different measurements in this framework, and, therefore, create a legacy interpretation of the collected data. This applies specifically to interpretations in a model-independent framework like EFT.
Effective theories as one type of indirect approaches have been used in measurements at the large experimental collaborations of ATLAS, CMS, and LHCb in multiple ways in the past. This section, as well as the following one, gives an overview of the main applications of effective theories in LHC physics focused on the Higgs boson, the beauty quark, and specifically in top quark-specific measurements. The interpretations are done in different EFT frameworks, since the measurements focus on a particular particle or interaction of interest. These EFT frameworks differ in the operator bases due to the particles involved, as well as the typical energy scales. The EFT frameworks at low energies, for example, do not contain all particles of the SM, because heavy resonances are integrated out. Therefore, the different bases conveniently describe the particular processes of interest.

Higgs measurements. Measurements of the various production and decay channels of the Higgs boson have very frequently been interpreted in the EFT framework [59–63]. Among recent measurements are the production of Higgs bosons with or without vector bosons, as well as combinations of large numbers of different Higgs measurements. The measurements are interpreted in terms of Higgs-specific operators collected in the HEFT framework that describe effects on the SM Higgs couplings through modification factors κ_i. The SM can be recreated by setting κ_i to $\kappa_i = 1$.

Beauty-quark measurements. Similarly to the Higgs sector, measurements of processes involving b-hadrons are interpreted in a particular framework of EFT. The operator basis used in this case is called the weak effective theory and contains a certain set of operators at the typical energy scale of these processes, the b quark mass. As mentioned above, in the case of the b quark, the top quark, as well as the Higgs boson and the W and Z bosons are integrated out, and thus are not available in this operator basis. Therefore, it is different from both the HEFT and the SMEFT bases. However, translations between the bases are possible. Prominent examples of EFT interpretations in this sector are, for instance, the aforementioned measurements of $b \to s\ell\ell$ transitions by the LHCb collaboration. Many of these measurements are interpreted individually as well as in combinations throughout the different data-taking periods at the LHCb experiment [64–67].

Top-quark measurements. Interpretations in the SMEFT framework are featured in measurements of many different production processes of top quarks. While older measurements do not frequently contain EFT interpretations, recent measurements of Run-2 data are much more commonly interpreted in the context of EFT. However, a number of interpretations in the related context of anomalous couplings exist, for example in relation of the Wtb-vertex [68, 69]. A large number of very diverse, recent measurements employ the EFT framework to search for BSM physics [70–84]. Among these measurements

are inclusive and differential measurements, e.g. of the production of pairs of top quarks in the various decay channels, measurements of spin correlations and charge asymmetry of the top quarks, the production of four top quarks as well as single and two top quarks in association with various vector bosons. Similarly to the measurement presented in this work, the EFT interpretations are performed in the SMEFT framework and focus on the specific operators related to the top quark. However, there is considerable overlap with the Higgs sector, which lies in the nature of the relation between the two particles. Due to the slightly different frameworks and bases involved, the translation between the SMEFT operators and κ-coefficients involves some difficulties.

3.2 The Top-Quark Sector of EFT

The EFT framework is a very general approach to model and correlate any kind of new physics among a set of operators and a multitude of potential observables. This comes at the cost of very high dimensionality. On the one hand, this introduces challenges, for example, in the numerical handling of such interpretations. However, with enough information and the necessary orthogonality in such interpretations, an increasing number of parameters can be included and the EFT space expanded. The orthogonality is introduced, since different measurements will be diversely impacted by potential EFT effects and therefore contain complementary information on the operators potentially involved. Therefore, to fully benefit from the bottom-up approach, it is essential to combine measurements in order to be able to increase the number of operators at play as well as to exploit the correlations. This additional *angle* on the effects of a certain operator can help to improve limits with a better disentanglement of the effects of multiple operators.

However, combinations of measurements are generally elaborate tasks. The most consistent statistical approach for interpretations of this kind would rely on a combined likelihood describing all measurements in the combination, but an approach like this, yields many challenges. Measurements of different collaborations, for example, use vastly varying software frameworks, modeling of uncertainties or phase spaces. Harmonizing these in a sound way is a big challenge. Furthermore, even within one collaboration, there are lots of variations of, e.g., methods for background or signal modeling and the corresponding uncertainties. Potential correlations between measurements are often hard or impossible to estimate. Therefore, global combinations in the framework of SMEFT usually employ certain simplifications.

Recent combinations [8, 85–87] use various datasets as well as methodologies. They all aim to cover increasingly large regions in the high-dimensional EFT coefficient space while exploiting potential correlations among the effects of the operators in the different measurements. Quite a few combinations of top-quark measurements have been performed at the LHC [85, 86] as well as a combination of these measurements with Tevatron data [8]. One of the most recent combinations includes Higgs and diboson measurements in addition to top-quark measurements [87]. This combination is able to constrain up to 50 dimensions in the EFT parameter space.

There are also combinations of measurements performed in different areas of the EFT framework, as discussed in the previous section. Some of these connect the top-quark sector with the b-quark sector [88–90], by combining observables from both fields. Several of these observables share the operators of interest. Therefore, by matching the different bases and energy scales, combinations of these measurements can provide very sensitive inputs to interpretations including a large variety of EFT operators. All of these combinations are reinterpretations of measurements, using a particular choice of EFT operators.

The other approach to interpreting data in the framework of EFT is as part of the measurement itself. An increasing number of top-quark related measurements [70–82, 91–93] by the CMS and ATLAS collaboration already contain EFT interpretations. While in the past, reinterpretations of measurements were common, this approach allows for tuning of the measurement to the sensitivity of potential EFT effects as well as thorough and sound treatment of all necessary information for the statistical analysis in the EFT framework. Furthermore, steps are taken towards combinations of top-quark measurements within the collaborations and among them. The advantage of combinations of measurements within a collaboration lies in the knowledge of correlations among the uncertainties in the measurement, which generally are unknown outside of the collaboration, as well as the similarity in the analysis methodology. Thus, the work towards such combinations aims at facilitating a sound handling of these aspects.
With the abundance of top-quark events in the datasets recorded at the LHC, differential measurements of the processes involving the top quark are becoming very precise. They describe the rates of these processes as functions of multiple kinematic variables, like the top-quark transverse momentum p_{T} or other observables like, e.g., the charge asymmetry. Differential cross-section measurements offer a more powerful way (as compared to e.g. a total cross-section) of constraining multiple EFT operators at once within a single measurement. The different bins of the differential measurements represent multiple correlated measurements, which can be used to break degeneracies among certain EFT operators, also called *blind directions*. Furthermore, measurements like this allow to exploit certain impacts of the EFT operators on kinematic features in the differential variable and to tune the measurement accordingly.

3.3 Statistical Concepts of the EFT Interpretation

In order to interpret the measurements in the context of the chosen framework of EFT, a statistical interpretation is used. It serves as the mathematical basis for making meaningful statistical statements based on the considered observations in the framework of a model. There are many methods and conventions to arrive at conclusions through statistical tests. These statistical tests are used in order to maintain objectivity when interpreting data. Generally, the statistical interpretation of probabilities and, therefore, their treatment is classified into two approaches: the *frequentist* and the *Bayesian* approaches. There are several differences and subtleties to the different interpretations, and often discussions about these take place on philosophical levels. However, the differences can lead to

different results or even affect the overall conclusions, although in most cases, results obtained using the two approaches will agree when assumptions are carefully aligned.
In the Frequentist interpretation, probability describes the asymptotic rate of an event in a growing set of data points obtained from an equivalent experimental procedure. While this somewhat intuitively applies to the nature of data taken at experimental set-ups like the ATLAS experiment, it does not necessarily yield an ad-hoc *interpretation* of the value in the context of the hypothesis to be tested. Applying this interpretation to a physical property like the top-quark mass, for example, does not come as natural. Interpreting a probabilistic statement about a hypothesis as a rate of infinite tests of said hypothesis is not a really tangible description of confidence.
In Bayesian reasoning, probabilities are interpreted differently. Here, they correspond to a more subjective seeming *degree of belief*. One may argue that in Bayesian statistics, this subjectiveness is not an additional feature when compared to Frequentist statistics, but rather just more obvious [94]. This subjective input, however, only applies to the interpretation of the data, whereas the construction and generation of data are more subtle in the frequentist approach. More exhaustive discussions of these subtleties can be found in Ref. [94–99]. In order to arrive at the Bayesian interpretation of a probability connected to the test of a hypothesis, the *prior beliefs* are a necessary input to the process of Bayesian inference. The a priori knowledge is encoded in a probability distribution as well, the prior. The prior is chosen by the scientist and can contain certain prior knowledge or assumptions as well as expectations on the relevant parameters or variables in the interpretation. It can, however, also be intentionally left uninformed or varied in order to test the impact. Combining a priori knowledge with observation to infer a better understanding of an observation in the framework of a model describes a quite intuitive concept of inferring knowledge. This way, the expectation will impact the result of the interpretation of the data. While this may seem like unwanted subjectiveness, it is a necessity for any high-level interpretation of data in the context of a given model or hypothesis. This way, the subjective input in the Bayesian approach to inferring knowledge from data is encapsulated. In this work, Bayesian reasoning is used to interpret the measurement in the framework of SMEFT.
In Bayesian inference, probability distributions are used to describe a parameter of a model in the context of, e.g., an observation. These distributions are called likelihoods, and basically assign probabilities to a parameter or a hypothesis. In contrast to this, the frequentist approach is based on testing hypotheses (and potentially rejecting them) without this probability description. Therefore, while a frequentist interpretation leads to statements on the hypothesis being true with a certain probability, the Bayesian interpretation actually assigns such a probability to, e.g., a model parameter. The construction of such a probability distribution for a given parameter of interest - like a physical observable - is based on the model framework used to describe it. All of the resulting knowledge at the end of the inference process is contained in the *posterior* probability distribution. It contains all the knowledge on a parameter given both the prior knowledge and the data used to infer further knowledge. Therefore, the observations or data used to infer knowledge on the parameter of interest as well as a priori knowledge about the parameter define the posterior. The posterior then gives the basis for the actual

interpretation of data. It is used to make statements about the updated expectation of the model parameters. Furthermore, it can be used to compare models, generate predictions, or quantify uncertainties.
The approach used in Bayesian reasoning was first described by Thomas Bayes in 1763 [100] and formulated into the theorem of Bayes and Laplace by Pierre Simon Laplace. Putting the above-mentioned objects in a mathematical context, the posterior probability distribution $p(\lambda|x)$ given a dataset x is the basis for the inference of knowledge on the parameters λ of a given model M. It is defined via the theorem of Bayes and Laplace,

$$p(\lambda|x) = \frac{p(x|\lambda) \cdot p(\lambda)}{p(x)} \tag{3.1}$$

where $p(x|\lambda)$ is the probability of the observation x - also called likelihood - if the theory with parameters λ is true, and $p(\lambda)$ is the prior probablity of the parameters λ. The denominator $p(x)$, often referred to as evidence, resembles a normalisation defined as the integral

$$p(x) = \int \mathrm{d}\lambda \, p(x|\lambda) \cdot p(\lambda) \tag{3.2}$$

over the parameter space of λ. The dimensionality of the probability distributions depends on the number of parameters of interest of the model, i.e. the dimensionality of λ. In the measurement presented in this work, the parameters λ are not measured directly, but the observations y_i have a functional dependence $y_i = y_i(\lambda)$ on the parameters of the model. In particular, the observed differential rates follow the model described in Equation (2.5). Thus the model M to be tested for is inserted via this dependence. The update of the prior knowledge on the model M encoded in the posterior distribution is therefore described by

$$p(\lambda|x, M) = \frac{p(x|\lambda, M) \cdot p(\lambda|M)}{p(x|M)} \,. \tag{3.3}$$

In this equation, the term $p(x|\lambda, M)$ then describes the probability distribution of observing the data x given the model M with its parameters λ. Thus this is the likelihood following from the model M. The observables are compared to the dataset x for the interpretation in a likelihood-based approach, which is generally applicable assuming multivariate Gaussian uncertainties. In many applications of parametric inference, likelihoods are used to describe the model parameters in light of observation. They are usually represented as the negative logarithm of the likelihood outlined here and can be written as

$$-2 \ln p(\mathbf{x}|\lambda) = (\mathbf{x} - (\lambda))^T C^{-1} (\mathbf{x} - (\lambda)) \,, \tag{3.4}$$

where the vector $\mathbf{x}$ represents the observed differential rates and $\sigma(\lambda)$ the model as a function of the model parameters which are the Wilson coefficients of interest. The covariance matrix C contains the uncertainties of the measurements as well as potential correlations among them. This object is described in more detail later. As outlined above, the inference relies on the prior distribution, which in this case is $p(\lambda|M)$, describing the model parameters λ in the model M prior to the data input. These can have any functional form appropriate for probability densities, but this is not a requirement. Priors

can incorporate, e.g., physical boundaries or prior knowledge about the probable range of the model parameters. However, they can also be chosen to minimize a priori knowledge. In the case of multiple observations of relevant data because of several different experimental sources or the sequential nature of the data, the knowledge update paradigm in Bayesian statistics also presents a natural way of iterative knowledge updating. Through the input of the prior distribution in the inference, the posterior of a first inference step can function as the prior to a second step of inference and so on. This way, a stringent knowledge update for, e.g., continuous data flux, is possible. This approach, however, does not differ from interpreting all data at once.

As described above, the posterior distribution for the parameters of a model M contains all the inferred information on the model. Thus, the dimensionality of the posterior equals the number of free parameters in the model or the size of λ.

Since parameters in a physical model, e.g., frequently describe fundamental objects which have meaning outside the particular manifestation of the model M (e.g., in an extended or more fundamental model), statistical statements on sub-groups or single parameters of the model are of interest. Furthermore, in order to describe correlations or the interplay of a sub-set of model parameters, a reduction of the posterior to said parameters is necessary. All of these statements are possible based on *marginalized* posteriors. Marginalized posteriors represent a projected version of the full posterior, where only information about certain dimensions of the model parameter space is included. This way, statements about single parameters or a sub-set of such can be made. In order to marginalize a posterior probability distribution, the posterior is integrated over all but the model parameters of interest. The marginalized posterior $p(\lambda_i|x, M)$ describing the knowledge on λ_i of the model M is thus described by

$$p(\lambda_i|x, M) = \int \Pi_{j\neq i}\, \mathrm{d}\lambda_j\, p(\lambda|x, M)\,. \tag{3.5}$$

A similar approach was already discussed earlier in light of the evidence in the denominator of Equation 3.1. In general, the marginalization of the posterior describing the knowledge about a multi-dimensional model is what facilitates making meaningful statements when aiming to infer knowledge on the fundamental parameters of the description of, e.g., a physical process. The posterior distribution in the context of EFT will incorporate all the observations to be interpreted in the EFT framework and can then be used in the statistical analysis. Since it describes the inferred knowledge about the parameter(s) of interest from the data, it is used to make statements about these parameters based on the analyzed observations.

After marginalizing a posterior distribution, the resulting probability density distribution can be used to find a *best guess value* for a parameter of the model. Assuming there is a true value of this parameter, the choice of the guess would be based on getting as close to this value as possible. In order to define what *close* means precisely in this context, there are specific metrics, also called loss functions. However, the true value of the model parameter is generally not known in applications of Bayesian inference like this. Therefore, the posterior distribution is used as input to construct the distance to what is *believed* - based upon the inference procedure described above - to be the best guess. Since it

describes the degree of belief as a function of the model parameter, one can, e.g., choose the value of the model parameter that maximizes that degree of belief. This value is called the global mode of the posterior. Additionally, the shape of the posterior contains information on the topology of the inferred knowledge. A very narrow peak of maximum degree of belief which contains a large portion of the probability within a small region of the parameter space, e.g., hints at a very strong constraint of that parameter based on the observation. On the other hand, a relatively flat posterior distribution does not allow for strong statements about the model parameter and hints at a small information content of the data with respect to the particular model parameter. This information can thus also be used to make statements about regions with a certain *content of belief* to contain the best guess value for a model parameter. There are many different ways to define and therefore construct this credibility region. One way to define a region of, e.g., 95 % probability is to find a region of the posterior which contains this amount of the probability. Generally, this would be an ambiguous problem since there is an infinite number of different regions which would fulfill this requirement. Thus, the interval is generally chosen to be the smallest one fulfilling this requirement. Therefore, in numerical calculations, the region is constructed starting from the point of maximum probability and then constructed by expanding the region around this maximum. For a one-dimensional posterior, the one-dimensional range would then yield an integral of 95 % when integrated within its limits. These limits then describe the region of interest and give a description of the inferred knowledge on a model parameter at the chosen confidence level.
However, in High-Energy Physics (HEP) it is generally not possible to solve the inference analytically and recover a functional description of the posterior distribution. There are severel reasons for this, with the high dimensionality and the estimation of correlations among measurements among them. Therefore, numerical samplings are commonly used in Bayesian inference approaches to describe the posterior.

3.3.1 Numerical Modeling of Bayesian Inference

In order to perform the numerical computations for the Bayesian inference, i.e., the sampling of probability distributions and the numerical integration of these, the framework EFT*fitter* [101] is used in this work. EFT*fitter* is a tool for numerically calculating likelihoods for parameters of a given model from data. It makes use of the Bayesian Analysis Toolkit (BAT) [102], which uses the likelihood to sample distributions and performs numerical integrations to, e.g., facilitate combinations and interpretations of measurements. BAT in turn is using the theorem of Bayes and Laplace, as shown in Equation 3.3, to, e.g., perform the inference. These frameworks are used to interpret this measurement in the context of EFT and derive limits on the Wilson coefficients of interest.
In order to describe the various probability distributions in the statistical approach used here, numerical sampling algorithms are used. Per default, BAT uses Markov Chain Monte Carlo (MCMC) algorithms to perform this task. These algorithms provide a computationally efficient way to sample the distributions [103]. MCMC algorithms combine numerical simulations with the random number generation that characterizes Monte Carlo approaches, which are widely used in HEP. By using the large amount of readily available

computational power, these algorithms allow for solving many mathematical problems numerically to a degree of precision which allows for applications in the most precise measurements. MCMC algorithms use a sequence of states in order to quickly converge to a sample of the object of interest. This way, e.g., the posterior distribution of the parameters of a model can be estimated at great precision even though a direct calculation of the functional description is not possible. The sampling is done using a series of states, which need to satisfy the *Markov property*: the transition probability of a given state to the next state can only depend on these two states and needs to be independent of the rest of the sequence's history. There are different algorithms to determine the next state. Once the functional description of a given state to be followed by another one becomes independent of the current step in the sequence, it is called stationary. This implies that every sequence has a certain length before reaching this point. Therefore one of the goals of employing MCMC algorithms is to reduce the length of this phase, as well as reliably determine the point of convergence. In the case of Bayesian inference, the posterior distribution is described by sampling at the stationary point.
The sampling in the MCMC algorithm can, e.g., be done using the Metropolis-Hastings algorithm [104]. This algorithm generates a chain of sampling points S starting from an initial point S_0. The goal of the sequence of sampling points is to converge towards a **stationary** set of sampling points that describe the distribution π, based on an unnormalized functional description g. This way, a numerical description of the sampled distribution becomes available. The algorithm starts from an initial point S_0, which is used to suggest a new point S_1. The suggestion is based on the initial point and a random draw from a **proposal distribution** $P(S_1|S_0)$. In the Bayesian approach, this is where the prior distribution enters and shapes the sampling process. The drawn sampling point is then either accepted or rejected as the following link in the chain. This decision is made based on a second distribution called **transition probability distribution** $T(S_0|S_1)$. The probability of moving to a new point S_{i+1} in the chain is then described by

$$p(S_{i+1}|S_i) = P(S_{i+1}|S_i) \cdot T(S_{i+1}|S_i)\,. \tag{3.6}$$

In the Metropolis-Hastings algorithm, the transition probability distribution is chosen as

$$T(S_{i+1}|S_i) \equiv \min\left(1,\, \frac{g(S_{i+1})}{g(S_i)} \cdot \frac{P(S_{i+1}|S_i)}{P(S_i|S_{i+1})}\right) \tag{3.7}$$

which follows the Metropolis criterion. This is equivalent to the principle of detailed balance, which in the Markov chain manifests as the factorization of probabilities of the decision of steps in the chain. This makes the steps in the chain reversible because the probability of the state change is as well. The Markov chain ends after a finite number of steps once stationary behavior occurs. However, since the choice of S_0 impacts the sampling in the early phase of the chain when the sampling points do not necessarily represent a good approximation of the target distribution, they are usually discarded. This *burn in phase* can be handled in various ways (see e.g. Ref. [95, 96]).

EFT Interpretation of a Differential Measurement

4

In order to interpret a differential measurement in the framework of EFT, multiple steps, besides the statistical approach described in Section 3.3, are necessary. The structure of a differential measurement of top-quark data to be interpreted in the EFT framework is outlined in this section.
There are recent guidelines of the LHC EFT WG [105] as well as of the ATLAS Top WG [106] on the structure of EFT interpretations of several kinds of measurements. Both of these documents are very recent, and the latter one is the first version and was first available halfway through this project, showing the relevance and relative timeliness of this approach. Within the ATLAS top physics community, this work is among the first of this kind, and the approaches used in such analyses are still an evolving field of work. The following sections outline the principle steps from collider data to an interpretation in the framework of EFT as is performed in this work.

4.1 Process Definition and Modeling

For a given process of interest to be measured, there are certain established steps. Among the first are the definitions of the measurement. For any measurement, a **signal** has to be defined. This signal can be a certain process - like the production of a pair of top quarks - or a combination of processes that yield a particular final state of objects in the detector. Therefore, in order to define these properties, the reconstruction of physics objects from the data is necessary. These can represent particles like, e.g., muons or more complex objects like jets which consist of a multitude of particles and can be used as proxies for an initial parton in the hadronization process. Additionally, the measurement is based on certain **selection criteria**, following from the signal definition and characterizing the respective events in the data. Among them are selections of the phase space of the measurement based on kinematic variables of the objects involved and criteria to select the exact signal final state or channels of the signal process(es).
Generally, for any given signal process represented by a selection based on physical quantities, there will be events from multiple background processes passing this selection and contaminating the selected events. These can be processes mimicking the final state of the signal, events containing misidentified objects, or random combinations of objects of different origin passing the selection criteria. In order to define requirements to select signal events over background events, the data needs to be translated into reconstructed and identified physics objects. This reconstruction of physics objects uses the information from the multiple detector systems to generate meaningful data to perform a physics

analysis on.
All of these selections affect which EFT operators are potentially at play in this process and what the sensitivity of such a measurement to these operators is. The signal definition defines the vertices for possible EFT operators in the Feynman diagrams. Depending on the process or channel, the group of possible couplings, as well as their probability of appearance, will change. The selection criteria set the stage for potential enhancements of sensitivity based on the respective operators' kinematic features. Because of these features, potential EFT effects can change drastically depending on the phase space.
The actual measurement process of the signal itself involves multiple steps as well. Among them is, e.g., the **modeling** of the signal and background topology. The theory expectation of how a certain signature (background or signal) looks like in data is mostly based on simulations. However, in certain cases, data-driven methods are used, which utilize measurements when simulations are not feasible or not precise enough. These simulations are the basis for adopting the above-mentioned analysis steps. They are used to perform the tuning of the selection to select the signal and suppress the backgrounds as well as possible.
Here and through other steps of this chain, certain systematic uncertainties are introduced. They describe the uncertainties in, for example, the estimation of the prediction, the calibration of physical objects in data, or the measurement of the integrated luminosity, corresponding to the collected data. Therefore, they play a vital role in any measurement in order to determine the accuracy and thus the significance of an observation. In order to estimate them, several different methods are used, mostly based on simulations. The signal selection, as well as the simulations used in this analysis are discussed in Section 6.4, while the theoretical basics of the signal process are described in Section 2.2.

4.2 Detector Effects

Data recorded by a detector like ATLAS will contain a specific profile of characteristic *distortions* when compared to the underlying physical *truth*. The distortions are defined by the detector design and specifications. The detector's characteristics consist of, e.g., finite precision of the various detector-systems, the acceptance of the detector, as well as the calibrations of the different physics objects. Therefore, data on this level (detector or reconstruction level) needs to be interpreted in a specific way in order to infer information on certain characteristics of the underlying physics. In particular, the characteristics of the detector need to be understood very precisely to compare the measurements with any model prediction. Thus, in order to interpret the measurement in a way that is as independent of these effects as possible and therefore allows for comparisons with theory predictions and other measurements in a more straightforward way, the data can be corrected for these effects. To facilitate this, the effects are accurately modeled in simulations. These simulations are then used to solve the inverse problem of removing the distortion in data. The process of removing the detector specifics and performing the measurement at a level of certain physics objects of interest is called *unfolding*. Since the unfolding procedure relies on simulated data which in turn assumes the SM, tests

for potential biases toward the SM are necessary in order to interpret the measurement within a BSM model.
Interpretations of measurements can also be performed on the detector-level measurements. Instead of unfolding the data, the model predictions are extrapolated to the detector level using the aforementioned modeling of the detector. The advantage of such an interpretation over the one based on unfolding evolves around the above-mentioned potential bias toward the SM when unfolding. Furthermore, since the step of adding (or similarly removing) the detector characteristics changes the observed distributions in an a priori non-trivial way, potential EFT effects can change the strength of their impact on the measurement when comparing the two levels. Therefore, an interpretation of the measurement can lead to potentially quite differently stringent limits when comparing the two approaches. There are, however, cases where an unfolding is very difficult or not feasible to employ. In cases of a non-existent, or very feeble signal rate compared to the backgrounds, for example, an unfolding can become problematic due to the large statistical uncertainties it would introduce.
Unfolded measurements are, however, generally easier to interpret, especially in the context of various theory frameworks. Furthermore, such measurements facilitate easier combinations and comparisons with other measurements, which is an important advantage when employing the EFT framework for interpretations. However, both kinds of measurements are valid inputs to an EFT interpretation, with the specific sets of caveats. In this measurement, the interpretation is performed at particle level after unfolding the measurement. The unfolding process is described in Section 7.2, and the above-mentioned caveats of interpreting an unfolded measurement in the context of EFT are addressed in Section 11.

4.3 The EFT Model

In order to interpret these measurements, a model is necessary. In the case of this measurement, the model is constructed in the framework of EFT. The EFT approach at dimension six provides a large set of operators, which can be reduced to around 59 top-philic[1] operators, as mentioned in Section 2.4. In order to define the specific model for this measurement, the choice of operators needs to be specified more. The number of operators to be constrained at the same time is limited by the number of measurements. However, there is no a priori prescription of operators for a given process since the specifics of the interpretation very much depend on the measured observables and the details of the measurement mentioned above. Furthermore, since, in most cases, a selection has to be made among the operators to constrain the dimensionality of the EFT model, the choice of operators can be influenced by other factors as well: e.g., a comparison with current global limits or matches to certain BSM models can hint at particularly interesting candidates. The choice of operators in this measurement is described in Section 9.1.

[1]This set of operators is aimed at describing interactions of the top quark, and therefore contains operators affecting only top-quark interactions. Furthermore, certain choices for adequate linear combinations of operators due to their appearance in top-quark interactions are made [8].

Once the EFT model and its parameters are defined, similar to the statistical model M in Section 3.3, a functional description of the observables in this framework is necessary. For a differential measurement, the observables consist of each bin of each variable in the interpretation. The functional description shown in Equation (2.5) is the basis that needs to be adapted to the specifics of the measurement. In order to do that, modeling of the EFT effects is necessary. Like for other models, this is achieved by simulating the potential EFT effects in Monte Carlo simulations. The simulations used in this measurement are described in Section 9.2, followed by the construction of the EFT model in Section 9.5. The modeling is done using the common tools for the generation of collision data, which are then extended by a model for the necessary EFT modifications to the calculations of the scattering process.
Once the EFT model is adapted to the measurement's specifics, a choice for the observables to be interpreted needs to be made. Generally, any observable can be interpreted in the framework of EFT. However, one is usually interested in optimizing the potential to find BSM physics effects, or, in their absence, constrain the EFT parameter space as much as possible. In the absence of BSM effects in the interpretation, the constraints on potential effects from certain operators are valuable inputs to combinations, as well as indications for the compatibility of the data with the SM. Such constraints therefore also hint at the potential for BSM searches of certain regions of the vast EFT operator space. Thus, since the EFT effects can vary a lot among different observables, the choice of observables needs to be tuned for sensitivity. This choice can be based on multiple metrics. The first one is the expected sensitivity to EFT effects in the observable. This sensitivity is already indicated by the effects, the operators of interest have on the observable. However, making a quantitative statement from this is not trivial, especially if multiple operators are involved. Aspects like the ability to disentangle the effects of multiple operators and the kinematic dependence of the operator are not apparent from the direct effects on the observables. Additionally, the uncertainties significantly impact the sensitivity of a measurement as well. Therefore, the final discriminant will be the expected limits when using the observable in a pseudo-data fit. These expected limits in the context of the choice of the observable are described in Section 10.
In addition, there are other, more subtle factors to consider when choosing the observable of choice. The accuracy of the predictions plays a role as well: bad modeling of the EFT effects in (regions of) an observable will negatively affect the ability to constrain the EFT contributions. These factors are discussed in Section 10.2.2. Finally, potential biases towards the SM need to be considered as well. Observables that introduce significant biases towards the SM or of any other kind are not well suited to guarantee an unbiased interpretation, even if they lead to stronger limits. Biases can, e.g., be introduced by the unfolding procedure or any other step in the analysis chain which relies on SM predictions. The aforementioned systematic uncertainties aim at covering such biases. Upon introducing potential new signal, like EFT contributions, however, particularly the unfolding procedure needs to be scrutinized. In Section 11, a general validation of the EFT model set-up is discussed.
The statistical and numerical set-up used for the EFT interpretation are described in Section 3.3 and outlined for this measurement in Section 10.1.

Overview of the ATLAS Detector at the LHC 5

The LHC [107] at CERN is the biggest particle accelerator in the world. It represents the last stage of the accelerator complex at CERN, which consists of multiple machines which sequentially accelerate a beam of protons or heavy ions like, e.g., lead. During Run 2, as a first step protons were accelerated by the linear accelerator LINAC2, which then injects these into the Proton Synchrotron Booster (BOOSTER), the first circular accelerator. The BOOSTER then creates the bunches that make up the substructure of the proton beam. A proton beam is created, which is then injected into the bigger Proton Synchrotron (PS) and the even larger Super Proton Synchrotron (SPS). These two circular accelerators increase the energy to 450 GeV before injecting the beam into the LHC. Upon injection, two proton beams are created, which circulate in opposite directions in the storage ring. The LHC then accelerates the protons to a maximum energy of 6.5 TeV and stores the proton beams.
With a resulting center-of-mass energy of $\sqrt{s}$ =13 TeV it provided proton-proton collisions during Run 2 between 2015 and 2018 at the highest energy ever recorded. The proton beams consist of bunches of protons. At the LHC, the proton beams are brought to a collision at four interaction points (IP), where at each a dedicated experiment is placed to record the produced events. The maximum rate of bunch crossings is 40 MHz. The LHC was designed to provide an instantaneous luminosity of $10^{34}\,\mathrm{cm}^{-2}\mathrm{s}^{-1}$, which was already exceeded by up to a factor of 2 in the Run 2 data-taking period [108].
The ATLAS detector [109–111] is one of the four large experiments at the LHC. It is a multi-purpose[1] detector and surrounds one of the IPs at the LHC. A schematic view of the 44 m long and 25 m high cylindrical detector is shown in Figure 5.1. During Run 2 the ATLAS detector recorded a dataset corresponding to $139\,\mathrm{fb}^{-1}$. The detector consists of an inner tracking system surrounded by a superconducting solenoid producing a 2 T axial magnetic field, electromagnetic and hadronic calorimeters and an external muon spectrometer incorporating three toroidal magnet assemblies. It is designed to detect the tracks and measure energies of particles emerging from the collisions, covering as much of the solid angle as possible. Additional to the solenoid magnet, the magnetic system consists of eight large barrel toroids arranged in a concentric symmetry around the barrel region ($|\eta| < 3,2$) as well as smaller toroid magnets at the end-caps, covering the forward region ($3.1 < |\eta| < 4.9$). This magnet system creates magnetic fields in all parts of the detector, that are facilitating measurements of tracks and, therefore, allows to determine charge and momenta of charged particles.
The geometrical description of the measured objects is based on a right-handed coordinate

[1] The detector is designed to cover a large variety of specific particle-physics phenomena, such as various searches for BSM physics, rather than being specialized on certain signatures.

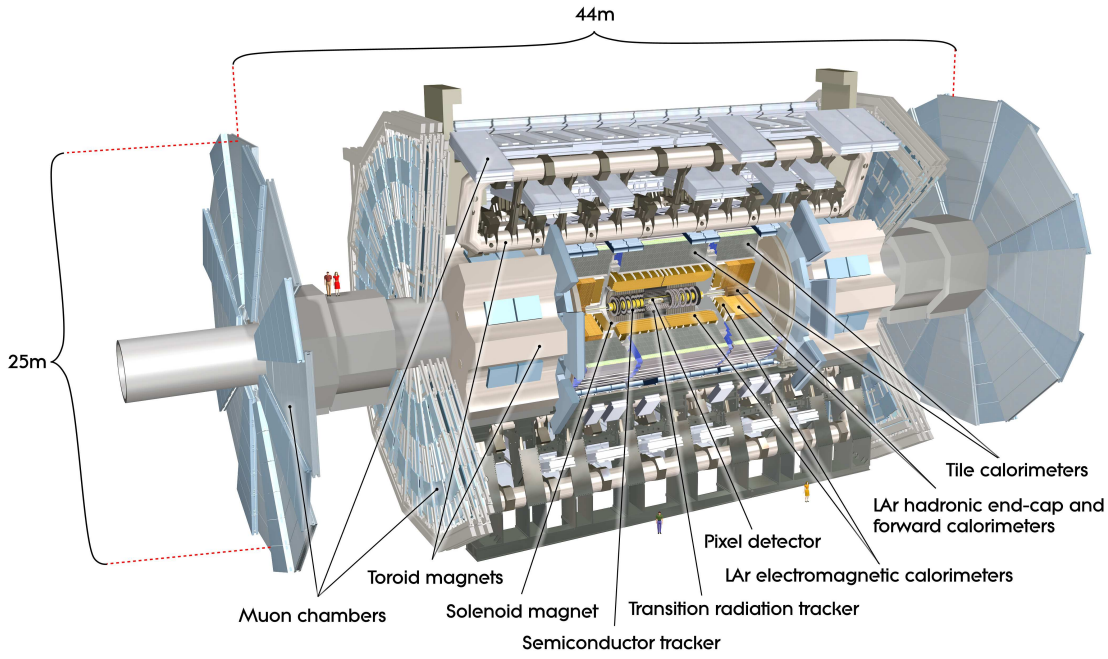

Figure 5.1: Schematic cut-away view of the ATLAS detector during the Run 2 data-taking period. The detector is located at one of the collision points of the LHC and its dimensions are 25 m in height and 44 m in length [109].

system, which emerges from the collision point at the center of the detector. The z-axis follows the beam pipe, while the x-axis points towards the center of the LHC ring. The y-axis is thus chosen to point from the IP towards the surface. Due to the shape of the detector, cylindrical coordinates are used to describe events within the detector volume. The transverse plane is described by the tuple (r, ϕ), where r is the distance to the IP in the x-y plane and ϕ is chosen as the azimuthal angle around the z-axis. The pseudo-rapidity η is defined based on the polar angle θ as $\eta = -\ln \tan(\theta/2)$, whereas angular distances are described via $\Delta R \equiv \sqrt{(\Delta\eta)^2 + (\Delta\phi)^2}$.

The inner tracking system [110] takes an important role in the tracking of charged particles emerging from the collision point. It comprises the part of the detector closest to the collision point. By using the 2 T axial magnetic field of the solenoid, which surrounds the ID, charged particle tracks are curved, which enables to determine their charge and momentum. Furthermore, the primary vertex (PV) and potential secondary decay vertices (SV) are essential properties measured in the inner tracker. Most tracking subdetectors consist of silicon sensors which are arranged in a cylindrical shape called *barrel* in three different sub-detectors around the IP. The material choice was made, since it combines an excellent spatial resolution with radiation hardness. The latter is needed since the tracking detectors need to withstand the most extensive amounts of radiation and radiation damage, due to the proximity to the IP. The innermost layer of the pixel detector, called insertable B-layer (IBL), was added to the detector set-up during long shutdown 1. Its purpose is to extend the tracking detector closer to the beam pipe and provide measurements with

finer granularity. Furthermore, the pixel detector consists of three layers, surrounding the IBL, and *disks* at the end of the barrel aligned with the cylindrical ends. It has a specific resolution of 10 µm in the transverse plane (described by (r, ϕ)) and a resolution of 115 µm in z direction and radial direction in the end-caps. The pixel detector is surrounded by the silicon microstrip tracker (SCT), which consists of four layers. The layers consist of double layers of small-angle strips, as well as additional disks for the end-caps of the detector. The resolution in the transverse plane is typically 17 µm, while the resolution in z direction and radial direction in the end-caps is 580 µm. The inner detector's acceptance lies within $|\eta| < 2.5$. The outermost part of the inner detector (ID) covering $|\eta| < 2$ is the transition radiation tracker (TRT). This sub-detector uses straw-tubes filled with gas to track traversing particles and additionally provide information on transition radiation, which is important in the identification of electrons. Due to the strong magnetic field of the solenoid magnet, charged particles traversing the ID move on bent trajectories, which allow for determining the charge and momentum of the particles.
Similarly, the ATLAS calorimeters consist of a number of different detectors. The calorimeters perform energy measurements of the traversing particles. By alternating absorber material like lead and the actual sensors, particles are forced to interact with the material and deposit energy, which is measured in the instrumented detector material. The goal of calorimetry is to stop and contain electromagnetic and hadronic particles. These create multiple other particles while traversing the detector, which lead to shower-like signatures in the calorimeters. This guarantees precise energy and thus missing energy[2] measurements and allows in addition to prevent those showers from spilling into the subsequent detector layers. The calorimeter systems are arranged in a rotation-symmetric manner around the ID and therefore cover the full angle ϕ around the beam axis, while measurements within $\eta < |4.9|$ are possible.
The electromagnetic calorimeters (ECal) are spread over three parts, a barrel, and two end-caps and are the calorimeters closest to the beam-line due to the properties of the particles they are primarily targeted at: particle showers originating from electrons and photons. These have much smaller interaction lengths in the detector than, e.g., hadrons. The granularities of the detectors are much finer within the ID acceptance to allow for precise measurements of electrons and photons, while the other regions have more coarse structures which are sufficient for, e.g., measuring jets. The fine granularity in this part of the detector also allows good resolution of the shapes of the showers, which is used to identify the particles. The ECal consists of lead interaction layers, while the detector material consists of liquid Argon (LAr), where the layers are arranged in an accordion-like shape. While the barrel solely contains the electromagnetic barrel calorimeter, the two end-cap cryostats each contain an electromagnetic calorimeter, a hadronic calorimeter (HCal), and a forward calorimeter (FCal). The HCal in the end caps is located behind the EM calorimeter. The HCal consists of 3 sub-detectors: the tile calorimeter, the end-cap calorimeter, and the forward calorimeter. The Tile HCal is located right outside

[2]The reconstruction of neutrinos in the ATLAS detector is not possible, due to their tiny interaction rates. Therefore, such particles leave the detector, carrying a certain fraction of energy which is missing from the reconstructed event.

the ECal in the barrel region and consists of a sampling calorimeter using scintillating tiles alternating with steel absorber layers. The end-cap calorimeter, located behind the end-cap ECal consists of two wheels per end-cap and uses copper plates interleaved with layers of LAr sampling detectors. Finally, the FCal is located close to the beam axis at $|\eta| > 3.1$ to cover the region closest to the beam. It is integrated around the beam axis, surrounded by the other end-cap calorimetry detectors and consists of detector layers suited for both hadronic and electromagnetic measurements. To facilitate this, the interaction layers consist of copper, followed by ones made of tungsten, which show good interaction properties for the different shower types. The instrumented detector material is LAr.
The muon spectrometer system is the outermost part of the ATLAS detector and covers both sides of the end of the detector as well as the barrel region, as shown in Figure 5.1. Its purpose is to track charged particles leaving the calorimeter systems of the detector in order to determine the trajectories and momenta in the magnetic field. This field is created by the barrel and end-cap toroid magnets. The only detectable particles reaching this detector part are muons, because of their longevity and low interaction probability. The detector consists of multiple wheels, in turn consisting of concentric cylindrical shells of *Monitored Drift Tube chambers* (MDTs) around the beam axis. These precision-tracking chambers are located between and covering the eight coils of the toroid magnets in the barrel region (analogous to the ϕ-symmetry of the magnets) as well as in front of the two end-caps. The MDTs measure traversing particles with a precision of 35 µm per chamber. The multi-wire proportional chambers located in the forward region ($2 < |\eta| < 2.7$) consist of cathode-strip chambers due to their resistance to the higher rates as well as the better time resolution.
In order to be able to efficiently store relevant data, the ATLAS detector read-out system operates a trigger system [112]. This system only records events which show certain characteristics that hint at the potential relevance of the event. The trigger system consists of two levels, the hardware-based first-level trigger L1 and a subsequent, software-based high-level trigger (HLT). The L1 trigger utilizes granular information of certain sub-systems, such as the calorimeters and muon detectors to decide whether to store an event. The passing regions of interest, which already reduce the event frequency to 100 kHz, are then processed by the HLT trigger. This trigger level utilizes finer-granularity information from the calorimeters, the muon system and tracking information from the ID. By applying these additional requirements, the data-taking rate is reduced to about 1 kHz, at which the data is stored to mass storage devices. The combination of these different subdetectors enables ATLAS to collect very precise data on particle trajectories as well as their energies and momenta, which are used to identify particles and reconstruct their properties. This way, the large collision frequency of the LHC and the matching read-out speed of the ATLAS detector allow for large amounts of data to be collected.

6 Data Samples and Event Selection

In this work, a number of different datasets are used. Alongside the observed data, there are several simulated data samples used as predictions throughout this analysis.
Next to the modeling of the signal process mentioned in the previous chapters and outlined in more detail in Section 6.4, there are several background processes mimicking the signal topology. In order to select a dataset with a high purity of signal events these need to be removed from the data. In order to suppress the effects of these backgrounds, a selection is applied to all events, which aims at providing a high purity of signal events while keeping as many signal events as possible. The selection criteria are based on the background predictions and thus rely on precise modeling of these processes. Therefore, dedicated simulations are necessary in order to predict the effects of these processes and provide a pure dataset. This selection is described in Section 6.4 as well.

6.1 Signal and Background Processes

Measurements in high-energy particle physics generally focus on a process of interest – the signal. This process can be motivated by its properties, the participating particles, or a connection to potential BSM physics. In certain cases, however, also non-signal processes can be of interest to a measurement. If, for example, the modeling of such processes is particularly difficult data-driven estimates may be necessary. The data selection, based on the definition of the process of interest, uses specific features of the data. These contain the type and kinematic properties of final state particles derived from the various sub-detectors of the experiment. Since such features can never be exclusively attributed to a single process, the selected data will contain events from other processes than the signal for any given process. Typically these events contain a similar collection of measured particles or a number of misidentifications, e.g., due to the limited efficiency and acceptance of the measurement, which lead to a similar final state.
The signal process in this analysis is the production of a pair of top quarks as outlined in Section 2.2. Since the W bosons from the decays of the top quarks have several possible decay channels, there are several final states to this process. As sketched earlier, these decay channels are classified by the number of leptons produced in the decay of the W bosons, ranging from zero to two. In this measurement, the final state with exactly one lepton is defined to be the signal process. The detailed selection is described in Section 6.4.
The most prominent background arises from the production of a single top quark in association with a W boson. It is described in more detail in Section 6.5. This process creates the same final state as the signal. The top quark decays predominantly into a

W boson and a b quark, leading to the same $WbWb$ state as in the decay of the $t\bar{t}$ signal. Following this background process, the production of a pair of top quarks in association with a vector boson V (which can be a W or Z boson) or in association with a Higgs boson H contributes the most. Here, the additional bosons can add leptons or more jets to the final state. While, the leptonic decays of the vector bosons are well suppressed, events containing additional jets can pass the signal selection. Next to the hadronic decays of the W and Z bosons, these can, for example, originate from a $H \to b\bar{b}$ decay, although the b jets then need to falsely be untagged.

However, these processes already only contribute very little (at the order of 1 %) to the selected data. Other background contributions stem from the production of multiple jets or a vector boson in association with jets, as well as the production of two vector bosons.

6.2 Simulating Collision Data

In high-energy physics and collider physics in particular, the predictions from the theoretical description need to be translated to the observational data. This data, which is collected by the detector from particle collisions, like proton-proton collisions at the LHC, strongly depends on the detector used in the measurement. However, there are multiple fundamental models describing the various processes from the collision to the measurement. These models are used to numerically describe objects and their features in realistic collision data. In order to model this, computational simulations are used, which produce specific numerical predictions, which can then be compared to observations.

The simulation of the predictions starts at the theoretical prediction outlined in Section 2. For a given process, the SM is used to calculate the probability of such a process which is proportional to the matrix element (ME) of the Feynman diagrams involved. However, there are two different regimes of interactions, depending on the energy scales. The perturbative regime allows for analytical calculations of probabilities of certain processes in the respective theory. Interactions described by QCD, for example, show small coupling constants α_s in a sense that the participating partons are asymptotically free[1] and the perturbative description holds. Below a certain energy scale called the factorization scale μ_f, this perturbative description fails. The perturbative description provides very precise descriptions of the ME of the interactions. The probability is given as a cross-section, which represents the interaction probability as an area in the unit *barn*. The cross-section of a particular process is proportional to the square of the ME. For the collision of protons at LHC the cross-sections need to be weighted by the probabilities of the various initial states based on the structure of the proton. The structure is described by the PDFs of the partons and depends on the energy of the collision. In general, the factorization theorem describes the interplay of the perturbative and non-perturbative processes and allows to separately describe the two regimes. For the prodcution of n particles from 2 initial

[1] This asymptotic freedom appears at small interaction distances and is attributed to the behavior of the strong coupling constant at different energies, as described in Section 2.

particles a and b, it describes the cross-section of the given process as

$$\sigma_{2\to n} = \sum_{a,b} \int_0^1 \mathrm{d}x_a \mathrm{d}x_b \int \mathrm{d}\Phi_n f_a(x_a, \mu_F) f_b(x_b, \mu_F) \cdot \frac{1}{2\hat{s}} |\mathcal{M}(ab \to n)|^2 (\Phi_n, \mu_F, \mu_R) \,.$$

For a given process, this sums over all possible production channels and includes the full initial-state phase space (represented by the momentum fractions x of the initial particles). The PDFs of the participating partons are represented by the function f. The squared matrix element $|\mathcal{M}(ab \to n)|^2$ includes the perturbative calculations, as well as the incoming parton flux $\frac{1}{2\hat{s}}$, which in turn includes the center-of-mass energy. This product is integrated over the full phase space Φ_n of the final state particles n.
In the collisions, a plethora of particles is generated after the hard-scattering process of the simulated process. Those interacting via the strong interaction produce cascades of new particles, following the color confinement characteristic for this interaction. These cascades increase in particle multiplicity while decreasing in their kinematic energies. These processes generally end in the decays into stable particles. In order to simulate this process, parton shower models are used. These model the physical processes at the transition from the perturbative matrix element description to the non-perturbative regime. As such, the models include higher-order corrections to the ME calculations in form of additional low-energy (soft) and colinear radiation of particles from both the initial and final state particles. Such effects, called inital state radiation (ISR) and final state radiation (FSR), are particularly well described by these models in contrast to the ME calculations. The radiated particles, for example, consist of gluons radiated from the color charged particles, due to the nature of QCD interactions, but can also include, e.g., photons. Once, color-charged particles reach a particular low-energy scale $\Lambda_{\mathrm{QCD}} \approx 1\,\mathrm{GeV}$, they are captured in as hadrons, composite particles consisting of quarks. This hadronization of quarks falls within the non-perturbative region and can therefore not be described in perturbation theory. Following from the factorization theorem, the perturbative description and the non-perturbative description are matched and merged in order to benefit from the advantages of either one in a consistent description. Low-momentum radiation of gluons can additionally happen outside of ISR and FSR. Such contributions, which are part of the *underlying event*, can emerge from additional interactions in the pp collisions and are modeled based on data-driven methods.
The produced particles will interact with the various systems of the detector during the measurement. Furthermore, long-lived particles like, for example, b-Mesons traverse the detector on macroscopic scales before decaying. The interaction with the detector is simulated using dedicated models for the ATLAS detector, which incorporate the detector response for these interactions, as well as further steps in the reconstruction of the data. Among the simulation is the numerical description of the statistical process of the interactions with the material, the read-out of the produced signals, the digitization of these signals, and all the reconstruction steps to produce the physics objects, used to describe the physics processes. The modeling of the detector response is done using either the full simulation of the ATLAS detector [113] facilitated by the GEANT4 framework [114], or using a faster simulation based on parameterized showers in the calorimeters [115]. The reconstruction of the digitized events is done using the same reconstruction software [116]

in simulations and data. During the collisions of the two proton beams, the number of pp interactions fluctuates. The effects of multiple collisions during a single bunch crossing (pile-up) are therefore simulated as well. This is done by generating additional inelastic pp collisions using the parton showering algorithm Pythia 8 [117] and the A3 [118] set of parameters, which are overlayed onto the primary events.

6.3 Data and Simulated Event Samples

The observed and simulated data are described in more detail in the following sections. The top-quark mass (m_t) is set to 172.5 GeV in all simulated data samples aside from those used to study the impact of the uncertainty in m_t.

6.3.1 Observed Data Set

The observed data analyzed in this work was collected from proton-proton collisions at $\sqrt{s} = 13\,\text{TeV}$ during 2015–2018. The data set corresponds to an integrated luminosity of $139\,\text{fb}^{-1}$, where the luminosity measurement is performed by the LUCID-2 detector [119] with an uncertainty of 1.7 % [120]. The events are selected to fulfill standard data quality requirements [121] and to pass a single-electron or single-muon trigger [122, 123].

6.3.2 $t\bar{t}$ Signal

The nominal dataset, used to model the signal $t\bar{t}$ process was generated using the framework Powheg Box v2 [124–126] (Powheg in short). Powheg provides matrix elements for various processes like the production of a pair of top quarks at NLO in the strong coupling constant. The PDF of the proton is modeled using the NNPDF3.0nlo [127] PDF set in the five-flavor scheme, where the active number of flavors is restricted to five. The h_{damp} parameter is set to $1.5m_t$ [128]. In Powheg this parameter controls the matching and effectively regulates the high-p_{T} radiation against which the $t\bar{t}$ system recoils. The aforementioned parton showering is simulated by Pythia 8.230, including the hadronization of QCD particles and underlying event, using the A14 set of tuned parameters [129] and the NNPDF2.3LO [130] set of PDFs. In the figures in the following chapters, data from this sample is referred to as PWG+PY8. All variations of the $t\bar{t}$ signal are normalised to the cross-section prediction at NNLO in QCD including the re-summation of next-to-next-to-leading logarithmic (NNLL) soft-gluon terms calculated using Top++2.0 [131–137]. In this measurement of proton-proton collisions at a centre-of-mass energy of $\sqrt{s} = 13\,\text{TeV}$ the cross-section is predicted to be

$$\sigma(t\bar{t})_{\text{NNLO+NNLL}} = (832 \pm 51)\,\text{pb} \tag{6.1}$$

where a top-quark mass of $m_t = 172.5\,\text{GeV}$ is used. The prediction includes uncertainties due to the choice of modeling parameters like the PDF and α_{S}. They are derived using the PDF4LHC prescription [138], where the MSTW2008 68% CL NNLO [139, 140], CT10 NNLO [141, 142] and NNPDF2.3 5f FFN [130] PDF sets are used.

6.3.3 Alternative $t\bar{t}$ Predictions

In order to assess systematic uncertainties in the modeling of the signal process, alternative predictions are used. Furthermore, the comparison of variations in the predictions to data gives information on potential mismodeling and allows for quantifying the general agreement of predictions and data. The alternative samples are generally produced by varying parameters or frameworks in the predictions. Among the varied parameters are the scale choices for μ_{r} and μ_{f}, as well as the h_{damp} parameter. The latter is varied as described in Ref. [143]. The impact of the choice of ME generator is evaluated using simulations generated with MadGraph5_aMC@NLO 2.6.0 and the NNPDF3.0nlo PDF set instead of Powheg. The choice of scales in this variation is equal to the nominal sample and the events are also interfaced with Pythia 8.230. Variations of the simulation of parton showering and the hadronization models are produced using Powheg interfaced to Herwig 7.0.4 [144, 145] instead of Pythia 8.230. The showering framework Herwig 7.0.4 is set up using the H7UE set of tuned parameters [145] and the MMHT2014LO PDF set [146]. Another parameter to be varied is the mass of the top quark. The impact of the choice of this parameter is evaluated by varying the parameter to 169, 172, 173 and 176 GeV.
Additionally, the effects of higher-order corrections to the ME generation are investigated using additional signal samples. For this, MC predictions using Sherpa 2.2.10 [147] are generated, which include additional orders up to NLO in the predictions for up to one additional jet at ME level. Furthermore, LO predictions for up to four additional partons are included using the Comix [148] and OpenLoops [149–151] libraries.

6.3.4 Signal Modeling at NNLO

The most precise prediction at particle level of the production of a pair of top quarks and subsequent decay to a single-lepton final state are calculated at NLO and not yet available at NNLO. However, the impact of the missing orders in these QCD predictions can be evaluated using a reweighting procedure. For this, the MC predictions at parton level are reweighted to match the higher-order predictions. The reweighting is facilitated by an iterative procedure using three observables of the topology (p_{T}^{t}, $m^{t\bar{t}}$, $p_{\mathrm{T}}^{t\bar{t}}$) including initial and final state radiation. These variables are reweighted to match the higher-order predictions, which for p_{T}^{t} and $m^{t\bar{t}}$ are calculated at NNLO in QCD with NLO EW corrections [152] using the NNPDF3.0QED PDF set. The higher-order prediction for $p_{\mathrm{T}}^{t\bar{t}}$ is calculated at NNLO in QCD [153, 154] using the NNPDF3.0 PDF set and setting renormalization and factorisation scales to $H_{\mathrm{T}}/4$. The top-quark mass is set to be $m_t = 173.3\,\mathrm{GeV}$ in all cases. The iterative procedure to derive the reweighting is described in Ref. [155]. It is constructed to arrive at a set of weights that change the MC predictions of all three variables at NLO to have good agreement with the higher-order prediction. This way, the effects of the missing orders can be quantified in a comparison. However, this does not equal a proper prediction at NNLO in QCD, but rather a good estimation of the effects on these variables. The predictions produced this way are referred to as being reweighted to NNLO (or NNLO rw.) in the remainder of the document.

6.3.5 Background Predictions

As described in Section 6.1, there are several processes relevant to the described final state besides the $t\bar{t}$ signal. These processes constitute the background in this measurement, which is reduced by the selection criteria outlined in the next section. Similar to the MC predictions described in the previous sections, the background processes are simulated using particular generator set-ups. The modeling of the production of a single top quark in association with a W boson (tW) as well as the s-channel production of a single top quark is performed using Powheg [156, 157]. The predictions are generated at NLO in the five-flavor scheme using the NNPDF3.0nlo set of PDFs with the showering performed by Pythia 8.230. The t-channel production of a single top quark is modeled in the four-flavor scheme [158], but otherwise using an identical setup. As sketched in Section 6.5, there is overlap between $t\bar{t}$ production and the single top process at NLO. The separation of the two processes is achieved using the diagram removal (DR) scheme [159], which excludes the overlapping diagrams, as well as interference terms of such.
Background processes, including the production of jets in association with a vector boson – either a W or Z boson – are simulated using Sherpa 2.2.1. Similarly, processes including two vector bosons are modeled using Sherpa. The modeling includes ME at NLO in QCD for up to two additional partons and at LO for up to three additional partons. The generated events for both of these processes are interfaced to Sherpa for showering and hadronization.
The production of a pair of top quarks in association with a vector boson ($t\bar{t}V$) is modeled using MadGraph5_aMC@NLO 2.3.3 [160] at NLO, while the production of a pair of top quarks in association with a Higgs boson ($t\bar{t}H$) are modeled using Powheg. Both predictions use the NNPDF3.0nlo PDF set and are interfaced to Pythia 8.230 for showering and hadronization.

6.4 Event Selection and Object Reconstruction

As mentioned in Section 1, this analysis is selecting proton–proton collision events creating a pair of top quarks, that subsequently decay via the semileptonic $t\bar{t}$ decay channel ($t\bar{t} \to WbWb \to \ell\nu bqq'b$). Therefore, the signal event topology consists of exactly one lepton, two b-tagged jets, a neutrino manifesting as missing transverse momentum and the resulting jets from the hadronically decaying top quark. Furthermore, additional jets from hard scattering processes are allowed in the selection. A schematic view of one example decay channel is shown in Figure 6.1.
In order to describe this process with the collected data, three measurement levels are defined. The levels differ in a set of characteristics, which, among others, consist of the objects used to describe data as well as the modeling steps (like showering and detector simulation) included. The lowest level is called *parton level*. On this level, data is described by objects corresponding to particles directly involved in the hard-scattering process, like the top quark. These particles are described by the aforementioned ME calculations. The *particle level*, on the other hand, consists only of objects corresponding to stable particles. Stable in this context corresponds to a lifetime $\tau > 30\,\text{ps}$. These objects can,

e.g., be a top-tagged jet which is a composite object that can be linked to a top quark on parton level. Furthermore, there is a direct correspondence between certain particles on parton level and particle level, like for photons or neutrinos, for example. Generally, all particles interacting in the detector volume can be reconstructed on particle level. Finally, on *detector* or *reconstruction level*, the particle level objects are reconstructed using the various sub-detectors. Recovering a description of the corresponding particle-level objects is the goal of the aforementioned unfolding procedure. However, due to the specific response characteristics of the sub-detectors, as well as the aforementioned detector effects, certain distortions are applied on detector level. The different objects defined to describe this process and used to select signal events are described below.

Electrons Electrons are reconstructed based on tracks identified in the inner detector as well as in the ECal. They are required to pass $E_{\mathrm{T}} > 27\,\mathrm{GeV}$ as well as the *Tight* likelihood-based identification requirement [161]. Furthermore, they need to pass $|\eta| < 2.47$ as well as not be within the calorimeter transition region between barrel and end-cap, namely $1.37 < |\eta| < 1.52$. In order to assure good isolation from other activities in the vicinity, the *Tight* requirements are imposed on the calorimeter vicinity and nearby tracks, as outlined in Ref. [161]. Potential electron tracks must have transverse and longitudinal impact parameter significances of $|d_0|/\sigma_{d_0} < 5$ and $|\Delta z_0 \sin\theta| < 0.5\,\mathrm{mm}$ respectively. The longitudinal impact parameter is calculated relative to the event's PV, with θ being the polar angle of the track.

Muons Muon tracks are reconstructed from inner-detector tracks as well as information from the muon spectrometers. They have to pass $p_{\mathrm{T}} > 27\,\mathrm{GeV}$ and $|\eta| < 2.5$. Additionally, *Medium* identification as well as *Tight* isolation requirements [162] are imposed. Finally, candidates must have transverse and longitudinal impact parameter significances of $|d_0|/\sigma_{d_0} < 3$ and $|\Delta z_0 \sin\theta| < 0.5\,\mathrm{mm}$ respectively.

Jets Jets are a collection of decay products originating from a specific original particle. They are reconstructed by clustering tracks generated by combining information from the calorimeter system and track measurements. These are combined using the anti-k_T clustering algorithm with $\Delta R = 0.4$. This is facilitated using the particle flow algorithm [163]. To select Jets within the inner detector acceptance, they are required to have $|\eta| < 2.5$. Furthermore, jets must have $p_{\mathrm{T}} > 26\,\mathrm{GeV}$ and additional pile-up rejection criteria are applied to jets with $p_{\mathrm{T}} < 60\,\mathrm{GeV}$ using the multi-variate jet-vertex tagger JVT [164]. Jets that are closer than $\Delta R = 0.2$ to an electron are vetoed to prevent double-counting of the electron energy. Similarly, jets containing less than three tracks and either being close to a muon ($\Delta R < 0.2$) or sharing a track with a muon are removed to avoid the muons' energy deposits as jets. Additionally, jets have to

be well separated ($\Delta R > 0.4$) from electrons and muons, or else the leptons are rejected. Jets originating from a b quark are tagged using the DL1r tagging algorithm [165, 166] at a working point (WP), resulting in an efficiency of 77 %.

Top-tagged jet Boosted ($p_{\mathrm{T}} \gtrsim 2m_t$) top quarks create decay products that collimate in a way which does not allow for precise resolution of the sub-jets anymore. Therefore, they are reconstructed as a single *reclustered* jet (RC jet) in the detector. These large radius jets contain all decay products and are therefore used as a proxy for the hadronically decaying top quark. They are reconstructed by applying the anti-k_T clustering algorithm with $R = 1.0$ to the $R = 0.4$ jets, that would contain at least 5 % of the resulting jet's p_{T}. Removing low p_{T} sub-jets (Trimming [167, 168]) suppresses potential pile-up effects. The resulting large radius jet is required to have $p_{\mathrm{T}} > 355\,\mathrm{GeV}$ and $|\eta| < 2.0$, as well as to contain at least one b-tagged jet. Furthermore, the reconstructed mass must be within [120 GeV, 220 GeV]. To avoid high-p_{T} electrons to be the seed of the jet, a cut of $\Delta R(e, t) > 1.0$ is applied as well. In the case of more than one candidate, the one with the highest p_{T} is chosen.

Leptonic top quark The leptonic top quark kinematics are estimated from a combination of the four momenta of its decay products. Among these are the lepton, the b quark closest to the lepton, and the neutrino. The reconstruction of the neutrino four momentum is discussed in Appendix 4.

$\mathbf{E_T^{miss}}$ Events are expected to contain missing transverse energy, e.g., stemming from the neutrinos in the leptonic top decay. This missing energy is reconstructed via the negative vector sum of the calibrated leptons, small-radius jets, and the soft term, calculated using other tracks associated with the PV. The objects used here are expected to fulfill the respective requirements, mentioned above.

The selected signal events are then required to contain exactly one lepton, at least two b-tagged jets, and one top-tagged jet to fit the event topology shown in Figure 6.1. Therefore, there must be at least one b-tagged jet outside the top-tagged jet, and the lepton is required to be in the vicinity ($\Delta R < 2.0$) of a b-tagged jet, which, itself, is separated from the top-tagged jet by passing $\Delta R > 1.0$. Due to the production of a neutrino in the signal process and in order to reduce contamination from multi-jet background processes, a minimum of 20 GeV of missing transverse energy is required. The sum of the missing transverse energy and the transverse mass of the m_{T}^W boson is furthermore required to be greater than 60 GeV.
The selection criteria are summarised in Table 6.1. It contains the detailed selection criteria described above for the selection on particle- as well as detector-level. The selection on

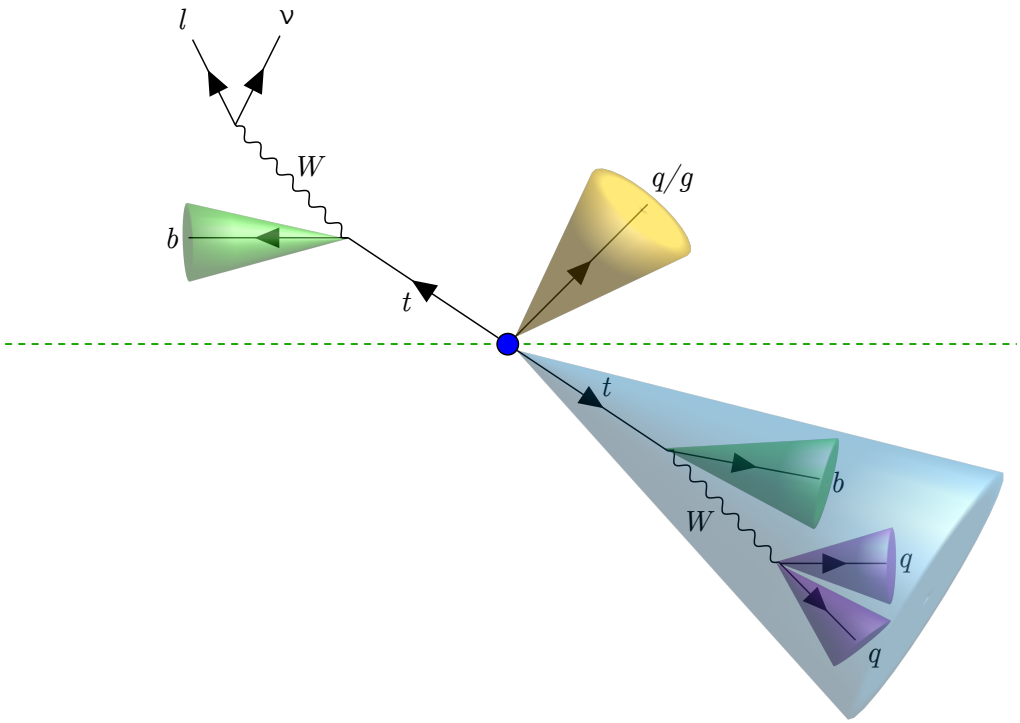

Figure 6.1: Diagram of an example signal topology. The pp-collision (blue circle) produces a pair of top quarks and possible extra QCD radiation. The top quarks decay into a b quark, producing a jet (green cones) and a W boson, which in turn decays either hadronically (bottom case) or leptonically (top case). In the signal, the two top quarks are required to decay in different channels (one hadronically and one leptonically). The hadronically decaying top quark produces two jets from the W decay (purple cones). The analysis targets hadronically decaying top quarks with a high momentum which leads to all its direct decay products being collimated into a large-radius jet (blue cone). The leptonically decaying top quark produces a muon or electron and a neutrino, manifesting as missing transverse momentum.

detector- or reconstruction-level is used to select a subset of the events with a high purity of signal events, as outlined above. However, since the measurement will be unfolded to particle level, a similar selection is applied at this level. This selection ensures a good agreement of the two levels and, therefore, a consistent extrapolation between the two measurement levels.
The selection criterion on the reconstructed mass $m_{\ell b}$ of the lepton and associated b quark is used to suppress contributions from the tW background processes. It also reduces this analysis' sensitivity to certain modeling uncertainties in this background process. The choice of this selection and discussion of the effects is described in the following section.

Selection Criterion	Detector-level		Particle-level
leptons	**Exactly 1 lepton in event**		**Exactly 1 lepton in event**
	Electrons	Muons	
	$p_T > 27\,\text{GeV}$	$p_T > 27\,\text{GeV}$	$p_T > 27\,\text{GeV}$
	$\lvert\eta\rvert < 1.37$ or $1.52 < \lvert\eta\rvert < 2.47$	$\lvert\eta\rvert < 2.5$	$\lvert\eta\rvert < 2.5$
b-tagging	DL1r tagger at 77 % working point		Ghost-matched b-hadron
Small-R jets (R=0.4)	$p_T > 26\,\text{GeV}$ $\lvert\eta\rvert < 2.5$		Same as detector-level
b-tagged jets (R=1.0)	≥ 1 **b-tagged jet is constituent of top-jet** ≥ 1 **b-tagged jet near lepton:** ΔR(lepton,lep-b-jet) < 2.0 ΔR(top-jet,lep-b-jet) > 1.0		Same as detector-level
Hadronic top-jet (R=1.0)	≥ 1 **top-tag RC-jet candidate** $p_T > 355\,\text{GeV}$ $\lvert\eta\rvert < 2.0$ $120\,\text{GeV} < M < 220\,\text{GeV}$ ≥ 1 b-tagged sub-jet		Same as detector-level
MET & $\text{m}_\text{T}^\text{W}$	$\text{MET} > 20\,\text{GeV}$ $\text{MET} + \text{m}_\text{T}^\text{W} > 60\,\text{GeV}$		Same as detector-level
Electron Isolation	ΔR(electron,top-jet) > 1.0		None
mlb	$\text{m}_{\ell b} < 180\,\text{GeV}$		Same as detector-level

Table 6.1: Selection criteria on the objects used to select the $t\bar{t}$ signal at both detector and unfolded particle level.

6.5 Reducing the tW Background and related Uncertainties

Among the various background processes in this measurement, the production of a single top quark in association with a W boson is one of the largest with an amount of 2 % of the expected event yield. Furthermore, there are large uncertainties in the modeling of this process. This is due to the way this background is modeled. The signal $t\bar{t}$ production is modeled in the narrow width approximation, which approximates the top quark as a stable, on-shell particle, effectively factorizing the production and the decay. This way, the $t\bar{t}$ production is separated from the same final state of the production of a single top quark in association with a W boson and a b quark. However, the similarity in the final states of these processes ($pp \to WbWb$) causes interference between the two channels. Thus, a proper physical distinction between the two channels is difficult, as they display significant overlap. The two most common approaches to modeling the process are called *diagram removal* (DR) and *diagram subtraction* (DS) [159]. Both simulate the full set of amplitudes contributing to the production of a single top quark in association with a W boson. In the DR scheme, all the amplitudes containing two on-shell top quarks (doubly-resonant) are then removed from the calculation of the matrix element. In the DS scheme, the calculation of the matrix element is extended by additional, locally

gauge-invariant terms, which are built such that they exactly cancel out the contributions from doubly-resonant amplitudes. Both procedures aim at separating the two channels but can only give approximations. The uncertainty due to this approximation can have a significant impact on the measurement. In order to improve the modeling of this process, several strategies are persued in recent developments of these predictions. The ATLAS collaboration is working on accurately modeling the production of $t\bar{t}$ including the tW contributions and interferences in a dedicated prediction [169].

It has been shown that for a pair of leptonically decaying top quarks, the reconstructed mass m_{lb} of a b-jet and one of the leptons is particularly sensitive to the interference of the two channels [170]. In the case of a two-lepton final state, the combinatorial ambiguity of choosing among the two leptons and the b-jets is lifted by a combination of choosing the minimum and maximum value. In this measurement, however, unlike the case of two leptonically decaying top quarks, there is no ambiguity in the construction of this observable in the semileptonic case. Therefore, the reconstructed mass of the lepton and the associated b-jet is used to reduce sensitivity to the tW modeling uncertainties by applying a requirement to the events passing the selection.

Figure 6.2 shows the fiducial particle-level distribution of m_{lb} in the signal prediction and the two modeling schemes of the tW background normalized to unity, as well as the ratio of the two modeling schemes for the tW background in the bottom figure. The top figure shows that the majority of signal events lie in the low m_{lb} region, while a majority of tW events have larger m_{lb}. At the same time, the bottom ratio shows that the largest differences between the two tW modeling schemes lie at large m_{lb}. Therefore removing events with large m_{lb} will remove not only tW background events relative to the signal fraction in the sample but also the phase space, which is especially affected by modeling uncertainties of the background process. Therefore, a selection criterion based on the reduction of the tW background as well as the uncertainty of the modeling via the difference between the two schemes is chosen. The metrics for this selection are shown in Figure 6.3 as functions of the requirement on the maximum m_{lb} between 150 GeV and 280 GeV. The blue lines show the absolute deviation of the ratio of the two tW modeling schemes from 1, averaged over the bins of the $p_{\mathrm{T}}^{t,h}$. This way the effects on all bins are incorporated. The dashed blue line shows this value in the absence of any requirement on m_{lb}. The black lines show the efficiencies of this selection on the $t\bar{t}$ signal and the tW background in the two modeling schemes DR and DS.
The differences between the DR and DS scheme are already significantly reduced compared to the absence of this requirement when adding the loosest requirement of $m_{lb} < 280$ GeV. Throughout the tested range, this effect is relatively constant, with the edges trending towards an increase in uncertainty. The effect on the selection efficiencies on the signal and the tW background, on the other hand, shows the expected trend: the more stringent the requirement on m_{lb}, the smaller the efficiencies. However, the efficiency of the signal only notably decreases for very stringent cuts around $m_{lb} < 160$ GeV. Therefore, requiring $m_{lb} < 180$ GeV is added to the selection to reduce the contributions of this background, while also constraining the resulting phase space to a region that is less prone to the

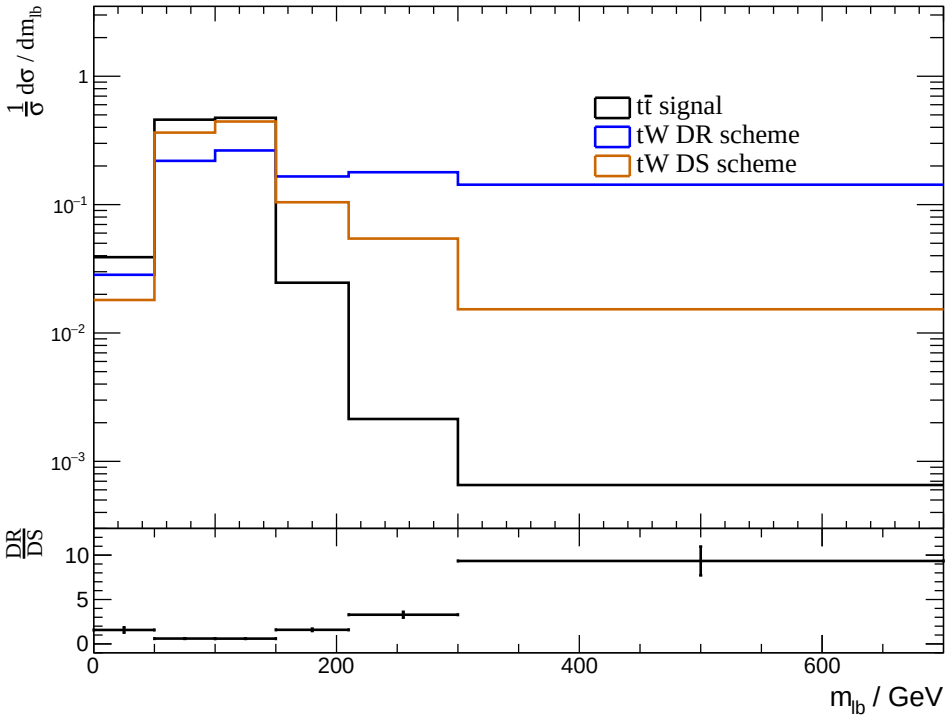

Figure 6.2: Normalized distribution of m_{lb} for the $t\bar{t}$ signal prediction and the two modeling schemes of the tW background. The bottom figure shows the ratio of the two modeling schemes of the tW background. The top figure shows that the majority of signal events lie in the low m_{lb} region, while a majority of tW events have larger m_{lb}.

above-mentioned modeling uncertainties.
Applying the requirement increases the overall percentage of signal $t\bar{t}$ events in the prediction from 95.4 % to 96.4 %, while reducing the uncertainties on the detector level total cross-section from the various backgrounds from 0.76 % to 0.54 %. The effect is particularly prominent, e.g., in the tails of the $p_{\mathrm{T}}^{t,h}$ spectrum, where the background modeling uncertainties are reduced to 2.3 % from 7 %.

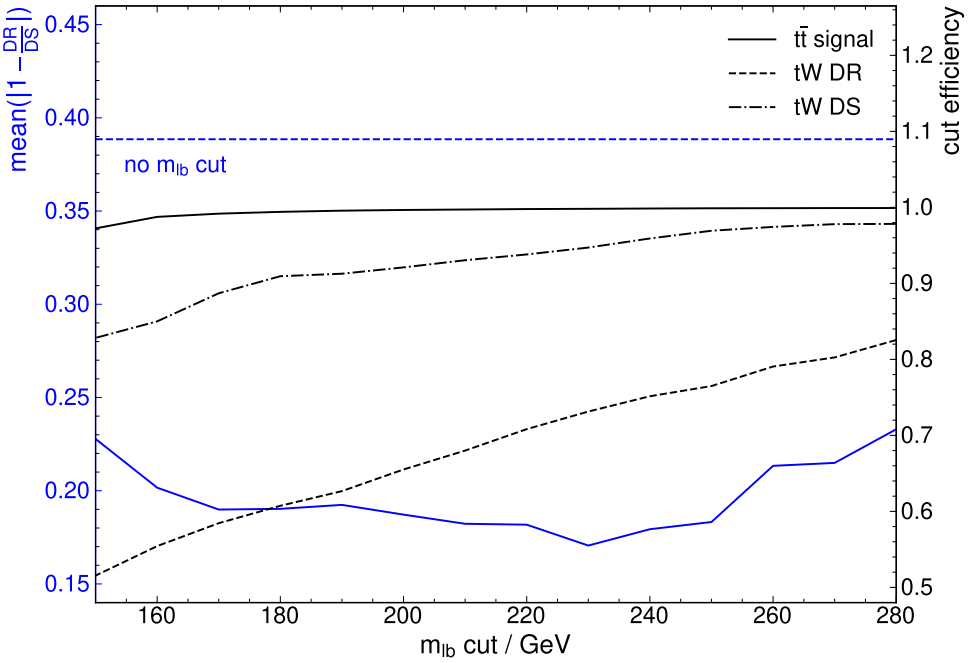

Figure 6.3: The metrics used for the m_{lb}-based selection as functions of the requirement on the maximum m_{lb} between 150 GeV and 280 GeV. The blue lines show the absolute deviation of the ratio of the two tW modeling schemes from 1, averaged over the bins of the $p_{\mathrm{T}}^{t,h}$. The dashed blue line shows this value in absence of any requirement on m_{lb}. The black lines show the efficiencies of this selection on the $t\bar{t}$ signal and the tW background in the two modeling schemes DR and DS.

7 Cross-section Measurements

There are several steps to gaining knowledge on the underlying physics by measuring the physical observables from the data. In this measurement, the properties of the process of interest are measured using differential cross-sections. These show the observed frequency of the process in different regions of particular kinematic properties of the participating particles, as well as potential higher-level properties. However, in order to interpret the measured data in terms of these observables, certain corrections and selections need to be applied. Since there are many possible observables to choose from, a selection is necessary based on the properties of interest and the intention of the measurement.
Among the corrections to the data are the effects that are imposed on the data by the characteristics of the detector used in the measurement. In order to allow for easier comparisons with predictions as well as combinations with other measurements, the data are corrected for these in a process called unfolding.
Furthermore, in order to reduce the effects of uncertainties arising from the modeling of the jets in this measurement, the energies of these are corrected for differences between simulations and measurement.
Lastly, an essential property of the measurement is the estimation of the uncertainties. Among these are the statistical uncertainties due to the statistical nature of the measured processes, as well as, systematic uncertainties. The latter follow from the various steps in, e.g., the model predictions, the modeling of the detector and the reconstructed objects, as well as the used algorithms.

7.1 Correction of the Jet Energy

From the event selection criteria outlined in Section 6.4 it becomes clear that this measurement heavily relies on the reconstruction of jets. Therefore, the uncertainties related to these objects generally make up a large part of the total uncertainty of the measurement. This has also been shown in similar measurements by the ATLAS collaboration [17, 171, 172], as well as the CMS collaboration [173–175]. Among the primary sources of these jet-related uncertainties are those related to the jet energy scale (JES), describing the precision of the reconstructed energy of the jets, as well as the jet energy resolution (JER), describing the accuracy of the reconstructed energy of the jets. Reducing these uncertainties will thus significantly increase the accuracy of the measurement. This is why the analysis strategy used in the measurement presented in this work is adapted to reduce the sensitivity to these uncertainties; conceptually similar to the reduction of uncertainties on the tW backgrounds by applying the cut on m_{lb} in the event selection. This approach uses the reconstructed mass of the large-radius jet originating from the

hadronically decaying top quark as well as the top-quark mass used in the simulations. Generally, the performance of this procedure is limited by the precision of the knowledge of the top-quark mass. Since it is used in the approach to absorb the energy differences of jets in data and MC simulations, systematic uncertainties in this method depend on this precision. Therefore, only due to the very high precision of recent measurements [17, 175], this method can be used successfully to reduce the jet-energy-related uncertainties.

The large-radius jet consists of multiple small-radius jets as outlined in Section 6.4. Thus, a direct kinematic relation exists between the reconstructed mass of the large-radius jet and the energies of the small-radius sub-jets used in the construction of the large-radius jet. The energies of these sub-jets are just the parameters which carry the JES uncertainties, especially if there is a systematic difference between the energies in data and among the various simulated predictions. Therefore, a method is used to reduce this potential difference. Similar approaches have been used in measurements of the top-quark mass [17, 175–181], however, utilizing the W-boson mass instead of the top-quark mass. It is assumed that the overall difference between the measured energy of the small-radius sub-jets and the simulated events can be corrected by scaling them with a factor called jet scale factor (JSF). This multiplicative model is a simple approach that is able to capture overall shifts like the ones this methodology aims at reducing. This factor is then applied to the energies of the small-radius jets in the data sample as well as all simulated samples and their systematic variations and is individually derived for each of these samples. The corrected energies can be described by the simple multiplication

$$E_{\text{jet}}^{\text{corrected}} = E_{\text{jet}}^{\text{measured}} \cdot \frac{1}{\text{JSF}} \,. \tag{7.1}$$

In order to apply this correction, the analysis is extended by additionally measuring the JSF in data. The JSF is chosen in such a way that a difference between the jet energies in data and in the multiple simulated samples, which can be encoded in a multiplicative way like this, will be removed. This way, the overall difference between the energies will be reduced. Correcting the jet energies this way changes the distribution of the reconstructed mass of the large-radius jet due to their kinematic relation. This shift in the mass spectrum is shown in the left distribution in Figure 7.1 for the nominal $t\bar{t}$ signal prediction. Applying a JSF > 1 will shift the distribution's shape towards larger values of $m^{t,h}$, while a JSF < 1 will do the opposite. Since this affects kinematic features used in the selection of events, a JSF $\neq 1$ also impacts the acceptance of events. Generally, selection criteria require, for example, a momentum to exceed a minimum, which is why a JSF > 1 leads to a larger acceptance. This effect also translates to the mean $\overline{m^{t,h}}$ of this distribution. This relation is what is used to derive the JSF.
The relation of the mean of the reconstructed mass of the large-radius top jet to the JSF is parametrized using parametric inference, by systematically applying different JSFs to the full prediction, including the nominal signal simulation as well as the various backround predictions. The resulting functional description, as well as the predictions used in the inference, are shown on the right of Figure 7.1. The mean of the mass spectrum is calculated within the shown range and follows a linear dependence on the energies of the

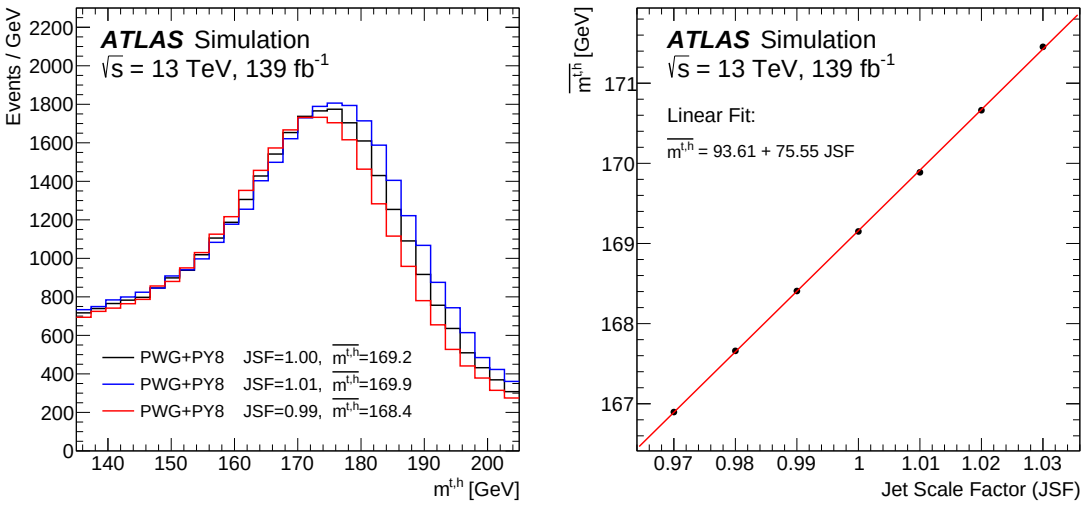

Figure 7.1: Comparison of the predited spectra of the reconstructed mass of the top-quark jet for the $t\bar{t}$ signal for JSF= 1 (in black) to small variations in the JSF (in red and blue) on the left. The effect of the JSF method on the mean of the distributions is given in the legend. On the right the linear parametrisation of the mean $\overline{m^{t,h}}$ of the top-jet distribution is shown as a function of the JSF derived on the signal simulations.

small-radius jets. This is expected because the large-radius jet is described kinematically as the sum of the small-radius jets' four-vectors. The linear relation between the two derived from the nominal MC simulations is used to determine the different JSF values in data and the simulated samples from their respective mean reconstructed top-quark mass. The JSF method, therefore, corrects the distributions for their respective mean. This way, the sensitivity to systematic variations is reduced on average. Especially uncertainty sources, which are directly related to the jet energy (i.e., JES) will be reduced by the effects captured with the JSF method. However, uncertainties which do not have an impact on the jet energy directly, but affect the $m^{t,h}$ distribution (like the uncertainty on the top-quark mass) used to derive the JSF, are expected to increase in their impact. Since the JSF method employs an average shift to equalize the mean of the $m^{t,h}$ distributions, it can not account for all the possible differences among the data and various predictions. For certain regions of this measurement the JSF method is, therefore, expected to increase jet-related uncertainties, if the shift in the energy locally increase differences among the systematic variations, used to estimate the systematic uncertainties. Relating this to Figure 7.1, for example, the application of a JSF different from unity may change the spectrum of $m^{t,h}$ in a way, which improves the overall agreement among different predictions. However, it may introduce additional discrepancy in small regions (e.g., the tails) of the spectrum, due to the nature of the average shift in this procedure. Using this methodology, the JSF is determined for each of the systematic variations of the signal sample, as well as all background predictions and the data, used in this measurement. The statistical uncertainty on the JSF due to the limited number of events is evaluated using a

Poisson smearing. The number of entries in the data $m^{t,h}$ distribution is varied according to a Poisson distribution with the number of entries as the expected value. The effects of variations within the smearing limits are propagated to the JSF in order to estimate the uncertainties. This procedure is applied for both observed and simulated data, where for the simulated data a smearing is used according to a Gaussian distribution with the mean equal to the content of the particular $m^{t,h}$ bin and the standard deviation equal to the sum of the weights of the specific sample squared.

7.2 Corrections for Detector Effects

The limited acceptance and resolution of every experimental apparatus modify the underlying physical distributions, resulting in the measured distributions. These effects create differences between the observed distributions (detector-level) and the underlying physical spectra (for example, particle-level). A priori, this does not constitute an obstacle to the measurement, but makes understanding these effects necessary in order to make meaningful predictions and generate knowledge based on the observations. In order to make the interpretation of data, for example, in the case of particular theory predictions more straightforward and accessible to a public without detailed knowledge of the detector characteristics, the effects can be accounted for by applying an unfolding technique that aims to remove the detector effects from the distributions and recover the particle-level spectra. The resulting distributions can then be compared with other experiments' results and theoretical predictions without the need for detector simulations.
The observed spectra in this measurement consist of binned one- and two-dimensional (single- or double-differential) distributions. In the unfolding approach, the cross-section in the bin j of the particle-level distribution is defined as

$$\frac{d\sigma_j}{dX_j} = \frac{1}{L \cdot \Delta X_j} \frac{1}{f_j^{\text{eff}}} \sum_i M_{ij}^{-1} f_i^{\text{acc}} (N_i^{\text{Data}} - N_i^{\text{background}}) \,, \tag{7.2}$$

where i represents a detector-level bin, X describes a single or double differential observable and ΔX_j represents the bin width of bin j. N^{Data} represents the data histogram obtained after the event selection described in Section 6.4 and $N^{\text{background}}$ represents the histogram of the estimated backgrounds. f^{eff}, M^{-1} and f^{acc} are the unfolding corrections that are derived using the nominal PWG+PY8 prediction of the $t\bar{t}$ signal. The acceptance correction accounts for events passing the detector-level selection but failing the fiducial requirements, that therefore need to be removed from the particle level spectra. It is defined as

$$f_i^{\text{acc}} = \frac{N_i^{\text{detector}} \wedge N_i^{\text{particle}}}{N_i^{\text{detector}}} \,, \tag{7.3}$$

where the numerator represents events passing both the detector- and particle-level selections while the denominator consists of events passing the detector-level selection. The efficiency correction accounts for events passing the particle-level requirements but

failing the detector-level ones. It is defined as

$$f_j^{\text{eff}} = \frac{N_j^{\text{detector}} \wedge N_j^{\text{particle}}}{N_j^{\text{particle}}}, \tag{7.4}$$

where the numerator represents events passing both the detector- and particle-level selections while the events in the denominator are only required to pass the particle-level selection.
The detector effects on the observable are furthermore encoded in M^{-1}. Among these effects are migrations of events to a different bin when making the transition between the two levels due to resolution effects, which can generally be described by a linear transformation through a migration matrix M. This matrix is generally derived by simulating these detector effects and quantifying their impact. These effects are not removed by a simple inversion of the linear transformation but by using an unfolding technique called iterative bayesian unfolding (IBU) [182], as implemented in RooUnfold [183]. This approach uses Bayesian inference by iteratively applying the theorem of Bayes and Laplace to create the unfolded particle-level distribution from the observed data. The iterations serve as a regularization in this approach. The number of iterations is optimized to minimize the average correlation factor among the bins [184]. Since this approach is based on simulations, which in turn assume the SM, it is prone to potential effects of bias towards the SM when interpreting the results in the framework of EFT. This applies similarly to the determination of the acceptance and efficiency corrections, mentioned above. Therefore, these effects are tested for. The discussion of these tests is presented in Section 11.1. Additionally, even in the absence of BSM physics, the unfolding procedure is prone to biases toward potentially imperfect modeling of the predictions. In order to test for the presence of such effects, the procedure is run on skewed distributions, based on the agreement of the shapes of predictions and measurement as shown in Section 7.4. This procedure showed excellent closure, proving the robustness of the approach in this measurement. More details can be found in Appendix 3.
The binning of the observables is chosen based on the migration matrix determined in the unfolding procedure, as well as the statistical uncertainty. The one-dimensional distributions are required to have a maximum statistical uncertainty in each bin of 1.2 %, and at least 65 % of the events in the diagonal entries of the migration matrix.

7.2.1 Construction of the Covariance Matrix

The different bins of the final unfolded measurement do not only carry uncertainties from various sources but are also generally correlated. The uncertainties and correlations are encoded in covariance matrices, which contain the various sources of uncertainties on each bin as well as the correlations among the bins. These correlations, on the one hand, originate from the regularisation in the unfolding procedure, which introduces connections among the bins by describing the migration matrix. On the other hand, bins generally share systematic uncertainties, which are usually correlated as well. There are two independent components to the final covariance matrix: a statistical one and a

systematic one. The statistical covariance matrix contains the statistical uncertainties of the different bins. It is derived numerically by creating a large number of random replicas of the initial distribution for both the data and the prediction. In both cases, 10 000 replicas are generated by randomly varying the initial distribution according to a smearing within the statistical uncertainties. The uncertainties used in the smearing are assumed to follow a Gaussian distribution in the case of the predictions and a Poisson distribution for the data. The replicas are then passed through the nominal unfolding procedure, and the resulting alternative unfolded samples are used to create the statistical covariance matrix.
The covariance matrix containing the systematic uncertainties and their correlations are built using the relative up and down variations of the uncertainties $\delta_i^{\text{up/down}}$ of the unfolded distributions. These are symmetrised in δ_i^{S} according to

$$\delta_i^{\text{S}} = (|\delta_i^{\text{up}}| + |\delta_i^{\text{down}}|)/2\,.$$

The full covariance matrix is then built as a sum of the components. The latter are encoded in the C_{ij} for each systematic uncertainty using the aforementioned uncertainties of the various sources of systematic uncertainties as well as the measured cross-section $\sigma_{i/j}^{\text{data}}$ in bin i or j and the correlation factors ρ_{ij} between the bins i and j, according to

$$C_{ij} = \rho_{ij} \cdot \delta_i^{\text{S}} \cdot \sigma_i^{\text{data}} \cdot \delta_j^{\text{S}} \cdot \sigma_j^{\text{data}}\,. \tag{7.5}$$

The correlation factors describe the systematic shift of the systematic variations on the measured cross-section. They are based on the product of the signs of the systematic shifts of the up and down variations induced by the respective systematic uncertainty in the respective bins. The correlation factor for the up variation, e.g., is given as

$$\rho_{ij}^{\text{up}} = \text{sign}(\delta_i^{\text{up}}) \cdot \text{sign}(\delta_j^{\text{up}})\,.$$

This covariance matrix is then later used to encode the uncertainties and correlations in the EFT interpretation.

7.3 Choice of Observables

This measurement consists of multiple different measurements of differential cross-sections of the signal process in various kinematic variables. These variables consist of those particularly sensitive to the modeling of this process, variables that describe the most important kinematics of the signal process and the involved particles, variables that are particularly sensitive to BSM effects described by EFT operators, and previously not measured kinematics of the signal, which add valuable input to understanding and validating the modeling in this phase space.
The variables probing the signal kinematics also with respect to potential additional jets are:

$p_{\text{T}}^{t,h}$ the transverse momentum of the hadronically decaying top-quark jet

$p_{\mathrm{T}}^{t,\ell}$	the transverse momentum of the leptonically decaying top-quark
$\lvert y^{t,h}\rvert$	the rapidity of the jet of the hadronically decaying top quark
$\lvert y^{t,\ell}\rvert$	the rapidity of the leptonically decaying top-quark
$\lvert y^{t\bar{t}}\rvert$	the rapidity of the top-quark pair
$m^{t\bar{t}}$	the reconstructed mass of the top-quark pair
$\Delta\phi(b_\ell, t_h)$	the separation of the hadronically decaying top quark to the b-tagged jet associated with the leptonically decaying top quark in the azimuthal angle
$H_{\mathrm{T}}^{t\bar{t}}$	the scalar sum of the transverse momenta of the constituents of the $t\bar{t}$ system

Among those, the rapidities are expected to be sensitive to the modeling of the PDF functions [185], while the others give a more precise update of variables which have been measured in previous datasets [12, 15]. Variables particularly probing the additional QCD radiation causing the additional jets are

$p_{\mathrm{T}}^{t\bar{t}}$	the transverse momentum of the top-quark pair
N^j	the additional-jet multiplicity
$p_{\mathrm{T}}^{j,1}$, $p_{\mathrm{T}}^{j,2}$	the transverse momenta of the two leading additional jets
$\Delta\phi(j_1, t_h)$, $\Delta\phi(j_2, t_h)$	the separation of the hadronically decaying top quark to the leading additional jets in the azimuthal angle
$\Delta\phi(j_1, j_2)$	the separation of the two leading additional jets in the azimuthal angle
$\Delta\phi(t_h, t_\ell)$	the separation of the two top quarks in the azimuthal angle
$m(j_1, t_h)$	the reconstructed invariant mass of the hadronically decaying top-quark pair and the leading additional jet
$H_{\mathrm{T}}^{t\bar{t}+\mathrm{jets}}$	the scalar sum of the transverse momenta of both top quarks and the additional jets

7.4 Observed Data Distributions

The dataset after applying the selection criteria outlined in Section 6.4 consists of 75 743 events, with an expected signal purity of $> 95\,\%$. The observed number of events is approximately 14 % smaller than the predicted event yield. This is a consistent phenomenon also seen in the previous measurement [10].
Figure 7.2 shows the observed distribution of a selection of the measured kinematic variables at reconstruction level. The shown rates are normalized to their respective bin width to conserve the distributions' shapes. Among these variables are the number of additional

jets in the event N^j, the reconstructed mass of the $t\bar{t}$ system $m^{t\bar{t}}$, the scalar sum of the transverse momenta of the $t\bar{t}$ system $H_{\mathrm{T}}^{t\bar{t}}$ and the transverse momentum of the hadronically decaying top quark $p_{\mathrm{T}}^{t\bar{t}}$. The observations are compared to the predictions for the signal and various background categories, which in turn are normalized to the data event yields in order to highlight the agreement of the shapes of the distributions. The modeling of these variables is in reasonable agreement with the measurement, especially, e.g., for the $p_{\mathrm{T}}^{t,h}$ distribution. There are, however, regions with worse agreement of prediction and data. In particular the shape of $H_{\mathrm{T}}^{t\bar{t}}$ as well as the events with high additional jet multiplicities show deviations from the predictions. This shows the overall lack in modeling of additional radiation in the process, which leads to a general mismodeling of the $t\bar{t}$ system. The measurement shows an increased number of high jet-multiplicity events and a softer $H_{\mathrm{T}}^{t\bar{t}}$ spectrum than the nominal PWG+PY8 prediction. The generally softer kinematics of the top quarks is also apparent in the $m^{t\bar{t}}$ distribution, although not as significant. Therefore, these observables will (among others in this measurement) serve as valuable input for improving the modeling frameworks.

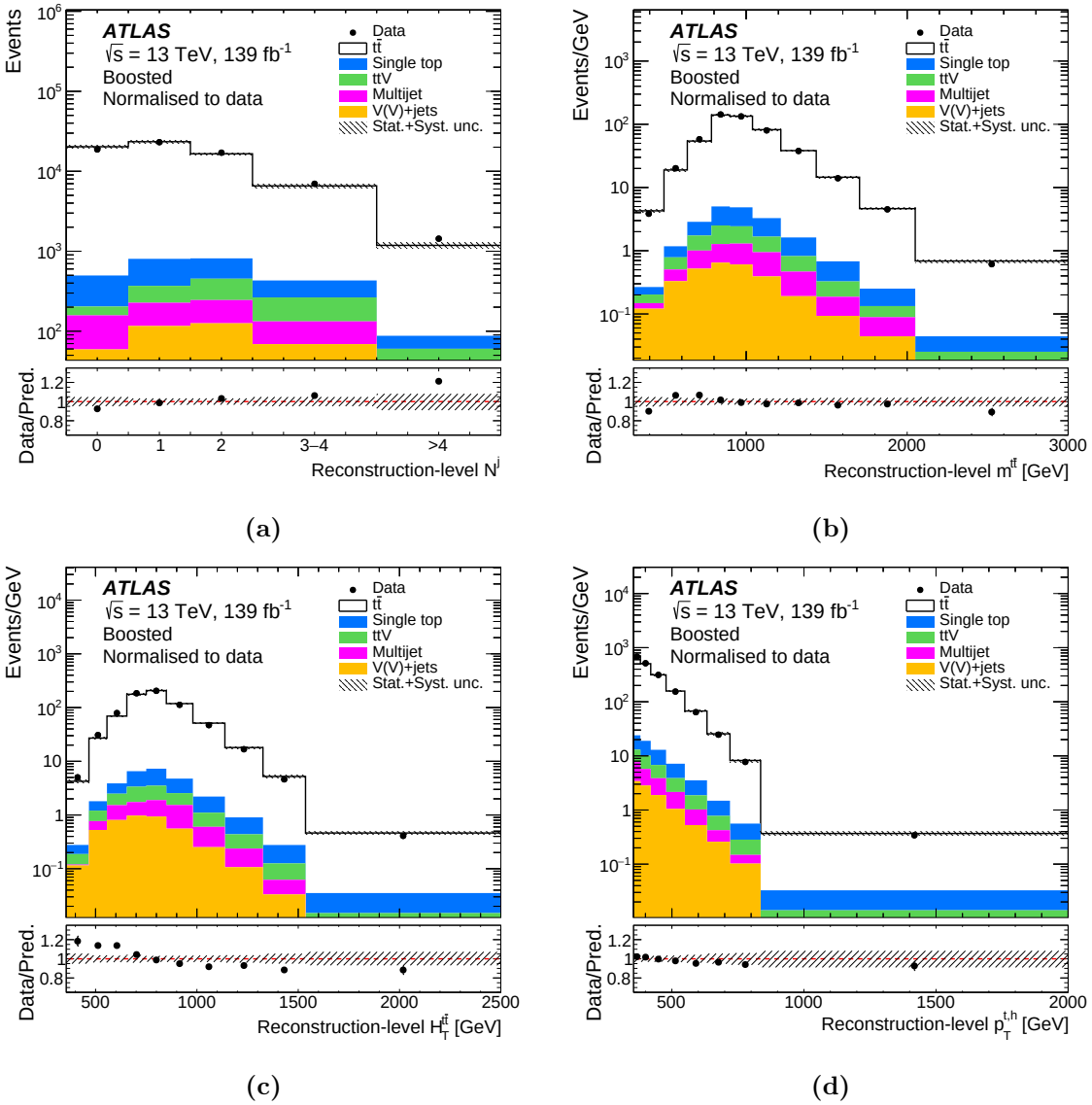

Figure 7.2: Observed distributions of the number of additional jets N^j (a), the reconstructed mass of the $t\bar{t}$ system $m^{t\bar{t}}$ (b), the scalar sum of the transverse momenta of the $t\bar{t}$ system (c) and the transverse momentum $p_{\mathrm{T}}^{t,h}$ of the hadronic top-jet (d) at reconstruction level compared to the predictions, which in turn are normalised to the data event yields. The contributions from the various background processes are shown in the different colors with the signal contribution in white.

7.5 Systematic Uncertainties

As mentioned in Section 4, the uncertainties in the measurement consist of uncertainties due to the statistical nature of the physics interactions but also originate from systematic sources. There are various choices of, e.g., parameters or frameworks used in the modeling of the various processes, which introduce uncertainties in the final measurement. The effects these choices have on the measurement are evaluated by varying the corresponding parameter, e.g., the choice of the top quark's mass. The resulting variations in all the necessary predictions are then propagated through the whole analysis. This way, the effects of the variation on the measurement are quantified and used as an estimate of the uncertainty from this source, while the potential correlations in these variations are fully accounted for. The various effects of the sources of systematic uncertainties are then used to determine the combined total uncertainty in the measurement. In this procedure, they are assumed to be uncorrelated, if not particularly constructed as such. In presence of a large dataset allwoing for high statistical precision, the total uncertainty in the measurement can easily be dominated by systematic uncertainties, depending on the analysis strategy. For example, because of the large impact of jet-related uncertainties, the aforementioned JSF method is applied to reduce the impact of these specific systematic uncertainties. The various sources of systematic uncertainties, as well as the impact of the JSF method, are briefly discussed in this section.

7.5.1 Lepton Reconstruction and Identification

The identification and reconstruction of leptons are affected by uncertainties on their efficiencies and the energy scales and resolution of the leptons' momenta. The uncertainties on the reconstruction and identification efficiencies of the electrons and muons in this measurement are determined using $Z \to ee$ and $Z \to \mu\mu$ events, respectively. The procedures for electrons and muons are outlined in Ref. [161] and Ref. [162] respectively as well as for the trigger efficiencies in Ref. [122] and Ref. [123]. Furthermore, the uncertainties on the reconstruction of the leptons' energies and momenta are determined using decays of the Z and J/Ψ resonances as outlined in Ref. [161] and Ref. [186].

7.5.2 Jet Reconstruction and b-Tagging

Systematic uncertainties on the energies of the small-radius jets used in this analysis are estimated using a set of 30 parameter variations [187]. All of these variations modify the energies of the jets (JES). Furthermore, the uncertainties on the resolution of the jet energies (JER) are estimated using a scheme consisting of variations to eight parameters modifying the JER. Especially the JES uncertainties are the major motivation for the use of the JSF method in order to reduce the impact on the measurement. The uncertainties on the energy properties of the small-radius jets are intuitively propagated to the large-radius jets since these are constructed directly from the small-radius jets. This allows for consistent treatment of these uncertainties for all jets in the measurement.
The impact of the JSF method, described in Section 7.1, on the uncertainties related to

the jet reconstruction are shown at particle level in Figure 7.3. It shows the fractional uncertainties for the number of additional jets N^j in the event and the reconstructed mass $m^{t\bar{t}}$ of the pair of top quarks. The figure contains the total uncertainty as well as the JES component for the cases before and after applying the JSF method. The effect on the JES component in red is found to be very strong; the uncertainty is reduced by at least 50 % throughout the whole distribution of $m^{t\bar{t}}$ and almost completely vanishes in certain bins. The total uncertainty, including all systematic and statistical sources, is reduced throughout the whole distribution, showing that the trade-off between jet-related uncertainties and, e.g., the top quark mass-related ones is excellent.

A very similar picture emerges for the N^j distribution, with a significant reduction of the JES uncertainty in the whole spectrum - except for the first bin. Here, the JSF method increases the impact of the JES uncertainty. This is due to the nature of the JSF model, which can not recover differences in kinematic regions which differ much from the average kinematics of the particular variable, as discussed in Section 7.1.

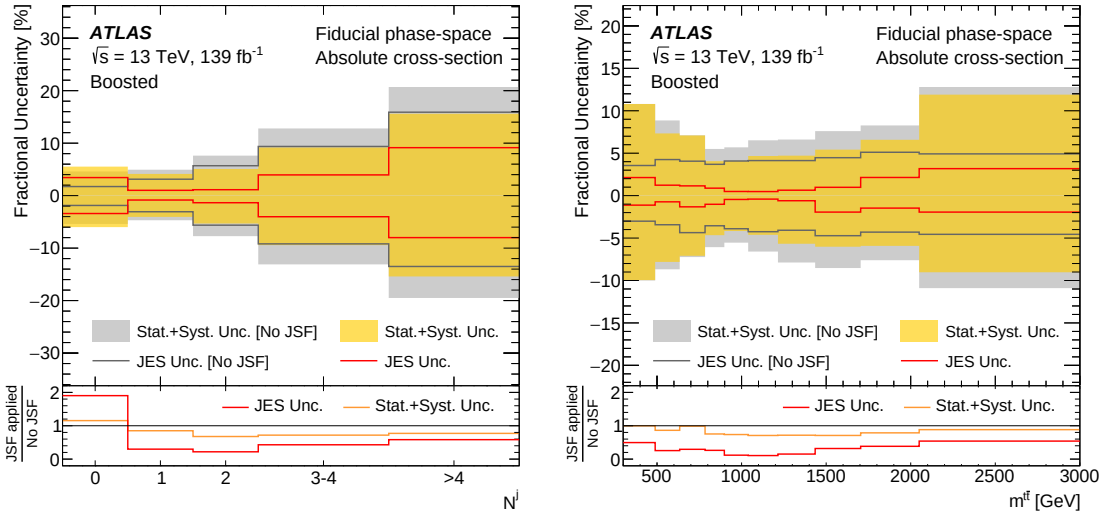

Figure 7.3: Fractional uncertainties for the bins of the number of additional jets N^j in the event on the left and the reconstructed mass $m^{t\bar{t}}$ of the pair of top quarks on the right. The total uncertainties including all sources of systematic and statistical uncertainties are shown in orange and grey, respectively, as well as the JES component in red before and after applying the JSF method.

The uncertainty on the total cross-section due to the JES is reduced from 4.0 % to 0.4 % by applying the JSF method.

The efficiency of the tagging of b-jets carries uncertainties as well. The performance of the algorithm was calibrated in data [165], and the uncertainties are estimated by varying respective sets of parameters for the different flavors (b, c, and light jets). The resulting parametrisation is constructed by decorrelating the various sources, yielding uncorrelated sets of uncertainties.

7.5.3 $t\bar{t}$ Modeling

The modeling of the $t\bar{t}$ signal prediction directly affects the results of this measurement. As the unfolding procedure heavily relies on this prediction, the results of the unfolding are affected by the choices for the modeling of the process. Furthermore, they impact the procedure to determine the JSF by, e.g., affecting the $m^{t,h}$ distribution. Therefore, the effects of the choices of the frameworks to calculate the ME and the subsequent showering and hadronization as well as various modeling parameters are investigated and incorporated into systematic uncertainties on the prediction. The various simulated predictions are described in Section 6.3.

Firstly, the uncertainties due to the choice of the showering and hadronization models are estimated using a predicition modeled by Powheg+Herwig. These incorporate different hadronization models and other non-perturbative effects of the parton showering. The effects are investigated by re-running the analysis using the alternative sample as pseudo-data input and comparing the results to the prediction after unfolding. The effects are found to be quite significant and largest at low $p_{\mathrm{T}}^{t,h}$.

Furthermore, the choice of various parameters in the showering as well as in the hard-scattering process is varied to evaluate the impacts. Among the parameters are the scale choices for μ_{r} and μ_{f}, as well as h_{damp}. The scale choices are varied by factors of 0.5 and 2.0 while the scale choices in the showering are varied as prescribed in the Var3c eigentune of the A14 set of tuned parameters [129] using Powheg+Pythia. The uncertainties due to the choice of h_{damp} are evaluated by varying the parameter to 1.5 times its nominal value. The alternative predictions using varied scale choices in the hard scattering, as well as the showering process, are referred to as ISR variations, whereas the changes affecting the scales in the final state parton shower are called the FSR variations.

Uncertainties due to the choice of the modeling of the hard-scattering process as well as the matching between hard scattering and the subsequent parton showering are evaluated using an alternative prediction based on MadGraph5_aMC@NLO+Pythia. Since this alternative prediction uses a particular parameter set varying in several settings affecting the parton showering and additionally does not employ matrix element corrections, these uncertainties convolute several effects.

Lastly, not only the predictions of several kinematic variables but especially the ones used in the extraction of the functional description of the JSF depend strongly on the choice of the mass of the top quark. The top quark mass is known to a precision of 0.5 GeV [17, 175]. In order to investigate the effects of the choice of 172.5 GeV, predictions with varied masses of the top quark are used. The mass is varied to 169 GeV and 176 GeV, and the effects are scaled by 1/7 in order to estimate the effects at the current uncertainty. Uncertainties due to the choice of the proton PDF function are evaluated using the 30 eigen-vectors available in the PDF4LHC30 set [138].

7.5.4 Background Modeling

Analogously to the signal modeling, the predictions for the various background processes are varied to evaluate the systematic uncertainties. The dominant background contributions arise from the production of a single top quark. For these predictions, similar variations as for the $t\bar{t}$ signal process are used to assess the uncertainties. The uncertainties due to the scale choices for μ_{r} and μ_{f} in the hard scattering and the showering of the events are evaluated as described for the $t\bar{t}$ signal. Similarly, the parameters summarised in the FSR variations for the $t\bar{t}$ signal are varied for the single top background processes. One source of substantial uncertainty on the single top backgrounds concerns the modeling of the sub-process of the production of a top quark in association with a W boson. As outlined in more detail in Section 6.5, the discrimination between this process and the $t\bar{t}$ signal is not possible at NLO. However, there are multiple approaches to approximating the separation of the processes (DR and DS). These are described in more detail in the discussion of the $m_{\ell b}$ selection criterion in Section 6.5. In order to assess the uncertainties in this modeling, alternative samples using the diagram subtraction method are used. Despite this effect being limited to tW, the uncertainty has a large impact on the single top background, since this channel makes up about 72 % of this background component. Finally, uncertainties on the NNLO cross-section, which normalizes the single-top background contributions, are included.

The uncertainty on the estimation of the W+jets background is derived using alternative predictions with variations in the scale choices for the hard-scattering and showering processes, which dominate the uncertainties on this small background contribution.

Uncertainties in the modeling of the $t\bar{t}+V$ backgrounds (with $V = W, Z$) are covered by uncertainties on the cross-sections of the processes. The uncertainty for the top quark pair production in association with a Higgs boson is the largest at 13 % and is considered for all three components (H, W, Z). In order to cover any potential uncertainties on the tiny contributions from Z+jets and diboson backgrounds, conservative uncertainties of 50 % are assigned to the predictions.

Finally, uncertainties on multi-jet backgrounds are derived from an alternative prediction based on fitting MC templates to $E_{\mathrm{T}}^{\mathrm{miss}}$ and $E_{\mathrm{T}}^{\mathrm{miss}}$+$m_{\mathrm{T}}^{W}$ distributions. This results in an uncertainty of 65 % on the estimate of this background.

7.5.5 Luminosity and other Sources

In order to perform the measurement and as shown in Equation (7.2), the luminosity corresponding to the analyzed dataset needs to be known as precisely as possible. The uncertainty on the integrated luminosity measurement is 1.7 % [120]. While it is among the largest uncertainties in the inclusive cross-section measurement, it is less important in the measurements of differential cross-sections.

Other uncertainties in this measurement concern the modeling of multiple interactions in the bunch crossings of the LHC (pile-up), the calibration of additional low-p_{T} tracks from the hard scattering process, and the statistical uncertainties due to the finite number of simulated events. The accuracy of the modeling of pile-up is estimated by varying the

mean number of interactions in the modeling. The effects of these variations are then propagated through the analysis chain, and the impact on the measurement is found to be small. The low-p_{T} tracks are used to estimate the missing transverse energy of the event, as described in Section 6.4. Uncertainties arising from the calibration of these tracks are estimated from comparisons of the p_{T}-imbalance of hard and soft tracks in data and simulation, as described in Ref. [167]. Finally, since the simulation of events in the various predictions models the statistical nature of the processes as well, there is a statistical uncertainty due to the limited number of simulated events in these predictions. The impact of this statistical uncertainty is estimated by applying a Gaussian smearing to the predictions within their statistical uncertainties. This uncertainty is also found to be small and within the statistical uncertainty of the measured data.
The uncertainty origintaing from the use of the JVT in suppressing pile-up jets is evaluated by varying the scale factor associated with this tagging.

8 Results of the Differential Measurement

In this section, the results of the measurement are shown and discussed. The measured JSF value in data is discussed in Section 8.1. The observed cross-section of the production of a pair of top quarks in the boosted phase-space, defined in Section 6.4, is given in Section 8.2, while the observed differential cross-sections on particle-level are discussed in Section 8.3. As outlined earlier, the observations are compared to predictions from various models in order to validate them and allow for future improvements.

8.1 Measured JSF in Data

The correction of the energies of the small-radius jets, as discussed in Section 7.1 is also applied to the observed data. The distribution of the reconstructed mass $m^{t,h}$ of the top jet used to derive the mean reconstructed mass is shown on the left of Figure 8.1. The predictions are normalized to the data yield in order to highlight the agreement of the shapes of the prediction when compared to the data. Since the JSF method can only incorporate shifts of the mean $m^{t,h}$ of the reconstructed mass distribution, the overall normalization is not relevant here. The distribution shows that the agreement between data and prediction before applying the JSF method is already very good. The JSF value is therefore expected to be compatible with one within its uncertainties. The JSF for the observed data distribution is determined to be 0.99965 ± 0.00087, which is in good agreement with one within the statistical uncertainties. The measured JSF value is applied to the energy scales of all small-radius jets in the observed data in the following results. The linear parametrization on the right of Figure 8.1 shows the functional description used to derive the JSF value in data and the various simulated samples.

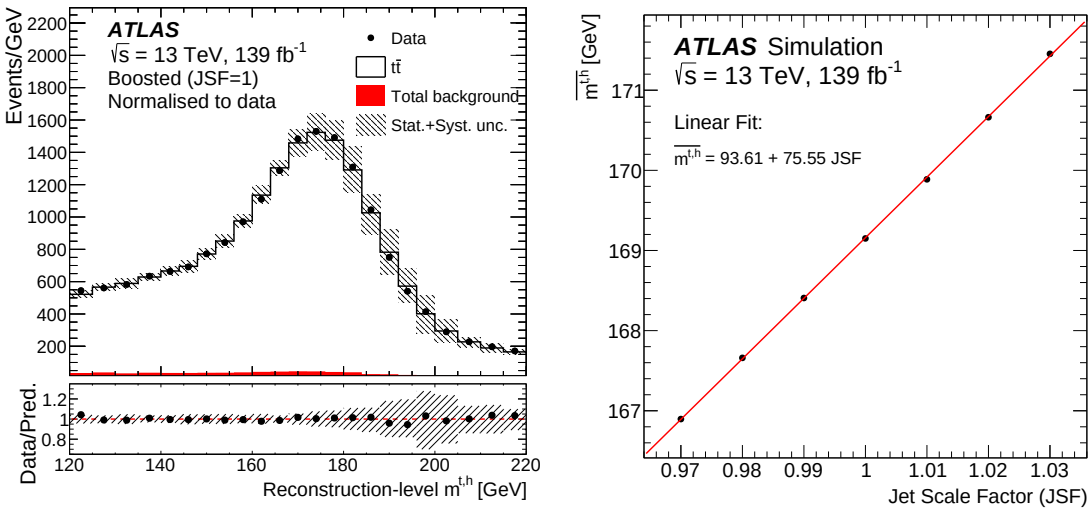

Figure 8.1: Comparison of the measured reconstructed mass of the top-quark jet to the prediction of the $t\bar{t}$ signal (in white) and the various backgrounds combined (in red) on the left. The predictions are normalized to the data yield in order to highlight the agreement of the shapes of the prediction when compared to the data. On the right, the linear parametrization of the mean $\overline{m^{t,h}}$ of the top-jet distribution is shown as a function of the JSF derived from the signal simulations.

8.2 Measured Fiducial Cross-Section

The particle-level fiducial cross-section of the production of a pair of top quarks in the selection of events is measured to be $1.267 \pm 0.005(\text{stat.}) \pm 0.053(\text{syst.})$ pb. The measurement is thus dominated by systematic uncertainties, with the uncertainties due to the luminosity measurement and modeling uncertainties being among the largest. The breakdown of the fractional uncertainties is given in Table 8.1, also for the case of not employing the JSF method. As expected, the JSF method reduces uncertainties related to jets significantly and subsequently also reduces the total systematic uncertainties on the cross-section measurement. However, it introduces slight increases in uncertainties related to the top-quark mass, as is expected due to the greater importance of this value in the additional JSF measurement. Furthermore, an additional statistical uncertainty in the measurement of the JSF value is introduced.

Figure 8.2 shows the comparison of the observed fiducial cross-section at particle level (dashed line) to several NLO predictions (black markers). The predictions are normalized to the NNLO+NNLL prediction for the total cross-section of a pair of top quarks. Predictions represented by open markers were reweighted at parton level to match NNLO predictions, as described in Section 6.3.4. For the various predictions, PWG+PY8 corresponds to the Powheg+Pythia sample, PWG+H7 to the Powheg+Herwig sample, and MCatNLO+PY8 to the MadGraph5_aMC@NLO+Pythia sample.

The total uncertainty of the cross-section measurement is represented by the yellow band,

Source	Uncertainty [%]	Uncertainty [%] (no JSF)
b-tagging	$^{+2.44}_{-2.42}$	$^{+2.42}_{-2.40}$
Hadronisation	$^{+1.97}_{-1.97}$	$^{+1.75}_{-1.75}$
Luminosity	$^{+1.76}_{-1.76}$	$^{+1.76}_{-1.76}$
Radiation (IFSR + h_{damp})	$^{+0.99}_{-1.56}$	$^{+1.43}_{-2.26}$
Top-quark mass	$^{+0.83}_{-1.06}$	$^{+0.09}_{-0.07}$
Lepton	$^{+0.78}_{-0.76}$	$^{+0.78}_{-0.76}$
Jets	$^{+0.67}_{-0.66}$	$^{+4.20}_{-4.13}$
Backgrounds	$^{+0.65}_{-0.58}$	$^{+0.62}_{-0.56}$
Hard scatter	$^{+0.45}_{-0.45}$	$^{+0.82}_{-0.82}$
Statistical (data)	$^{+0.38}_{-0.38}$	$^{+0.38}_{-0.38}$
Pile-up	$^{+0.38}_{-0.39}$	$^{+0.02}_{-0.02}$
JSF statistical	$^{+0.38}_{-0.38}$	$^{+0.00}_{-0.00}$
Statistical (MC)	$^{+0.14}_{-0.14}$	$^{+0.14}_{-0.14}$
$E_{\mathrm{T}}^{\mathrm{miss}}$	$^{+0.13}_{-0.13}$	$^{+0.13}_{-0.13}$
PDF	$^{+0.05}_{-0.05}$	$^{+0.05}_{-0.05}$
Total systematics	$^{+4.07}_{-4.28}$	$^{+5.77}_{-5.97}$
Total	$^{+4.09}_{-4.29}$	$^{+5.79}_{-5.98}$

Table 8.1: Breakdown of the fractional uncertainties in the various uncertainty categories for the inclusive $t\bar{t}$ cross-section measurement for both with the JSF method applied (left column) and without the JSF method applied (right column).

while the orange band shows only the statistical uncertainty.
The observed cross-section is measured at a precision of 4.2 % and is thus more precise than the calculated $t\bar{t}$ cross-section at NNLO+NNLL. All of the cross-section predictions shown in Figure 8.2 yield a larger cross-section than the observed one. The predictions of PWG+PY8 and MCatNLO+PY8 show the largest deviation from the measurement, while PWG+H7 gives a prediction closer to the observation. However, no significant deviations are observed. All of these three predictions are also reweighted at particle-level to match NNLO predictions. After the reweighting, all predictions show improved agreement with the measurement and are found to be consistent with the observed value. This indicates that the higher-order corrections are of importance for predictions in comparison with a measurement in this phase space and at this precision.

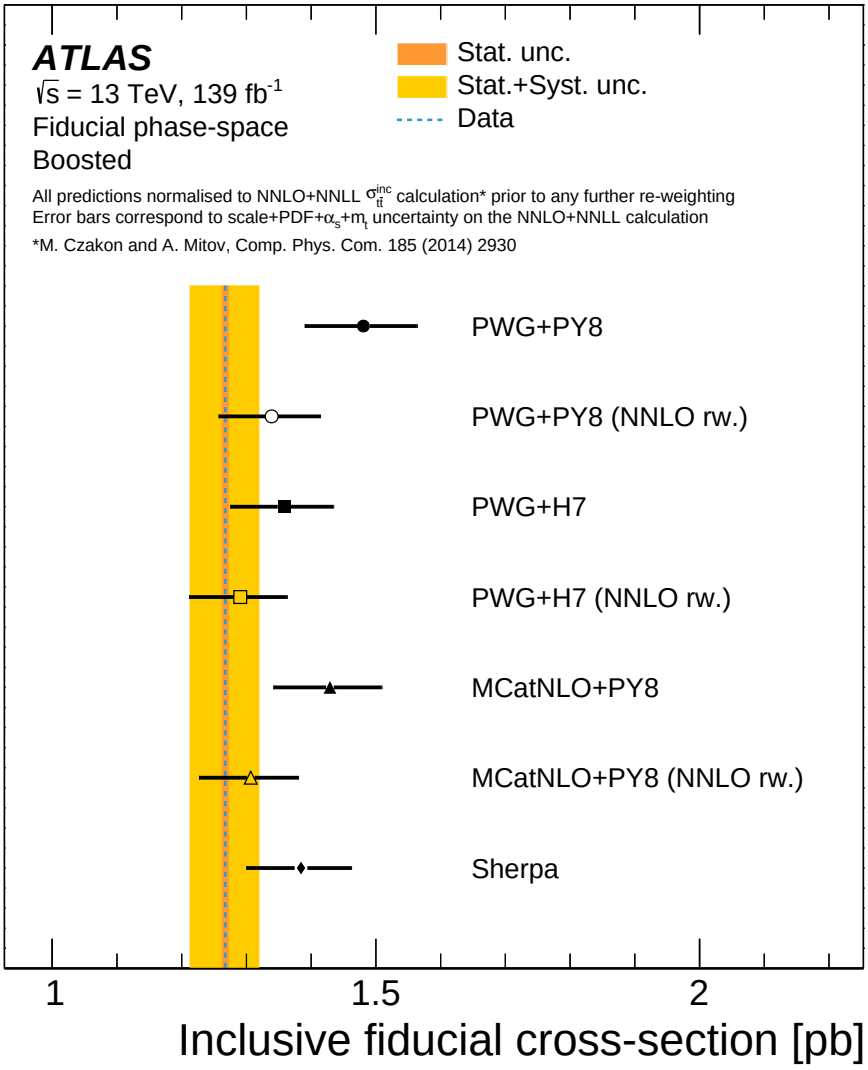

Figure 8.2: Comparison of the observed fiducial cross-section of the production of a pair of top quarks at particle level (dashed line) to several NLO predictions (black markers). The predictions are normalized to the NNLO+NNLL prediction for the total cross-section of a pair of top quarks. Predictions represented by open markers were reweighted at parton level to match NNLO predictions. The total uncertainty of the cross-section measurement is represented by the yellow band, while the orange band shows only the statistical uncertainty. PWG+PY8 corresponds to the Powheg+Pythia sample, PWG+H7 to the Powheg+Herwig sample, and MCatNLO+PY8 to the MadGraph5_aMC@NLO+Pythia sample.

8.3 Measured Particle-Level Differential Cross-Sections

The main goal of this measurement is to measure the cross-sections of this process in differential distributions of the variables listed in Section 7.3. These differential measurements are unfolded to particle-level using the procedure described in Section 7.2. Figure 8.3 shows a selection of the measured differential distributions for $H_{\mathrm{T}}^{t\bar{t}+\mathrm{jets}}$, $H_{\mathrm{T}}^{t\bar{t}}$, $p_{\mathrm{T}}^{t,\ell}$, $p_{\mathrm{T}}^{t,h}$ and $m^{t\bar{t}}$ compared to several predictions. Additional measured differential distributions are shown in Appendix 1. The bottom panels contain the ratios of the various predictions to the unfolded data and are spread over two panels for better readability. The agreement varies a lot among the variables and within the respective spectra. All of the shown top quark-related variables have a softer spectrum in data when compared to the NLO predictions, leading to an overestimation of the predicted events at high energy. This is very prominent e.g. in the $H_{\mathrm{T}}^{t\bar{t}}$ spectrum (Figure 8.3b) for the Powheg+Pythia and MadGraph5_aMC@NLO+Pythia predictions, but also shows large effects in the p_{T} spectra of the two top quarks (Figures 8.3c and 8.3d). The observation of such softer spectra in data is consistent with previous measurements [13, 15, 188]. This already suggests that additional higher-order corrections to the predictions may play a role since additional orders will lead to a softer spectrum in such observables. Indeed, this is what the comparison to the predictions reweighted to NNLO shows: the prediction of Powheg+Pythia for $p_{\mathrm{T}}^{t,h}$ (Figure 8.3d) reweighted to NNLO shows much better agreement and an overall softer spectrum. Furthermore, better agreement among the predictions is observed in the reweighted spectra.
A similar picture emerges for variables sensitive to the radiation of extra jets, like $H_{\mathrm{T}}^{t\bar{t}}$ and $p_{\mathrm{T}}^{t\bar{t}}$. For $H_{\mathrm{T}}^{t\bar{t}}$ e.g. the predictions made by Sherpa agree best with the measurement. This indicates that the addition of the extra-jet radiation to the calculation of the matrix element is essential in the modeling of such variables. None of the various predictions tested in this measurement show good modeling of all the measured variables.
The fractional uncertainties for the p_{T} spectrum of the hadronically decaying top quark are shown in Figure 8.4. As in most variables, the largest component of the systematic uncertainties is the modeling of the $t\bar{t}$ signal. This modeling contains the hard-scatter process as well as the hadronization and variations in the amounts of extra radiation in the process. The dominant detector uncertainty arises from the flavor tagging of heavy-flavor jets. Furthermore, the $p_{\mathrm{T}}^{t,h}$ spectrum shows significant contributions of systematic uncertainties related to jets in the tail of the distribution, with more than 8 % in the last bin. Among these are foremost uncertainties on the JES, which were not reduced by the JSF method as much in these regions of the phase space.

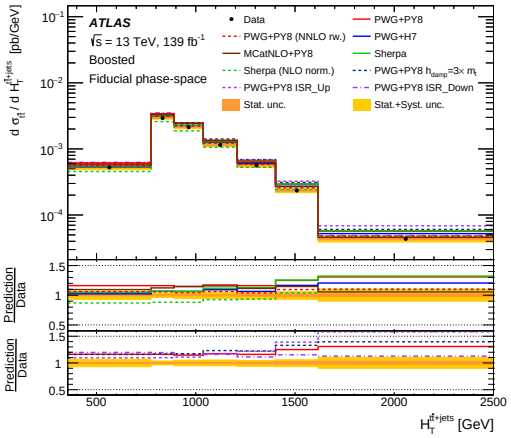

(a) $H_{\mathrm{T}}^{t\bar{t}+\mathrm{jets}}$

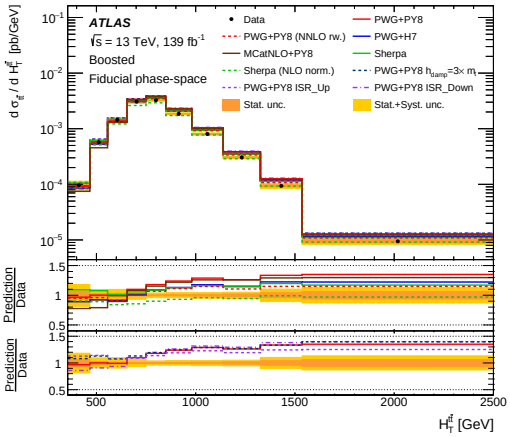

(b) $H_{\mathrm{T}}^{t\bar{t}}$

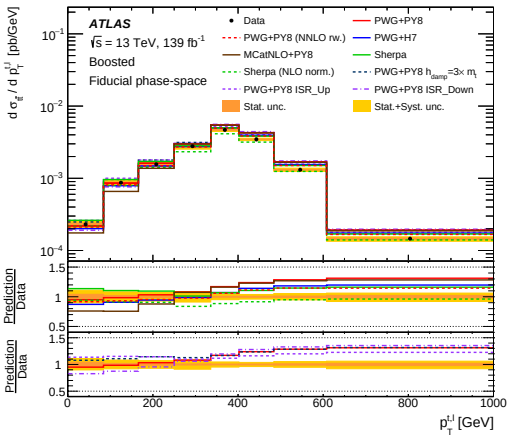

(c) $p_{\mathrm{T}}^{t,\ell}$

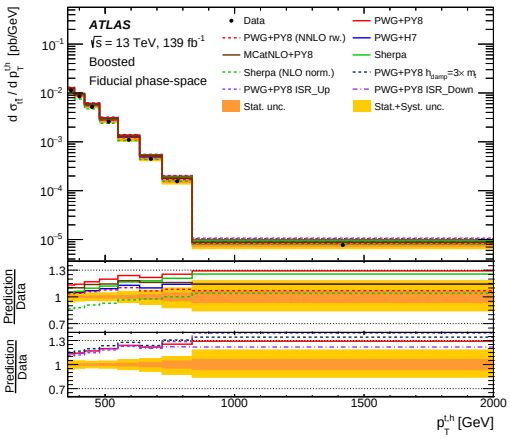

(d) $p_{\mathrm{T}}^{t,h}$

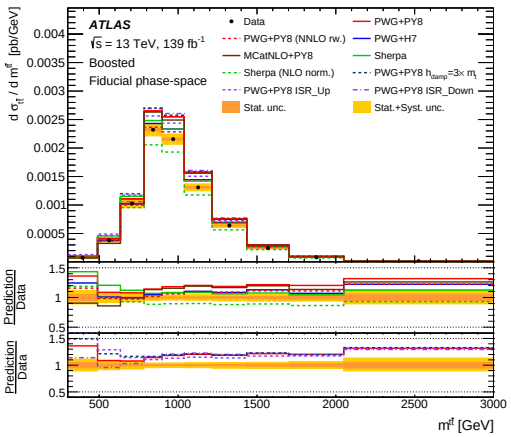

(e) $m^{t\bar{t}}$

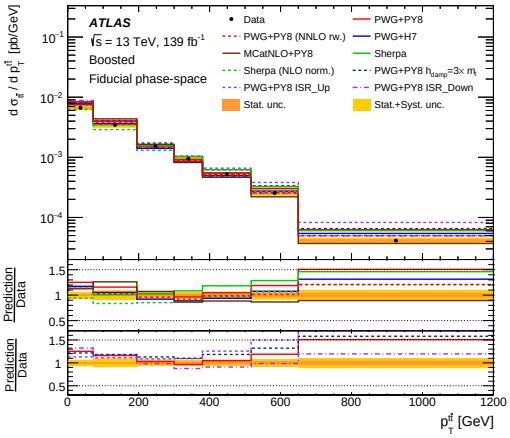

(f) $p_{\mathrm{T}}^{t\bar{t}}$

Figure 8.3: Differential distributions of the unfolded data for the observables $H_{\mathrm{T}}^{t\bar{t}+\mathrm{jets}}$, $H_{\mathrm{T}}^{t\bar{t}}$, $p_{\mathrm{T}}^{t,\ell}$, $p_{\mathrm{T}}^{t,h}$, $m^{t\bar{t}}$ and $p_{\mathrm{T}}^{t\bar{t}}$ are compared to several predictions. The solid colored histograms show the various models used for the predictions, while the dashed lines show the latter reweighted to NNLO.

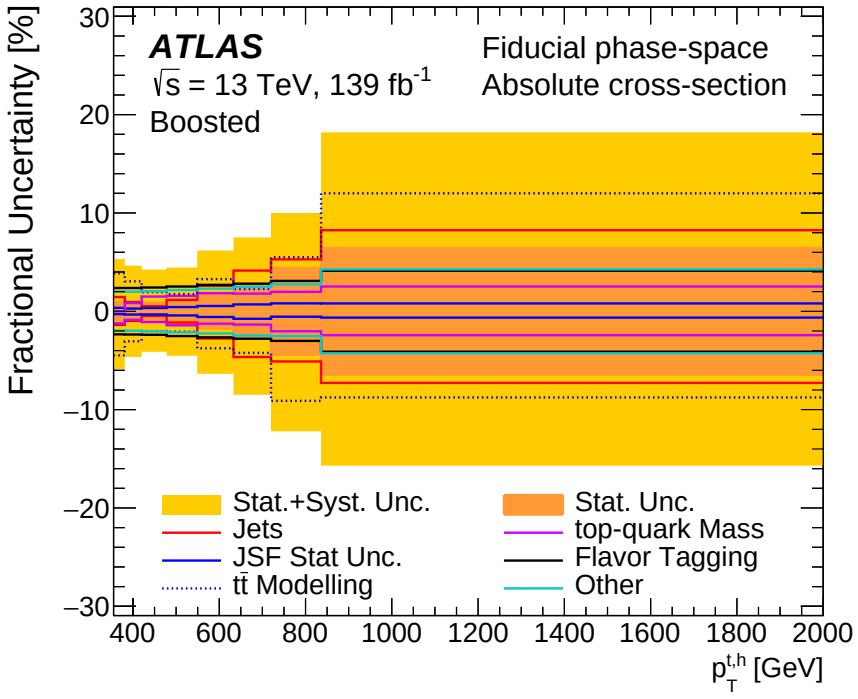

Figure 8.4: Differential distributions of the fractional uncertainties for the $p_{\mathrm{T}}^{t,h}$ spectrum. The total uncertainty on the measurement is shown in yellow, with its statistical component in orange. Various components to the systematic uncertainties are shown as the colored lines.

9 Construction of the EFT model

In order to interpret the measurement in the framework of EFT, the model needs to be adapted to the particular analysis at hand. This involves the choice of EFT operators, which are allowed to give non-zero contributions, as well as the treatment of the backgrounds and the choice of the observable for the interpretation. All of these depend on the particular phase-space and signal topology of the measurement. The choice of these, as well as the construction of the differential model based on these choices, are discussed in this section.

9.1 Choice of EFT Operators

In the production of a pair of top quarks, there are generally two classes of EFT operators potentially contributing: operators involving couplings to gluons and the four-quark operators modifying couplings of the top quark to other quarks [86]. The most important operator in terms of effects on the production of two top quarks is the chromomagnetic dipole operator O_{tG}. It affects the coupling of top quarks to gluons, as represented by the black dot in Figure 9.1. The right diagram in the same figure shows that this operator also creates effective $ggt\bar{t}$ couplings.

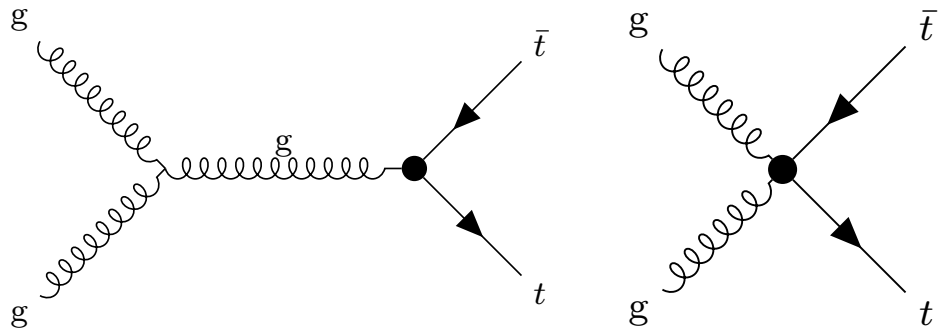

Figure 9.1: Feynman diagrams of couplings possibly affected by the chromomagnetic dipole operator O_{tG} in the production of a pair of top quarks. The black dot shows the coupling of the top quarks to the gluon which can be affected by this potential BSM physics contribution.

The definition of this operator in the Warsaw basis [16] is

$$O_{tG} = ig_S(\bar{Q}\sigma^{\mu\nu}T^A t)\tilde{\Phi}G^A_{\mu\nu}\,. \tag{9.1}$$

Here, the operator is normalized by the strong coupling constant g_S. The Higgs doublet is denoted by $\tilde{\Phi}$, the T^A are the strong SU(3) generators, $G^A_{\mu\nu}$ represents the gauge field tensor

of the gluons, t denotes the right-handed top quark, $\bar{Q}$ is the left-handed quark doublet of the third generation and $\sigma^{\mu\nu}$ are the Pauli matrices. Here, a $\mathrm{U}(2)_q \times \mathrm{U}(2)_u \times \mathrm{U}(2)_d$ flavor symmetry is imposed among quarks of the first and second generation. Since the production channel shown in Figure 9.1 is the dominant one at the LHC, the operator is at the core of the production of a pair of top quarks. Due to the high luminosity of affected vertices, this operator has a large impact on the total cross-section of the process, as well as on the differential distributions [86]. The magnetic dipole operator is furthermore expected to show no strong energy enhancements in the linear term at $\mathcal{O}(\Lambda^{-2})$, but only in the quadratic terms at $\mathcal{O}(\Lambda^{-4})$.
Another operator affecting the couplings of gluons in this channel is the operator O_G, which potentially modifies the gluon self-coupling. However, this operator is not part of the set of top-philic EFT operators since it does not involve a top quark. Furthermore, other processes like the production of multiple jets have better sensitivity to this operator and, therefore, lead to stronger limits than in the measurement of the production of a pair of top quarks.
The second class of operators, the four-fermion operators, affect the coupling of the top quark to other quarks. In the production of a pair of top quarks at LO in QCD these couplings correspond to the one shown in Figure 9.2. Since the luminosity of initial quarks in this production channel at the LHC is much smaller than the one of gluon fusion, these operators are suppressed. Due to the rate of the coupling, they lead to much smaller effects than the ones from, e.g., O_{tG}, when it comes to modifying the properties of the production of a pair of top quarks.

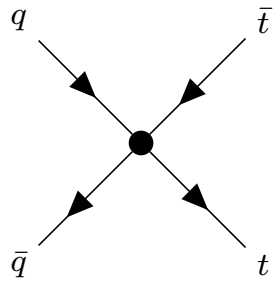

Figure 9.2: Feynman diagram of a coupling possibly affected by the four-fermion operators in the production of a pair of top quarks. The black dot shows the coupling of the top quarks to other quarks which can be affected by this potential BSM physics contribution.

There are different ways to group this class of operators. Since many of these operators have a similar content of involved particle fields or whole groups of operators affect a given process, they are sometimes grouped by the coupling structure. For the production of a pair of top quarks, one can create linear combinations of four fermion operators through their behavior under top-quark charge conjugation, as shown in Ref. [86].
The definition of the four-fermion operator $O_{tq}^{(8)}$ in the Warsaw basis is given as

$$O_{tq}^{(8)} = (\bar{q}_i \gamma^\mu T^A q_i)(\bar{t} \gamma_\mu T^A t)\,. \tag{9.2}$$

Here, the q_i denote the quark doublets of the first two generations, and γ_μ is the Dirac matrix. This operator affects the same couplings as shown in Figure 9.2. The operator $O_{tq}^{(8)}$ is expected to be among the four-fermion operators with the strongest effect on this measurement [189]. Unlike O_{tG}, it shows a much stronger energy dependence already in the linear EFT expansion at $\mathcal{O}(\Lambda^{-2})$, which is even stronger in the full expansion at $\mathcal{O}(\Lambda^{-4})$. Despite the production channel starting from initial quarks being a sub-leading one, the effects of this operator are expected to be enhanced in this measurement. This is due to the PDFs of the partons. The quark luminosities at large momenta are enhanced with respect to the gluon luminosities. This effect, combined with the larger energy enhancements of $O_{tq}^{(8)}$ makes the boosted phase-space – especially in the tails of the differential distributions – the ideal region to constrain $O_{tq}^{(8)}$. Resolving this fundamental difference in the effects of these operators, therefore, is the key to constraining both operators at the same time and ideally extending interpretations to higher-dimensional models (i.e., including more non-zero EFT coefficients at the same time). Thus, with the expected scaling of the parton luminosities as well as the different energy scaling of the two operators, multiple effects add expected features to this measurement which can be used to disentangle the effects of the two operators.
Other operators can furthermore enter through the signal process. Among those are operators affecting the Wtb vertex in the decay of the top quark, like O_{tW}. Such operators can potentially change the angular properties of the top quarks. However, the observable chosen for the interpretation in this work is $p_{\mathrm{T}}^{t,h}$ and is, therefore, to first order independent of the angular distribution of the decay products. Therefore, there are no obvious places for additional EFT operators to modify the interpretation. It should furthermore be noted that the goal of this work is to show the potential of a differential measurement in disentangling multiple operators and the particular sensitivity of this phase space to the family of four-quark operators in the top-quark sector. Thus, it does not aim to provide a comprehensive interpretation of the signal process including all potential operators.

9.2 Modeling of the EFT Effects

Similar to the modeling of the signal and background processes, the EFT effects need to be translated to the level of the observations. Therefore, the modeling of the EFT effects is performed through MC simulations similar to the ones described in Section 6.3. There are multiple models which facilitate this. They differ in various points like the choice of quark flavor symmetry or the set and definitions of the included EFT operators. Therefore, many of the models are tuned to certain areas of the EFT framework, like the weak effective theory, the Higgs sector, or the top-quark sector. Common frameworks (called UFO models) in the top-quark sector are the `dim6top` model [105], the `SMEFTsim` model [190] and the `SMEFTatNLO` model [189]. In this measurement the SMEFTatNLO 1.0.0 UFO model [189] at LO is used to add the EFT framework to the ME generation. The ME generation is facilitated through the MadGraph5_aMC@NLO framework, while the showering of the events is performed using Pythia 8.230. The renormalisation and factorisation scales were set to $\mu_r = \mu_f = m_t$ and the $\{m_W, m_Z, G_f\}$ EW input scheme is used as outlined

in Ref. [191]. The advantage of the chosen masses used in this input scheme is the model-independent way, in which they can be measured. The EFT model described later in Section 9.5 contains six free parameters, which need to be determined from simulations. In order to sufficiently sample the EFT space with these simulations, the EFT simulations are generated at nine different points with $(C_{tG}, C_{tq}^{(8)}) = (\pm 1 \text{ or } 0,\ \pm 1 \text{ or } 0)$, always applying $\Lambda = 1\,\text{TeV}$. The choice of energy scale of the EFT operators does not affect the interpretation, until it is matched to a particular theory. Therefore, the convenient choice of 1 TeV is made. Two different statistically independent sets of simulations are generated this way: one set including the linear EFT model with terms up to $\mathcal{O}(\Lambda^{-2})$, and one set including the quadratic EFT model with terms up to $\mathcal{O}(\Lambda^{-4})$. The simulation of the ATLAS detector is performed using the faster simulation of the detector effects based on parameterized showers in the calorimeters [115]. In order to test for biases of the unfolding procedure in the presence of non-zero EFT effects, these predictions, including the detector simulation, are used, as outlined in Section 11.1. For this purpose, an additional dataset is generated as a prediction for the EFT effects at $(C_{tG}, C_{tq}^{(8)}) = (0.2, 0.2)$, which is used to test for such effects at a realistic point in the EFT space resembling the expected limits.

9.3 Effects of the EFT Operators

As mentioned in Section 9.1, the two EFT operators O_{tG} and $O_{tq}^{(8)}$ have very different effects on the measured process. The expected impact of a given non-zero contribution of BSM physics through O_{tG} is much larger than that from $O_{tq}^{(8)}$. One of the reasons for this is the aforementioned difference in luminosities of the necessary couplings in the production of a pair of top quarks, with the coupling of the top quark to the gluon being the dominant one. Figure 9.3 shows the change of the total cross-section as a function of the two Wilson coefficients C_{tG} and $C_{tq}^{(8)}$ in units of the SM prediction for the linear and quadratic EFT models. The effects on the total cross-section for O_{tG} are much stronger than those of the four-fermion operator, resulting in a more significant slope in the linear EFT model. The effects of $O_{tq}^{(8)}$ on the total cross-section are only of the order of 1 %, even at the edge of the considered range. In the inclusive phase space, this also applies to the quadratic EFT model. When comparing the effects in the phase space selected by requiring the signal selection outlined in Section 6.4 to the inclusive phase space, however, the slope is bigger for both operators. This already shows that the selected phase space favors the effects of the two EFT operators, resulting in a higher sensitivity. For the quadratic model, the EFT effects generally also become stronger, e.g., when comparing the slopes close to the SM prediction. The increase in slope is particularly big for $O_{tq}^{(8)}$, originating from the increase in luminosity of suitable production channels for this operator.

The quadratic model shown in Figure 9.3b clearly shows the effects of the additional $\mathcal{O}(\Lambda^{-4})$ terms. As expected from the mathematical parametrization, the effects follow a parabola shape. This introduces a possible ambiguity in the value of the Wilson coefficient for a given value of the cross-section. Furthermore, the quadratic model is restricted to a certain parameter range in the predicted cross-section. In particular, it is not capable

of modeling a cross-section below a certain fraction of the SM cross-section due to the strictly positive quadratic terms. However, also for this model, the slope and, therefore, the change of the cross-section at the SM is much larger for O_{tG}. Similarly to the linear model, applying the signal selection criteria increases the impact of the EFT contributions in relation to the SM.
Considering differential distributions, the observations are resolved as a function of the given observable and thus, give a more detailed picture of the EFT effects. Therefore, a differential $p_{\mathrm{T}}^{t,h}$ distribution, for example, allows to examine the effects of these operators in different slices of the energy scale. The constellation of the two operators of interest in this work allows for a potential distinction by their behavior at varying energy scales. As mentioned in Section 9.1, an enhancement of the effects of $O_{tq}^{(8)}$ is expected in the tails of the p_{T} spectra of the collision products due to the increasing parton luminosities of initial quarks at large transverse momentum [8].
Furthermore, the two operators are expected to show different energy dependencies. While the impact of O_{tG} relative to the SM is expected to scale linearly as a function of energy-scale sensitive observables like $p_{\mathrm{T}}^{t,h}$ or $m^{t\bar{t}}$, effects of $O_{tq}^{(8)}$ are expected to display a quadratic growth [86]. The combination of such behavior makes a differential measurement, which can resolve these effects at the tails of such variables, a well-suited basis to constrain impacts of such operators.
The effects of the two operators on the signal process in the phase space outlined in Section 6.4 are shown in Figure 9.4. It shows the differential distributions of $p_{\mathrm{T}}^{t,h}$ for the SM and different setups of the EFT contributions through the two Wilson coefficients C_{tG} (a) and $C_{tq}^{(8)}$ (b). The histograms show the SM predictions modeled by the LO EFT MC ($C_{tG} = C_{tq}^{(8)} = 0$) in black as well as the linear EFT prediction in blue and the quadratic EFT prediction in red, both for ($C_{tG} = 1 \vee C_{tq}^{(8)} = 1$). For O_{tG} the linear model shows only a small dependence on $p_{\mathrm{T}}^{t,h}$ when compared to the quadratic model. Both predictions yield enhanced rates throughout the spectrum by at least 30 %, showing the large impact of this operator on the total cross-section of the signal process. Furthermore, the full quadratic EFT model clearly shows the expected linear energy dependence of O_{tG}.
For $O_{tq}^{(8)}$, both, the linear and the quadratic EFT prediction have a very small effect on the low p_{T} range when compared to O_{tG}, showing the small expected impact of this operator on the total cross-section. However, they show a stronger dependence on the observable than O_{tG}, with the effects rising above the ones by O_{tG} at the same value of the Wilson coefficient at the end of the p_{T}-spectrum. This shows the expected stronger energy dependence of this operator.

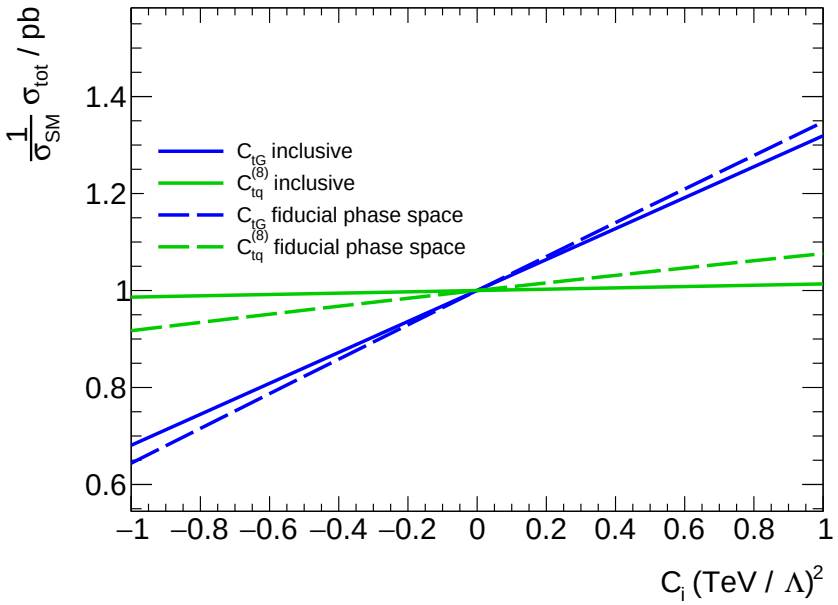

(a) Linear EFT model ($\mathcal{O}(\Lambda^{-2})$)

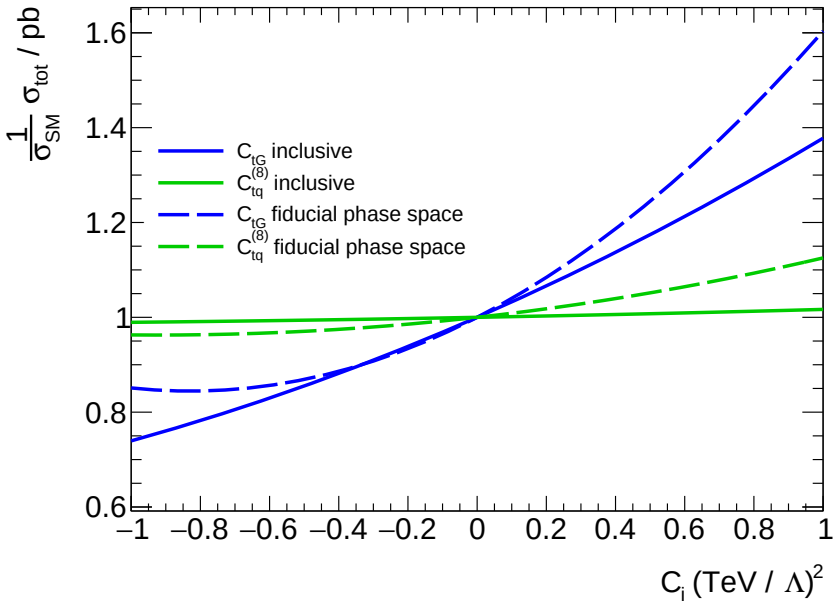

(b) Quadratic EFT model ($\mathcal{O}(\Lambda^{-4})$)

Figure 9.3: Change of the total cross-section as a function of the two Wilson coefficients C_{tG} and $C_{tq}^{(8)}$ in units of the SM prediction for the linear (a) and quadratic (b) EFT models. The cross-section change is normalized to the SM prediction modelled by the LO EFT MC prediction (with all coefficients set to zero). The impact of the EFT contributions is shown in the inclusive phase space (without any of the selection criteria outlined in Section 6.4 applied) as well as in the fiducial phase space, requiring the signal selection.

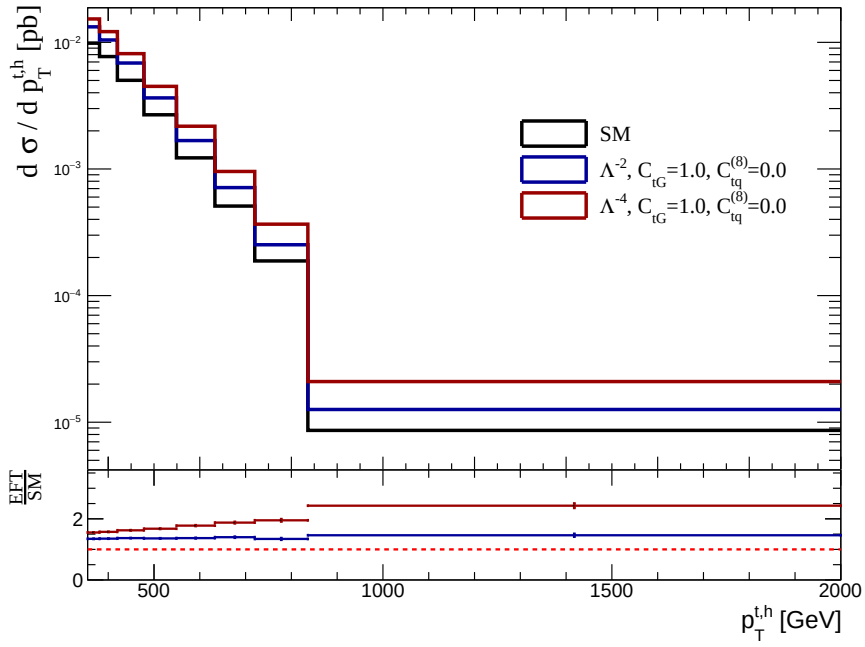

(a) Impact of O_{tG} for $C_{tG} = 1$.

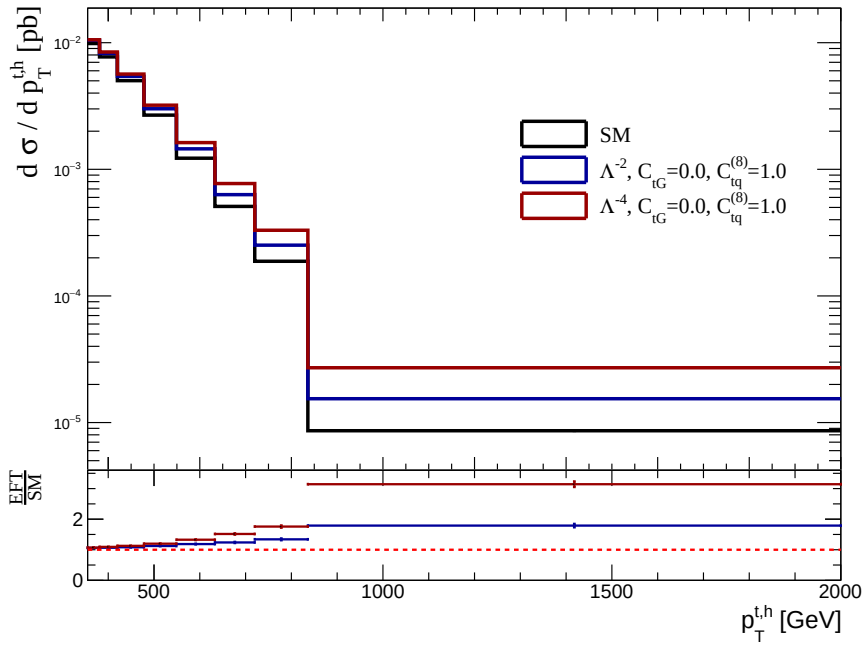

(b) Impact of $O_{tq}^{(8)}$ for $C_{tq}^{(8)} = 1$.

Figure 9.4: Differential distributions of $p_{\mathrm{T}}^{t,h}$ for the SM and different setups of the EFT contributions via the two WC C_{tG} (a) and $C_{tq}^{(8)}$ (b). The histograms show the LO EFT MC predictions with SM prediction (with all coefficients set to zero) in black, the SM + EFT contributions up to $\mathcal{O}(\Lambda^{-2})$ in blue and the SM + EFT contributions up to $\mathcal{O}(\Lambda^{-4})$ in red.

9.4 Treatment of EFT Effects in Backgrounds

Since the EFT approach, unlike the general choice of signal processes, does not generally distinguish between different physics processes by their respective final states, multiple processes can contribute to potential EFT effects besides the signal process. On the one hand, contributions from EFT operators relevant in the signal topology can occur in background processes if they share the respective vertex of the EFT operator. On the other hand, the background processes can introduce potential EFT effects of other operators not taken into account in the signal process, which can dilute the interpretation of the signal process in terms of other operators. An EFT interpretation of a classical measurement of a signal process thus needs to be extended to also include these considerations, unless they can be neglected. This can be the case for very pure measurements, which are not affected by background processes to any significant degree, or if EFT effects on the background are tiny and therefore do not affect the interpretation.

In this measurement, the observed data after the selection outlined in Section 6.4 show a very high purity. The events after the selection consist of 96.4 % signal events. This already shows that any EFT contributions only affecting a background process will have a minimal effect on the measurement.

However, since a differential measurement is used for the EFT interpretation in this work, the signal purity needs to be evaluated in all bins, as each of the bins constitutes a measurement which potentially can be diluted by EFT effects in the background processes. The fractions of events belonging to the signal and to the various background processes for the $p_{\mathrm{T}}^{t,h}$ distribution are shown in Figure 9.5.

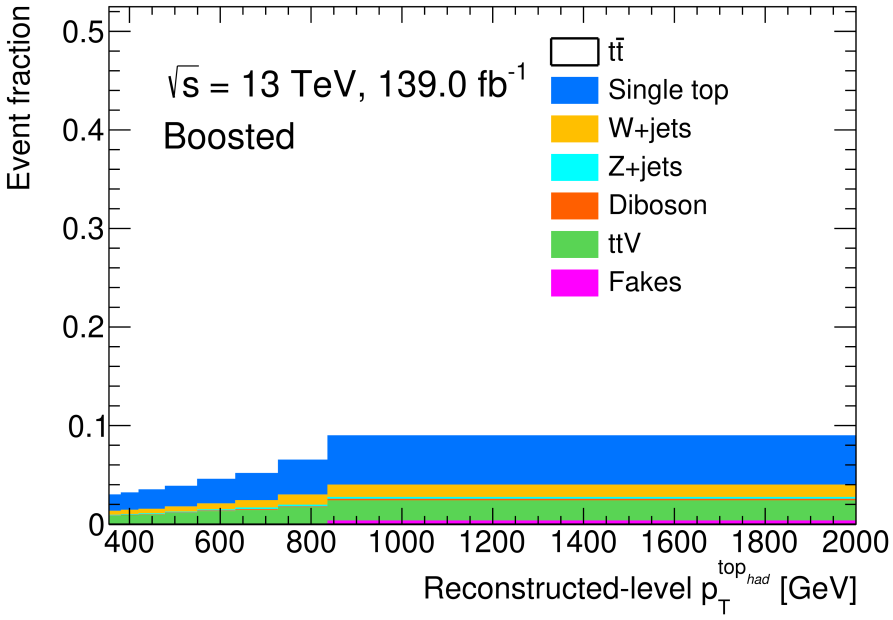

Figure 9.5: Differential distributions of the event fractions in the $p_{\mathrm{T}}^{t,h}$ spectrum for the signal and different background processes in the measurement phase space.

It shows the $t\bar{t}$ signal in white and the various backgrounds in the colored histograms. The distribution shows a trend for the signal purity to slightly decrease towards the tail of the distribution. Starting from a background fraction of about 3 % in the first bin of the spectrum, the purity drops to about 91 % in the last bin of the distribution. The production of a single top quark in association with a W boson constitutes the biggest contribution among the background events, with none of the other processes reaching more than a 2 % fraction among the individual $p_{\mathrm{T}}^{t,h}$ bins.
The single-top background adds both potential EFT contributions, since it shares operators with the signal process and is sensitive to other operators. Like the $t\bar{t}$ signal, this process is also affected by the chromomagnetic dipole operator O_{tG}, as well as other operators not included in the interpretation of the signal process like, for example, O_{tW}. However, the effects are not expected to be significant for this interpretation. As shown in Section 8.3, the uncertainties on the $p_{\mathrm{T}}^{t,h}$ distribution are found to be between 4 % to 20 % with an increase at high p_{T}. Studies of the expected limits with a preliminary set of systematic uncertainties[1] show, that the EFT effects lie at similar orders. Therefore, EFT effects of this order on contributions of a few percent of the events would have to be at orders of the expected tW SM contribution to have an effect coming close to the effects on the signal. Considering that the measured cross-sections for the tW processes are in agreement with the SM [192, 193], such strong EFT contributions are not expected.
For the tW backgrounds, a similar argument can be made for other tW-specific EFT operators, e.g. for those affecting the Wtb vertex like O_{tW}. Effects of these operators through the background process are implausible to reach non-negligible rates.
Thus, since the selected events show such high purity, any effects of EFT operators on the backgrounds are not taken into account in the interpretation.

9.5 Differential EFT Model

In order to perform a quantitative interpretation of the differential measurements, a model describing the various measurements (i.e., bins) is necessary. As pointed out previously, each bin of the differential measurement is treated as a distinct measurement, which is correlated to the other bins in the distribution. Therefore, each of the bins needs a dedicated description in the EFT framework. The basis of this model is described in Equation (2.5). It represents a quadratic function in the Wilson coefficients, with the dimensionality of the model representing the number of Wilson coefficients considered. In this work, the general EFT model, including the two Wilson coefficients C_{tG} and $C_{tq}^{(8)}$ for the rate σ^j in a bin j of the differential distribution has the form

$$\sigma^j\left(C_{tG}, C_{tq}^{(8)}\right) = p_0^j + p_1^j \cdot C_{tG} + p_2^j \cdot C_{tq}^{(8)} + p_3^j \cdot (C_{tG})^2 + p_4^j \cdot \left(C_{tq}^{(8)}\right)^2 + p_5^j \cdot C_{tG} \cdot C_{tq}^{(8)} \,. \quad (9.3)$$

The parameters p_i^j with $i \geq 1$ are the proportionality factors translating the Wilson coefficient values to the rates or cross-sections. They are determined from the EFT

[1] These studies were performed during the course of this work using a preliminary set of systematic uncertainties excluding, e.g., the theory uncertainties.

simulations described in Section 9.3 after applying the selection process outlined in Section 6.4 using parametric inference. The EFT model outlined in Equation (9.3) has six free parameters p_i^j. Thus, at least six points in the EFT space are necessary to determine these. In order to have an over-determined system, the EFT simulations are generated at nine different points with $(C_{tG}, C_{tq}^{(8)}) = (\pm 1 \text{ or } 0,\ \pm 1 \text{ or } 0)$, always applying $\Lambda = 1\,\text{TeV}$. After generating the differential EFT predictions for these nine points, the p_i^j are determined for every bin j of the $p_{\text{T}}^{t,h}$ distribution by performing a fit to the LO EFT simulations mentioned above.

Two separate models are used in the interpretation according to the highest order of considered EFT contributions, as outlined in Section 2.4. The linear model does not contain any terms quadratic in the Wilson coefficients, corresponding to $\left(p_3^j, p_4^j, p_5^j\right)$ in Equation (9.3), while the quadratic model contains the full expansion in Equation (9.3). Thus, the linear model contains EFT terms up to Λ^{-2} in the observable, while the quadratic model contains EFT terms up to Λ^{-4}. This allows the impact of the Λ^{-4} terms on the sensitivity of the results to be examined and to disentangle the energy response of the two models.

From the mathematical description it follows that the two models behave quite differently in their predictions of the Wilson coefficients for a given cross-section, which is shown here in more detail. Firstly, the linear model covers the whole cross-section range, while the quadratic model usually has a non-zero minimum predicted cross-section. Furthermore, the predicted cross-section for a given value of a Wilson coefficient in the one-dimensional linear Λ^{-2} model will change symmetrically when varying the value of the Wilson coefficient in either direction. For the quadratic Λ^{-4} model, assuming that the linear terms p_1 and p_3 in the respective Wilson coefficient are not coincidentally zero, this symmetry will only appear for a cross-section measurement at exactly the minimum predicted cross-section for the respective Wilson coefficient[2]. Thus, the quadratic model is expected to yield asymmetric limits under the SM assumption. The linear model, on the other hand, is symmetric for any given measurement. Lastly, the quadratic model differs from the linear one in being degenerate. While for a given cross-section there is generally only one corresponding value for the Wilson coefficient in the one-dimensional linear EFT model, the quadratic model can yield two solutions.

The parameters p_0^j describe the SM prediction and are replaced after the fit to the EFT simulations. In order to not be biased by the LO SM prediction used in the EFT simulations, this model parameter is replaced by the value of the SM prediction from the nominal PWG+PY8 sample after reweighting it to the NNLO prediction. This step is necessary because the EFT extensions to the SM are not yet available in simulations at higher orders. The LO predictions are known to significantly mismodel the SM and to disagree with more precise predictions at higher orders. Using these predictions as the baseline SM in the EFT model would therefore introduce artificial deviations in the obtained limits. Therefore, the agreement between the two SM predictions is among the decisive factors for the choice of observable. In the future, proper higher-order predictions

[2]While not being exactly symmetric, some approximation of the linear symmetry may also appear in the linear regime of the quadratic function.

including EFT effects, will make this procedure obsolete. The EFT contributions encoded by the p_i^j with $j \geq 1$ are kept to contain the relative EFT contributions at LO.

10 Expected Sensitivity to EFT Effects

In order to test the set-up for inferring knowledge on the two Wilson coefficients C_{tG} and $C_{tq}^{(8)}$, and to quantify the sensitivity of the measurement, expected limits are derived. These limits are determined using a typical set-up for the uncertainties of the measurement. The goal is to define the expectation and test the EFT model using Asimov data. Furthermore, the expected EFT limits represent the ultimate metric when choosing the best-suited measurement for the interpretation. In this chapter, the numerical set-ups of the EFT model used for deriving the expected and, later, the observed limits are described. Furthermore, the choice of observable is motivated using the expected limits, which in turn are discussed in more detail for the variable of choice. Finally, the potential of the measurement to disentangle the effects of both EFT operators is discussed.

10.1 Numerical Set-Up of the Statistical Model

The statistical model for the interpretation, which is discussed in Section 3.3, needs to be applied to the specifics of this measurement. In order to construct the particular model, three steps are performed.

1. The measured observable to be interpreted in the EFT framework is selected.

2. The EFT model outlined in Equation (9.3) is adapted to the prediction in the selected signal region and phase space.

3. The covariance matrix containing the uncertainties in the different bins of the observable is defined.

The choice of the observable for the EFT interpretation is based on two metrics and is outlined in detail in the following Section 10.2. Using the described metrics, the p_{T} of the hadronically decaying top quark $p_{\mathrm{T}}^{t,h}$ is found to be best suited for the interpretation.
In order to describe the quantitative EFT predictions in the bins of the $p_{\mathrm{T}}^{t,h}$ distribution, the binned EFT model is constructed as described in Section 9.5. Parametric inference is used to determine the proportionality factors p_i of the EFT model based on the EFT MC simulations. The SM prediction p_0 is then replaced by the nominal signal prediction using the PWG+PY8 SM prediction reweighted to NNLO. In order to create independent modeling of both EFT models – the linear and the quadratic model – this step is performed for both of these models on the independent MC simulations described in Section 9.3.

In order to include the uncertainties of the observations as well as their correlations among the different measurements, the covariance matrix determined from the unfolding procedure is used. It is a combination of experimental and theoretical uncertainties, where the experimental uncertainties correspond to the ones described in Section 8. Since the SM prediction in the EFT interpretation is built on the signal prediction obtained from simulating the $t\bar{t}$ signal process in Powheg and then reweighting the result to NNLO, it is used as the basis for the uncertainties in the EFT interpretation.
The theoretical uncertainties contain multiple components. Firstly, the uncertainty on the prediction contains a component modeling the uncertainties due to scale choices. For this, a seven-point scale variation is performed for the renormalization and factorization scales μ_r and μ_f. The seven variations follow from varying the scales within $\{1/2\mu, 2\mu\}$ with the condition $1/2 \leq \mu_r/\mu_f \leq 2$. The envelopes of the impacts of these variations on the variables used for the reweighting to NNLO are then the basis for deriving varied predictions. In detail, the distributions are reweighted to capture the shape difference in the envelopes only, while the normalization is kept fixed. This way, two new variations for each of the three variables are obtained. Each of these six variations is then used to repeat the reweighting procedure, yielding six new predictions reweighted to NNLO with one of the three variables replaced by one of its variations. The effects of the variations are then evaluated on the new prediction of the $p_\mathrm{T}^{t,h}$ spectrum, as shown in Figure 10.1.

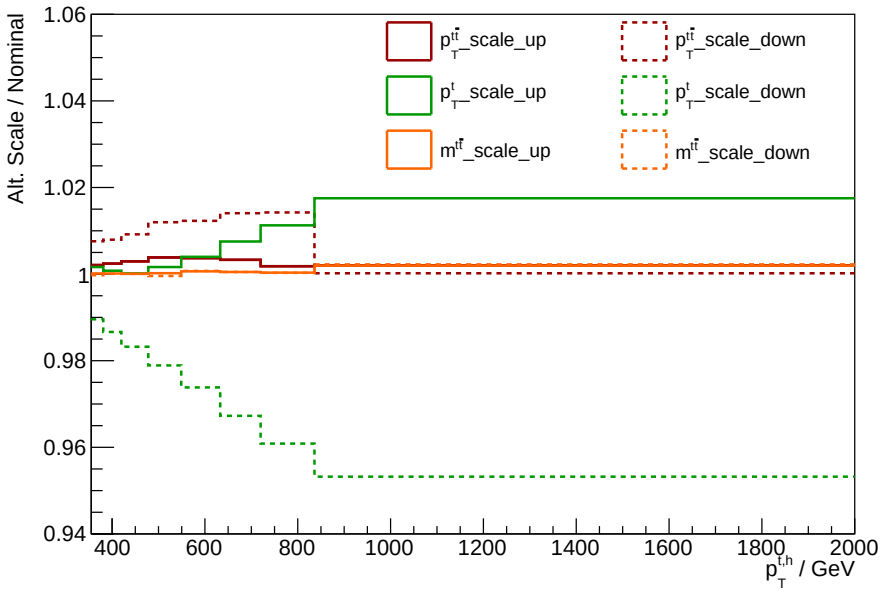

Figure 10.1: Ratio of the NNLO reweighted $p_\mathrm{T}^{t,h}$ spectrum obtained with the alternative scales to the nominal signal prediction for the six variations. The variations are obtained by fixing the normalisation and shifting the shape of the prediction according to the scale variations of μ_r and μ_f.

As expected, variations of $p_\mathrm{T}^{t,h}$ in the alternation of scales have the largest impact on the

$p_{\mathrm{T}}^{t,h}$ distribution. However, due to the correlations of the variables and the event selection based on, e.g., the $p_{\mathrm{T}}^{t,h}$ variable, each alternative sample shows a variation in this variable. In order to facilitate a conservative estimate of these effects, all of the variations are included as uncertainties and conservatively assumed to be uncorrelated.
Since these variations are constructed to cover the uncertainties on the shape of the prediction, a separate uncertainty is assigned to the normalization of the signal prediction. It consists of three components: firstly, the factorization and renormalization scales are varied independently and the effects are added to this uncertainty. Secondly, the choice of PDF[1] and the strong coupling constant α_S are varied, according to the recommendations given in the PDF4LHC prescription [138]. Lastly, the mass of the top quark used in the prediction is varied by 1 GeV. The resulting normalization uncertainty has a size of about 6 %.

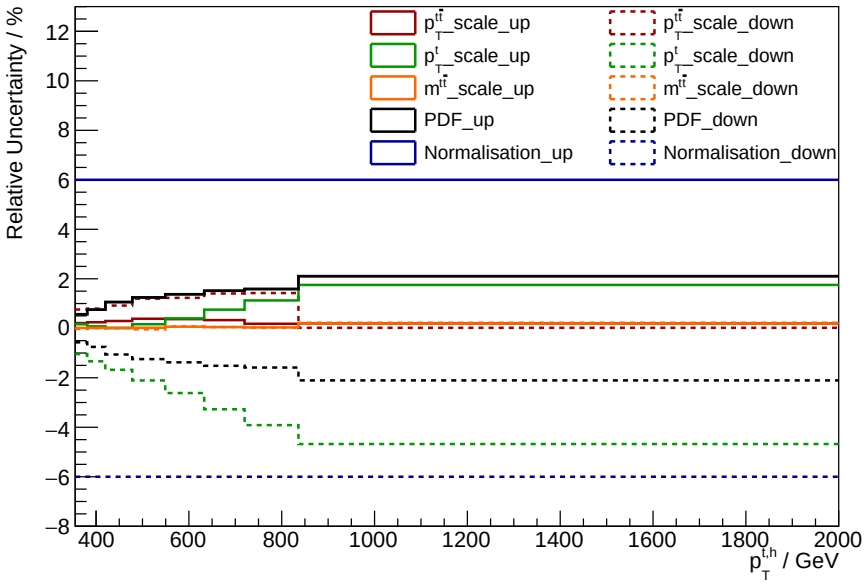

Figure 10.2: Components of the theory uncertainties relative to the $p_{\mathrm{T}}^{t,h}$ spectrum. The uncertainties show the alternative scales as well as the PDF and the normalisation uncertainties.

The relative size of the various components of the uncertainties summarized in the theory covariance is shown in Figure 10.2.
Among the theory uncertainties, there is no mechanism to facilitate a dependence on the Wilson coefficients. Therefore, the uncertainties are assumed to be independent of the EFT effects and, thus, similar for the EFT contribution. Since the EFT contributions represent predictions at LO, the question of additional uncertainties on this prediction may be raised. However, on the one hand, the statistical set-up does not allow for separate

[1]The MSTW2008 68% CL NNLO [139, 140], CT10 NNLO [141, 142] and NNPDF2.3 5f FFN [130] PDF sets are used.

uncertainties specifically on the EFT model. Secondly, such exclusive uncertainties on the EFT contributions would again represent minor effects on already small contributions. Assuming the EFT effects are of the order of the uncertainties on the prediction, they vary between $\mathcal{O}(1\,\%)$ and $\mathcal{O}(10\,\%)$ across the $p_{\mathrm{T}}^{t,h}$ distribution, with the last bin in the $p_{\mathrm{T}}^{t,h}$ spectrum showing the largest uncertainty. Assuming an uncertainty of $\mathcal{O}(20\,\%)$ in that particular bin, the effect on the total uncertainty would sum to an $\mathcal{O}(1\,\%)$ effect in the total uncertainty as compared to the uncertainty of about 18 % in that bin. Therefore, such effects are neglected in the theory uncertainties.

The Bayesian inference is based on a prior probability distribution, which allows for the insertion of prior knowledge. In this work, the prior is chosen to be uniform and therefore does not incorporate prior knowledge on the shape of the probability distribution. It is, however, constrained to be between -5 and 5 in the two Wilson coefficients' parameter space, which loosely incorporates recent limits on the two operators. The prior is thus proportional to

$$\Pi(C_i) \propto \begin{cases} 0, & \text{if } |C_i| > 5 \\ 1, & \text{otherwise.} \end{cases} \tag{10.1}$$

It has been tested that this choice of the bounds in the prior does not significantly affect the resulting EFT limits.

10.2 Choice of Observable

Since potential EFT contributions affect the various differential distributions in different ways, there generally are differences in the sensitivities of the measurements to certain EFT operators. The affected particles and, therefore, observables change depending on the involved vertices. Furthermore, the various EFT operators show different coupling structures, which in turn influence the resulting effects on the observables. In order to take such effects into account and choose the differential observable best suited for the EFT interpretation, dedicated studies are performed.
Starting from the theory expectations, one can already find a few distinctive features of the two operators. Both operators are expected to show an increasing effect at higher energy scales [86]. This growth is expected to be stronger for the four-quark operator $O_{tq}^{(8)}$, which is what the modeling of these effects already shows for the $p_{\mathrm{T}}^{t,h}$ spectrum in Section 9.3. This shows that kinematic distributions, which are sensitive to the energy scale of the process, will show concentrations of the EFT effects at large energy scales. This implies that observables describing the kinematics of the particles in the hard scattering process are expected to show similar effects. Among such variables are the transverse momenta $p_{\mathrm{T}}^{t,h}$, $p_{\mathrm{T}}^{t\bar{t}}$, $H_{\mathrm{T}}^{t\bar{t}}$, $H_{\mathrm{T}}^{t\bar{t}+\mathrm{jets}}$ or $p_{\mathrm{T}}^{t,\ell}$, as well as variables sensitive to the overall energy scale like, e.g., the reconstructed mass of the two top quarks $m^{t\bar{t}}$. Observables with shapes that are largely independent of the energy scale of the process, like pseudo-rapidities or the number of additional jets, are thus expected to not profit from this effect, since such enhancements will be diluted across the spectrum.

Furthermore, the four-quark operator $O_{tq}^{(8)}$ only enters via processes involving initial quarks, since such processes contain the necessary $q\bar{q}t\bar{t}$ vertex at LO. Due to the PDFs of the partons, the probability of such processes is increased at large momenta [8]. The sea quarks in the proton are likely to carry momentum fractions close to $1/3$ of the total proton momentum. Therefore, processes with quark initial states are expected to happen at larger luminosities with large momenta. This feature also suggests that the regions corresponding to high energy scales – like high-p_{T} tails – are expected to be most sensitive to potential EFT effects. This is due to this effect translating to the final state particles in the signal process and, therefore, the observables.

10.2.1 Expected Sensitivity

In order to find the kinematic variable best suited for the EFT interpretation, the expected limits on the two EFT operators are used. Depending on the behavior of potential EFT effects in the particular variable, these effects may show distinct features or get diluted in the differential distribution. Since the measurements in differential bins will generally be less precise[2] than an inclusive cross-section, for example, such features creating particularly sensitive regions within the spectra are necessary to retain or increase the sensitivity of a differential measurement. This is especially necessary since the uncertainties across the distributions may vary significantly, and particularly sensitive regions in different variables may suffer from uncertainties at very different orders of magnitude. Therefore, the modeling of the expected limits is done using realistic uncertainties and correlations among the bins of the distributions, in order to determine the sensitivities of variables.

All of these features generally apply to any single EFT operator. However, since in this interpretation two operators are modeled, their interplay is essential as well. Beyond setting limits on the contributions of singular operators, the interpretation also aims at disentangling the effects of the two operators, constraining both in a simultaneous fit. Therefore, the relative differences in the effects of the two operators within a kinematic distribution matter as well.

To incorporate all of these effects, limits are derived using the full statistical model in a realistic set-up. This approach is based on the linear EFT model derived on the simulated EFT predictions, as described in Section 9.5 and using the set-up described in Section 10.1. The model is then utilized to derive limits on the same SM prediction, used when building the model. Interfacing a dataset like this is commonly referred to as using an Asimov dataset. The SM distribution used to derive these expected limits is given the full covariance matrix of the respective particle-level distribution derived in the unfolding procedure. The studies in this section are performed using the NLO Powheg prediction for the SM value, and with no theoretical uncertainties included in the covariance matrix. Since these studies are only assessing the relative merit of the different

[2]For example, the statistical uncertainty on a single bin, containing only a subset of all events as compared to a total cross-section, will always be larger.

variables, it should be safe to neglect the small NNLO corrections to the SM prediction and the corresponding theoretical uncertainties. With a set-up like this, the expectation is to reproduce the SM case with both Wilson coefficients being zero. Furthermore, the set-up provides an estimation for the credibility levels (CL) for the analysis. Using EFT*fitter*, the constraining power of the different distributions can be measured via the marginalized and two-dimensional CLs. Since the full covariance matrix and, therefore, realistic statistical and systematic uncertainties and correlations are included, a realistic picture of the sensitivity of the different observables emerges. In this test, the prior probability is set to be

$$\Pi(C_i) \propto \begin{cases} 0, & \text{if } |C_i| > 2 \\ 1, & \text{otherwise.} \end{cases} \tag{10.2}$$

To compare different kinematic observables, limits are derived using the set-up described above for the whole distribution of each observable. Inferring the EFT model on each observable and generating the expected limits based on this observable alone allows to compare the sensitivities. The marginalized limits on C_{tG} and $C_{tq}^{(8)}$, as well as the global and marginalized modes, are shown in Figure 10.3 for a variety of the observables presented in Section 7.3. The variables are sorted by the size of the marginalized limits on the respective Wilson coefficients. Every variable tested in this set-up reproduces 0 for both Wilson coefficients in the global mode, which is expected since it corresponds to the SM case used as pseudo-data input in this set-up. This is an important technical cross-check of the statistical model. The size of the expected limits depends on the interplay of the EFT effects in the respective variable and the uncertainties. There are kinematic variables like the rightmost six variables in the top panel of Figure 10.3 which show almost no potential for constraining $C_{tq}^{(8)}$ in this measurement, since the expected limits completely cover the allowed parameter space in the posterior from -2 to 2.
On the other hand, the expected limits when using the left-most variables from the ranking in the top and center panel of Figure 10.3 show excellent potential for strong limits on both operators. As expected from the energy-scale dependence of the EFT effects, variables sensitive to the scale, like $H_{\mathrm{T}}^{t\bar{t}}$, $p_{\mathrm{T}}^{t,\ell}$, $m^{t\bar{t}}$ and $p_{\mathrm{T}}^{t,h}$ show very strong constraints on effects of the chromomagnetic dipole operator O_{tG}. The top variables ranked by the size of the marginalized limit on $C_{tq}^{(8)}$ consist of similar kinematic variables, but the order in terms of sensitivity is slightly different.

In order to also include the interplay of the two operators in this decision, the resulting area of the smallest two-dimensional 90 % interval is used. This value is derived from numerically integrating the two-dimensional posterior in the smallest limits containing 90 % of the probability volume. The ranking of possible kinematic variables for the EFT interpretation by the resulting area of the smallest two-dimensional 90 % interval is shown in the bottom panel of Figure 10.3. Judging by this metric, which incorporates the limits on both Wilson coefficients simultaneously, the four most sensitive variables for the EFT interpretation are $H_{\mathrm{T}}^{t\bar{t}}$, $p_{\mathrm{T}}^{t,\ell}$, $m^{t\bar{t}}$ and $p_{\mathrm{T}}^{t,h}$. This is expected since these are the same variables that showed good sensitivity in the one-dimensional case, and therefore the two-dimensional volume shows a similar trend.

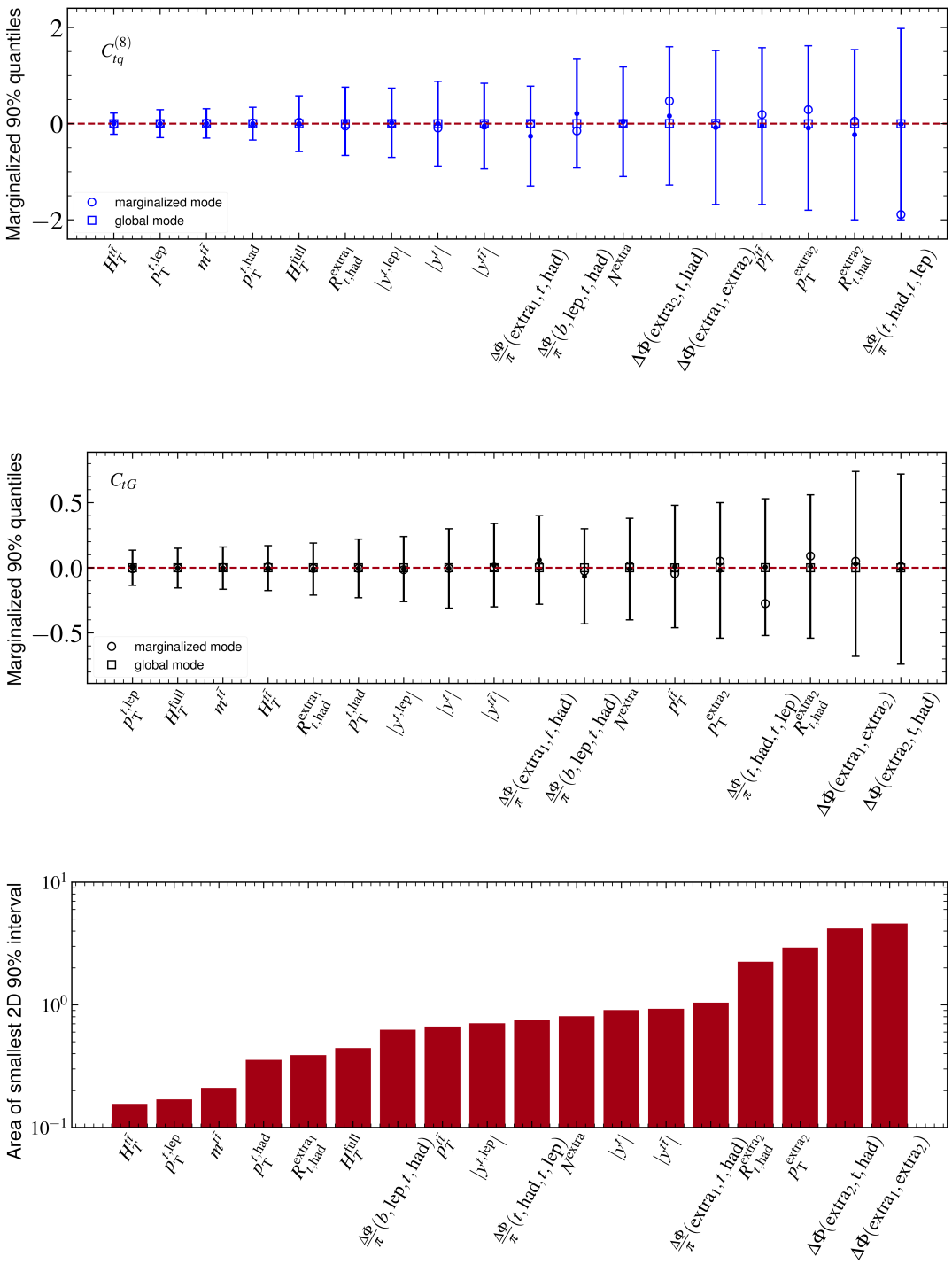

Figure 10.3: Marginalized 90 % intervals for $C_{tq}^{(8)}$ (top) and C_{tG} (center) when using all bins of the respective variable and the full covariance as input to EFT*fitter*. The filled dot represents the center of the interval, while the circle and the square represent the marginalized and global mode, respectively. The bottom figure shows the ranking of the kinematic variables by the size of the area of the two-dimensional 90 % intervals of the posterior distribution.

Thus, $H_{\mathrm{T}}^{t\bar{t}}$, $p_{\mathrm{T}}^{t,\ell}$, $m^{t\bar{t}}$ and $p_{\mathrm{T}}^{t,h}$ are overall favored by the expected constraints and the expected power to disentangle the two operators' effects. The final choice on the observable is made based on the effects of higher-order contributions to the modeling of the ME, as described in the following section.

10.2.2 Effects of Higher-Order Contributions

As mentioned in Section 9.5, the SM prediction used in the EFT model function is not based on the MG5+PY8 LO prediction from the EFT MC simulations, but is replaced by the NLO PWG+PY8 predictions after reweighting it to NNLO. In this model, the EFT effects derived on the LO EFT MC simulations stay encoded in the p_i^j with $j \geq 1$ in the model function. In this section, the MG5+PY8 LO SM prediction is compared to the PWG+PY8 SM prediction reweighted to NNLO. The goal of this comparison is to quantify the impact of the additional orders in the distributions reweighted to NNLO as compared to the LO in the SM predictions. Since the different orders are combined in the EFT model, large inconsistencies between these can pose a problem. For example, underpopulated regions of certain variables at LO when compared to the higher-order calculations, will also suffer from a large statistical uncertainty in the EFT modeling. This will lead to an artificial shift of the importance of the EFT interpretation away from these regions. From this it follows that variables showing such effects will have a limited sensitivity in undersampled parts of the phase space. To avoid such effects, this feature is taken into account for the choice of the variable for the interpretation.
Figure 10.4 shows the differential distributions of the top four variables from the ranking of the expected limits $p_{\mathrm{T}}^{t,\ell}$, $p_{\mathrm{T}}^{t,h}$, $m^{t\bar{t}}$ and $H_{\mathrm{T}}^{t\bar{t}}$ for both the LO MG5+PY8 and the PWG+PY8 SM predictions after reweighting them to NNLO. A significant difference is observed in the p_{T}-distribution of the $t\bar{t}$ system, with the LO sample having a much softer distribution. This is expected due to the lack of the simulation of additional radiation in the ME in the LO sample. The extra radiation in the higher-order predictions will lead to softer spectra due to the radiative energy loss. This lack of additional radiation also translates to the other variables. In particular, the low $p_{\mathrm{T}}^{t,\ell}$ and low $m^{t\bar{t}}$ regions correspond to events where the $t\bar{t}$ system has high p_{T}, due to the p_{T} requirement on the hadronic top. Hence, large differences are observed in those regions. The overpopulation in the high-energy bins and simultaneous underpopulation of the low-energy bins is especially obvious in the $H_{\mathrm{T}}^{t\bar{t}}$, $p_{\mathrm{T}}^{t,\ell}$ and $m^{t\bar{t}}$ spectra. Especially the underpopulated bins at the low end of, e.g., the $p_{\mathrm{T}}^{t,\ell}$ spectrum affect the EFT sensitivity. Because of the significant lack of such events, the modeling of the EFT effects in this region is prone to fluctuations as well. Compared to the other variables, the $p_{\mathrm{T}}^{t,h}$ spectrum shows the best agreement, with the whole spectrum being well populated in the LO sample. The shape effects are much smaller, and the overall agreement of the two predictions is better than for the other variables.
Therefore, $p_{\mathrm{T}}^{t,h}$ is the observable of choice, to use as input to the EFT interpretation. It is among the most sensitive variables in the expected limits and shows a very good potential to disentangle the two EFT operators' effects while also being very robust when adding higher-order terms to the calculation of the SM prediction.

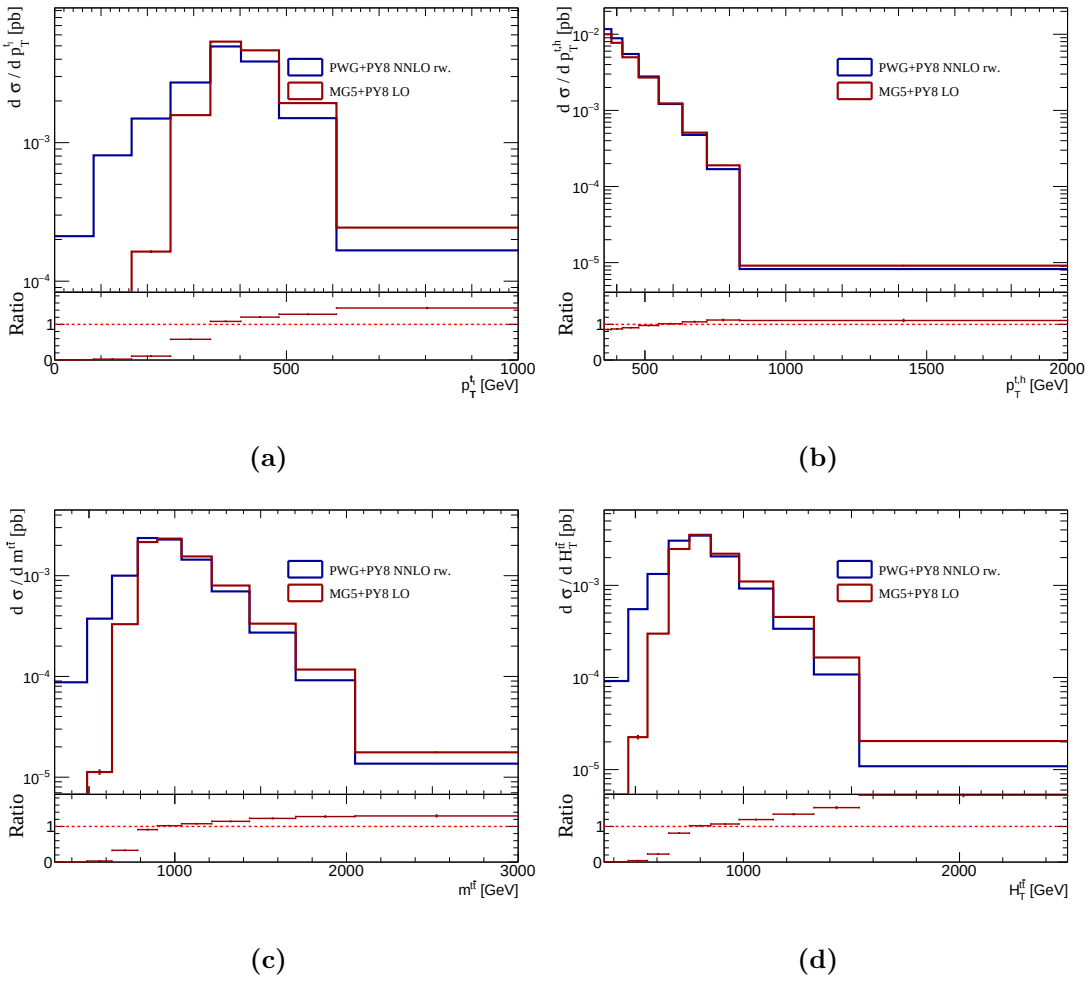

Figure 10.4: Differential distributions of $p_{\mathrm{T}}^{t,\ell}$, $p_{\mathrm{T}}^{t,h}$, $m^{t\bar{t}}$ and $H_{\mathrm{T}}^{t\bar{t}}$ for both the LO MG5+PY8 (in red) and the PWG+PY8 SM predictions after reweighting them to NNLO (in blue).

10.3 Expected Sensitivity of the $p_{\mathrm{T}}^{t,h}$ Spectrum

In order to determine the expected sensitivity of the $p_{\mathrm{T}}^{t,h}$ spectrum to the EFT effects, expected limits are derived in an Asimov-like set-up similar to the sensitivity studies discussed in Section 10.2. The expected limits are an important reference for the expectation based on the exact SM prediction, in order to interpret the observed limits correctly. Furthermore, they give an adequate estimate of the possible constraints on the EFT coefficients, that can be achieved with the precision of this measurement.

Unlike the sensitivity studies discussed in Section 10.2, the expected limits are derived using the final set-up of the EFT model using the SM prediction reweighted to NNLO. Additionally, the full covariance matrix, including the theory uncertainties and all uncertainties of the measurement, is used. As mentioned, the SM prediction is used as

pseudo-data input for the expected limits. Therefore, the same SM prediction reweighted to NNLO, that is used to determine the p_0 in the EFT model functions, is interfaced as input to the statistical interpretation. The values for the model parameters in the linear and quadratic model are given in Table 10.1.

	p_0 / 10^{-8}pb		p_1 / 10^{-8}pb		p_2 / 10^{-8}pb	
Bin	Λ^{-2}	Λ^{-4}	Λ^{-2}	Λ^{-4}	Λ^{-2}	Λ^{-4}
1	1 169 105±2040	1 169 105±2040	340 401±2848	347 145±6411	−1447±4934	171 765±11 104
2	885 852±1451	885 852±1451	271 216±689	274 313±6392	2410±1194	140 749±11 072
3	550 350±939	550 350±939	180 242±1485	184 413±3384	821±2572	113 583±5861
4	278 675±605	278 675±605	97 594±231	99 885±2191	−2739±400	71 630±3795
5	121 226±368	121 226±368	46 206±224	48 349±776	−1445±388	43 135±1344
6	47 606±228	47 606±228	19 498±302	20 427±591	524±522	21 664±1024
7	16 905±118	16 905±118	6995±179	7418±215	−347±311	10 747±372
8	823±8	823±8	368±8	382±31	−7±14	790±54
	p_3 / 10^{-8}pb		p_4 / 10^{-8}pb		p_5 / 10^{-8}pb	
Bin	Λ^{-2}	Λ^{-4}	Λ^{-2}	Λ^{-4}	Λ^{-2}	Λ^{-4}
1	51 904±2848	51 544±6411	1382±4934	5294±11 104	2008±3489	6364±7852
2	52 840±689	49 052±6392	585±1194	7773±11 072	4855±844	6994±7829
3	40 266±1485	44 275±3384	−723±2572	10 898±5861	−1308±1819	9598±4145
4	31 862±231	32 379±2191	−1194±400	15 404±3795	−397±283	4962±2683
5	21 354±224	21 914±776	1129±388	15 571±1344	782±274	3931±950
6	13 213±302	12 650±591	−740±522	11 621±1024	63±369	1756±724
7	7011±179	7033±215	4±311	7970±372	453±220	1206±263
8	628±8	630±31	11±14	1261±54	6±10	197±38

Table 10.1: Results for the six coefficients (columns) of the EFT model function from the fit to the EFT MC data for the 8 bins (rows) of the $p_{\mathrm{T}}^{t,h}$ spectrum. The uncertainties represent the square-root of the variance of the parameter estimate.

Because of the missing quadratic EFT terms in the case of the linear model, the coefficients p_2, p_4 and p_5 are very small compared to p_0, p_1 and p_3 and more or less compatible with zero within the fit uncertainties. This differs significantly in the quadratic model (Λ^{-4}): here the coefficients p_2, p_4 and p_5 take much larger values. Especially p_2, representing the quadratic C_{tG} contributions, increases by more than two orders of magnitude. Furthermore, the linear effects of O_{tG}, represented by p_1, are by far the largest of the EFT effects except for the last two bins of the distribution where linear contributions through $C_{tq}^{(8)}$ are dominant.
The covariance matrix of the SM prediction used as pseudo-data input contains all uncertainties described in Section 10.1 and includes all the experimental uncertainties, as discussed in Section 7. The correlations among the bins are determined from the unfolding procedure, as outlined in Section 7.2.

Including the full covariance matrix and the SM prediction reweighted to NNLO as pseudo-data input, the statistical interpretation is performed using the derived EFT model. Since the EFT model is built on the exact SM prediction that is used as pseudo-data input, the limits are expected to recover the SM prediction, i.e., both Wilson coefficients being at zero. This, again, gives a clear technical check of the constructed EFT model. Based on the accurate covariance matrix used in this set-up, the size and shape of the EFT

limits are expected to give a picture close to the final fit to data. Since the magnitude of the resulting EFT limits in (pseudo-)data for a given fixed EFT model only depends on the size of the uncertainties of that input data, this magnitude of the EFT limits in the observations is expected to not differ significantly from the resulting limits in this set-up.

The resulting sampled one- and two-dimensional posterior distributions for the two Wilson coefficients C_{tG} and $C_{tq}^{(8)}$ are shown in Figure 10.5. It shows the marginalized posterior distributions for both Wilson coefficients, as well as the two-dimensional posterior for the linear model on the left and for the quadratic model on the right. The two-dimensional posterior distributions for both models show the SM case as the black star and the global mode of the resulting inference in the EFT model as the black circle. In both cases, the SM is recovered correctly. Since the linear terms p_1 and p_3 in the respective Wilson coefficient are non-zero in the quadratic case, the model is not symmetric in the Wilson coefficients around zero, but has an offset in the minimum of the parabola. Unlike the linear model, the quadratic model is therefore expected to yield asymmetric limits under the SM assumption, which can indeed be seen for both Wilson coefficients.

The linear model, on the other hand, is symmetric for any given measurement. These symmetry features of the model occur in the posterior distributions for both models. The linear two-dimensional posterior distribution in Figure 10.5 shows a very accurate symmetry in the elliptical shape of the posterior distribution. This symmetry is also visible in the one-dimensional posterior distributions. In the quadratic model, however, the discussed asymmetry leads to a skewed posterior distribution, with a significant preference for negative values of the Wilson coefficients. While the global modes are not biased and accurately recover the SM, the posterior distributions and, therefore, the resulting limits in the quadratic model have the tendency to be shifted to negative values. This is due to the quadratic model having an offset towards negative values space in the respective Wilson coefficient, originating from p_1 and p_3 being > 0. In both models, an excellent distinction between the effects of both operators is observed. This disentanglement is represented by the absence of blind directions, which would manifest as broad marginalized posterior distributions for either or both of the Wilson coefficients, with their widths of the order of the allowed parameter space. This shows that the measurement is expected to have sensitivity to both operators.

The marginalized 95 % and 68 % limits on the two Wilson coefficients C_{tG} (in black) and $C_{tq}^{(8)}$ (in blue) for the linear (Λ^{-2}) and quadratic (Λ^{-4}) model are shown in Figure 10.6 and the numerical values are given in Table 10.2. The expected shift of the limits towards negative values in the Λ^{-4} model is very prominent for $C_{tq}^{(8)}$, while the resulting limits for C_{tG} are very similar among the two models. This shows that the additional terms in the quadratic model for $O_{tq}^{(8)}$, which significantly change the shape of the EFT effects, have an impact on the interpretation. The change in shape shows a stronger pull toward negative values, because the quadratic model shows a much smaller slope toward the negative values, e.g., in the total cross-section (Figure 9.3). Due to that shift, the expected limits particularly on $C_{tq}^{(8)}$ differ between the linear and quadratic model.

The sizes of the expected marginalized limits indicate the great potential of this measurement already. Both operators are expected to be constrained to $|C_i| < 1$. The

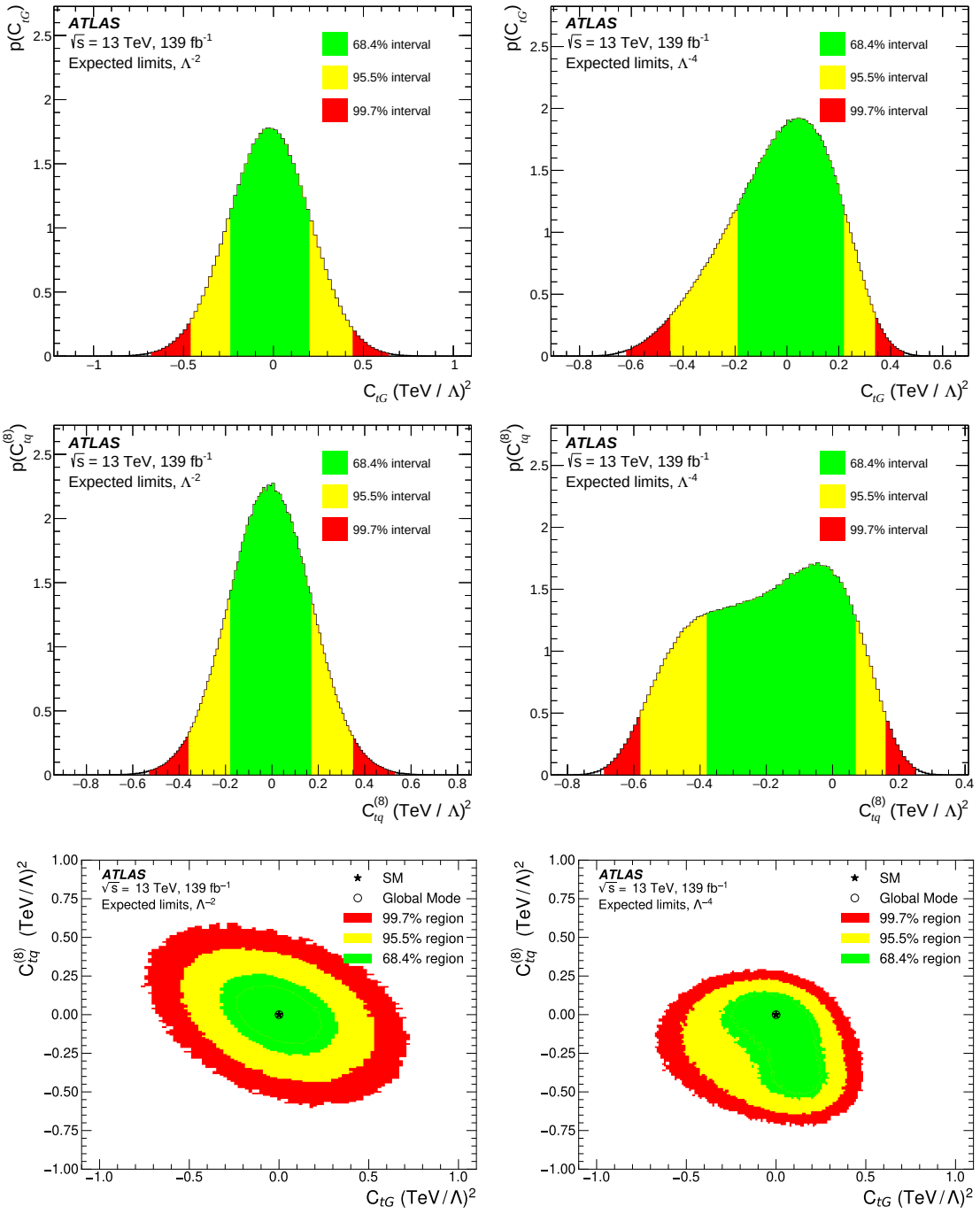

Figure 10.5: One- and two-dimensional posterior distributions for the two Wilson coefficients C_{tG} and $C_{tq}^{(8)}$ when using the $p_{\mathrm{T}}^{t,\mathrm{had}}$ distribution as pseudo-data input. The left column shows the Λ^{-2} set-up, while the right column shows the Λ^{-4} model. The top and center figures show the marginalized posteriors for C_{tG} and $C_{tq}^{(8)}$. The 68.3 %, 95.5 % and 99.7 % intervals are shown in green, yellow and red respectively. The same color code applies to the two-dimensional posterior distributions shown in the bottom figures.

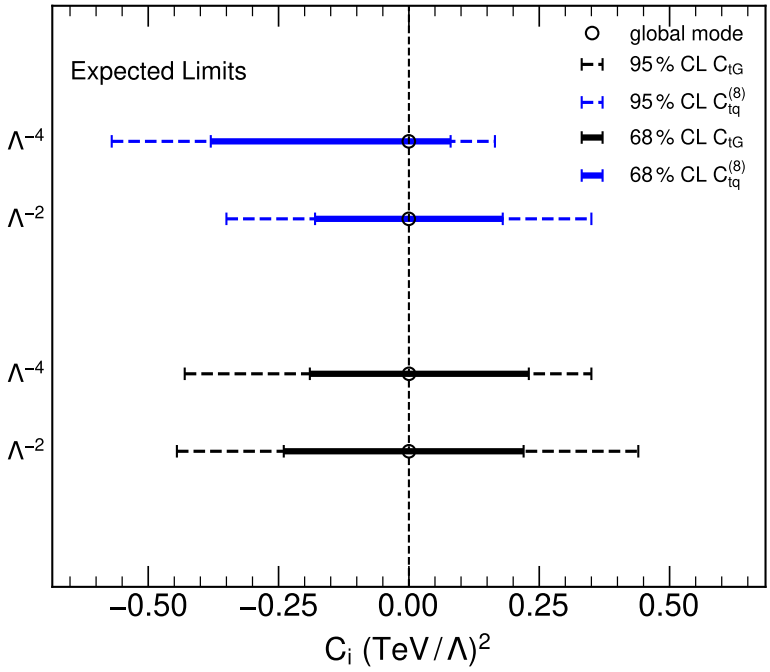

Figure 10.6: Expected marginalized 95 % and 68 % limits of the two Wilson coefficients C_{tG} (in black) and $C_{tq}^{(8)}$ (in blue) for the linear (Λ^{-2}) and quadratic (Λ^{-4}) model. The limits are obtained using the SM prediction for the $p_{\mathrm{T}}^{t,h}$ distribution including the full covariance of the unfolded particle-level distribution as pseudo-data input. The global modes are represented by the black circles.

limits on $C_{tq}^{(8)}$ are slightly stronger than those on C_{tG}. This indicates the potential of a differential measurement since the sensitivity on a total cross-section for C_{tG} is expected to be much stronger. Table 10.2 also shows the individual limits. These are derived using a one-dimensional model with only one of the Wilson coefficients being non-zero. This corresponds to setting all p_i associated with the respective Wilson coefficient to zero – including the interference term p_5.

10.3.1 Disentangling the EFT Effects with a Differential Distribution

Next to potentially higher sensitivity to EFT effects of single bins in the differential measurement, the ability to disentangle the effects of multiple EFT operators is one of the main advantages of combining measurements in an EFT interpretation, e.g., in the form of a differential measurement. Therefore, in order to investigate the potential to disentangle the effects of the two EFT operators in this measurement, the roles of the single bins are investigated in more detail.

As shown in Section 9.3, the effects of both operators O_{tG} and particularly $O_{tq}^{(8)}$ increase with the energy scale and therefore are stronger in the tails of variables like $p_{\mathrm{T}}^{t,h}$. Thus,

Model	C_i $(\Lambda/\text{TeV})^2$	Marginalised 95 % intervals	Individual 95 % intervals
Λ^{-4}	C_{tG}	$[-0.44, 0.35]$	$[-0.44, 0.28]$
	$C_{tq}^{(8)}$	$[-0.57, 0.17]$	$[-0.57, 0.18]$
Λ^{-2}	C_{tG}	$[-0.44, 0.44]$	$[-0.41, 0.42]$
	$C_{tq}^{(8)}$	$[-0.35, 0.35]$	$[-0.34, 0.27]$

Table 10.2: Expected 95 % intervals for the Wilson coefficients (C_i). The marginalized limits are derived using the full EFT model, where both Wilson coefficients are included as inference parameters. For the individual intervals, only the Wilson coefficient under study is allowed to differ from zero, and all terms containing the other Wilson coefficient are set to zero – including the interference term p_5.

they are expected to have a high sensitivity to potential EFT effects. However, the uncertainties in these bins are also much larger than in the low-p_{T} region of the spectrum. To quantify this interplay among the EFT effects and the uncertainties across the bins of the $p_{\text{T}}^{t,h}$ spectrum, the effects of single bins are tested. In order to quantify the interplay of EFT effects and uncertainties, the EFT fit is performed using the same set-up as described in the previous section but excluding single measurements. Using this set-up, a single bin is removed from the EFT fit at a time, and the resulting difference in the area of the two-dimensional 95 % limit is used as the measure for the importance of the respective bin. The relative changes to the area of the two-dimensional limit for the linear and the quadratic model are shown in Figure 10.7. Using the measure of the increase in the resulting 95 % area, the larger the value, the more the respective bin constrains the EFT model's parameter space. While the interpretation of the entire measurement will also make use of correlations among the bins, which may not get resolved in this set-up, this test still paints a clear picture of the sensitivity of the different bins in context to their respective precision.

This procedure shows that in the linear and quadratic EFT models, the last bin of the $p_{\text{T}}^{t,h}$ spectrum shows the strongest impact on the resulting two-dimensional limit. In both cases, the second largest impact comes from the second highest bin of the spectrum. The impact of the last bin is much bigger in the linear EFT model. The other bins of the distribution show relatively small impacts on the size of the two-dimensional limit. The first bin is in third place in the linear and fourth place in the quadratic model. This test shows that the expected large impact of the high-p_{T} tails of the $p_{\text{T}}^{t,h}$ spectrum give a large part of the constraining potential in this interpretation. The effect in the last bin is even stronger in the quadratic model due to the energy increase in the EFT effects at high-p_{T}. However, the first bin of the spectrum as the most precise measurement also impacts the limits in both models. From the shape of the EFT effects, this is expected to primarily influence the limits on C_{tG}.

In order to further discuss the effects of the energy scaling of the two EFT operators,

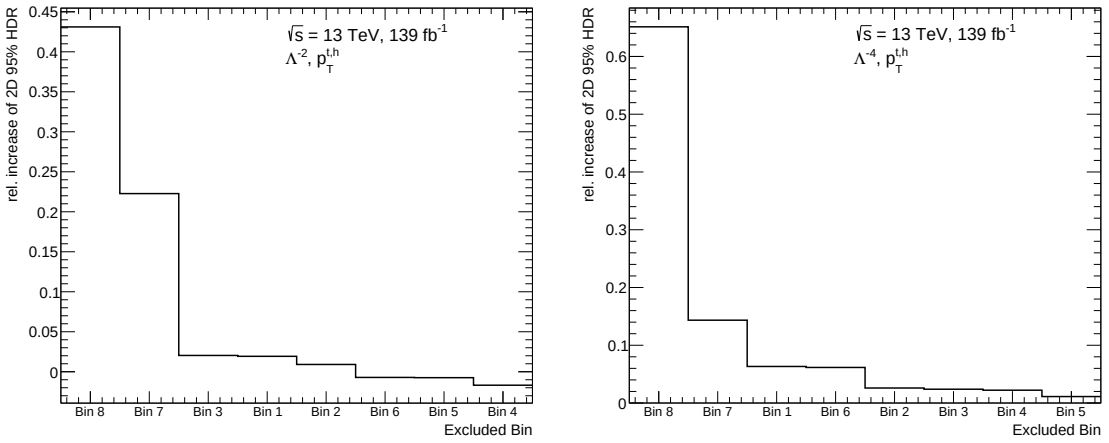

(a) Λ^{-2} EFT model **(b)** Λ^{-4} EFT model

Figure 10.7: Relative change of the area of the two-dimensional 95 % CL limit for the Wilson coefficients C_{tG} and $C_{tq}^{(8)}$ in the linear and the quadratic EFT model. The bins of the $p_{\mathrm{T}}^{t,h}$ distribution used in the Asimov set-up are enumerated increasing to the high-p_{T} tail. Using the measure of the increase in the limit area, the larger the value, the more the respective bin constrains the EFT model's parameter space.

another test is performed. When gradually adding bins to the interpretation, the resulting two-dimensional 95 % CL limits for the two Wilson coefficients are determined. This way, the data input to the EFT interpretation is gradually increasing in its energy reach, following the bin edges of the histogram. Such a methodology, on the one hand, shows the resulting EFT interpretation at different energy scales, and, on the other hand, highlights the energy scaling of the operators. The addition of bins starts with the low-p_{T} bin of the distribution and continues with the following bins towards the tail of the distribution. The first set-up thus only consists of a single measurement. In this case, breaking the degeneracy of the EFT model is not possible. Since the linear model allows for unconstrained positive and negative contributions of the two Wilson coefficients to the cross-section, the resulting allowed marginalized parameter space is potentially unconstrained. Large contributions by one EFT operator can be balanced by similar destructive effects of the other operator and vice versa. In the quadratic model, the negative contributions to the rates are limited by the strictly positive contributions of the quadratic terms, which makes such a behavior impossible.

The limits derived from a single bin represent a single cross-section measurement. The resulting limits when adding the bins follow the increase of the EFT effects towards larger energy scales. Figure 10.8 shows the expected two-dimensional 95 % CL limits for the linear (Figure 10.8a) and the quadratic EFT model (Figure 10.8b). The same set-up as for the expected sensitivity in Section 10 is used.

The colored areas represent the different 95 % CL limits for the steps of adding bins of the $p_{\mathrm{T}}^{t,h}$ distribution to the interpretation with the ranges indicated in the legend.

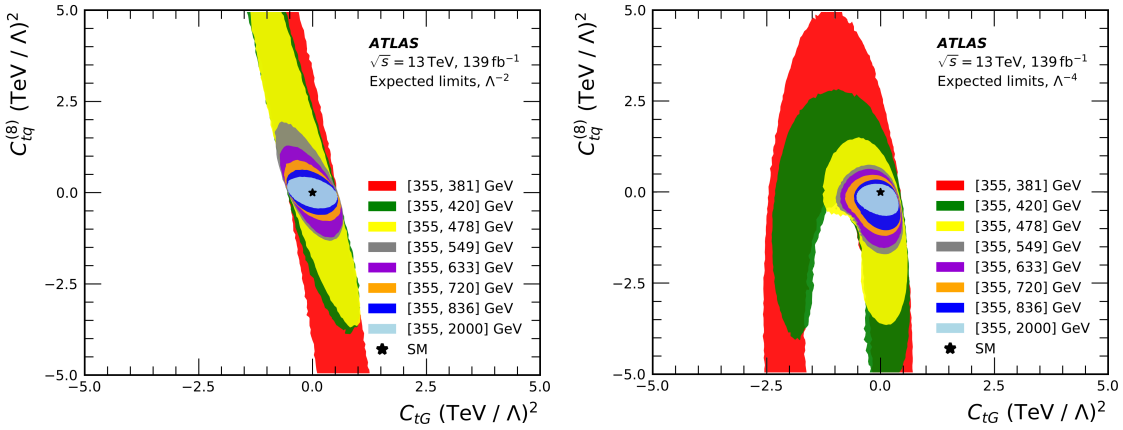

(a) Λ^{-2} EFT model **(b)** Λ^{-4} EFT model

Figure 10.8: Expected two-dimensional 95 % CL limits for the linear (a) and the quadratic EFT model (b). The same set-up as for the expected sensitivity in Section 10 is used. The colored areas represent the different 95 % CL limits for the steps of adding bins of the $p_{\mathrm{T}}^{t,h}$ distribution to the interpretation with the ranges indicated in the legend. The SM is indicated by the black star.

The black star indicates the SM with both Wilson coefficients set to zero. The linear model shown in Figure 10.8a shows the expected degeneracy for the interpretation of a single bin, shown in red. For the SM case (as in the pseudo-data set-up), there are infinite combinations of the two operators which will reproduce the SM rate, where one of them acts destructively. For the case of a single measurement, there is almost no constraining power on $C_{tq}^{(8)}$, while the width of the distribution in the dimension of C_{tG} is much smaller. As expected, this shows the large effect of O_{tG} on the overall cross-section normalization as opposed to $O_{tq}^{(8)}$. On the other hand, when adding one more bin, the 95 % CL area already excludes values of $C_{tq}^{(8)} < -4$. Upon adding more bins, the 95 % CL space for $C_{tq}^{(8)}$ shrinks rapidly, while the allowed space in the dimension of C_{tG} does the same at a much smaller scale. This shows very strongly how the set of differential bins gradually breaks the blind direction that was present for $C_{tq}^{(8)}$ with just the first bin. The additional bins add increasingly orthogonal information to the interpretation, which results in the good disentanglement of the two operators.

The quadratic model shown in Figure 10.8b behaves similarly in many ways, albeit with certain differences. Firstly, the quadratic model shows the expected degeneracy, including multiple allowed regions for the respective coefficients, represented by the elliptical ring shape of the posterior distribution in red. Since the potential for destructive EFT effects in the quadratic model is limited due to the stronger impact of the strictly positive effects of the quadratic terms, the allowed parameter space is already limited for both operators with a single measurement. Furthermore, the resulting posterior is not symmetric around the SM, as discussed before. Although the two-dimensional representation does not show this intuitively, the limits on C_{tG} with the single measurement are stronger than those

using the differential cross-section in this model as well. Analogously to the linear model, the allowed parameter space decreases significantly when adding the second bin to the interpretation. The orthogonality of the additional bins in the interpretation is even stronger in the quadratic model. When adding the third bin to the interpretation, the entire negative half of the ring-shaped limit is excluded. Similar to the linear model, the use of the full distribution finally constrains the EFT parameter space to a single island, showing that each bin adds additional constraining power to the interpretation.

This constraining power of the differential distribution becomes even clearer when comparing the resulting posteriors of the differential interpretation to the interpretation of the inclusive cross-section. This comparison is shown in Figure 10.9.

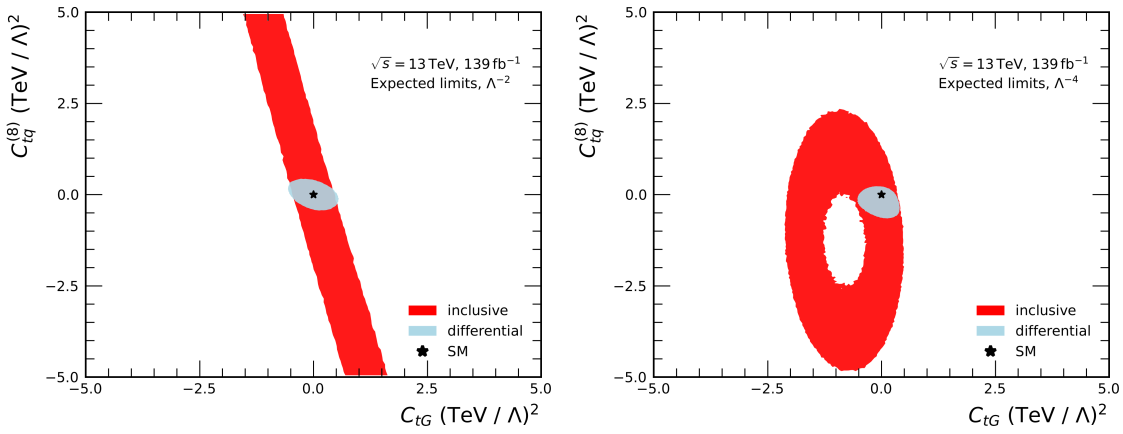

(a) Λ^{-2} EFT model **(b)** Λ^{-4} EFT model

Figure 10.9: Expected two-dimensional 95 % CL limits for the linear (a) and the quadratic EFT model (b) using the inclusive cross-section or the full differential spectrum, respectively. The same set-up as for the expected sensitivity in Section 10 is used. The colored areas represent the different 95 % CL limits for the the inclusive cross-section (red) and the full differential $p_{\mathrm{T}}^{t,h}$ distribution (blue). The SM is indicated by the black star.

Not only does the differential interpretation allow for disentangling the effects of the two operators and constraining both at the same time, but the resulting limits are much stronger when introducing the additional information in the combination of the differential bins. This underlines the expected sensitivity of the differential distribution due to the resolution of energy growth effects in the EFT operators in the high-p_{T} bins. These relatively small effects get diluted in the inclusive measurement. Even so, they add large constraining power to the interpretation of the differential measurement, despite the better precision of the inclusive measurement. This precision, however, does not dominate the sensitivity of the measurement, even though the posterior distributions show larger exclusions when compared to the interpretation of just the first bin of the differential measurement.

11 Validation of the EFT Model

As outlined previously, several steps in this measurement potentially impact the interpretation in the framework of EFT. Among them are the unfolding procedure described in Section 7.2, which may introduce biases. Furthermore, the modeling of the EFT effects at LO (on top of the higher-order SM prediction) directly affects the EFT interpretation. Therefore, the chosen validation procedures are outlined in this chapter and the validity of the EFT approach is tested.

11.1 Validity of EFT in Unfolding

The unfolding procedure in this measurement is based on the nominal signal simulations, which in turn are modeling the SM. However, the shape of kinematic distributions can be changed significantly by the EFT operators considered in this analysis (see Section 9.3). Therefore, the unfolding procedure needs to be tested for possible biases in the presence of BSM contributions. Especially for a regularized procedure, like the IBU, this is necessary in order to make sure that the potential BSM effects are not diluted by a biased unfolding procedure.
In order to test for potential biases, an EFT signal is injected into a pseudo-dataset. This injected sample is then unfolded using the procedure derived from the SM $t\bar{t}$ signal. The injected samples were constructed to model an EFT signal at the level of the expected sensitivity of this analysis, based on the preliminary set of uncertainties at that point. This set is, for example, missing the theory uncertainties described in Section 10.1. The expected limits on the two operators in this configuration are of the order of 0.25. For the linear EFT model, the injection sample is constructed based on the linearity of the effects in this model. Therefore, the EFT signal at $C_{tG} = 0.25$ or $C_{tq}^{(8)} = 0.25$ is modeled as

$$N_i^{\text{injection}} = N_i^{\text{SM}} + \sum_j 0.25 \cdot \left(N_i^{\text{EFT, } C_j=1} - N_i^{\text{EFT, } C_j=0} \right) . \tag{11.1}$$

Here, for the rate $N_i^{\text{injection}}$ in bin i of the injected sample, the SM contribution is replaced by the nominal PWG+PY8 prediction represented by N_i^{SM}. Therefore, the LO SM contribution $N_i^{\text{EFT, } C_j=0}$ in the EFT sample is removed. Finally, the EFT rates $N_i^{\text{EFT, } C_j=1}$ at $C_j = 1$ for the two Wilson coefficients are scaled by the factor 0.25 after removing the SM contribution. For the quadratic model, a simple linear scaling is not possible, so a separate, statistically independent, sample is simulated at $(C_{tG}, C_{tq}^{(8)}) = (0.2, 0.2)$. This sample is transformed into the injection sample in a similar

way as shown in Equation (11.1). However, because the dedicated $(C_{tG}, C_{tq}^{(8)}) = (0.2, 0.2)$ sample is used instead of scaling a $C_j = 1$ sample, the scale factor is not needed. This way, the pure EFT effects at the level close to the expected limits are superimposed on the SM prediction used to derive the unfolding procedure. In order to test the impact of the EFT effects and, therefore, the robustness and potential bias of the unfolding procedure, the $p_{\mathrm{T}}^{t,h}$ distributions of the signal-injected samples are interfaced into the unfolding set-up as pseudo-data. This means that the nominal unfolding set-up used in the measurement of the differential $p_{\mathrm{T}}^{t,h}$ spectrum is used to unfold the signal-injected distribution. The result of the unfolding procedure is then compared to the true particle-level distribution, which is derived similarly on the particle-level simulations (either by scaling in the Λ^{-2} case or using the dedicated sample in the Λ^{-4} case).

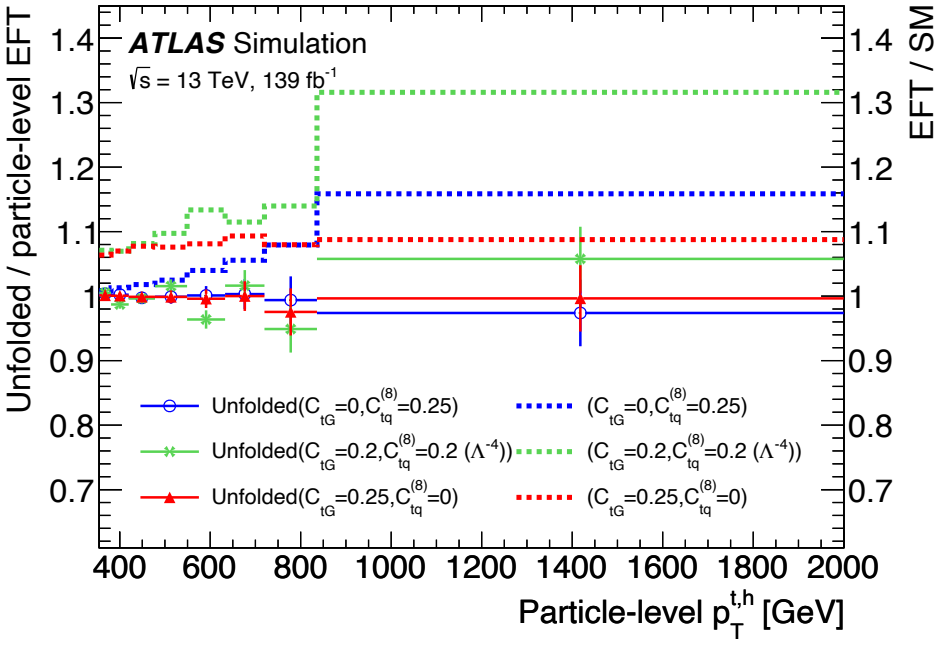

Figure 11.1: Particle level distributions of the $t\bar{t}$ production cross-section as a function of $p_{\mathrm{T}}^{t,h}$. The continuous and dashed lines are ratios, where the denominator is the respective EFT particle-level distribution. The numerators of the ratios shown as continuous lines are the unfolded EFT distributions for different Wilson coefficient values, while for the dotted lines, the numerators are the nominal PWG+PY8 distributions. The dotted lines show the EFT effects and, in this context, the ratio of a maximum biased unfolding. The continuous line should therefore be compatible with unity to consider the test as passed. The uncertainty on the continuous lines is the statistical uncertainty on the reweighted pseudo-data.

Figure 11.1 shows the results of this test. It contains ratios of the particle-level distributions of the $t\bar{t}$ production cross-section as a function of $p_{\mathrm{T}}^{t,h}$. The continuous lines are ratios, where the denominator is the respective EFT particle-level distribution. The numerators

of the ratios shown as continuous lines are the unfolded EFT distributions for different values of the Wilson coefficient. Thus, these ratios show the effects of the unfolding on the particle-level distribution. The dotted lines show the ratios of the various EFT predictions to the nominal SM prediction, i.e., the PWG+PY8 distributions. Therefore, the dotted lines show the EFT effects compared to the SM and, in this context, the ratio of a maximum biased unfolding. If the unfolding were to reconstruct the SM prediction perfectly, regardless of the presence of potential EFT effects, the dashed line would represent the resulting ratio of this test. The opposite case - a perfectly unbiased result - is characterized by the ratios being in good agreement with one, and thus the unfolding recovering the true particle-level distribution.
The test is performed for three different set-ups: setting the two Wilson coefficients to 0.25 one at a time for the linear model and setting both Wilson coefficients to 0.2 at the same time for the full quadratic model. As Figure 11.1 shows, the EFT effects are most prominent in the latter case. The ratios of the unfolded EFT-injected distribution to the desired particle-level distribution for both linear set-ups (red and blue lines) are in very good agreement with one. They furthermore show no trends towards the dotted lines and thus the SM, which would show potential biases.
The injected quadratic EFT effects are shown in green. Similar to the linear model, there is no overall trend toward the dotted green line and, therefore, no bias towards the SM. However, the fluctuations in the ratio of the unfolded distribution to the underlying particle-level distribution are slightly larger. Despite that, the ratio is overall in good agreement with one, and thus there is no bias in the unfolding procedure.
This test shows that the unfolding in this measurement is well suited for an unbiased and robust analysis of the potential EFT effects of the two EFT operators of interest. The effects of the unfolding are also tested in a similar set-up for their direct impact on the resulting limits. The results of this test show good closure and no biases in the unfolding procedure as well. A detailed description can be found in Appendix 2.

11.2 Effects of Additional Orders in the EFT Modelling

The prediction of the EFT contribution using the SMEFTatNLO 1.0.0 UFO model in this work is calculated at LO. The UFO model allows for NLO calculations for some of the operators like O_{tG}, but not yet for the 4-quark operators, like $O_{tq}^{(8)}$. Therefore, current recommendations [105, 106] on EFT predictions with this model suggest uniform modeling at LO. As discussed in Section 10.2.2, the modeling of $p_{\mathrm{T}}^{t,h}$ at LO is the best among the particularly sensitive variables, when compared to the predictions reweighted to NNLO. It is therefore expected to be robust when replacing the SM prediction in the EFT model with the reweighted NLO prediction. However, to investigate the relevance of these higher-order terms in the EFT prediction, the effect on the resulting limits is quantified in this section.
To estimate the effect of the difference between LO and (N)NLO contributions on the expected EFT limits, a fit on a rescaled EFT model, including only the Λ^{-2} terms for simplicity, is performed. In this set-up the EFT model shown in Equation (9.3) is modified.

The p_i (excluding the replaced SM prediction p_0) derived from the LO EFT samples (shown in Table 10.1) are rescaled to match higher-order predictions. As discussed in Ref. [194], the NLO k-factor of C_{tG} is similar to that of the SM. The scaling of the EFT effects added to the SM prediction can, as a result, also be performed using similar scale factors as for the SM case. The similarity can be explained by the dominance of the QCD production of the pair of top quarks at such energies, which is precisely the channel containing the coupling modified by O_{tG}. Since, in this measurement, the NLO SM prediction is reweighted to NNLO, the impact of higher-order corrections on C_{tG} is evaluated by applying the scale factors between the LO and NNLO predictions shown in Figure 10.4 to the coefficients p_1 and p_2, which are describing the impact of pure C_{tG} contributions. For $C_{tq}^{(8)}$ only inclusive k-factors are available in the literature, see Ref. [189]. The SM k-factor is not applicable here as the $C_{tq}^{(8)}$ Feynman diagrams are quark-initiated and therefore do not follow the natural behavior of the bulk of signal events, unlike the $t\bar{t}$ production via gluon-gluon fusion. Therefore, in the case of $C_{tq}^{(8)}$, the coefficients p_3 and p_4 are rescaled by the k-factor of 0.95 [189] throughout the differential distribution. The scaling factors for the two coefficients in the bins of the $p_{\mathrm{T}}^{t,h}$ spectrum are shown in Table 11.1.

	bin 1	bin 2	bin 3	bin 4
NNLO/LO C_{tG}	1.16843	1.14731	1.10376	1.03186
NLO/LO $C_{tq}^{(8)}$	0.95	0.95	0.95	0.95
	bin 5	bin 6	bin 7	bin 8
NNLO/LO C_{tG}	0.982012	0.933627	0.89087	0.901884
NLO/LO $C_{tq}^{(8)}$	0.95	0.95	0.95	0.95

Table 11.1: Scale factors to test the effects of higher-order corrections in the EFT operators for the $p_{\mathrm{T}}^{t,h}$ spectrum. The scale factors for C_{tG} (NNLO/LO C_{tG}) are derived bin-wise from the ratios of the SM prediction from the LO EFT samples to the PWG+PY8 prediction reweighted to NNLO. The scale factors for $C_{tq}^{(8)}$ (NLO/LO $C_{tq}^{(8)}$) show a flat scaling derived from the inclusive scale-factor in Ref. [189].

Table 11.2 contains the expected one-dimensional limits at the 95 % CL on both coefficients for the different set-ups. These limits are derived with the EFT model containing only one non-zero Wilson coefficient at a time, which also means that the interference term of the two coefficients p_5 is also set to zero. The full covariance matrix is used in this set-up. The effect on the limits for the two Wilson coefficients agrees with the expectation from the rescaling. The scale factors for C_{tG} shown in table 11.1 introduce an increase of the order of 10 % in the EFT contributions in the low-p_{T} bins. Since these have the smallest uncertainties and C_{tG} does not introduce a strong shape effect that could be exploited from other bins in the EFT fit, they show the strongest sensitivity to C_{tG}. Therefore, the

increase through the rescaling leads to slightly stronger limits on C_{tG} of about the same order as the size of the rescaling with approximately 6 % smaller intervals.
In the case of $C_{tq}^{(8)}$, the limits are found to be around 5 % weaker in the rescaled case, which is consistent with the rescaling by the k-factor of 0.95, leading to smaller contributions originating from $O_{tq}^{(8)}$.

Coefficient	Nominal	Rescaled C_{tG}	Rescaled $C_{tq}^{(8)}$
C_{tG}	$[-0.41, 0.415]$	$[-0.385, 0.39]$	–
$C_{tq}^{(8)}$	$[-0.345, 0.355]$	–	$[-0.365, 0.37]$

Table 11.2: Expected limits on the Wilson coefficients at 95 % CL for the full covariance matrix using the modified one-dimensional EFT model (only one non-zero coefficient at a time) derived from the nominal LO EFT predictions (Nominal) and the model using the rescaled p_1 and p_2 (Rescaled C_{tG}) as well as p_3 and p_4 (Rescaled $C_{tq}^{(8)}$). The cross-term represented by p_5 is set to zero in all cases.

The rescaling, therefore, shows that the effects of higher-order contributions are larger for C_{tG}, but in both cases, do not have a particularly large effect on the resulting limits. While future higher-order predictions will thus improve the precision of this modeling and make some steps of the EFT model building obsolete (e.g., the replacement of the SM), the checks performed here demonstrate, that the interpretation in this measurement is not strongly influenced by missing orders. Therefore the EFT prediction, used in this work, shows no biases due to the employed unfolding procedure and is not significantly affected by missing higher-order contributions in the EFT modeling. As a next step, this methodology is thus applied to data.

12 EFT Interpretation of the Measurement

After defining and constructing a dedicated EFT model for the interpretation of this measurement and validating the approach, the measurement can be interpreted in the framework of EFT. In this chapter, the results of using the observed differential distribution of the p_{T} of the hadronically decaying top-quark, $p_{\mathrm{T}}^{t,h}$, to derive limits on the two EFT parameters of choice are discussed. The obtained constraints are then compared to recent global limits.

12.1 Observed Limits on EFT Effects

The differential $p_{\mathrm{T}}^{t,h}$ distribution is used to set limits on the effects of the two EFT operators O_{tG} and $O_{tq}^{(8)}$. The observed spectrum is unfolded to particle level using the unfolding described in Section 7.2. The eight bins of the measurement are combined in the interpretation. As outlined in the previous sections, each bin represents a measurement that is parametrized in the EFT framework, with all bins being combined for the final interpretation. The covariance matrix containing the uncertainties of each measurement as well as the correlations among the bins is described in Section 10.1. The parameters of both the linear and quadratic EFT models are given in Table 10.1.
The resulting limits on the two Wilson coefficients in the combined fit of both dimensions in the EFT parameter space, as well as the individual limits with only one non-zero coefficient, are given in Table 12.1.

Model	C_i $(\Lambda/\mathrm{TeV})^2$	Marginalised 95 % intervals		Individual 95 % intervals	
		Expected	Observed	Expected	Observed
Λ^{-4}	C_{tG}	[-0.44, 0.35]	[-0.53, 0.21]	[-0.44, 0.28]	[-0.52, 0.15]
	$C_{tq}^{(8)}$	[-0.57, 0.17]	[-0.60, 0.13]	[-0.57, 0.18]	[-0.64, 0.12]
Λ^{-2}	C_{tG}	[-0.44, 0.44]	[-0.68, 0.21]	[-0.41, 0.42]	[-0.63, 0.20]
	$C_{tq}^{(8)}$	[-0.35, 0.35]	[-0.30, 0.36]	[-0.35, 0.36]	[-0.34, 0.27]

Table 12.1: Expected and observed 95 % CL intervals for the Wilson coefficients C_{tG} and $C_{tq}^{(8)}$. The marginalized, as well as the individual limits, are shown. The marginalized limits are determined from the nominal fit where both Wilson coefficients are varied. The individual intervals are determined from the interpretation with only the Wilson coefficient under study taking non-zero values.

The limits are also shown in Figure 12.1, where the marginalized 95 % and 68 % limits on the two Wilson coefficients are shown for the nominal EFT model, which allows both Wilson coefficients to take non-zero values.

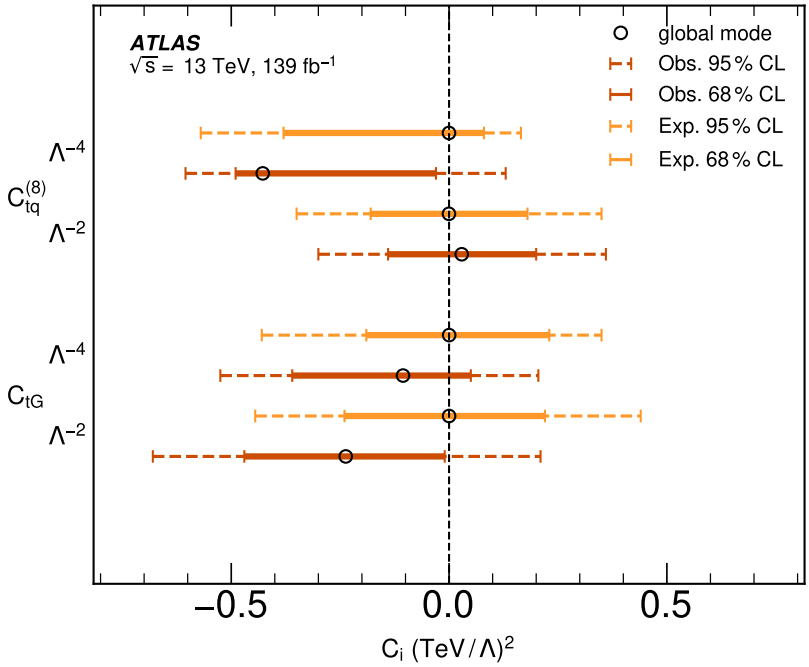

Figure 12.1: Expected and observed marginalised 95 % and 68 % limits on the two Wilson coefficients C_{tG} and $C_{tq}^{(8)}$ for the linear and quadratic EFT model. The 95 % limits are represented by the dashed lines, while the solid line shows the 68 % interval. The global mode is shown as the black circle on the respective line. All limits are derived from the two-dimensional EFT model, which allows for both Wilson coefficients to take non-zero values.

The observed limits for both coefficients and both models are in agreement with the SM prediction of zero for both coefficients. The largest deviation is seen for $C_{tq}^{(8)}$ in the quadratic model and C_{tG} in the linear model, where the SM lies just outside the 1σ interval. All observed intervals are in agreement with the expected limits in their size. However, except for the limit on $C_{tq}^{(8)}$ in the linear model, all limits are shifted towards the negative parameter space. This effect shows how the EFT model incorporates the smaller observed event yield with respect to the prediction. The same effect can also be seen in the observed one- and two-dimensional posterior distributions, as shown in Figure 12.2. Both two-dimensional posterior distributions (at the bottom of Figure 12.2) show the probability density shifted towards the negative parameter space. For the linear model, these effects only manifest as the above-mentioned offset in the C_{tG} dimension. The quadratic model, on the other hand, shows offsets from the SM in both directions. This indicates that the difference in the effects of the two EFT models, particularly in shape,

influences the shape of the resulting limits. The global modes mirror this behavior as well, although only the global mode in the quadratic model is significantly shifted towards negative values for $C_{tq}^{(8)}$. This shows that in particular the quadratic terms arising from $O_{tq}^{(8)}$ seem to model the difference between the SM prediction and the measurement well. The one-dimensional posterior distributions show that the asymmetry in the quadratic model is dominated by $C_{tq}^{(8)}$.

Overall, the comparison of the linear to the quadratic EFT model shows that the resulting global modes significantly depend on the quadratic terms. Including these terms changes the position of the global mode, particularly for $C_{tq}^{(8)}$. The positions of the limits differ slightly as well, depending on the EFT model. However, the differences are of the same order as the determined constraints, and there is a significant overlap among the limits derived using the two EFT models.

This shows that while the quadratic terms are important to include, especially for the four-fermion operator, the effects of terms of the order $\mathcal{O}(\Lambda^{-4})$ are not changing the limits beyond the order of the achieved sensitivity. From the pure effects of the suppression through the energy scale Λ, this may hint at the importance of further terms at this order arising from, e.g., dimension-eight operators.

The two-dimensional evolution of the 95 % CL limits when adding the bins of the differential measurement is shown in Figure 12.3 for both EFT models. The posterior distributions for the linear EFT model are shown in Figure 12.3a and the posterior distributions for the quadratic EFT model in Figure 12.3b. Comparing the observed posterior distributions shown here to the expected distributions for the SM pseudo-data, shown in Figure 10.8, exposes the similarity of the observation to the expectation. Both, the shapes of the posterior distributions as well as the effects of the various bins, agree very well with the expectation, besides the shift towards the negative EFT parameter space discussed before. The bins at the far ends of the distribution show very strong orthogonality, which allows for strong constraints on both operators at the same time. In the observed distribution, the third bin shows a stronger reduction of the posterior distribution than in the Asimov-like set-up for both EFT models. This indicates the particular importance of this measurement at the transition point of the differential distribution towards larger statistical uncertainties in the bins with smaller rates but simultaneously larger EFT effects. Furthermore, adding the sixth bin of the measured distribution shifts the allowed parameter space for $C_{tq}^{(8)}$ back towards the SM after the fifth bin shifted it away from the SM. This shows that among the two bins, the difference of data to the prediction does not follow the shape of the linear $C_{tq}^{(8)}$ contributions very well.

Additionally, the effects of the two operators are disentangled very well when interpreting the observed measurement, similar to the expected limits. The constraints on $C_{tq}^{(8)}$ in both EFT models are dominated by including the last bins of the distributions as well.

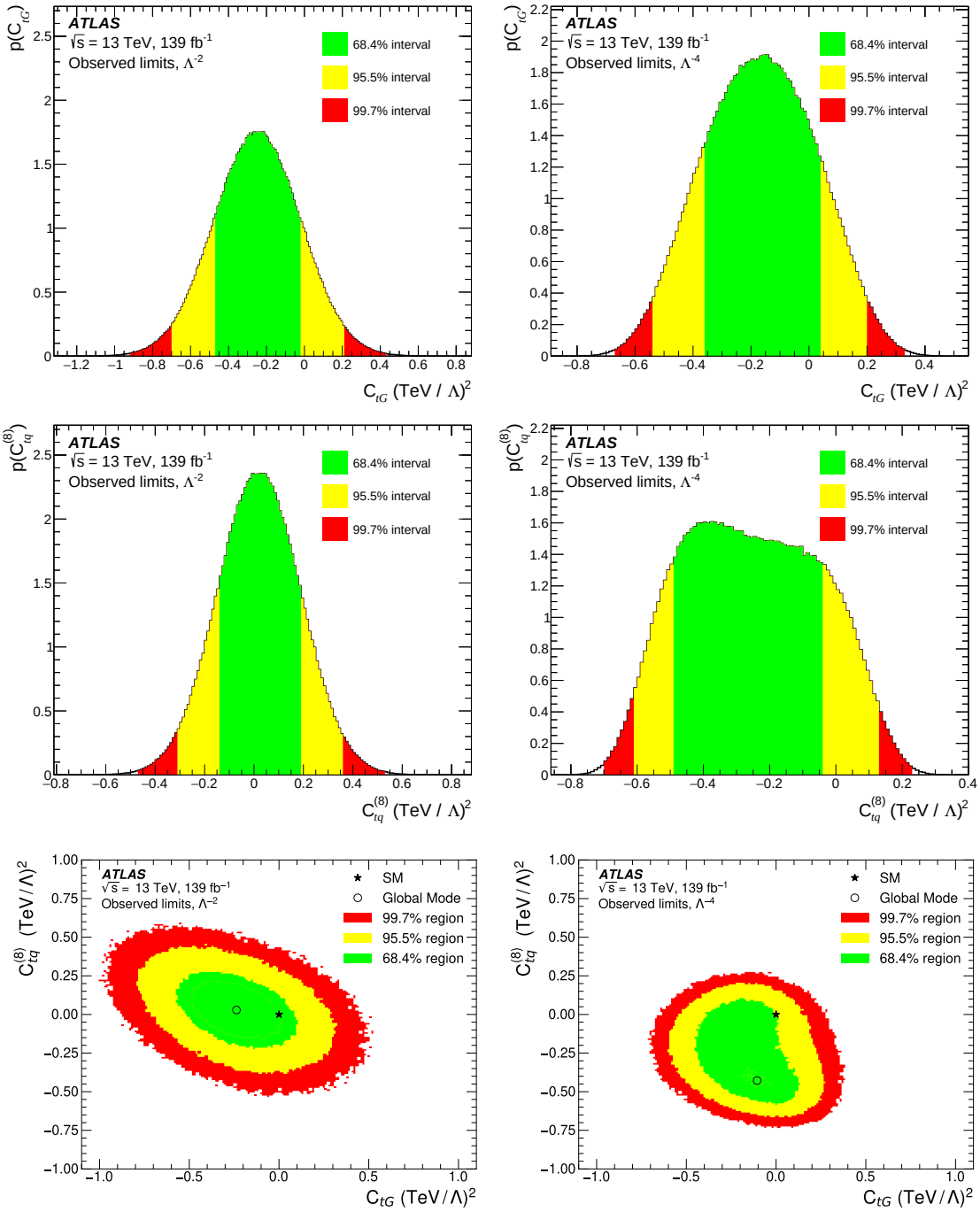

Figure 12.2: One- and two-dimensional posterior distributions for the two Wilson coefficients C_{tG} and $C_{tq}^{(8)}$ when using the $p_{\mathrm{T}}^{t,h}$ distribution as observation input. The left column shows the Λ^{-2} setup, while the right column shows the Λ^{-4} model. The top and center fgures show the marginalized posterior distributions for C_{tG} and $C_{tq}^{(8)}$. The 68.3 %, 95.5 % and 99.7 % intervals are shown in green, yellow and red, respectively. The same color code applies to the two-dimensional posterior distributions shown in the bottom figures.

The global modes of the two Wilson coefficients in both EFT models are found to be

$$\Lambda^{-2}: \quad C_{tG} = -0.24 \pm 0.23\,(\Lambda/\text{TeV})^2 \qquad C_{tq}^{(8)} = -0.03 \pm 0.17\,(\Lambda/\text{TeV})^2$$
$$\Lambda^{-4}: \quad C_{tG} = -0.11^{+0.16}_{-0.25}\,(\Lambda/\text{TeV})^2 \qquad C_{tq}^{(8)} = -0.43^{+0.40}_{-0.06}(\Lambda/\text{TeV})^2\,,$$

where the uncertainty ranges give the marginalized 68 % limits on the two operators. Again, the lower observed rates are reflected in the negative global modes for C_{tG}.

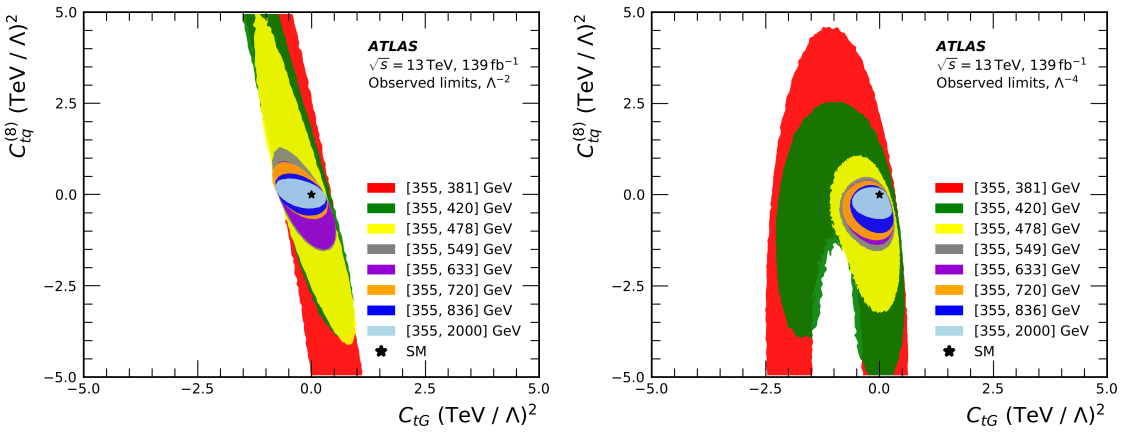

(a) Λ^{-2} EFT model **(b)** Λ^{-4} EFT model

Figure 12.3: Observed two-dimensional 95 % CL limits for the linear (Figure 12.3a) and the quadratic EFT model (Figure 12.3b). The colored areas represent the different 95 % CL limits when adding the individual bins of the $p_{\text{T}}^{t,h}$ distribution to the interpretation, with the ranges indicated in the legend. The SM is indicated by the black star.

In order to compare the EFT model prediction to the observation and SM prediction, the global modes are used. Based on the derived EFT model, the prediction for the $p_{\text{T}}^{t,h}$ distribution is determined at the respective global modes, which are derived using the two-dimensional EFT model. This allows for a direct comparison with the observation and the SM prediction. The quadratic and linear EFT models are used to predict the rates for the eight bins of the distribution by evaluating the functional descriptions at the observed global modes of the two Wilson coefficients. Figure 12.4 shows the predicted $p_{\text{T}}^{t,h}$ spectrum of the EFT model at the global modes in blue, the nominal SM prediction using PWG+PY8 reweighted to NNLO and the respective uncertainties (e.g., theory uncertainties) on this prediction in red, as well as the data in black. For the linear model shown in Figure 12.4a, the EFT model mainly absorbs the overall rate difference. This is indicated by the constantly shifted blue line in the ratio panel. This change in the rate increases the agreement to the data and follows from the linear terms of C_{tG}, while there is essentially no effect from $C_{tq}^{(8)}$.
The quadratic model, on the contrary, shows a much smaller effect from C_{tG}, while including a stronger influence from $C_{tq}^{(8)}$. Furthermore, this model achieves a very good agreement with data while also exhibiting more change to the shape of the distribution

with respect to the SM prediction. The additional energy dependence in the quadratic model allows the fit to follow the slight trend in the first five bins of the distribution. As discussed earlier, the change of this downward trend in the ratio of the data to the SM prediction in the sixth bin can be seen here as well. The upward trend in that bin results in a strong effect on the posterior distribution for $C_{tq}^{(8)}$ excluding larger negative values.

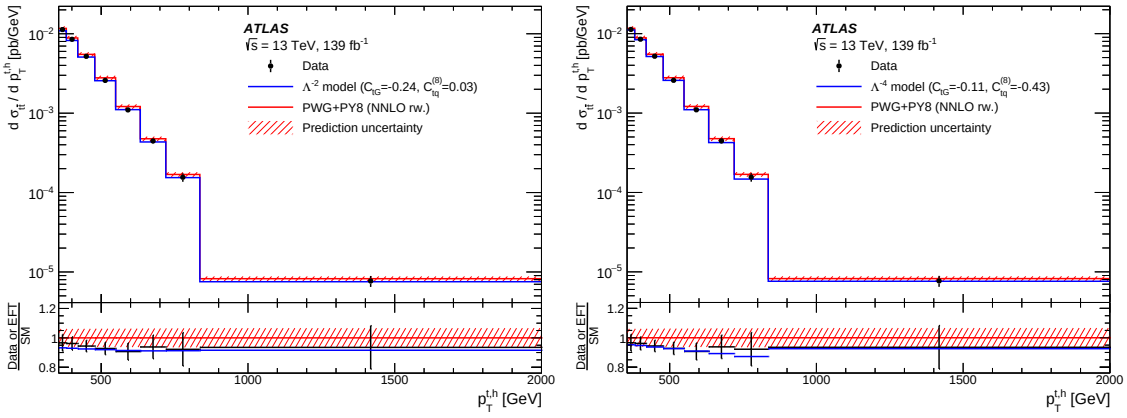

(a) Λ^{-2} EFT model **(b)** Λ^{-4} EFT model

Figure 12.4: The $p_{\mathrm{T}}^{t,h}$ spectrum predicted by the EFT model at the global modes (in blue) is compared to the nominal SM prediction using PWG+PY8 reweighted to NNLO (in red), with the respective uncertainties (e.g., theory uncertainties) on this prediction shown as the shaded band, and the data represented as the black points. The left figure shows the linear EFT model, while the quadratic model is shown on the right.

12.2 Observed EFT Limits in the Global Context

It has been shown that this measurement has great potential to constrain the effects of two EFT operators at the same time. The constraining power, as given by the size of the resulting marginalized limits on the two Wilson coefficients, is about the same for both coefficients. In order to assess the sensitivity of this measurement in the global context of the EFT framework in the HEP community, the limits are compared to recent fits and the currently most stringent limits. As outlined before, the EFT approach profits from the combination of multiple observations due to its global nature. The set of relevant EFT operators as well as their effects differ depending on the observable, which therefore contribute complementary information to an interpretation. This complementarity ideally results in orthogonal constraints, which maximally reduce the allowed parameter space, as, e.g., discussed in Ref. [86, 88].

Therefore, global fits use a large variety of measurements and observables, allowing them to constrain a large number of Wilson coefficients by making use of these effects. Thus, the

limits derived in this work are compared to a recent global fit combining multiple measurements. The combination performed in Ref. [87] uses top-quark measurements alongside measurements of processes involving the Higgs boson as well as diboson measurements. This combination is able to constrain up to 50 dimensions in the EFT parameter space. The comparison of this global fit to a single measurement is thus not entirely adequate considering the amount of information included through the observations. Furthermore, global combinations generally have to rely on a number of assumptions on the input measurements. The correlations of uncertainties, potential statistical overlap as well as differences in the measurement strategies introduce challenges, which sometimes require internal information of the collaborations to be overcome, or are hard to solve in general. Since in this thesis, the interpretation is facilitated as part of the measurement, none of these obstacles are present. However, since such combinations generally give the most stringent limits, they set the context for the strength of constraints on EFT contributions and, therefore, of this measurement.
The two operators of interest in this interpretation, O_{tG} and $O_{tq}^{(8)}$, are among the operators constrained in the global combination. The limits on the Wilson coefficients in the global fit are derived using a one-dimensional model, with only the Wilson coefficient under study being allowed to take non-zero values. The resulting individual limits from the global fit are compared to the limits derived in this measurement in Table 12.2.

Model	C_i $(\Lambda/\text{TeV})^2$	Individual 95 % intervals Observed	Global fit 95 % limits [87]
Λ^{-4}	C_{tG}	[-0.52, 0.15]	[0.006, 0.107]
	$C_{tq}^{(8)}$	[-0.64, 0.12]	[-0.48, 0.39]
Λ^{-2}	C_{tG}	[-0.63, 0.20]	[0.007, 0.111]
	$C_{tq}^{(8)}$	[-0.34, 0.27]	[-0.40, 0.61]

Table 12.2: Observed 95 % CL intervals for the Wilson coefficients C_{tG} and $C_{tq}^{(8)}$. The individual limits shown here are determined from the interpretation allowing only the Wilson coefficient under study to take non-zero values, and are given at both EFT orders. The results are compared with the individual limits obtained in Ref. [87].

Both sets of limits represent the 95 % CL intervals and are derived using the one-dimensional model. This makes the numbers independent of the number of EFT operators in the full EFT model. For both operators, the linear and quadratic model up to $\mathcal{O}(\Lambda^{-4})$ are compared. Comparing the sizes of the limits on C_{tG} shows very strongly that the sensitivity of the measurement, presented in this work, to the operator O_{tG} is not as large as the sensitivity obtained in the combination of measurements performed in Ref. [87]. The global combination gives 6-8 times stronger limits. However, considering this is a single measurement, the sensitivity is of the same order of magnitude, showing the potential this measurement can add to future combinations. The limits in this measurement are shifted towards negative values, while the global fit shows a slight shift towards positive ones.

For $C_{tq}^{(8)}$, the limits in both EFT models are competitive with the global analysis. In both cases, the limits obtained from this measurement are even more stringent, with the intervals being 13 % stronger in the quadratic model and 40 % stronger in the linear model. This shows furthermore how sensitive the observed region in this process is to the four-fermion $O_{tq}^{(8)}$, and four-fermion operators in general. These competitive limits indicate that this measurement could add sensitivity, in particular to limits on $C_{tq}^{(8)}$ and potentially other four-fermion operators in future global combinations. The size of the limits on $C_{tq}^{(8)}$, obtained in this work, compared to the global combination demonstrate the absence of similarly sensitive data in the combination presented in Ref. [87].

Due to the high sensitivity and precision of the data presented in this measurement, the resulting constraints on EFT contributions also add important inputs to the current context of EFT interpretations in the top-quark sector at the ATLAS and CMS experiments. Recent summaries of the two collaborations' results show the excellent sensitivity of the results presented in this measurement, particularly on the four-fermion operator $O_{tq}^{(8)}$ [195]. Figures 12.5 and 12.6 show a summary of marginalized limits of recent measurements in the top-quark sector by the ATLAS collaboration. The limits on the different top-quark specific dimension-six operators are given for the linear and linear+quadratic EFT models at 68 % and 95 % confidence level, if available. The constraints on C_{tG} derived from the measurement presented in this work are included in the two-fermion top quark operator summary in Figure 12.5 (Ref. [3] in Figure 12.5), while the limits on $C_{tq}^{(8)}$ contribute to the list of limits on four-fermion top-related operators in Figure 12.6 (Ref. [1] in Figure 12.6). The limits on effects of the four-fermion operator $O_{tq}^{(8)}$ derived on this measurement are among the strongest limits currently derived on top-quark measurements within the ATLAS collaboration. Furthermore, this measurement provides the first limits on C_{tG}, derived from top-quark measurements in the ATLAS collaboration. Comparing the limits to global LHC summaries also shows the good sensitivity of this measurement to the effects of this operator (see Ref. [195, 196]).

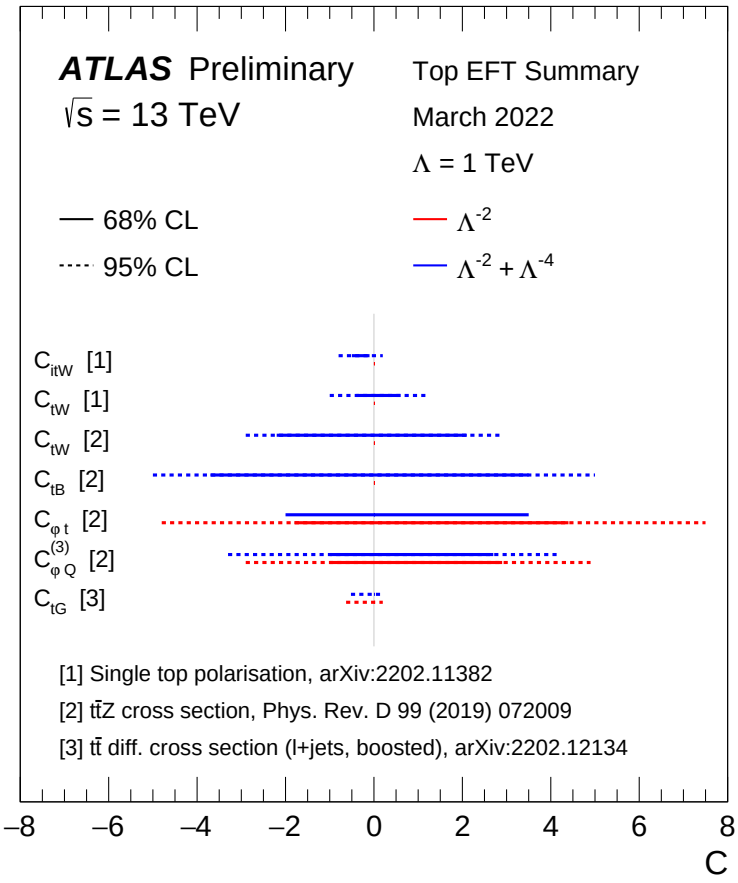

Figure 12.5: Summary of the recent limits on a selection of two-fermion EFT operators from the top-quark sector of SMEFT [195]. The limits are quoted from recent ATLAS measurements [78, 79, 84]. Depending on availability, the limits are given for both the linear and linear+quadratic EFT model and at 68 % or 95 % confidence. The measurement presented in this work contributes the limits on C_{tG} in this summary plot (denoted by Ref. [3]).

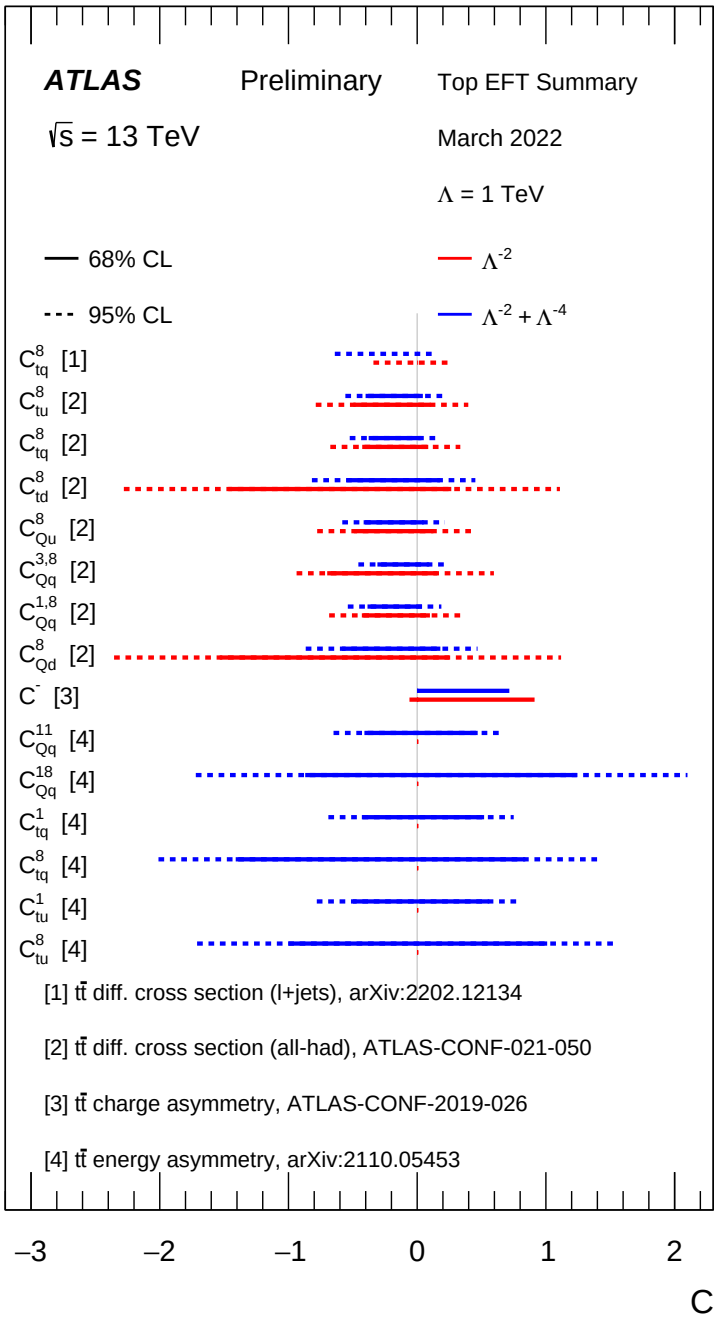

Figure 12.6: Summary of the recent limits on a selection of EFT operators from the top-quark sector of SMEFT [195]. The limits are quoted from recent ATLAS measurements [73, 80, 81, 84] for four-fermion operators. Depending on availability, the limits are given for both the linear and linear+quadratic EFT model and at 68 % or 95 % confidence. The measurement presented in this work contributes the limits on $C_{tq}^{(8)}$ in this summary plot (denoted by Ref. [1]).

13 Conclusions

In this thesis, I presented a cross-section measurement of the production of a pair of top quarks using proton-proton collision data collected with the ATLAS detector. The cross-section is measured as a function of various kinematic observables using the most extensive dataset collected by the ATLAS collaboration so far. This measurement is among the most precise ones in the large-p_{T} phase space.
The precision is primarily attributed to the large dataset and, thus, small statistical uncertainty, as well as to a reduced sensitivity to jet-related systematic uncertainties, due to the presented measurement strategy. The latter is achieved by using a novel method that employs a scaling of the energies of the jets in order to reduce jet-related uncertainties. The variables used for the differential cross-section measurements are chosen based on their particular benefit for testing our modeling of the SM, as well as their sensitivity to BSM physics. In particular, the modeling of certain aspects of the hard scattering process and the generation of additional radiation in the simulation of collision data are investigated. After re-weighting the SM predictions to match NNLO predictions in QCD, all predictions improve the accuracy with respect to the NLO predictions and are in good agreement with the SM. This leads to the conclusion that it is crucial to include higher-order contributions in the predictions in order to match the precision of the presented data. Neglecting these contributions shows several discrepancies in the modeling of the SM, particularly in observables sensitive to additional radiation. The good statistical precision of the dataset leads to the dominance of systematic uncertainties in the results. Therefore, further improvements in the precision of these kind of measurements will depend on reducing the systematic uncertainties. With the presented work we proved that such reductions can be achieved by using new methods like the JSF method.

In order to use this data as efficiently as possible, and effectively search for BSM physics in the absence of clear evidence for such, the indirect interpretation of data is a great opportunity. Assuming that, based on the lack of direct evidence for such, BSM physics lies at much larger energy scales than the direct reach of the LHC, EFT is a perfectly suited framework to search for such effects. The differential measurements presented in this work have great potential as probes for BSM physics in this framework. Exploiting the dependence of EFT effects on the energy scale of the studied process is only possible by using the additional information in resolving the data in certain variables. Such effects become visible in the shape of the differential measurements. Despite the larger uncertainties of performing a number of measurements on the same dataset, when compared to inclusive measurements, this leads to much stronger limits. More importantly, due to additionally resolving the data as function of kinematic variables, a differential cross-section measurement is able to disentangle the effects of multiple operators in a single

measurement. As shown in this work, the intentional construction of a measurement to exploit the behavior of the EFT operators of interest leading to significant orthogonality in the different parts of the measurement, benefits the resulting limits significantly. Thus, using the abundance of data presented in this measurement while employing the above-mentioned approach allows for much stronger statements about BSM physics in the EFT framework.
In this work, a BSM model consisting of two operators is used to interpret the data. The model contains the chromomagnetic dipole operator O_{tG} and the four-fermion operator $O_{tq}^{(8)}$. The measurement shows excellent sensitivity to the effects of both operators and is able to constrain both Wilson coefficients independently in a simultaneous fit. This disentanglement uses the orthogonality between the bulk and the tail of the $p_{\mathrm{T}}^{t,h}$ spectrum in the interpretation due to the difference in the energy scaling and rates of the EFT effects. As expected from predictions of these effects, the boosted regime, as probed in this measurement, shows excellent sensitivity to the four-fermion operator $O_{tq}^{(8)}$. Due to the strong energy scaling of such operators and the additional growth in parton luminosity of quark-initiated events, the tails of the $p_{\mathrm{T}}^{t,h}$ spectrum are the ideal phase space for probes of such operators in the $t\bar{t}$ signal. Interpreting this data – also in future combinations or re-interpretations – therefore significantly contributes to shedding light on this class of top-related EFT operators, which have not been constrained as much as others, in the past. This interpretation shows that limits on effects of $O_{tq}^{(8)}$ in this phase space are comparable to those on effects of O_{tG}, despite the much stronger effect of the chromomagnetic dipole operator on the bulk of the events. Furthermore, the limits on $C_{tq}^{(8)}$ based on this single measurement are 10 % to 40 % more stringent than such from recent global combinations of tens of measurements, while being performed as part of the measurement and thus making the need for assumptions, which is typical for global combinations, obsolete. This again shows the relevance of this data, as well as the large potential in an interpretation like this. In contrast, the sensitivity to effects of O_{tG} is not as strong in the data presented in this measurement, despite the resulting limits being very stringent as well.

In the context of EFT interpretations of measurements in top-quark physics at the LHC, this work presents an important test and one of the first detailed examples of how to interpret differential cross-section measurements, as part of the measurement, in the top-quark sector of EFT. The strategy and obstacles presented in this thesis contain important proofs of concept, as well as practical implementations for such interpretations and show the competitiveness of this approach even in comparison to global combinations. The procedure to build an EFT model and in particular to combine these with the current SM predictions, as well as the various tests on how to validate the model, support the robustness of this approach. Similarly, the statistical interpretation in this context, in particular while including an unfolding procedure, proved to be suitable approaches and important to the interpretation. The success of this approach shows that considerations in the context of EFT interpretations contribute significantly to stringent limits and, thus, making the best use of the collected data. In contrast to global combinations of measurements of mostly total cross-sections, this analysis is tailored to assure the validity of the EFT approach and to optimize the performance of the interpretation. The

access to a sound treatment of uncertainties and their correlations, as well as the validity checks of, e.g., the unfolding performed in this measurement, make the methodology much more stringent as well. Future interpretations, following these guidelines, will continue adding valuable information on the various operators in the EFT framework. In the future, measurements could take tailoring analyses to EFT interpretations a step further by constructing the analysis strategy (e.g., the signal selection) based on the signal operator content instead of a classical process definition. A first example of such dedicated measurements, which avoid competition among measurement precision and sensitivity to EFT effects, has been performed by the CMS collaboration [77].
An additional future approach to more stringent interpretations of the collected data will be increasingly complex combinations of measurements. As outlined in this work, potential BSM contributions would most likely appear on a global scale in the various operators of the EFT approach. Therefore, combinations of broader sets of EFT operators in the top-quark sector and beyond would profit from correlations of such effects and thus be more sensitive. To achieve this from currently available measurements, combinations of these are essential. There is a variety of big challenges to such combinations, which range from statistical overlap of measurements to the estimation of correlations among uncertainties. However, this interpretation, as well as similar ones, profile the necessary technical aspects of such combinations. In this context, the combination of the bins of this differential measurement with their respective uncertainties and correlations among these in a single interpretation represents the first approach in this direction within the controlled environment of a single measurement. As shown in this work, the orthogonality present in such a combination is essential to constraining more complex EFT models, starting from two operators, and leads to much more stringent limits.
Consequently, the approach presented in this work, especially when extended to the larger EFT framework, is an ideal tool to efficiently exploit the plethora of available precision measurements of the data collected with the ATLAS experiment in Run 2 at the LHC. The effective description allows for a direct connection of the precision data to potential BSM physics via the Wilson coefficients in the EFT framework. There are several challenges ahead in using such approaches on more global levels. For the combination of measurements, obstacles such as statistical overlap due to the same dataset, estimation of correlations of several aspects of different measurements and harmonisation of different measurement strategies need to be overcome. Additionally, the truncation of the EFT approach at dimension six and the inclusion of dimension-eight operators in EFT interpretations are fields of current research. However, even in the presence of these challenges, EFTs present an ideal framework for advancing high-energy physics. In the absence of clear evidence for BSM physics, this can lead the way toward a path for future searches, as well as making large amounts of data available for testing theories in a global and model-independent way, complementary to performing dedicated searches.

Bibliography

For closed access publications, also an open access preprint, usually from the arXiv, is provided, if available. Where an open access version could not been found, this is noted.

1. D0 Collaboration. "Observation of the Top Quark". *Phys. Rev. Lett.* 74, 1995.
   doi: 10.1103/physrevlett.74.2632. arxiv: 9503003
2. CDF Collaboration. "Observation of Top Quark Production in $\bar{p}p$ Collisions with the Collider Detector at Fermilab". *Phys. Rev. Lett.* 74, 1995.
   doi: 10.1103/physrevlett.74.2626. arxiv: 9503002
3. S. Weinberg. "Phenomenological Lagrangians". *Physica A: Statistical Mechanics and its Applications* 96, 1979.
   doi: https://doi.org/10.1016/0378-4371(79)90223-1
4. W. Buchmüller and D. Wyler. "Effective lagrangian analysis of new interactions and flavour conservation". *Nucl. Phys. B* 268, 1986.
   doi: https://doi.org/10.1016/0550-3213(86)90262-2
5. C. Burges and H. J. Schnitzer. "Virtual effects of excited quarks as probes of a possible new hadronic mass scale". *Nucl. Phys. B* 228, 1983.
   doi: https://doi.org/10.1016/0550-3213(83)90555-2
6. C. N. Leung, S. T. Love, and S. Rao. "Low-energy manifestations of a new interactions scale: Operator analysis". *Zeitschrift für Physik C Particles and Fields* 31, 1986.
   doi: 10.1007/BF01588041
7. C. Degrande et al. "Non-resonant New Physics in Top Pair Production at Hadron Colliders". *JHEP* 03, 2011.
   doi: 10.1007/JHEP03(2011)125. arxiv: 1010.6304
8. A. Buckley et al. "Constraining top quark effective theory in the LHC Run II era". *JHEP* 04, 2016.
   doi: 10.1007/JHEP04(2016)015. arxiv: 1512.03360
9. M. P. Rosello and M. Vos. "Constraints on four-fermion interactions from the $t\bar{t}$ charge asymmetry at hadron colliders". *Eur. Phys. J. C* 76, 2016.
   doi: 10.1140/epjc/s10052-016-4040-x. arxiv: 1512.07542
10. C. Englert et al. "Giving top quark effective operators a boost". *Phys. Lett. B* 763, 2016.
    doi: 10.1016/j.physletb.2016.10.021. arxiv: 1607.04304

11. ATLAS Collaboration. "Measurements of $t\bar{t}$ differential cross-sections of highly boosted top quarks decaying to all-hadronic final states in pp collisions at $\sqrt{s} = 13\,\text{TeV}$ using the ATLAS detector". *Phys. Rev. D* 98, 2018.
doi: 10.1103/PhysRevD.98.012003. arxiv: 1801.02052

12. CMS Collaboration. "Measurement of differential $t\bar{t}$ production cross sections using top quarks at large transverse momenta in pp collisions at $\sqrt{s} = 13\,\text{TeV}$". *Phys. Rev. D* 103, 2021.
doi: 10.1103/PhysRevD.103.052008. arxiv: 2008.07860

13. ATLAS Collaboration. "Measurement of the differential cross-section of highly boosted top quarks as a function of their transverse momentum in $\sqrt{s} = 8\,\text{TeV}$ proton–proton collisions using the ATLAS detector". *Phys. Rev. D* 93, 2016.
doi: 10.1103/PhysRevD.93.032009. arxiv: 1510.03818

14. CMS Collaboration. "Measurement of the integrated and differential $t\bar{t}$ production cross sections for high-p_{T} top quarks in pp collisions at $\sqrt{s} = 8\,\text{TeV}$". *Phys. Rev. D* 94, 2016.
doi: 10.1103/PhysRevD.94.072002. arxiv: 1605.00116

15. ATLAS Collaboration. "Measurements of top-quark pair differential and double-differential cross-sections in the ℓ+jets channel with pp collisions at $\sqrt{s} = 13\,\text{TeV}$ using the ATLAS detector". *Eur. Phys. J. C* 79, 2019.
doi: 10.1140/epjc/s10052-019-7525-6. arxiv: 1908.07305. Erratum: *Eur. Phys. J. C* 80, 2020.
doi: 10.1140/epjc/s10052-020-08541-3

16. B. Grzadkowski et al. "Dimension-Six Terms in the Standard Model Lagrangian". *JHEP* 10, 2010.
doi: 10.1007/JHEP10(2010)085. arxiv: 1008.4884

17. ATLAS Collaboration. "Measurement of the top quark mass in the $t\bar{t} \to$ lepton+jets channel from $\sqrt{s} = 8\,\text{TeV}$ ATLAS data and combination with previous results". *Eur. Phys. J. C* 79, 2019.
doi: 10.1140/epjc/s10052-019-6757-9. arxiv: 1810.01772

18. Y. Fukuda et al. "Evidence for Oscillation of Atmospheric Neutrinos". *Phys. Rev. Lett.* 81, 1998.
doi: 10.1103/physrevlett.81.1562. arxiv: 9807003

19. SNO Collaboration. "Measurement of the Rate of $\nu_e + d \to p + p + e^-$ Interactions Produced by ^{8}B Solar Neutrinos at the Sudbury Neutrino Observatory". *Phys. Rev. Lett.* 87, 2001.
doi: 10.1103/physrevlett.87.071301

20. SNO Collaboration. "Direct Evidence for Neutrino Flavor Transformation from Neutral-Current Interactions in the Sudbury Neutrino Observatory". *Phys. Rev. Lett.* 89, 2002.
doi: 10.1103/physrevlett.89.011301

21. Particle Data Group Collaboration. "Review of Particle Physics". *PTEP* 2020, 2020.
doi: 10.1093/ptep/ptaa104

22. F. Englert and R. Brout. "Broken Symmetry and the Mass of Gauge Vector Mesons". *Phys. Rev. Lett.* 13, 1964.
doi: 10.1103/PhysRevLett.13.321

23. P. W. Higgs. "Broken Symmetries and the Masses of Gauge Bosons". *Phys. Rev. Lett.* 13, 1964.
doi: 10.1103/PhysRevLett.13.508

24. ATLAS Collaboration. "Observation of a new particle in the search for the Standard Model Higgs boson with the ATLAS detector at the LHC". *Phys. Lett. B* 716, 2012.
doi: 10.1016/j.physletb.2012.08.020. arxiv: 1207.7214

25. CMS Collaboration. "Observation of a new boson at a mass of 125 GeV with the CMS experiment at the LHC". *Phys. Lett. B* 716, 2012.
doi: 10.1016/j.physletb.2012.08.021. arxiv: 1207.7235

26. ATLAS Collaboration. "Evidence for the spin-0 nature of the Higgs boson using ATLAS data". *Phys. Lett. B* 726, 2013.
doi: 10.1016/j.physletb.2013.08.026. arxiv: 1307.1432

27. ATLAS Collaboration. "Determination of spin and parity of the Higgs boson in the $WW^* \to e\nu\mu\nu$ decay channel with the ATLAS detector". *Eur. Phys. J. C* 75, 2015.
doi: 10.1140/epjc/s10052-015-3436-3. arxiv: 1503.03643

28. ATLAS Collaboration. "Study of the spin and parity of the Higgs boson in diboson decays with the ATLAS detector". *Eur. Phys. J. C* 75, 2015.
doi: 10.1140/epjc/s10052-015-3685-1. arxiv: 1506.05669. Erratum: *Eur. Phys. J. C* 76, 2016.
doi: 10.1140/epjc/s10052-016-3934-y

29. CMS Collaboration. "Study of the mass and spin-parity of the Higgs boson candidate via its decays to Z Boson Pairs". *Phys. Rev. Lett.* 110, 2013.
doi: 10.1103/PhysRevLett.110.081803. arxiv: 1212.6639

30. CMS Collaboration. "Constraints on the spin-parity and anomalous HVV couplings of the Higgs boson in proton collisions at 7 and 8 TeV". *Phys. Rev. D* 92, 2015.
doi: 10.1103/PhysRevD.92.012004. arxiv: 1411.3441

31. F. Zwicky. "Die Rotverschiebung von extragalaktischen Nebeln". *Helvetica Physica Acta* 6, 1933

32. G. Bertone, D. Hooper, and J. Silk. "Particle dark matter: evidence, candidates and constraints". *Physics Reports* 405, 2005.
doi: 10.1016/j.physrep.2004.08.031

33. *Particle Dark Matter: Observations, Models and Searches*. Cambridge University Press, 2010.
doi: 10.1017/CBO9780511770739

34. L. Canetti, M. Drewes, and M. Shaposhnikov. "Matter and antimatter in the universe". *New Journal of Physics* 14, 2012.
doi: 10.1088/1367-2630/14/9/095012. http://dx.doi.org/10.1088/1367-2630/14/9/095012

35. A. D. Sakharov. "Violation of CP Invariance, C asymmetry, and baryon asymmetry of the universe". *Pisma Zh. Eksp. Teor. Fiz.* 5, 1967.
doi: 10.1070/PU1991v034n05ABEH002497

36. LHCb Collaboration. *Test of lepton universality in beauty-quark decays*. 2021.
arxiv: 2103.11769 [hep-ex]

37. LHCb Collaboration. "Test of lepton universality with $\Lambda_b^0 \to pK^-\ell^+\ell^-$ decays". *JHEP* 05, 2020.
doi: 10.1007/jhep05(2020)040

38. LHCb Collaboration. "Test of lepton universality with $B_0 \to K^{*0}\ell^+\ell^-$ decays". *JHEP* 08, 2017.
doi: 10.1007/jhep08(2017)055

39. LHCb Collaboration. "Measurement of CP-averaged observables in the $B^0 \to K^{*0}\mu^+\mu^-$ decay". *Phys. Rev. Lett.* 125, 2020.
doi: 10.1103/physrevlett.125.011802. arxiv: 2003.04831

40. LHCb Collaboration. "Angular analysis of the $B^+ \to K^{*+}\mu^+\mu^-$ decay". *Phys. Rev. Lett.* 126, 2021.
doi: 10.1103/physrevlett.126.161802. arxiv: 2012.13241

41. LHCb Collaboration. "Test of lepton universality with $B^0 \to K^{*0}\ell^+\ell^-$ decays". *JHEP* 08, 2017.
doi: 10.1007/jhep08(2017)055. arxiv: 1705.05802

42. B. Abi et al. "Measurement of the Positive Muon Anomalous Magnetic Moment to 0.46 ppm". *Phys. Rev. Lett.* 126, 2021.
doi: 10.1103/physrevlett.126.141801

43. G. W. Bennett et al. "Final report of the E821 muon anomalous magnetic moment measurement at BNL". *Phys. Rev. D* 73, 2006.
doi: 10.1103/physrevd.73.072003

44. CDF Collaboration. "High-precision measurement of the W boson mass with the CDF II detector". *Science* 376, 2022.
doi: 10.1126/science.abk1781. eprint: https://www.science.org/doi/pdf/10.1126/science.abk1781

45. ATLAS Collaboration. "Measurement of the W-boson mass in pp collisions at $\sqrt{s} = 7\,\text{TeV}$ with the ATLAS detector". *Eur. Phys. J. C* 78, 2018.
doi: 10.1140/epjc/s10052-017-5475-4. arxiv: 1701.07240. Erratum: *Eur. Phys. J. C* 78, 2018.
doi: 10.1140/epjc/s10052-018-6354-3

46. LHCb Collaboration. "Measurement of the W boson mass". *JHEP* 01, 2022. doi: 10.1007/jhep01(2022)036

47. R. Benbrik et al. "Signatures of vector-like top partners decaying into new neutral scalar or pseudoscalar bosons". *JHEP* 05, 2020. doi: 10.1007/jhep05(2020)028

48. ATLAS Collaboration. "Search for top-squark pair production in final states with one lepton, jets, and missing transverse momentum using $36\,\mathrm{fb}^{-1}$ of $13\,\mathrm{TeV}$ pp collision data with the ATLAS detector". *JHEP* 06:6, 2018. doi: 10.1007/jhep06(2018)108

49. J. Montaño, H. Novales-Sánchez, and J. J. Toscano. "Effects of universal extra dimensions on top-quark electromagnetic interactions". *J. Phys. G: Nuclear and Particle Physics* 47, 2019. doi: 10.1088/1361-6471/ab4d93

50. A. Abada et al. "FCC-hh: The Hadron Collider". *Eur. Phys. J. Spec. Top.* 43, 2019. doi: 10.1140/epjst/e2019-900087-0

51. A. Abada et al. "HE-LHC: The High-Energy Large Hadron Collider". *Eur. Phys. J. Spec. Top.* 43, 2019. doi: 10.1140/epjst/e2019-900088-6

52. G. D'Ambrosio et al. "Minimal flavor violation: An Effective field theory approach". *Nucl. Phys. B* 645, 2002. doi: 10.1016/S0550-3213(02)00836-2. arxiv: hep-ph/0207036

53. R. Alonso et al. "Renormalization group evolution of the Standard Model dimension six operators III: gauge coupling dependence and phenomenology". *JHEP* 04, 2014. doi: 10.1007/jhep04(2014)159. http://dx.doi.org/10.1007/JHEP04(2014)159

54. S. Fichet, A. Tonero, and P. R. Teles. "Sharpening the shape analysis for higher-dimensional operator searches". *Phys. Rev. D* 96, 2017. doi: 10.1103/physrevd.96.036003. arxiv: 1611.01165

55. E. Fermi. "Ein Versuch einer Theorie der β-Strahlen". *Z. Physik* 88, 1934. doi: 10.1007/BF01351864

56. S. L. Glashow. "Partial-symmetries of weak interactions". *Nucl. Phys.* 22, 1961. doi: 10.1016/0029-5582(61)90469-2

57. S. Weinberg. "A Model of Leptons". *Phys. Rev. Lett.* 19, 1967. doi: 10.1103/PhysRevLett.19.1264

58. A. Salam. "Weak and Electromagnetic Interactions". *Conf. Proc. C* 680519, 1968

59. ATLAS Collaboration. *Combined measurements of Higgs boson production and decay using up to* 139 fb^{-1} *of proton-proton collision data at* $\sqrt{s} = 13$ *TeV collected with the ATLAS experiment*. Geneva, 2021.
https://cds.cern.ch/record/2789544.
Note: All figures including auxiliary figures are available at https://atlas.web.cern.ch/Atlas/GROUPS/PHYSICS/CONFNOTES/ATLAS-CONF-2021-053

60. CMS Collaboration. "Constraints on anomalous Higgs boson couplings to vector bosons and fermions in its production and decay using the four-lepton final state". *Phys. Rev. D* 104, 2021.
doi: 10.1103/PhysRevD.104.052004

61. ATLAS Collaboration. *Combination of measurements of Higgs boson production in association with a* W *or* Z *boson in the* $b\bar{b}$ *decay channel with the ATLAS experiment at* $\sqrt{s} = 13$ *TeV*. Geneva, 2021.
https://cds.cern.ch/record/2782535.
Note: All figures including auxiliary figures are available at https://atlas.web.cern.ch/Atlas/GROUPS/PHYSICS/CONFNOTES/ATLAS-CONF-2021-051

62. CMS Collaboration. *Constraints on anomalous Higgs boson couplings to vector bosons and fermions from the production of Higgs bosons using the* $\tau\tau$ *final state*. 2022.
arxiv: 2205.05120

63. CMS Collaboration. "Measurements of Higgs boson production cross sections and couplings in the diphoton decay channel at $\sqrt{\text{s}} = 13$ TeV". *JHEP* 07, 2021.
doi: 10.1007/jhep07(2021)027

64. B. Capdevila et al. "Patterns of New Physics in $b \to s\ell^+\ell^-$ transitions in the light of recent data". *JHEP* 01, 2018.
doi: 10.1007/jhep01(2018)093. arxiv: 1704.05340

65. M. Ciuchini et al. "Lessons from the $B^{0,+} \to K^{*0,+}\mu^+\mu^-$ angular analyses". *Phys. Rev. D* 103, 2021.
doi: 10.1103/physrevd.103.015030. arxiv: 2011.01212

66. G. Hiller and M. Schmaltz. "R_K and future $b \to s\ell\ell$ BSM opportunities". *Phys. Rev. D* 90, 2014.
doi: 10.1103/physrevd.90.054014. arxiv: 1408.1627

67. W. Altmannshofer and D. M. Straub. "New physics in $B \to K^*\mu\mu$?" *Eur. Phys. J. C* 73, 2013.
doi: 10.1140/epjc/s10052-013-2646-9. arxiv: 1308.1501

68. ATLAS Collaboration. "Probing the Wtb vertex structure in t-channel single-top-quark production and decay in pp collisions at $\sqrt{s} = 8\,\text{TeV}$ with the ATLAS detector". *JHEP* 04, 2017.
doi: https://doi.org/10.1007/JHEP04(2017)124

69. ATLAS Collaboration. "Analysis of the Wtb vertex from the measurement of triple-differential angular decay rates of single top quarks produced in the t-channel at $\sqrt{s} = 8\,\text{TeV}$ with the ATLAS detector". *JHEP* 12, 2017.
doi: https://doi.org/10.1007/JHEP12(2017)017

70. CMS Collaboration. "Search for new physics in top quark production in dilepton final states in proton-proton collisions at $\sqrt{s} = 13\,\text{TeV}$". *Eur. Phys. J. C* 79, 2019.
doi: 10.1140/epjc/s10052-019-7387-y

71. CMS Collaboration. "Measurement of the top quark polarization and $t\bar{t}$ spin correlations using dilepton final states in proton-proton collisions at $\sqrt{s} = 13\,\text{TeV}$". *Phys. Rev. D* 100, 2019.
doi: 10.1103/physrevd.100.072002

72. CMS Collaboration. "Search for the production of four top quarks in the single-lepton and opposite-sign dilepton final states in proton-proton collisions at $\sqrt{s} = 13$ TeV". *JHEP* 11, 2019.
doi: 10.1007/jhep11(2019)082

73. ATLAS Collaboration. *Measurement of the energy asymmetry in $t\bar{t}j$ production at 13 TeV with the ATLAS experiment and interpretation in the SMEFT framework*. 2021.
arxiv: 2110.05453

74. ATLAS Collaboration. "Search for flavour-changing neutral currents in processes with one top quark and a photon using 81 fb^{-1} of pp collisions at $\sqrt{s} = 13\,\text{TeV}$ with the ATLAS experiment". *Phys. Lett. B* 800, 2020.
doi: 10.1016/j.physletb.2019.135082

75. CMS Collaboration. "Probing effective field theory operators in the associated production of top quarks with a Z boson in multilepton final states at $\sqrt{s} =$ 13 TeV". *JHEP* 12, 2021.
doi: 10.1007/jhep12(2021)083

76. CMS Collaboration. "Measurement of top quark pair production in association with a Z boson in proton-proton collisions at $\sqrt{s} = 13$ TeV". *JHEP* 03, 2020.
doi: 10.1007/JHEP03(2020)056

77. CMS Collaboration. "Search for new physics in top quark production with additional leptons in proton-proton collisions at $\sqrt{s} = 13$ TeV using effective field theory". *JHEP* 03, 2021.
doi: 10.1007/jhep03(2021)095. arxiv: 2012.04120

78. ATLAS Collaboration. *Measurement of the polarisation of single top quarks and antiquarks produced in the t-channel collected with the ATLAS detector at $\sqrt{s} = 13$ TeV and bounds on the tWb dipole operator*. 2021.
https://cds.cern.ch/record/2773738

79. ATLAS Collaboration. "Measurement of the $t\bar{t}Z$ and $t\bar{t}W$ cross sections in proton–proton collisions at $\sqrt{s} = 13\,\text{TeV}$ with the ATLAS detector". *Phys. Rev. D* 99, 2019.
doi: 10.1103/PhysRevD.99.072009. arxiv: 1901.03584

80. ATLAS Collaboration. *Differential $t\bar{t}$ cross-section measurements using boosted top quarks in the all-hadronic final state with 139 fb^{-1} of ATLAS data*. Geneva, 2021.
https://cds.cern.ch/record/2782534

81. ATLAS Collaboration. *Inclusive and differential measurement of the charge asymmetry in $t\bar{t}$ events at 13 TeV with the ATLAS detector*. 2019.
https://cds.cern.ch/record/2682109

82. ATLAS Collaboration. "Search for flavour-changing neutral current top-quark decays $t \to qZ$ in proton–proton collisions at $\sqrt{s} = 13\,\text{TeV}$ with the ATLAS detector". *JHEP* 07, 2018.
doi: 10.1007/JHEP07(2018)176. arxiv: 1803.09923

83. ATLAS Collaboration. *Measurements of differential cross-sections in top-quark pair events with a high transverse momentum top quark and limits on beyond the Standard Model contributions to top quark pair production with the ATLAS detector*. Geneva, 2021.
https://cds.cern.ch/record/2777237.
Note: All figures including auxiliary figures are available at https://atlas.web.cern.ch/Atlas/GROUPS/PHYSICS/CONFNOTES/ATLAS-CONF-2021-031

84. ATLAS Collaboration. "Measurements of differential cross-sections in top-quark pair events with a high transverse momentum top quark and limits on beyond the Standard Model contributions to top-quark pair production with the ATLAS detector at $\sqrt{s} = 13$ TeV". *JHEP* 63, 2022.
doi: 10.1007/JHEP06(2022)063. arxiv: 2202.12134

85. N. P. Hartland et al. "A Monte Carlo global analysis of the Standard Model Effective Field Theory: the top quark sector". *JHEP* 04, 2019.
doi: 10.1007/jhep04(2019)100

86. I. Brivio et al. "O new physics, where art thou? A global search in the top sector". *JHEP* 02, 2020.
doi: 10.1007/jhep02(2020)131. arxiv: 1910.03606

87. J. J. Ethier et al. (SMEFiT Collaboration). "Combined SMEFT interpretation of Higgs, diboson, and top quark data from the LHC". *JHEP* 11, 2021.
doi: 10.1007/JHEP11(2021)089. arxiv: 2105.00006

88. S. Bißmann et al. "Synergies of top and B anomalies in SMEFT", 2021.
arxiv: 2105.05257

89. S. Bißmann et al. "Top and beauty synergies in SMEFT-fits at present and future colliders". *JHEP* 06, 2021.
doi: 10.1007/jhep06(2021)010

90. S. Bißmann, J. Erdmann, C. Grunwald, et al. "Constraining top-quark couplings combining top-quark and B decay observables". *Eur. Phys. J. C*, 2020.
doi: 10.1140/epjc/s10052-020-7680-9

91. ATLAS Collaboration. "Search for flavour-changing neutral current top-quark decays $t \to qZ$ in proton-proton collisions at $\sqrt{s} = 13$ TeV with the ATLAS detector". *JHEP* 07, 2018.
doi: 10.1007/jhep07(2018)176

92. ATLAS and CMS Collaborations. "Combination of the W boson polarization measurements in top quark decays using ATLAS and CMS data at $\sqrt{s} = 8$ TeV". *JHEP* 08, 2020.
doi: 10.1007/jhep08(2020)051

93. ATLAS Collaboration. *Search for flavor-changing neutral-current couplings between the top quark and the Z boson with LHC Run2 proton-proton collisions at $\sqrt{s} = 13$ TeV with the ATLAS detector*. Geneva, 2021.
https://cds.cern.ch/record/2781174

94. J. O. Berger and D. A. Berry. "Statistical Analysis and the Illusion of Objectivity". *American Scientist* 76, 1988.
https://www.jstor.org/stable/27855070

95. A. Vehtari et al. "Rank-Normalization, Folding, and Localization: An Improved $\hat{R}$ for Assessing Convergence of MCMC". *Bayesian Analysis*, 2021.
doi: 10.1214/20-ba1221. arxiv: 1903.08008

96. A. Gelman and D. B. Rubin. "Inference from Iterative Simulation Using Multiple Sequences". *Statistical Science* 7, 1992.
doi: 10.1214/ss/1177011136

97. B. Efron. "Why Isn't Everyone a Bayesian?" *The American Statistician* 40, 1986.
https://www.jstor.org/stable/2683105

98. G. D'Agostini. "Bayesian reasoning versus conventional statistics in High Energy Physics", 1998.
arxiv: 9811046

99. O. Behnke et al. *Data analysis in high energy physics – a practical guide to statistical methods*. Wiley-VCH, 2013

100. T. Bayes. "An essay towards solving a problem in the doctrine of chances. By the late Rev. Mr. Bayes, FRS communicated by Mr. Price, in a letter to John Canton, AMFR S". *Philosophical transactions of the Royal Society of London*, 1763

101. N. Castro et al. "EFTfitter—A tool for interpreting measurements in the context of effective field theories". *Eur. Phys. J. C* 76, 2016.
doi: 10.1140/epjc/s10052-016-4280-9. arxiv: 1605.05585

102. A. Caldwell, D. Kollar, and K. Kröninger. "BAT: The Bayesian Analysis Toolkit". *Comput. Phys. Commun.* 180, 2009.
doi: 10.1016/j.cpc.2009.06.026. arxiv: 0808.2552

103. J. S. Speagle. *A Conceptual Introduction to Markov Chain Monte Carlo Methods*. 2019. arxiv: 1909.12313

104. N. Metropolis et al. "Equation of State Calculations by Fast Computing Machines". *The Journal of Chemical Physics* 21, 1953

105. D. Barducci et al. *Interpreting top-quark LHC measurements in the standard-model effective field theory*. 2018. arxiv: 1802.07237

106. L. Barranco Navarro et al. *Guidelines for EFT interpretations within the Top WG in ATLAS*. Technical report. Geneva: CERN, 2021. https://cds.cern.ch/record/2748833. Note: This document is not publicly available, but restricted to members of the ATLAS collaboration.

107. L. Evans and P. Bryant. "LHC Machine". *JINST* 3, 2008. doi: 10.1088/1748-0221/3/08/s08001

108. J. T. Boyd. *LHC Run-2 and Future Prospects*. 2020. arxiv: 2001.04370

109. ATLAS Collaboration. "The ATLAS Experiment at the CERN Large Hadron Collider". *JINST* 3, 2008. doi: 10.1088/1748-0221/3/08/S08003

110. B. Abbott et al. "Production and integration of the ATLAS Insertable B-Layer". *JINST* 13, 2018. doi: 10.1088/1748-0221/13/05/T05008. arxiv: 1803.00844

111. ATLAS Collaboration. *ATLAS Insertable B-Layer: Technical Design Report*. ATLAS-TDR-19. 2010. https://cds.cern.ch/record/1291633. Addendum: ATLAS-TDR-19-ADD-1. 2012. https://cds.cern.ch/record/1451888

112. ATLAS Collaboration. "Performance of the ATLAS trigger system in 2015". *Eur. Phys. J. C* 77, 2017. doi: 10.1140/epjc/s10052-017-4852-3. arxiv: 1611.09661

113. ATLAS Collaboration. "The ATLAS Simulation Infrastructure". *Eur. Phys. J. C* 70, 2010. doi: 10.1140/epjc/s10052-010-1429-9. arxiv: 1005.4568

114. GEANT4 Collaboration. "Geant4 – a simulation toolkit". *Nucl. Instrum. Meth. A* 506, 2003. doi: 10.1016/S0168-9002(03)01368-8

115. ATLAS Collaboration. *The simulation principle and performance of the ATLAS fast calorimeter simulation FastCaloSim*. 2010. https://cds.cern.ch/record/1300517

116. ATLAS Collaboration. *The ATLAS Collaboration Software and Firmware*. 2021. https://cds.cern.ch/record/2767187

117. T. Sjöstrand et al. “An introduction to PYTHIA 8.2”. *Comput. Phys. Commun.* 191, 2015.
doi: 10.1016/j.cpc.2015.01.024. arxiv: 1410.3012

118. ATLAS Collaboration. *The Pythia 8 A3 tune description of ATLAS minimum bias and inelastic measurements incorporating the Donnachie–Landshoff diffractive model*. 2016.
https://cds.cern.ch/record/2206965

119. G. Avoni et al. “The new LUCID-2 detector for luminosity measurement and monitoring in ATLAS”. *JINST* 13, 2018.
doi: 10.1088/1748-0221/13/07/P07017

120. ATLAS Collaboration. *Luminosity determination in pp collisions at $\sqrt{s} = 13$ TeV using the ATLAS detector at the LHC*. 2019.
https://cds.cern.ch/record/2677054

121. ATLAS Collaboration. “ATLAS data quality operations and performance for 2015–2018 data-taking”. *JINST* 15, 2020.
doi: 10.1088/1748-0221/15/04/P04003. arxiv: 1911.04632

122. ATLAS Collaboration. “Performance of electron and photon triggers in ATLAS during LHC Run 2”. *Eur. Phys. J. C* 80, 2020.
doi: 10.1140/epjc/s10052-019-7500-2. arxiv: 1909.00761

123. ATLAS Collaboration. “Performance of the ATLAS muon triggers in Run 2”. *JINST* 15, 2020.
doi: 10.1088/1748-0221/15/09/p09015. arxiv: 2004.13447

124. P. Nason. “A new method for combining NLO QCD with shower Monte Carlo algorithms”. *JHEP* 11, 2004.
doi: 10.1088/1126-6708/2004/11/040. arxiv: hep-ph/0409146

125. S. Frixione, P. Nason, and C. Oleari. “Matching NLO QCD computations with parton shower simulations: the POWHEG method”. *JHEP* 11, 2007.
doi: 10.1088/1126-6708/2007/11/070. arxiv: 0709.2092

126. S. Alioli et al. “A general framework for implementing NLO calculations in shower Monte Carlo programs: the POWHEG BOX”. *JHEP* 06, 2010.
doi: 10.1007/JHEP06(2010)043. arxiv: 1002.2581

127. NNPDF Collaboration. “Parton distributions for the LHC run II”. *JHEP* 04, 2015.
doi: 10.1007/JHEP04(2015)040. arxiv: 1410.8849

128. ATLAS Collaboration. *Studies on top-quark Monte Carlo modelling for Top2016*. 2016.
https://cds.cern.ch/record/2216168

129. ATLAS Collaboration. *ATLAS Pythia 8 tunes to 7 TeV data*. 2014.
https://cds.cern.ch/record/1966419

130. R. D. Ball et al. “Parton distributions with LHC data”. *Nucl. Phys. B* 867, 2013.
doi: 10.1016/j.nuclphysb.2012.10.003. arxiv: 1207.1303

131. M. Beneke et al. "Hadronic top-quark pair production with NNLL threshold resummation". *Nucl. Phys. B* 855, 2012.
doi: 10.1016/j.nuclphysb.2011.10.021. arxiv: 1109.1536

132. M. Cacciari et al. "Top-pair production at hadron colliders with next-to-next-to-leading logarithmic soft-gluon resummation". *Phys. Lett. B* 710, 2012.
doi: 10.1016/j.physletb.2012.03.013. arxiv: 1111.5869

133. P. Bärnreuther, M. Czakon, and A. Mitov. "Percent-Level-Precision Physics at the Tevatron: Next-to-Next-to-Leading Order QCD Corrections to $q\bar{q} \to t\bar{t} + X$". *Phys. Rev. Lett.* 109, 2012.
doi: 10.1103/PhysRevLett.109.132001. arxiv: 1204.5201

134. M. Czakon and A. Mitov. "NNLO corrections to top-pair production at hadron colliders: the all-fermionic scattering channels". *JHEP* 12, 2012.
doi: 10.1007/JHEP12(2012)054. arxiv: 1207.0236

135. M. Czakon and A. Mitov. "NNLO corrections to top pair production at hadron colliders: the quark-gluon reaction". *JHEP* 01, 2013.
doi: 10.1007/JHEP01(2013)080. arxiv: 1210.6832

136. M. Czakon, P. Fiedler, and A. Mitov. "Total Top-Quark Pair-Production Cross Section at Hadron Colliders Through $O(\alpha_S^4)$". *Phys. Rev. Lett.* 110, 2013.
doi: 10.1103/PhysRevLett.110.252004. arxiv: 1303.6254

137. M. Czakon and A. Mitov. "Top++: A program for the calculation of the top-pair cross-section at hadron colliders". *Comput. Phys. Commun.* 185, 2014.
doi: 10.1016/j.cpc.2014.06.021. arxiv: 1112.5675

138. J. Butterworth et al. "PDF4LHC recommendations for LHC Run II". *J. Phys. G* 43, 2016.
doi: 10.1088/0954-3899/43/2/023001. arxiv: 1510.03865

139. A. D. Martin et al. "Parton distributions for the LHC". *Eur. Phys. J. C* 63, 2009.
doi: 10.1140/epjc/s10052-009-1072-5. arxiv: 0901.0002

140. A. D. Martin et al. "Uncertainties on α_S in global PDF analyses and implications for predicted hadronic cross sections". *Eur. Phys. J. C* 64, 2009.
doi: 10.1140/epjc/s10052-009-1164-2. arxiv: 0905.3531

141. H.-L. Lai et al. "New parton distributions for collider physics". *Phys. Rev. D* 82, 2010.
doi: 10.1103/PhysRevD.82.074024. arxiv: 1007.2241

142. J. Gao et al. "CT10 next-to-next-to-leading order global analysis of QCD". *Phys. Rev. D* 89, 2014.
doi: 10.1103/PhysRevD.89.033009. arxiv: 1302.6246

143. ATLAS Collaboration. *Studies on top-quark Monte Carlo modelling with Sherpa and MG5_aMC@NLO*. 2017.
https://cds.cern.ch/record/2261938

144. M. Bähr et al. "Herwig++ physics and manual". *Eur. Phys. J. C* 58, 2008.
doi: 10.1140/epjc/s10052-008-0798-9. arxiv: 0803.0883

145. J. Bellm et al. "Herwig 7.0/Herwig++ 3.0 release note". *Eur. Phys. J. C* 76, 2016.
doi: 10.1140/epjc/s10052-016-4018-8. arxiv: 1512.01178

146. L. Harland-Lang et al. "Parton distributions in the LHC era: MMHT 2014 PDFs". *Eur. Phys. J. C* 75, 2015.
doi: 10.1140/epjc/s10052-015-3397-6. arxiv: 1412.3989

147. E. Bothmann et al. "Event generation with Sherpa 2.2". *SciPost Phys.* 7, 2019.
doi: 10.21468/SciPostPhys.7.3.034. arxiv: 1905.09127

148. T. Gleisberg and S. Höche. "Comix, a new matrix element generator". *JHEP* 12, 2008.
doi: 10.1088/1126-6708/2008/12/039. arxiv: 0808.3674

149. F. Buccioni et al. "OpenLoops 2". *Eur. Phys. J. C* 79, 2019.
doi: 10.1140/epjc/s10052-019-7306-2. arxiv: 1907.13071

150. F. Cascioli, P. Maierhöfer, and S. Pozzorini. "Scattering Amplitudes with Open Loops". *Phys. Rev. Lett.* 108, 2012.
doi: 10.1103/PhysRevLett.108.111601. arxiv: 1111.5206

151. A. Denner, S. Dittmaier, and L. Hofer. "Collier: A fortran-based complex one-loop library in extended regularizations". *Comput. Phys. Commun.* 212, 2017.
doi: 10.1016/j.cpc.2016.10.013. arxiv: 1604.06792

152. M. Czakon et al. "Top-pair production at the LHC through NNLO QCD and NLO EW". *JHEP* 10, 2017.
doi: 10.1007/JHEP10(2017)186. arxiv: 1705.04105

153. S. Catani et al. "Top-quark pair production at the LHC: Fully differential QCD predictions at NNLO". *JHEP* 07, 2019.
doi: 10.1007/JHEP07(2019)100. arxiv: 1906.06535

154. M. Grazzini, S. Kallweit, and M. Wiesemann. "Fully differential NNLO computations with MATRIX". *Eur. Phys. J. C* 78, 2018.
doi: 10.1140/epjc/s10052-018-5771-7. arxiv: 1711.06631

155. L. Serkin. "Treatment of top-quark backgrounds in extreme phase spaces: the "top p_T reweighting" and novel data-driven estimations in ATLAS and CMS". In: *13th International Workshop on Top Quark Physics*. 2021.
arxiv: 2105.03977

156. E. Re. "Single-top Wt-channel production matched with parton showers using the POWHEG method". *Eur. Phys. J. C* 71, 2011.
doi: 10.1140/epjc/s10052-011-1547-z. arxiv: 1009.2450

157. S. Alioli et al. "NLO single-top production matched with shower in POWHEG: s- and t-channel contributions". *JHEP* 09, 2009.
doi: 10.1088/1126-6708/2009/09/111. arxiv: 0907.4076. Erratum: *JHEP* 02, 2010.
doi: 10.1007/JHEP02(2010)011

158. R. Frederix, E. Re, and P. Torrielli. "Single-top t-channel hadroproduction in the four-flavour scheme with POWHEG and aMC@NLO". *JHEP* 09, 2012.
doi: 10.1007/JHEP09(2012)130. arxiv: 1207.5391

159. S. Frixione et al. "Single-top hadroproduction in association with a W boson". *JHEP* 07, 2008.
doi: 10.1088/1126-6708/2008/07/029. arxiv: 0805.3067

160. J. Alwall et al. "The automated computation of tree-level and next-to-leading order differential cross sections, and their matching to parton shower simulations". *JHEP* 07, 2014.
doi: 10.1007/JHEP07(2014)079. arxiv: 1405.0301

161. ATLAS Collaboration. "Electron and photon performance measurements with the ATLAS detector using the 2015–2017 LHC proton–proton collision data". *JINST* 14, 2019.
doi: 10.1088/1748-0221/14/12/P12006. arxiv: 1908.00005

162. ATLAS Collaboration. "Muon reconstruction and identification efficiency in ATLAS using the full Run 2 pp collision data set at $\sqrt{s} = 13\,\text{TeV}$". *Eur. Phys. J. C* 81, 2020.
doi: 10.1140/epjc/s10052-021-09233-2. arxiv: 2012.00578

163. ATLAS Collaboration. "Jet reconstruction and performance using particle flow with the ATLAS Detector". *Eur. Phys. J. C* 77, 2017.
doi: 10.1140/epjc/s10052-017-5031-2. arxiv: 1703.10485

164. ATLAS Collaboration. "Performance of pile-up mitigation techniques for jets in pp collisions at $\sqrt{s} = 8\,\text{TeV}$ using the ATLAS detector". *Eur. Phys. J. C* 76, 2016.
doi: 10.1140/epjc/s10052-016-4395-z. arxiv: 1510.03823

165. ATLAS Collaboration. "ATLAS b-jet identification performance and efficiency measurement with $t\bar{t}$ events in pp collisions at $\sqrt{s} = 13\,\text{TeV}$". *Eur. Phys. J. C* 79, 2019.
doi: 10.1140/epjc/s10052-019-7450-8. arxiv: 1907.05120

166. ATLAS Collaboration. *Optimisation and performance studies of the ATLAS b-tagging algorithms for the 2017-18 LHC run.* 2017.
https://cds.cern.ch/record/2273281

167. D. Krohn, J. Thaler, and L.-T. Wang. "Jet Trimming". *JHEP* 02, 2010.
doi: 10.1007/JHEP02(2010)084. arxiv: 0912.1342

168. B. Nachman et al. "Jets from Jets: Re-clustering as a tool for large radius jet reconstruction and grooming at the LHC". *JHEP* 02, 2015.
doi: 10.1007/JHEP02(2015)075. arxiv: 1407.2922

169. ATLAS Collaboration. *Studies of $t\bar{t}/tW$ interference effects in $b\bar{b}\ell^{+}\ell^{-'}\nu\bar{\nu}'$ final states with Powheg and MG5_aMC@NLO setups*. Technical report. Geneva: CERN, 2021.
https://cds.cern.ch/record/2792254

170. ATLAS Collaboration. "Probing the Quantum Interference between Singly and Doubly Resonant Top-Quark Production in pp Collisions at $\sqrt{s} = 13\,\text{TeV}$ with the ATLAS Detector". *Phys. Rev. Lett.* 121, 2018.
doi: 10.1103/physrevlett.121.152002. arxiv: 1806.04667

171. ATLAS Collaboration. "Measurement of the $t\bar{t}$ production cross-section in the lepton+jets channel at $\sqrt{s} = 13\,\text{TeV}$ with the ATLAS experiment". *Phys. Lett. B* 810, 2020.
doi: 10.1016/j.physletb.2020.135797. arxiv: 2006.13076

172. ATLAS Collaboration. "Measurements of top-quark pair single- and double-differential cross-sections in the all-hadronic channel in pp collisions at $\sqrt{s} = 13\,\text{TeV}$ using the ATLAS detector". *JHEP* 01, 2021.
doi: 10.1007/JHEP01(2021)033. arxiv: 2006.09274

173. CMS Collaboration. "Measurement of the cross section for $t\bar{t}$ production with additional jets and b jets in pp collisions at $\sqrt{s} = 13\,\text{TeV}$". *JHEP* 07, 2020.
doi: 10.1007/JHEP07(2020)125. arxiv: 2003.06467

174. CMS Collaboration. "Measurement of differential cross sections for the production of top quark pairs and of additional jets in lepton+jets events from pp collisions at $\sqrt{s} = 13\,\text{TeV}$". *Phys. Rev. D* 97, 2018.
doi: 10.1103/PhysRevD.97.112003. arxiv: 1803.08856

175. CMS Collaboration. "Measurement of the top quark mass using proton–proton data at $\sqrt{s} = 7$ and $8\,\text{TeV}$". *Phys. Rev. D* 93, 2016.
doi: 10.1103/PhysRevD.93.072004. arxiv: 1509.04044

176. D0 Collaboration. "Precision Measurement of the Top Quark Mass in Lepton+Jets Final States". *Phys. Rev. Lett.* 113, 2014.
doi: 10.1103/PhysRevLett.113.032002

177. CDF Collaboration. "Top Quark Mass Measurement Using the Template Method in the Lepton + Jets Channel at CDF II". *Phys. Rev. D* 73, 2006.
doi: 10.1103/physrevd.73.032003

178. ATLAS Collaboration. "Measurement of the top quark mass with the template method in the $t\bar{t} \to$ lepton + jets channel using ATLAS data". *Eur. Phys. J. C* 72, 2012.
doi: 10.1140/epjc/s10052-012-2046-6. arxiv: 1203.5755

179. ATLAS Collaboration. "Measurement of the top quark mass in the $t\bar{t} \to$ lepton+jets and $t\bar{t} \to$ dilepton channels using $\sqrt{s} = 7\,\text{TeV}$ ATLAS data". *Eur. Phys. J. C* 75, 2015.
doi: 10.1140/epjc/s10052-015-3544-0. arxiv: 1503.05427

180. CMS Collaboration. "Measurement of the top-quark mass in $t\bar{t}$ events with lepton+jets final states in pp collisions at $\sqrt{s} = 7\,\text{TeV}$". *JHEP* 12, 2012.
doi: 10.1007/JHEP12(2012)105. arxiv: 1209.2319

181. CMS Collaboration. "Measurement of the top quark mass with lepton+jets final states using pp collisions at $\sqrt{s} = 13\,\text{TeV}$". *Eur. Phys. J. C* 78, 2018.
doi: 10.1140/epjc/s10052-018-6332-9. arxiv: 1805.01428

182. G. D'Agostini. "A multidimensional unfolding method based on Bayes' theorem". *Nucl. Instrum. Meth. A* 362, 1995.
doi: 10.1016/0168-9002(95)00274-X

183. T. Adye. "Unfolding algorithms and tests using RooUnfold". In: *Proceedings, 2011 Workshop on Statistical issues Related to Discovery Claims in Search Experiments and Unfolding (PHYSTAT 2011)* (CERN, Geneva, Switzerland, Jan. 17–20, 2011).
doi: 10.5170/CERN-2011-006.313. arxiv: 1105.1160

184. S. Schmitt. "Data Unfolding Methods in High Energy Physics". *EPJ Web Conf.* 137, 2017. Ed. by Y. Foka, N. Brambilla, and V. Kovalenko.
doi: 10.1051/epjconf/201713711008. arxiv: 1611.01927

185. M. Czakon et al. "Pinning down the large-x gluon with NNLO top-quark pair differential distributions". *JHEP* 04, 2017.
doi: 10.1007/JHEP04(2017)044. arxiv: 1611.08609

186. ATLAS Collaboration. "Muon reconstruction performance of the ATLAS detector in proton–proton collision data at $\sqrt{s} = 13\,\text{TeV}$". *Eur. Phys. J. C* 76, 2016.
doi: 10.1140/epjc/s10052-016-4120-y. arxiv: 1603.05598

187. ATLAS Collaboration. "Jet energy scale and resolution measured in proton–proton collisions at $\sqrt{s} = 13\,\text{TeV}$ with the ATLAS detector". *Eur. Phys. J. C* 81, 2020.
doi: 10.1140/epjc/s10052-021-09402-3. arxiv: 2007.02645

188. ATLAS Collaboration. "Measurements of top-quark pair differential cross-sections in the lepton+jets channel in pp collisions at $\sqrt{s} = 13\,\text{TeV}$ using the ATLAS detector". *JHEP* 11, 2017.
doi: 10.1007/JHEP11(2017)191. arxiv: 1708.00727

189. C. Degrande et al. "Automated one-loop computations in the standard model effective field theory". *Phys. Rev. D* 103, 2021.
doi: 10.1103/PhysRevD.103.096024. arxiv: 2008.11743

190. I. Brivio, Y. Jiang, and M. Trott. "The SMEFTsim package, theory and tools". *JHEP* 12, 2017.
doi: 10.1007/jhep12(2017)070. arxiv: 1709.06492

191. I. Brivio et al. *Electroweak input parameters*. Geneva, 2021.
arxiv: 2111.12515.
https://cds.cern.ch/record/2792440

192. CMS Collaboration. "Measurement of the production cross section for single top quarks in association with W bosons in proton–proton collisions at $\sqrt{s} = 13\,\text{TeV}$". *JHEP* 10, 2018.
doi: 10.1007/JHEP10(2018)117. arxiv: 1805.07399

193. ATLAS Collaboration. "Measurement of the cross-section for producing a W boson in association with a single top quark in pp collisions at $\sqrt{s} = 13\,\text{TeV}$ with ATLAS". *JHEP* 01, 2018.
doi: 10.1007/JHEP01(2018)063. arxiv: 1612.07231

194. D. Buarque Franzosi and C. Zhang. "Probing the top-quark chromomagnetic dipole moment at next-to-leading order in QCD". *Phys. Rev. D* 91, 2015.
doi: 10.1103/PhysRevD.91.114010. arxiv: 1503.08841

195. ATLAS Collaboration. *Top EFT summary plots March 2022*. Geneva, 2022.
http://cds.cern.ch/record/2805987.
Note: All figures including auxiliary figures are available at https://atlas.web.cern.ch/Atlas/GROUPS/PHYSICS/PUBNOTES/ATL-PHYS-PUB-2022-014

196. CMS Collaboration. "Measurement of the top quark polarization and $t\bar{t}$ spin correlations using dilepton final states in proton–proton collisions at $\sqrt{s} = 13\,\text{TeV}$". *Phys. Rev. D* 100, 2019.
doi: 10.1103/PhysRevD.100.072002. arxiv: 1907.03729

Appendix

1 Differential Measurements

Additionally to the unfolded differential measurements shown in Section 8.3, several other observables are measured using the described data. These additional distributions are shown in figures 1 and 2.

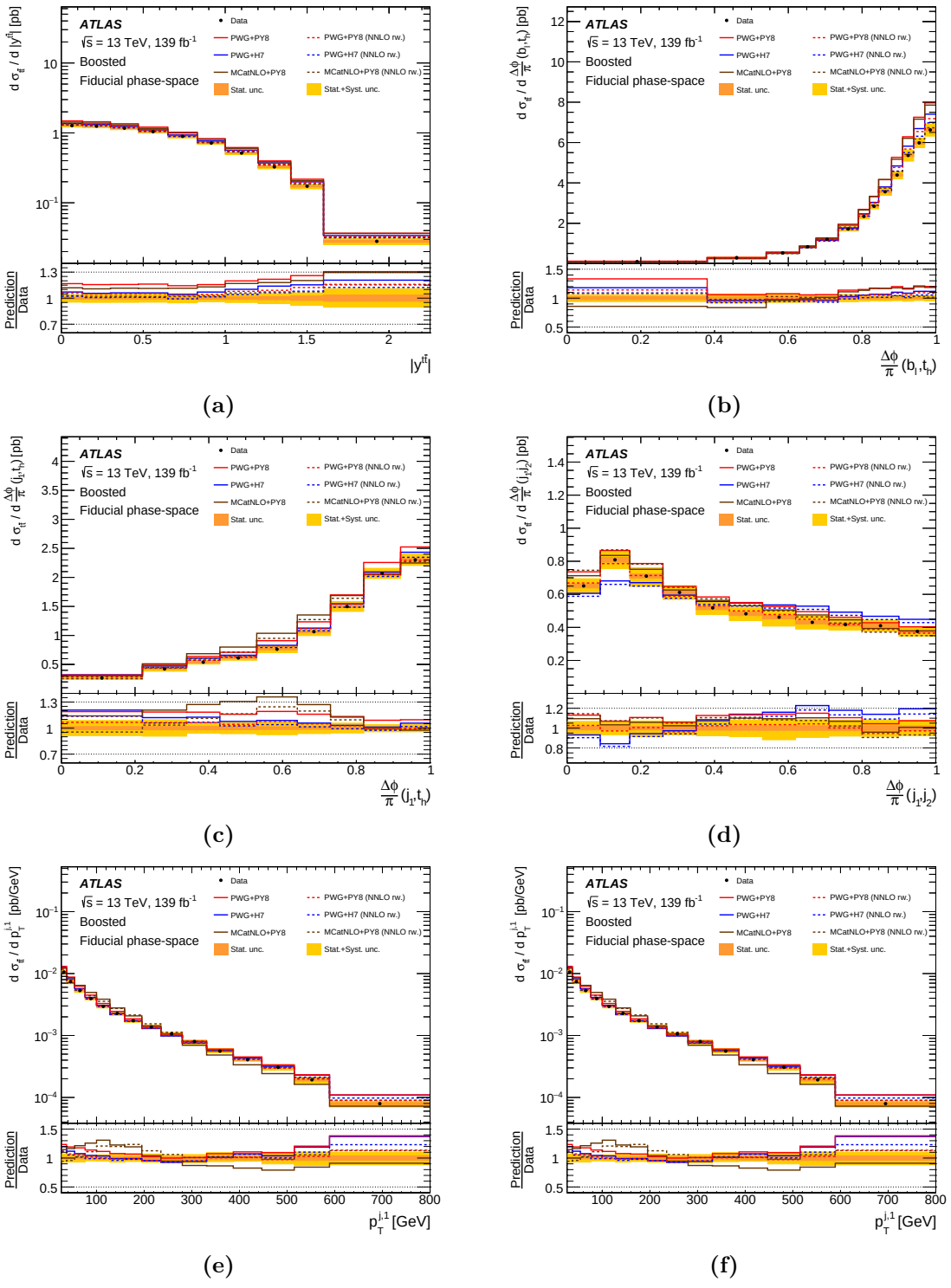

Figure 1: Differential distributions of the observed data for several observables are compared to several predictions. The measured distributions are unfolded to particle-level. The solid colored histograms show the various models used for the predictions, while the dashed lines show the latter reweighted to NNLO.

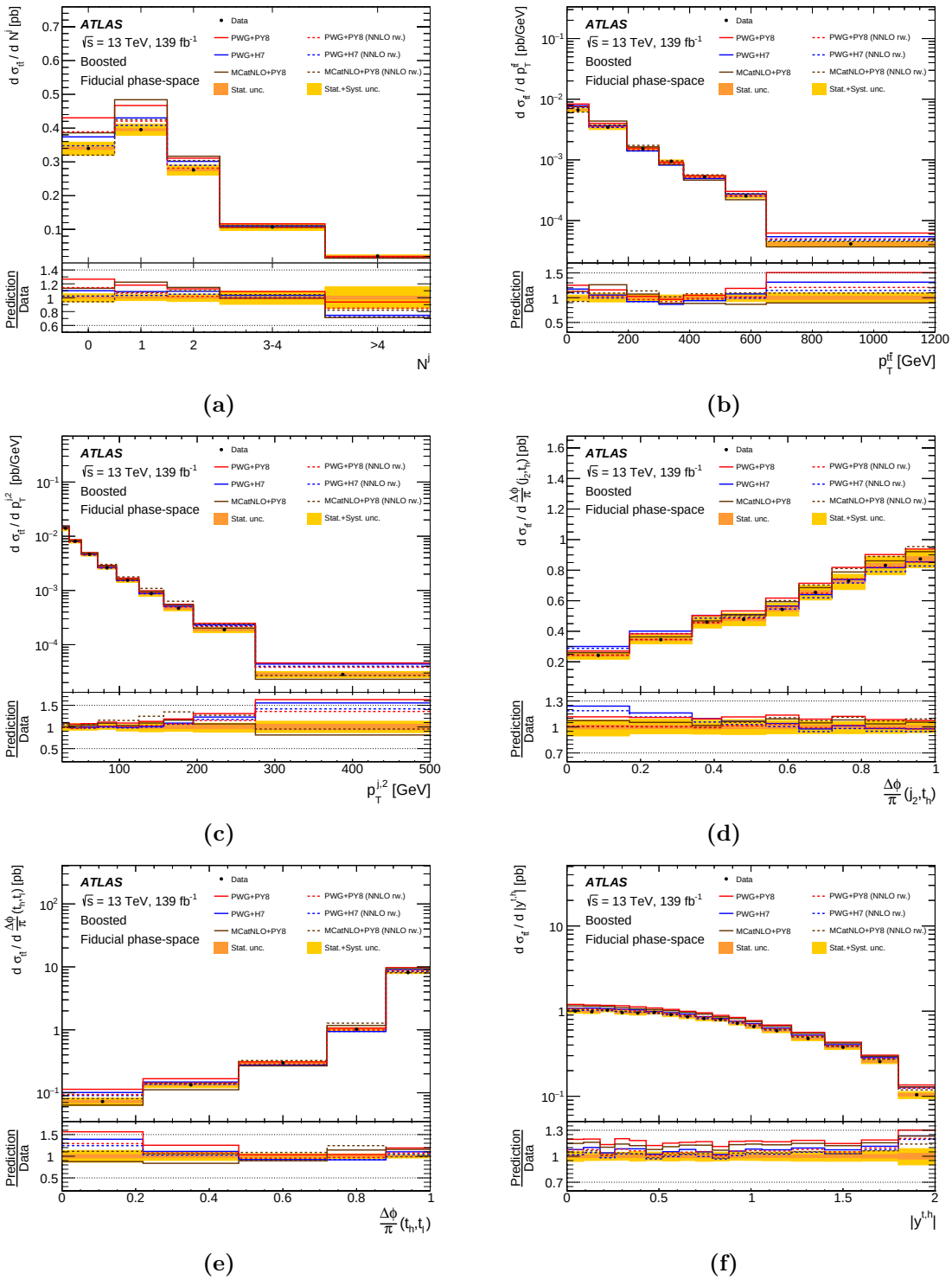

Figure 2: Differential distributions of the observed data for several observables are compared to several predictions. The measured distributions are unfolded to particle-level. The solid colored histograms show the various models used for the predictions, while the dashed lines show the latter reweighted to NNLO.

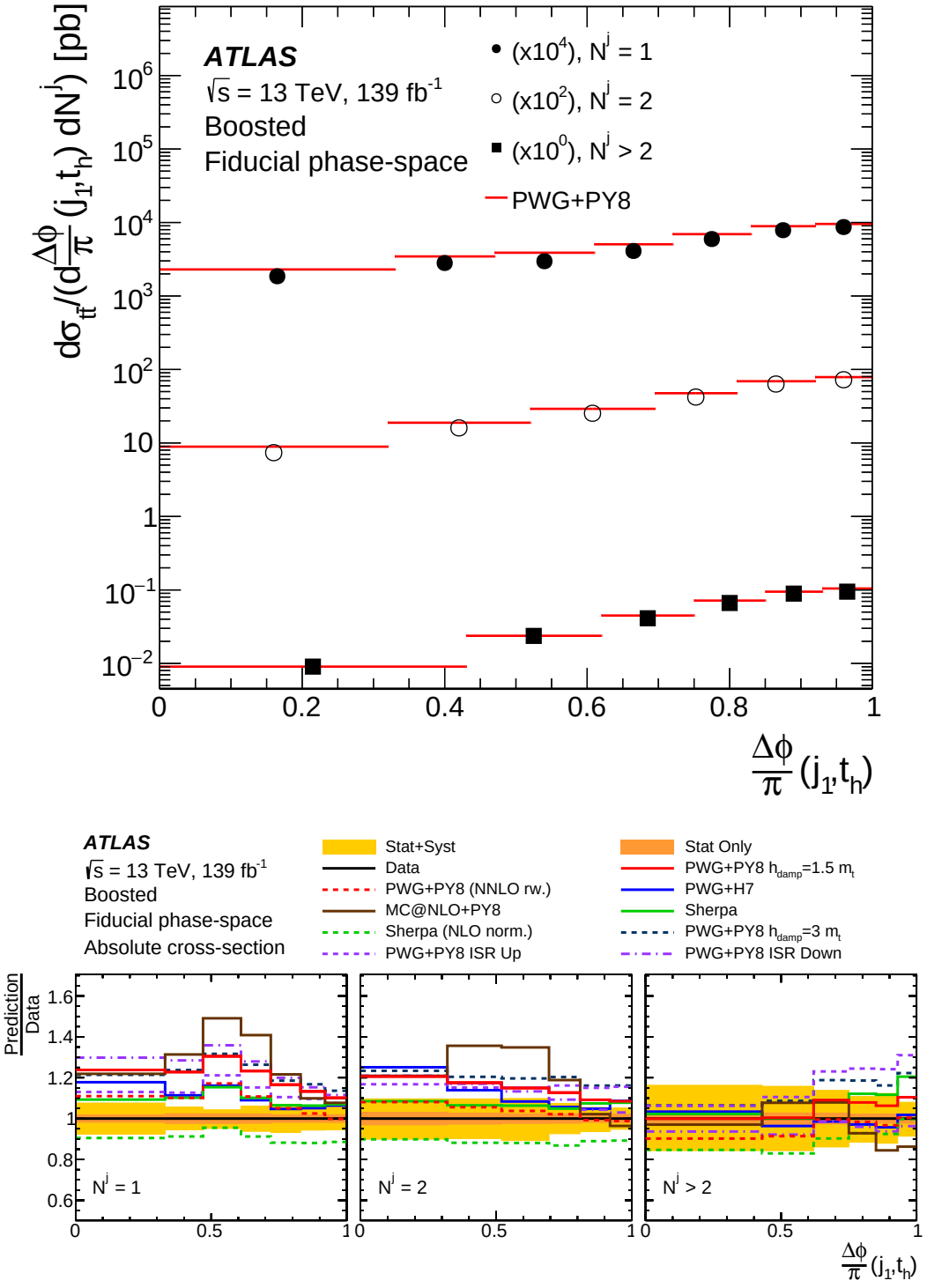

Figure 3: Two-dimensional differential cross-section of the prodcution of $t\bar{t}$ as function of the number of additional jets N^j and the angle $\Delta\phi(j, t_h)$ between the hadronic top quark and the leading additional jet. The top figure shows the rates scaled for the different bins in N^j, while the bottom panels show the ratio of the data to various predictions as well as th euncertainties of this measurement.

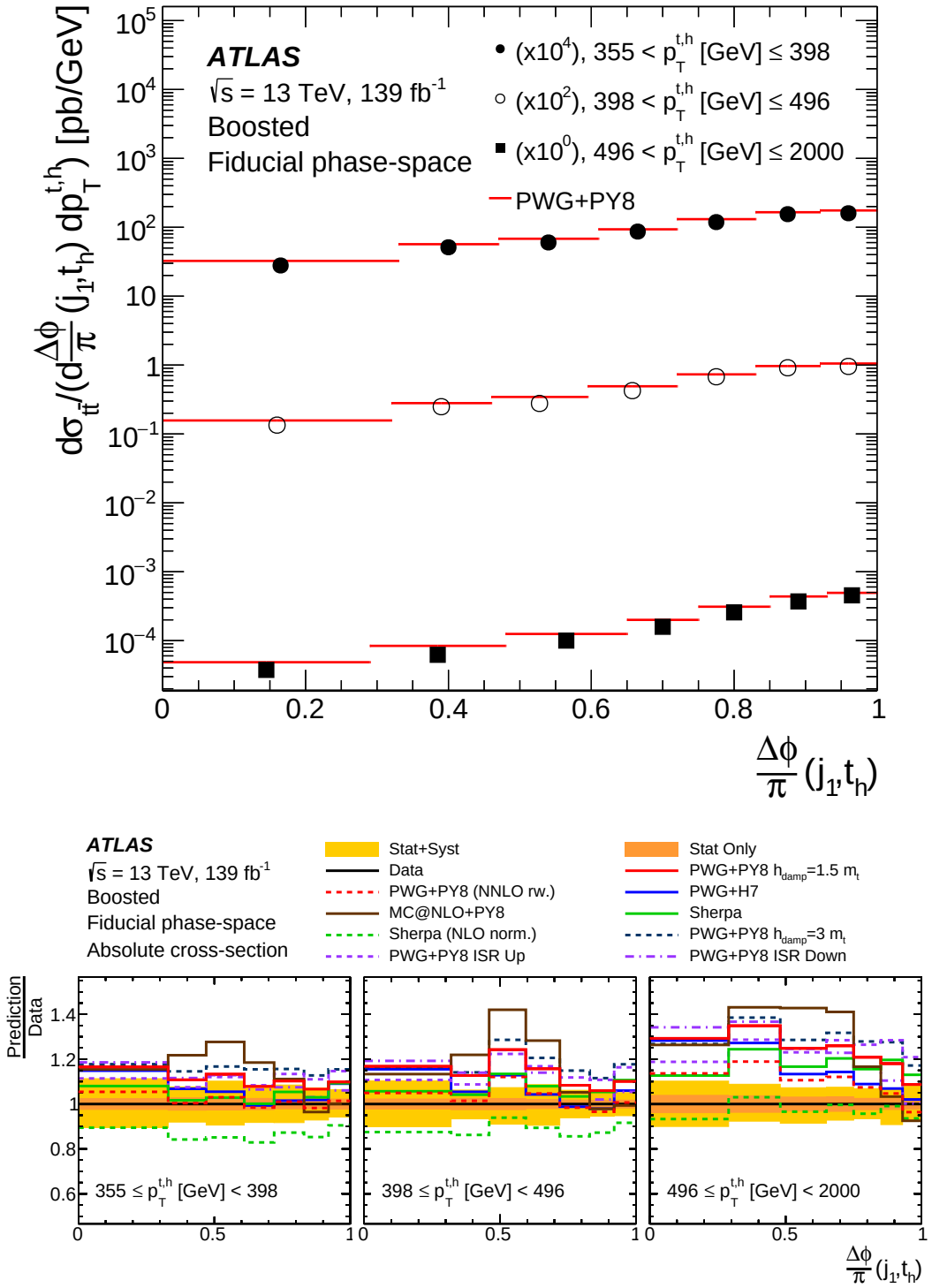

Figure 4: Two-dimensional differential cross-section of the prodcution of $t\bar{t}$ as function of the transverse momentum of the hadronic top-quark jet $p_{\mathrm{T}}^{t,h}$ and the angle $\Delta\phi(j, t_h)$ between the hadronic top quark and the leading additional jet. The top figure shows the rates scaled for the different bins in $p_{\mathrm{T}}^{t,h}$, while the bottom panels show the ratio of the data to various predictions as well as th euncertainties of this measurement.

1.1 Uncertainty Breakdown for Differential Measurements

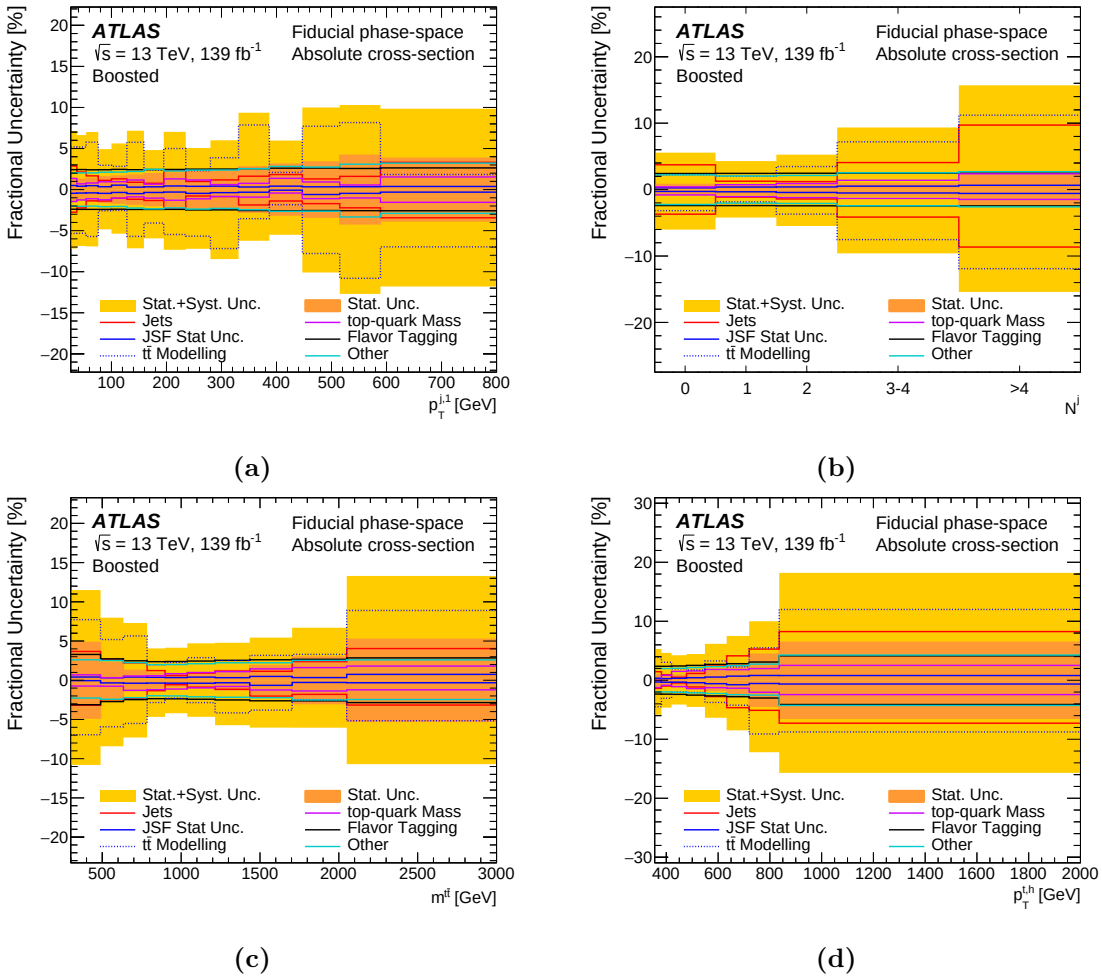

Figure 5: Fractional uncertainty breakdowns for the differential distributions of the observed data for several observables.

2 Validity of EFT in Unfolding

In order to investigate the effects of the unfolding on the EFT interpretation an additional injection test is performed. For this test pseudo data is used in a similar set-up as the one used to derive the expected limits on the two Wilson coefficients (Section 10). In order to quantify the effects of the unfolding, the limits are derived for two cases: using the dedicated simulated particle-level distribution of the $p_{\mathrm{T}}^{t,h}$ as pseudo-data input and secondly using the particle-level distribution derived from the nominal unfolding procedure. Since the simulated particle-level distribution is the target distribution of the unfolding, the difference shows potential effects of the unfolding. Propagating these changes to the EFT limits directly tests for potential biases. This section shows the effects of the

unfolding in the quadratic EFT setup ($\mathcal{O}(\Lambda^{-4})$) in more detail. For this model a separate statistically independent MC sample is used.
Figure 6 shows comparisons of the unfolded $p_{\mathrm{T}}^{t,h}$ MC distribution to its particle-level truth. The top figure shows the $p_{\mathrm{T}}^{t,h}$ distribution for the independent injection sample with $(C_{tG}, C_{tq}^{(8)}) = (0.2, 0.2)$ at the particle-level truth in blue and the unfolded sample in red. The comparison shows slight fluctuations of the unfolded distribution when compared to its particle-level truth at the order of 5 %. The impact of this on the EFT parametrisation can directly be seen on the bottom of Figure 6. It shows the particle-level truth as well as the unfolded sample compared to the prediction of the EFT model at $(C_{tG}, C_{tq}^{(8)}) = (0.2, 0.2)$. The blue ratio histogram shows the comparison of the injection sample to the expected distribution from the EFT parametrisation derived from the EFT MC as described in Section 10.3. It shows very small deviations of this sample to the EFT model. These are bigger for the unfolded sample, but match the differences seen between particle-level truth and the unfolded distribution.
In order to resolve these effects in terms of the single bins contributing a test using a similar setup is performed: the unfolded injection sample is used as pseudo data input to the EFT interpretation with uncertainties at the level of the statistical uncertainty in the data. Figure 7 shows the resulting limits and posteriors for this setup. This test shows, that limits from the unfolded distribution in the case of statistical uncertainties only, recover the true value of $(C_{tG}, C_{tq}^{(8)}) = (0.2, 0.2)$ within the resulting 95 % limits. However, they favour the second solution for the global mode. Within this setup using the data statistical uncertainty only and the statistically independent injection sample which is also only generated at data stat. precision the fit recovering the true value is considered to be the expected closure.
A very similar test is done using the same setup, but excluding each of the 8 bins one at a time. The resulting marginalized posteriors are shown in Figures 8- 10. Posteriors that recover the true EFT setup very well while excluding a certain bin suggest a particularly deviating effect of that particular bin. Following this intuition, bins 1 and 7-8 dominate the shift of the posterior toward the second more negative solution in the posterior.

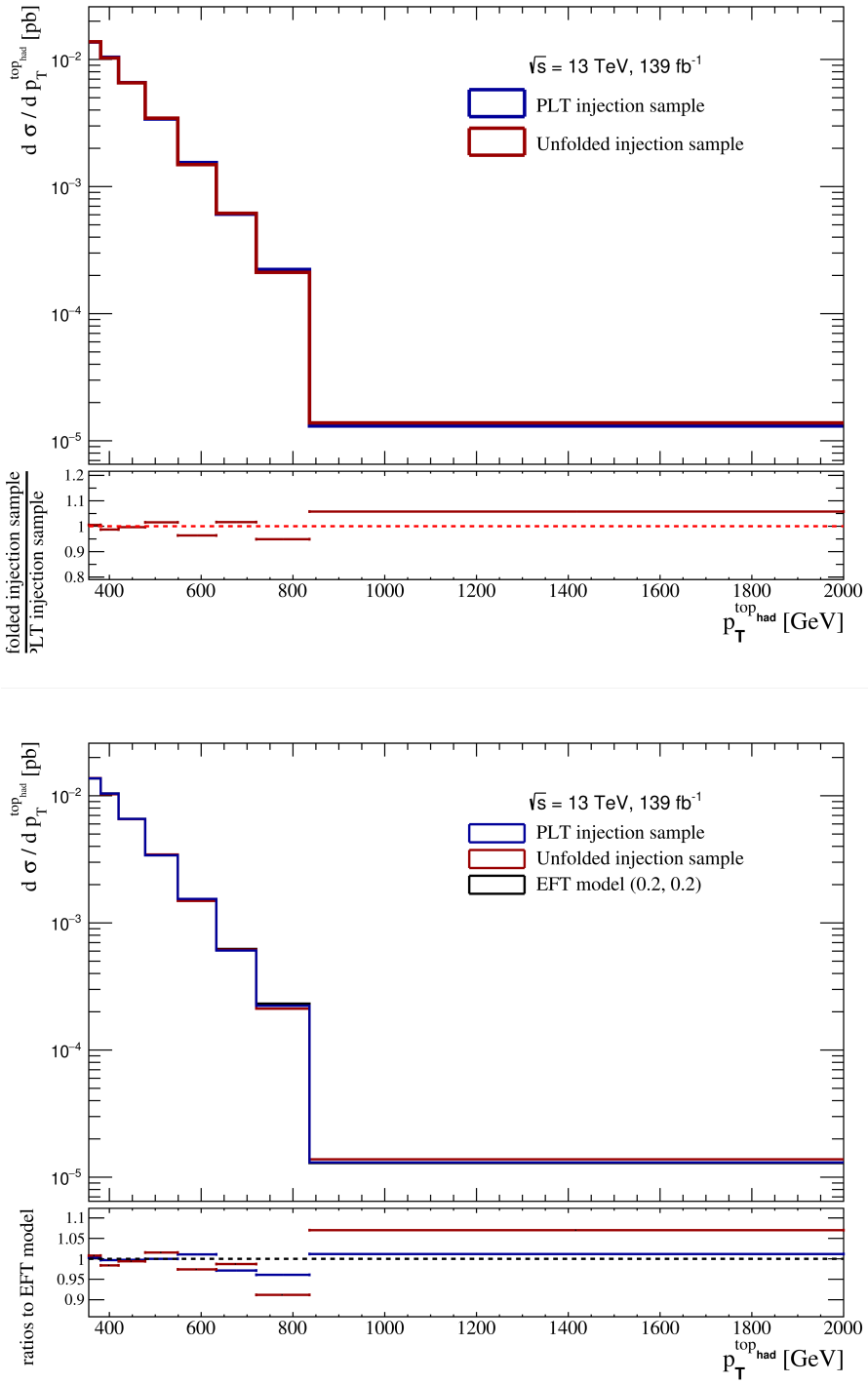

Figure 6: Comparison of the EFT injected MC distributions of the $p_{\mathrm{T}}^{t,h}$. The top figure shows the generated particle-truth distribution in blue and the unfolded distribution using the nominal unfolding as described in Section 7.2 in red. The bottom figure additionally shows the distribution generated by the EFT model as described in Section 10.3 in black and the ratio of the other two distributions to this model distribution.

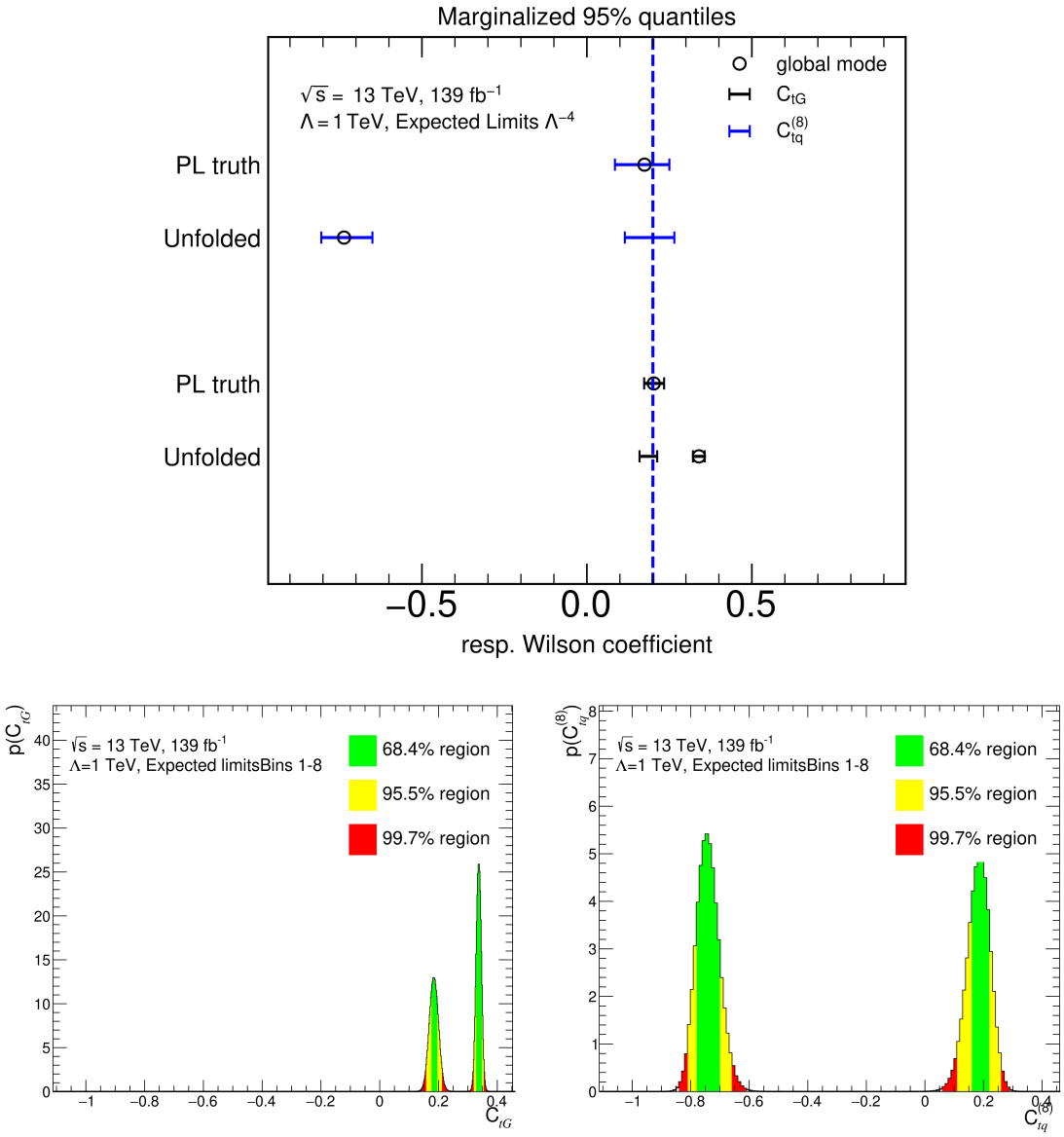

Figure 7: Resulting EFT limits for the statistically independent EFT injection sample using data statistical uncertainties for the particle-level truth and unfolded distribution of the $p_{\mathrm{T}}^{t,h}$(top) as well as the resulting marginalized posteriors for the two Wilson coefficients (bottom figures).

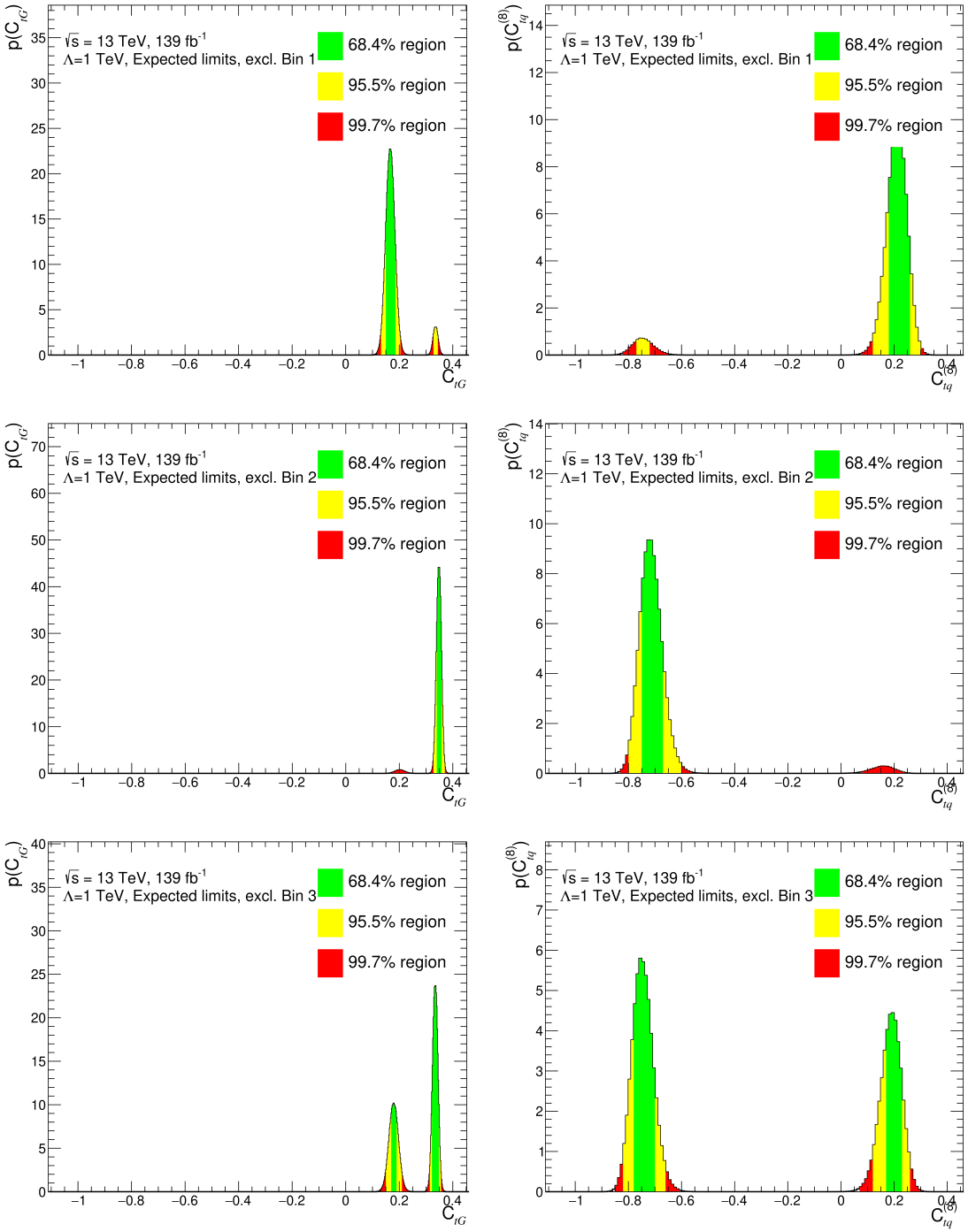

Figure 8: Marginalized posterior distributions of the two Wilson coefficients for the EFT injected pseudo data from the $p_{\mathrm{T}}^{t,h}$ distribution when excluding each of the 8 bins one at a time.

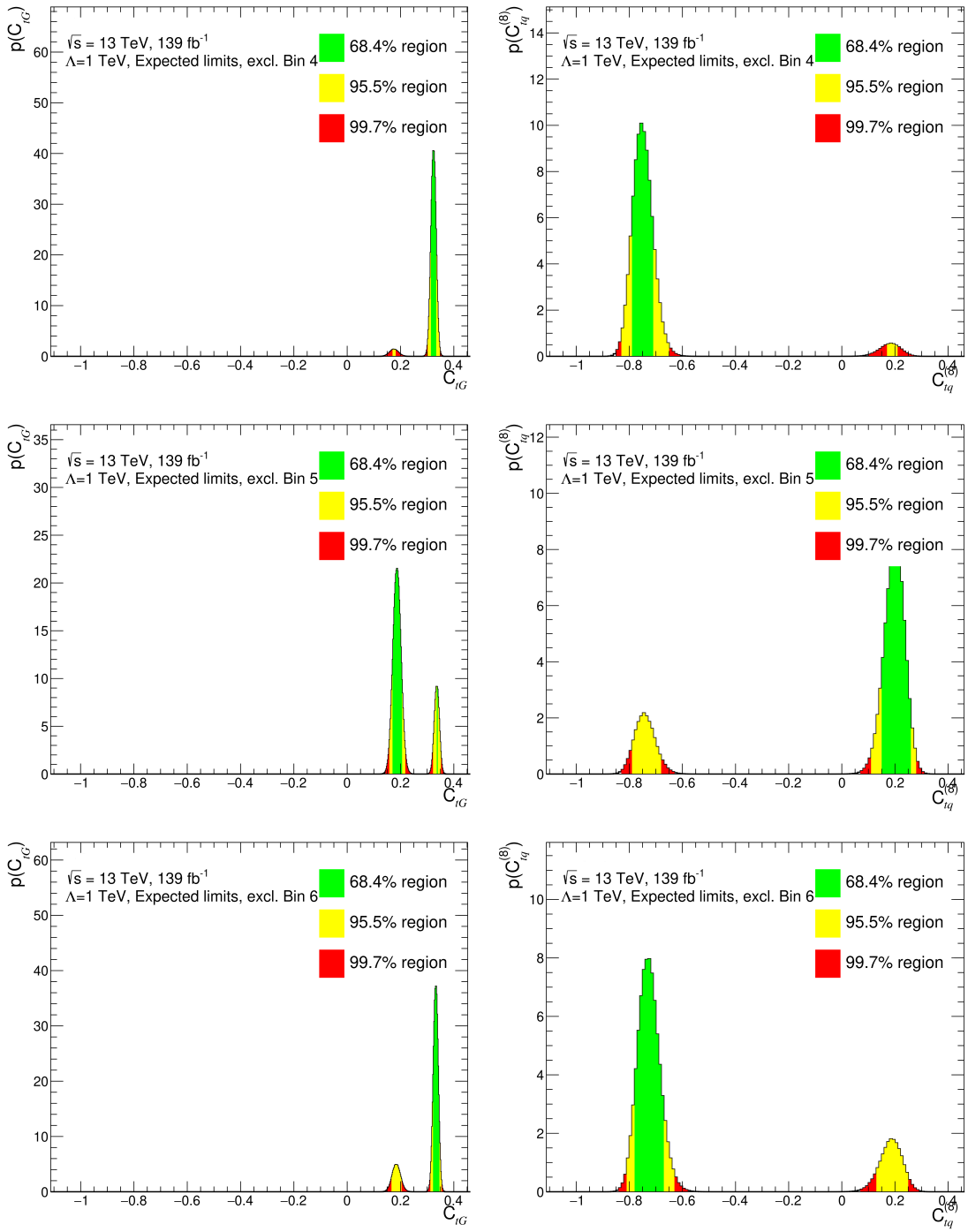

Figure 9: Marginalized posterior distributions of the two Wilson coefficients for the EFT injected pseudo data from the $p_{\mathrm{T}}^{t,h}$ distribution when excluding each of the 8 bins one at a time.

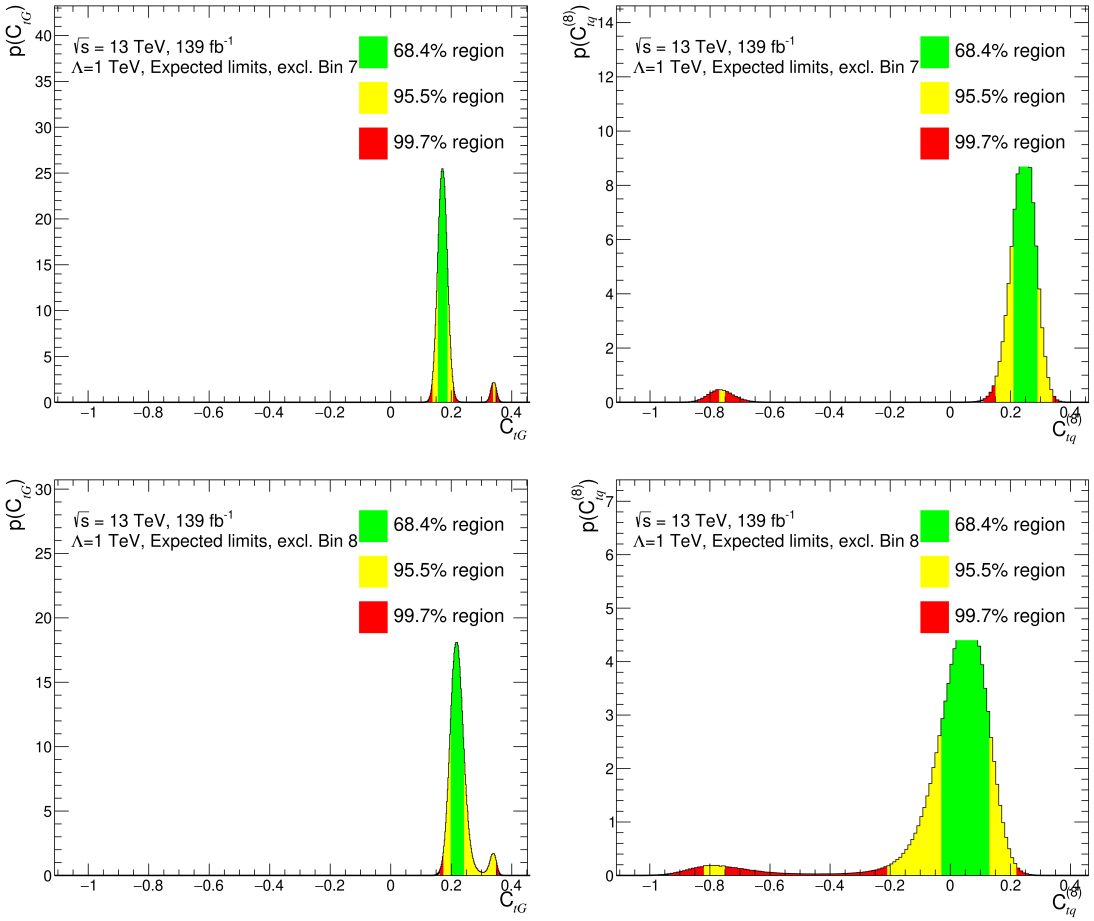

Figure 10: Marginalized posterior distributions of the two Wilson coefficients for the EFT injected pseudo data from the $p_{\mathrm{T}}^{t,h}$ distribution when excluding each of the 8 bins one at a time.

3 Validation of Unfolding

Any unfolding technique can introduce biases on the measured cross-section. In the IBU method the bias can origintae from the regularization and from the choice of the model used to derive the corrections applied to the data. The bias due to the choice of the model is evaluated applying the unfolding procedure to an alternative $t\bar{t}$ prediction used as pseudo-data, while keeping the nominal corrections derived with PWG+PY8. The unfolded result is compared with the alternative particle-level prediction and any deviation in the agreement between the two is considered as non-closure and taken as uncertainty, referred to as modelling uncertainty.
The second source of bias originates from the usage of a regularized unfolding technique. To test for the absence of this bias, a stress test is performed where the particle and detector level PWG+PY8 samples are re-weighted using a function $f(x)$, where x represents a particle-level observable, such as $m^{t\bar{t}}$ or $p_{\mathrm{T}}^{t,h}$ The events passing only the detector-level selection and not the particle level selection are not considered in this study. The re-weighted detector-level distributions are used as pseudo-data and unfolded using the nominal unfolding corrections. The result of the unfolding is compared with the re-weighted particle level distribution. Any difference between the re-weighted particle level spectrum and the unfolded pseudo-data is considered a bias. Several re-weighting functions $f(x)$ are employed, where all are derived starting from the difference between the data and the predictions observed on some observables. The re-weighting functions are shown in Figure 11, here the disagreement between the data and the predictions is modeled with a polinomial function for $\Delta\phi(t,\bar{t})$ and the number of additional jets, while with a linear function in the case of the hadronic top p_{T}. In the latter case the slope of the line is also increased by a factor 1.5 and 2.
The results of the stress test are shown in Figure 12 for the $p_{\mathrm{T}}^{t,h}$ spectrum. The uncertainty shown on the ratio between the unfolded re-weighted distribution and the re-weighted particle-level spectrum reflects the statistical uncertainty by the expected number of $t\bar{t}$ events at detector-level. The uncertainty is evaluated using 1000 pseudo-experiments, obtained by smearing the distributions according to a Poisson distribution. As shown in Figure 12, very good closure is observed in all bins of the distribution.

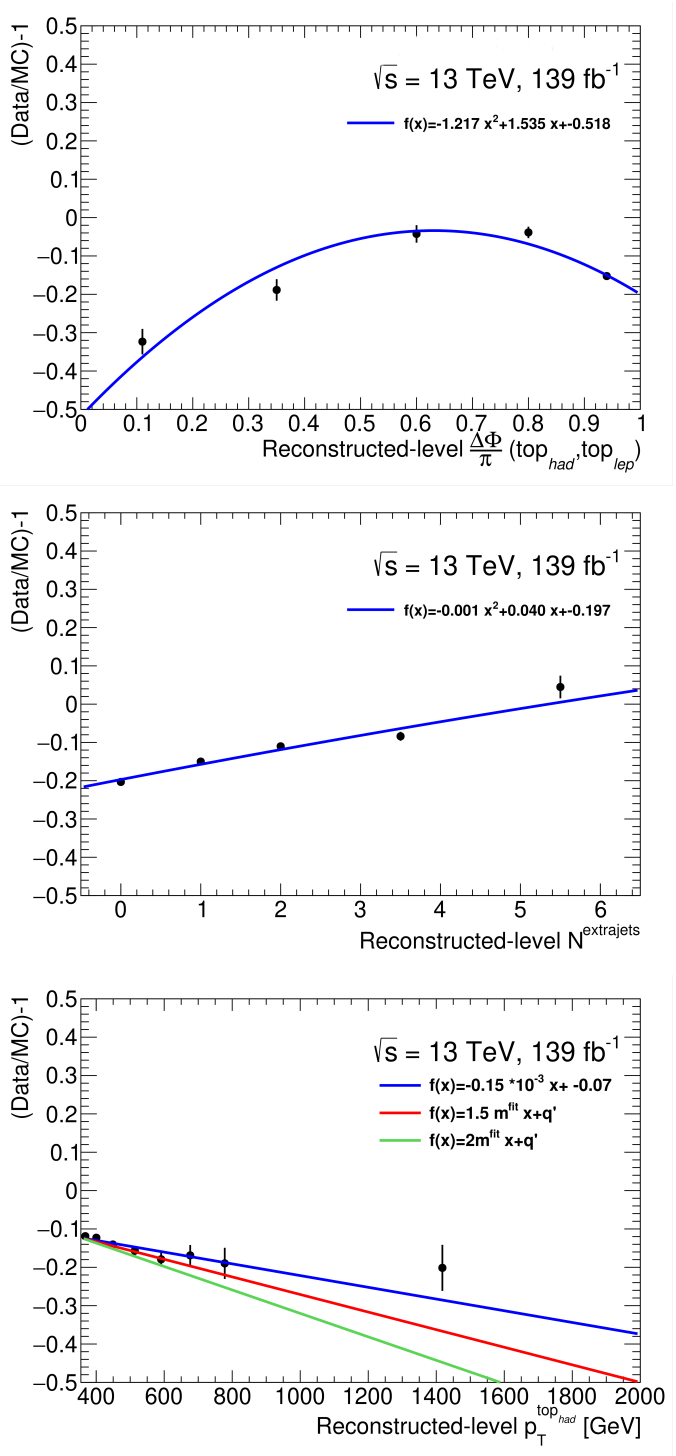

Figure 11: Functions used to re-weight the nominal for the stress-tests, obtained from a fit to the (Data/MC-1) agreement on the detector level distribuions of the $\Delta\phi(t,\bar{t})$, the number of additional jets and the hadronic top p_{T}. In the latter case the fit function is a line and additional functions with the slope increased by a factor 1.5 and 2 are also shown.

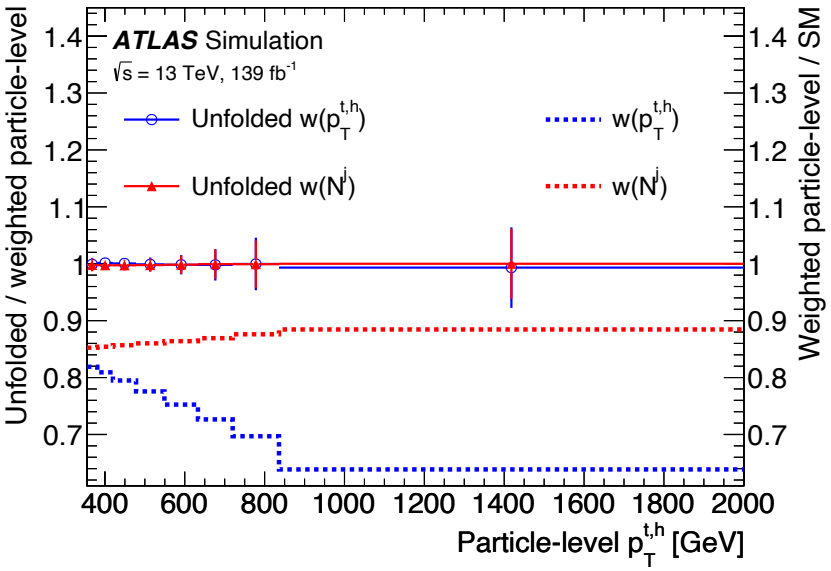

Figure 12: Particle level distributions of the $t\bar{t}$ production cross-section as a function of the transverse momentum of the hadronically decaying top quark $p_{\mathrm{T}}^{t,h}$. The continuous and dashed lines are ratios, where the denominator is the re-weighted PWG+PY8 particle-level distribution. The numerators of the ratios shown as continuous line are the unfolded re-weighted distributions, while for the dotted lines the numerators are the nominal PWG+PY8 predictions. The dotted lines show the function used for the re-weighting while the continuous line should be compatible with unity to consider the test as passed. The uncertainty on the continuous lines is the statistical uncertainty on the re-weighted pseudo-data.

4 Calculation of the Neutrino Four Momentum

The x and y components of the neutrino momentum can be inferred from the $E_{\mathrm{T}}^{\mathrm{miss}}$. The z component, however, is not directly measured. It is, therefore, estimated by assuming that the lepton-neutrino system has invariant mass equal to the W boson mass and solving for p_z. The final result of this is a quadratic formula for the missing neutrino z-momentum:

$$p_{z,\nu} = \frac{-b \pm \sqrt{b^2 - 4ac}}{2a}\,. \tag{1}$$

Where:

$$\begin{aligned} a =& E_\ell^2 - p_{z,\ell}^2 & b =& -2kp_{z,\ell} \\ c =& E_\ell^2 p_{T,\nu}^2 - k^2 & k =& \frac{m_w^2 - m_\ell^2}{2} + p_{x,\ell}p_{x,\nu} + p_{y,\ell}p_{y,\nu} \end{aligned}$$

Here, E_ℓ represents the energy of the lepton, $p_{x,\ell}$ and $p_{x,\nu}$ the x-component of the lepton and neutrino 3-momenta respectively, $p_{T,\nu}$ the component of the neutrino momentum transverse to the beam-line and m_W, m_ℓ the rest mass of the W boson and lepton respectively. If the solution given by equation 1 is complex the imaginary part is dropped and only the real part is used. In the case of two real solutions, the one resulting in the smallest invariant mass of the $lb\nu$ system is selected.

5 Choice of Points for the EFT Parametrization

The EFT model functions for every measurement (in this case each bin of the differential distributions) are determined by fitting the above described model (shown in Eq. (9.3)) to the grid of EFT MC samples. In order to test the stability of this fit to the choice of EFT sampling, i.e. the number of sampling points (9 in this analysis) and their positions, the fit is performed for different setups. In Figures 13 and 14 the 1D-projections of the fit results for all possibilities of removing one of the samples from the fit are shown in relation to using all samples ("complete fit"). To highlight the relative change of the particular exclusion, the deviation of the reduced model function (excluding the labelled EFT MC sample from the fit) for the bins of the $p_{\mathrm{T}}^{t,h}$ spectrum are shown, relative to including all samples. The black points represent the relative deviation of the MC data points to the complete fit. In this test the more complex full quadratic EFT model is used.
To get a better sense for the size of these effects around the expected region of the sensitivity of this analysis, a zoom of the region within the expected Asimov 90 % limits is shown in the small subplots. As expected the effects of reducing the number of EFT samples shows the strongest impacts on the fit result in the last bins of the $p_{\mathrm{T}}^{t,h}$ spectrum, which show the largest statistical uncertainties. Therefore the remaining EFT samples might lack the ability to catch the loss in constraining power by removing one sample. However, when looking at the region of intereset around the expected limits, the effects in all bins do not exceed 1 %. Therefore, the choice of sampling points in the EFT parameter space, does not impact the resulting modeling of the EFT effects.

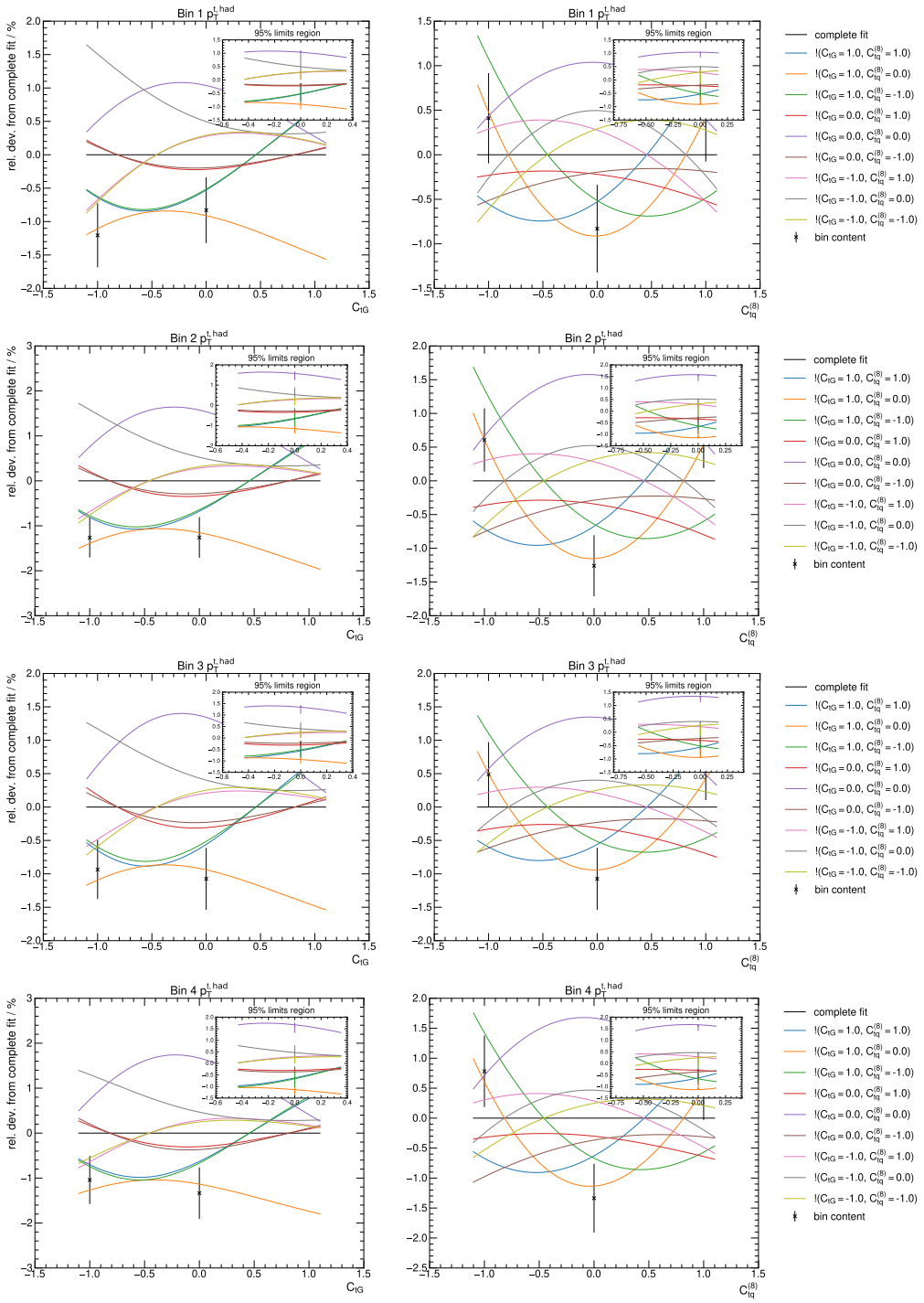

Figure 13: Deviations of the 1D-projections of the fit model function for the bins of the $p_T^{t,\mathrm{had}}$ spectrum when excluding the labelled EFT MC sample from the fit, relative to including all samples. The black points represent the relative deviation of the MC data points to the complete fit. A zoom of the region of the expected Asimov 90 % limits is shown in the small subplots.

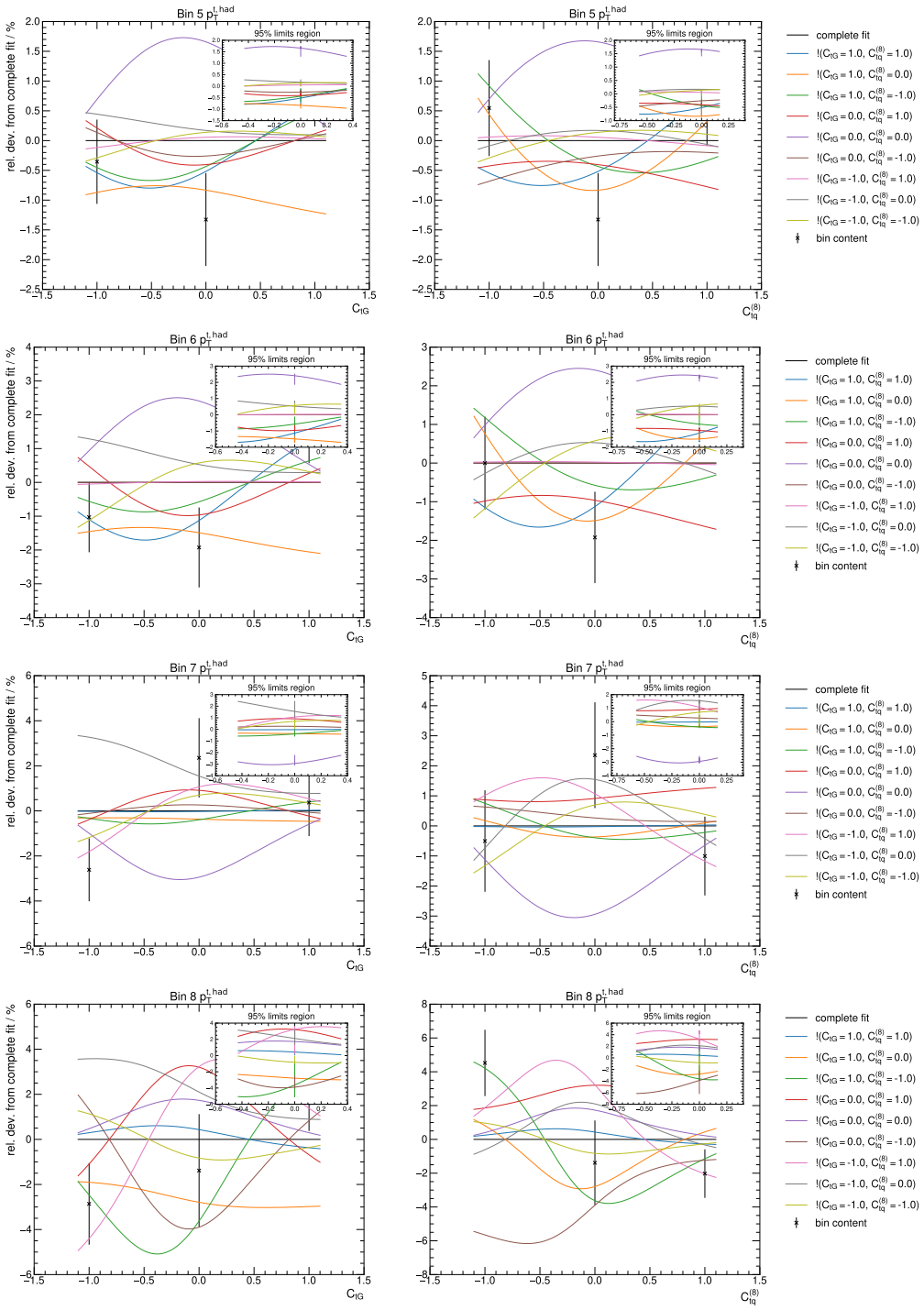

Figure 14: Deviations of the 1D-projections of the fit model function for the bins of the $p_T^{t,\mathrm{had}}$ spectrum when excluding the labelled EFT MC sample from the fit, relative to including all samples. The black points represent the relative deviation of the MC data points to the complete fit. A zoom of the region of the expected Asimov 90 % limits is shown in the small subplots.

6 Effects of the EFT Operators on the $p_T^{t,h}$ Spectrum

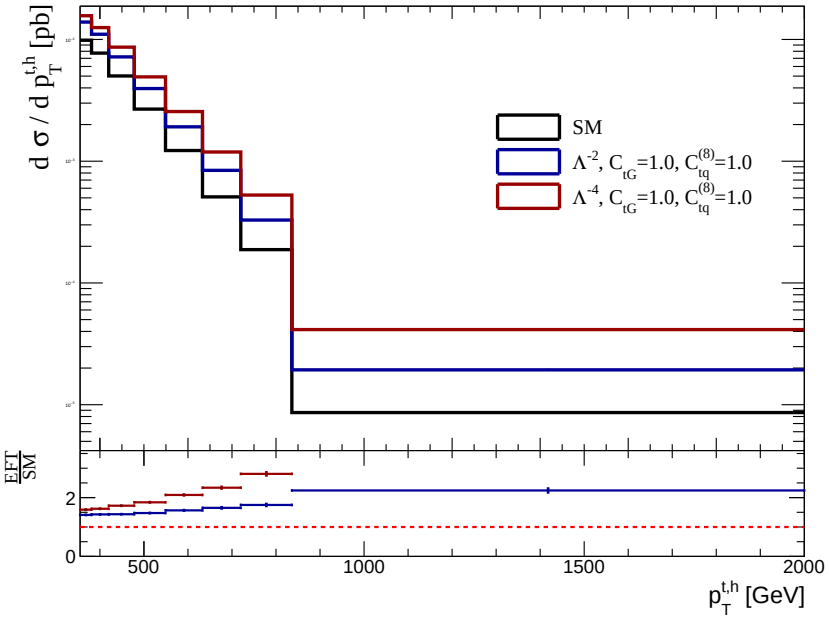

Figure 15: Differential distribution of the LO EFT prediction of the $p_{\mathrm{T}}^{t,h}$ spectrum. The SM is shown in black and the EFT prediction is shon in blue for the linear and red for the quadratic EFT model. The values of the Wilson coefficients are given in the legend.

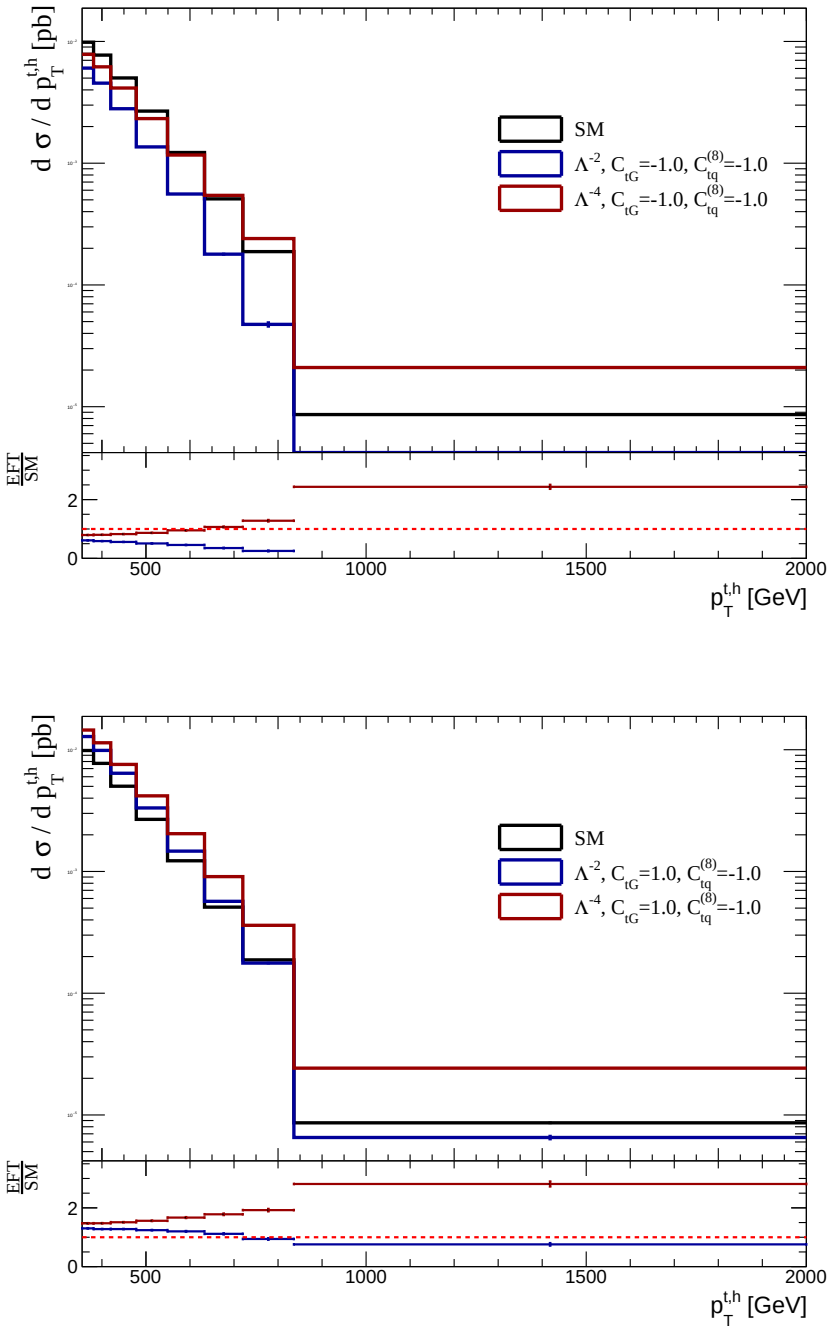

Figure 16: Differential distribution of the LO EFT prediction of the $p_{\mathrm{T}}^{t,h}$ spectrum. The SM is shown in black and the EFT prediction is shon in blue for the linear and red for the quadratic EFT model. The values of the Wilson coefficients are given in the legend.

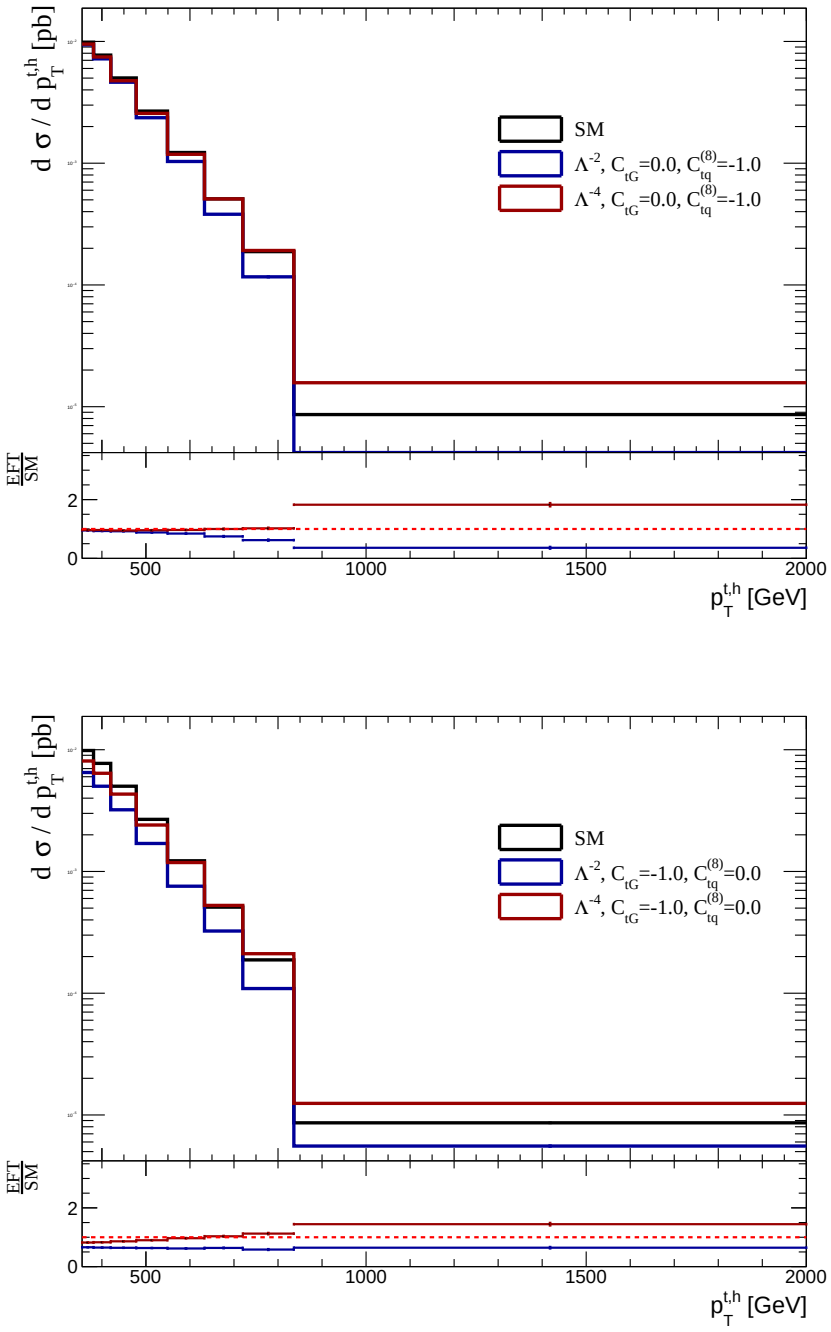

Figure 17: Differential distribution of the LO EFT prediction of the $p_{\mathrm{T}}^{t,h}$ spectrum. The SM is shown in black and the EFT prediction is shon in blue for the linear and red for the quadratic EFT model. The values of the Wilson coefficients are given in the legend.

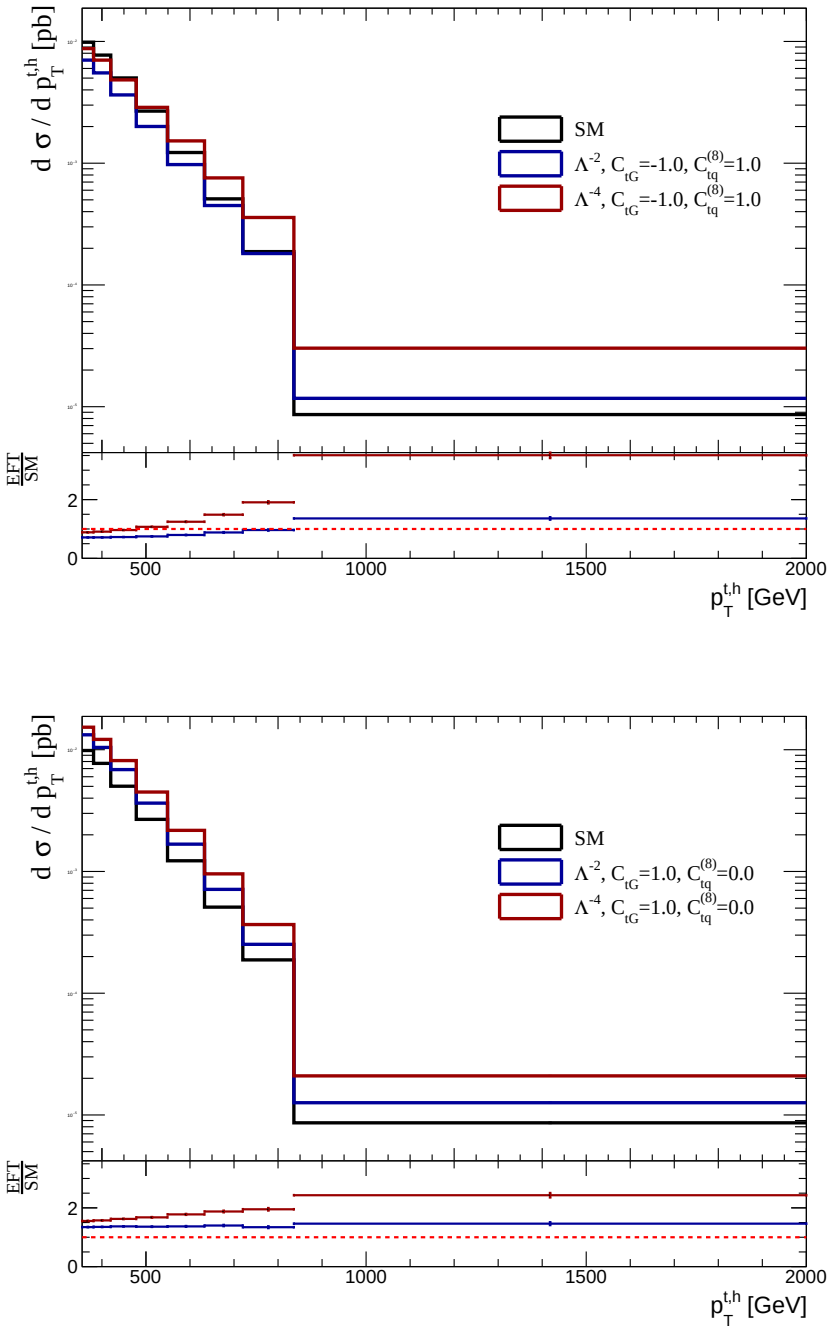

Figure 18: Differential distribution of the LO EFT prediction of the $p_{\mathrm{T}}^{t,h}$ spectrum. The SM is shown in black and the EFT prediction is shon in blue for the linear and red for the quadratic EFT model. The values of the Wilson coefficients are given in the legend.

7 Bin-Wise Evolution of the Observed Posterior

Figures 19, 20 and 21 show the two-dimensional posterior distributions on the right when using the set of bins of the $p_{\mathrm{T}}^{t,h}$ distribution indicated by the respective histograms on the left. Starting from no input at the top of Figure 19, the whole allowed posterior region is filled by the 95 % interval, because no measurement is constraining the posterior. Moving down, the first bin of the $p_{\mathrm{T}}^{t,h}$ distribution enters the interpretation, reducing the allowed 95 % CL region.

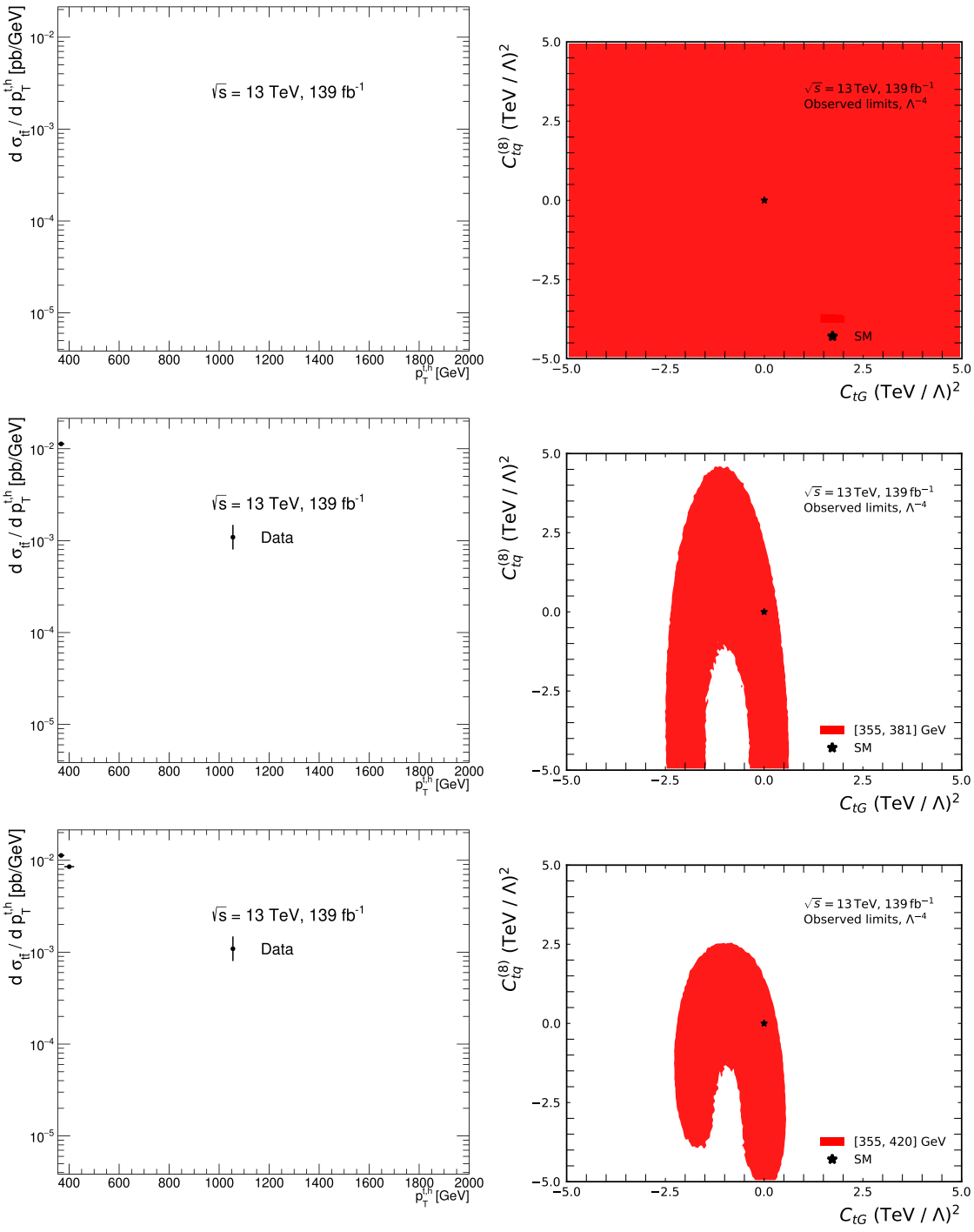

Figure 19: Two-dimensional posterior distributions on the right when using the set of bins of the $p_{\mathrm{T}}^{t,h}$ distribution indicated by the respective histograms on the left. The 95 % CL region is represented by the red area in the right figures.

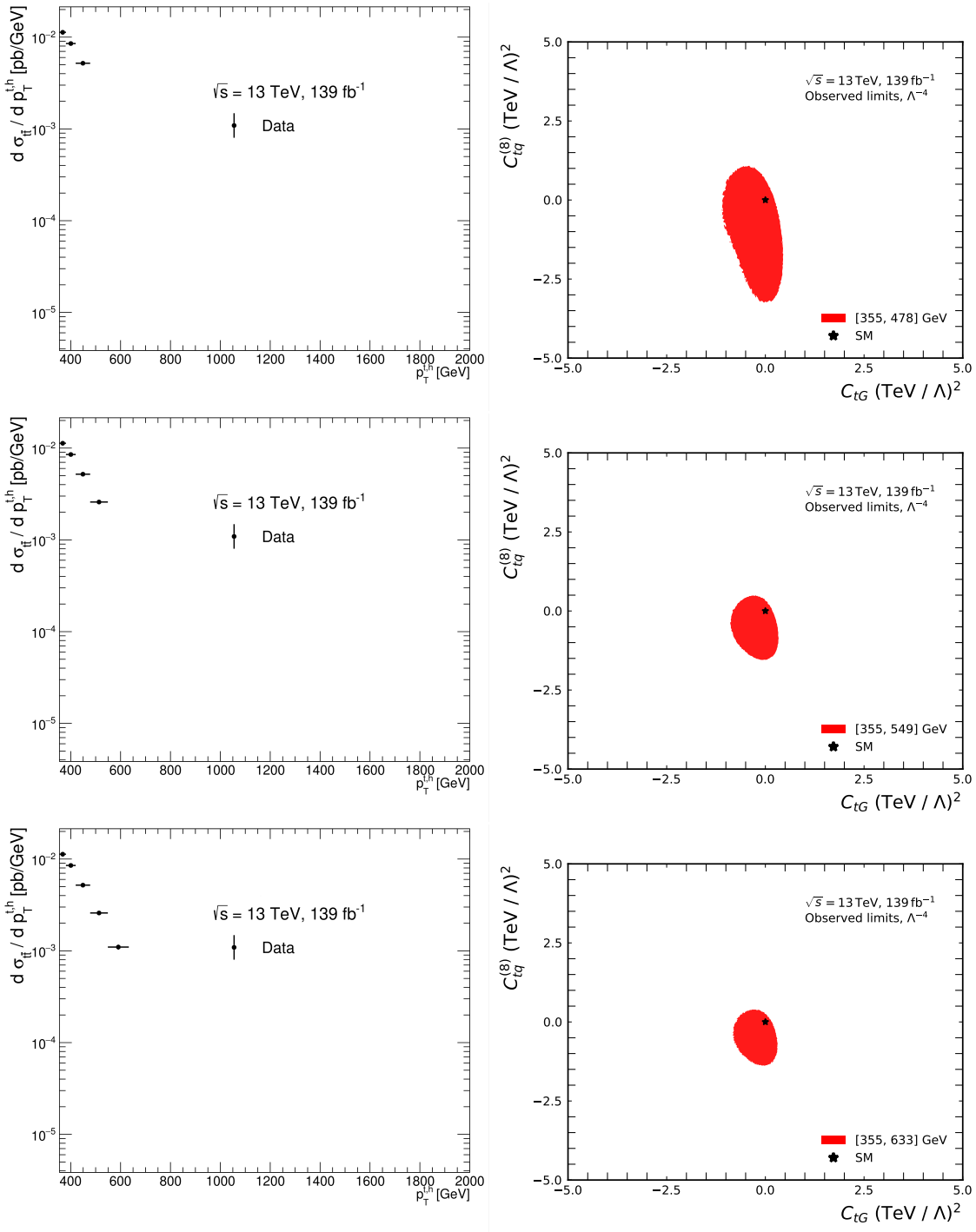

Figure 20: Two-dimensional posterior distributions on the right when using the set of bins of the $p_{\mathrm{T}}^{t,h}$ distribution indicated by the respective histograms on the left. The 95 % CL region is represented by the red area in the right figures.

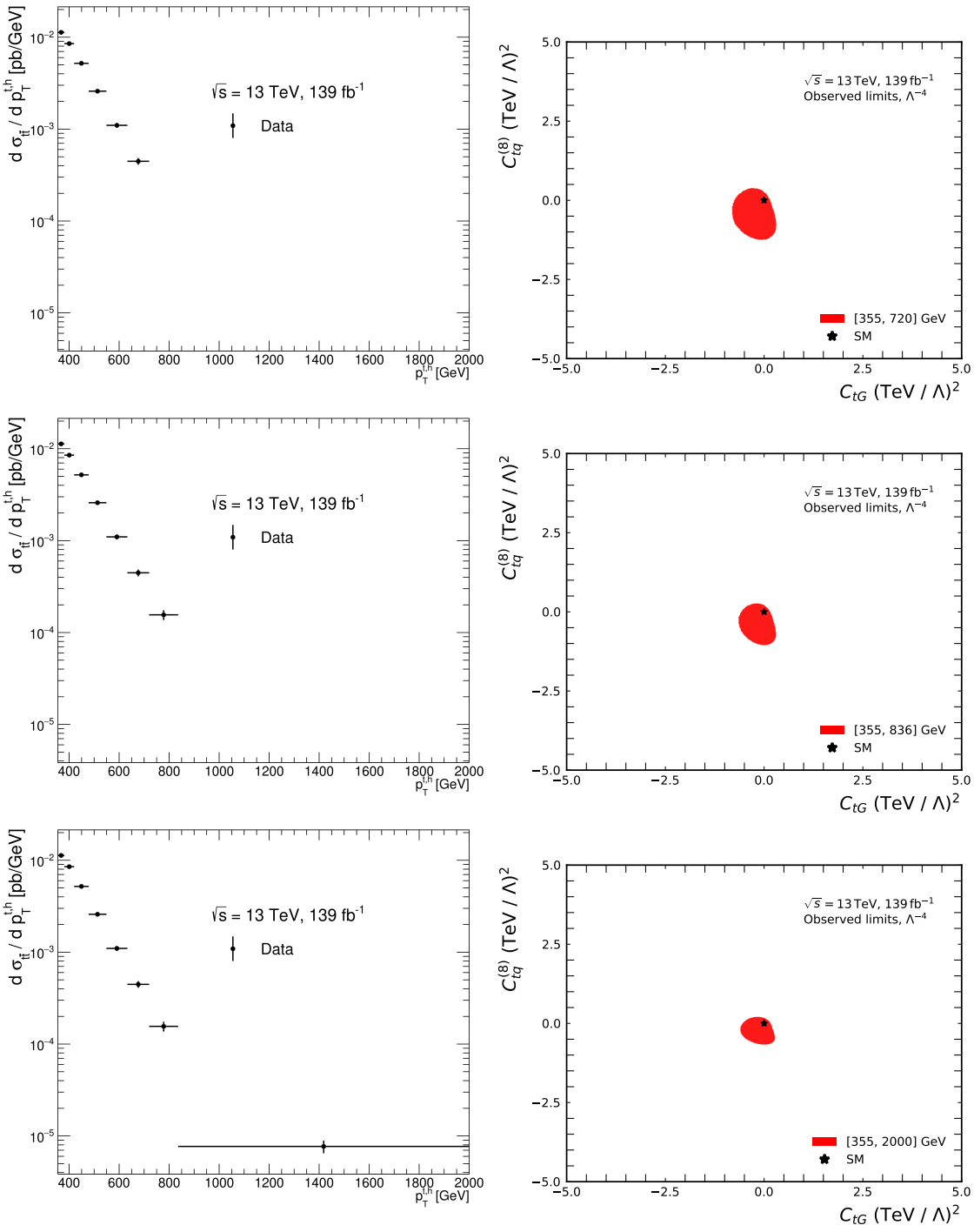

Figure 21: Two-dimensional posterior distributions on the right when using the set of bins of the $p_{\mathrm{T}}^{t,h}$ distribution indicated by the respective histograms on the left. The 95 % CL region is represented by the red area in the right figures.

8 Data Input and Covariance Matrix

Bin	Cross-Section / pb	Uncertainty / pb
1	0.01129500512456653	0.00094558488117929
2	0.008518550553329438	0.000668448404916491
3	0.005196488694950583	0.000401021742123613
4	0.002585358049209093	0.000209575265367790
5	0.0010992200882182284	0.0001023922779649443
6	0.00044660962207567417	0.00004481946139791688
7	0.00015587043617113516	0.00002002266142283371
8	0.00007694208444401423	0.00000134460362519071

Table 1: Data input for the cross-sections in the eight bins of the $p_{\mathrm{T}}^{t,h}$ distribution for the EFT interpretation. The uncertainties represent the square-root of the respectve entry in the cvariance matrix including all uncertainties in the interpretation.

Bin	Bin 1	Bin 2	Bin 3	Bin 4	Bin 5	Bin 6	Bin 7	Bin 8
1	1.0	0.9404466321298056	0.8618185027301744	0.8267332611893192	0.7396561754607415	0.5988757938186435	0.6306363751977485	0.05097542556413184
2	0.9404466321298056	0.9999999999999999	0.9516281692521273	0.9147915208562453	0.7910829866856328	0.6967717399748145	0.701638225028523	0.22462139195050965
3	0.8618185027301744	0.9516281692521273	0.9999999999999999	0.9627586100366556	0.8204470621616913	0.7850748200147363	0.7335363946650101	0.3433625192715446
4	0.8267332611893192	0.9147915208562453	0.9627586100366556	1.0000000000000002	0.8800873487267985	0.8221993394613355	0.7721143502554354	0.3862509526805279
5	0.7396561754607415	0.7910829866856328	0.8204470621616913	0.8800873487267985	1.0	0.818180243654515	0.6766229938886801	0.41808428646814394
6	0.5988757938186435	0.6967717399748145	0.7850748200147363	0.8221993394613355	0.818180243654515	1.0000000000000002	0.7752637923429523	0.5681055176709825
7	0.6306363751977485	0.701638225028523	0.7335363946650101	0.7721143502554354	0.6766229938886801	0.7752637923429523	1.0000000000000002	0.2915306328050216
8	0.05097542556413184	0.22462139195050965	0.3433625192715446	0.3862509526805279	0.41808428646814394	0.5681055176709825	0.2915306328050216	1.0

Table 2: Bin-to-bin correlations of the $p_{\mathrm{T}}^{t,h}$ distribution used as input in the EFT interpretation of the measurement.

Acknowledgements

Performing this measurement and writing this thesis would not have been possible, had it not been for the exceptional support of a number of people. Especially as part of the ATLAS collaboration, it would take pages over pages to thank every single one.

I do want to express my sincere gratitude to a selection of people, though.

Firstly, I want to thank my supervisor Prof. Dr. Kevin Kröninger for his support and for giving me the opportunity to work on this project in Dortmund and at CERN, as well as for his referee work on this thesis. Secondly, I want to thank Prof. Dr. Johannes Albrecht for taking on the role as second referee and for all the encouraging and informative discussions throughout my time in Dortmund.

I want to extend my gratitude to (now) Prof. Dr. Johannes Erdmann as well. Thank you for the extensive supervision and for sharing the fighting all the way to the publication of this work, as the top convener, my supervisor and a colleague. Thank you for all the discussions and sharing the struggles as well as the wins.

This analysis would never have happened had it not been for the amazing Scots on the analysis team. I want to thank Mark Owen, Federica Fabbri and Jonathan Jamieson for the very productive and close collaboration. It has been a pleasure working with a group of people that professional and that pleasant.

I want to thank the groups I had the pleasure of working in. The AG Kröninger in Dortmund, although a lot of this was taken from us in the last years. On the other hand, the months I shared the CERN office with Tomas and Noemi were a good alternative. Thanks for sharing *some tea* as well as all of the regular madness.

Thanks also to my favorite theorists Marcel and Jonathan. Thanks for all the climbing, and beers and all the things in between. I can't even summarize all the fun we had! Thanks for the biking, and climbing and all the trips, Marcel! And thanks for the ton of music, all the meetings in Geneva or *at the so-called boy* and so much more fun, Jonathan!

Thank you also to all the people along the way, Maik, Helena, Vukan, Kevin, Simone, Kevin, Felix, Rigo, Max, Kaiarno, all the *climbing theorists* and so many I'm forgetting.

Cheers to my favorite dentist, Julian! What crazy 12 years so far, and finally this summer we made it.

I also want to thank the crowd of "CERN people" that made my stay there so many times better! Thanks for the hikes, tent pitching, drinks, drinks-while-in-a-tent-on-top-of-a-mountain, whiskies, lake time, skiing, wine, jammy jams, river floats and all the things

I'm forgetting in my post-writing delirium. Thanks to Haider, Anders, Andrés, Grace, Tal, Dylan, Sam, Arild, Melissa, Ola, Jeff and Sophie, as well as, *the Italians*.

I want to particularly thank one of the main people who made this time what it was and kept me sane many times: Björn! Ja, well, I can't possible even choose among all the things that happened, but I am sure that most of them would have been much harder and much less fun without you. Thanks for sharing the regular PhD madness, the computing crazyness and the overall physics insanity. So many things were great beacuse of you and it's a pitty that this will end now, but off to new shores, I guess. Thanks also for the proof reading and truly making this a *stimulating environment*. I'm proud we managed to not set the servers on fire once and I'm sure there is more good stuff to come!

Although they might be shy to take any credit for all of this, there is no way at all any of this would have succeeded, had it not been for my parents. I can write this, only because of the fight you put up to make all of this possible, and for this you can take just as much credit. Thanks for all the support and everything you made possible! And thank you for trying to understand what I do! And, well, also for not trying to do that for too long for all of our sakes.

Last, but quite the opposite of least, I owe an infinite amount of gratitude to my love, Janina! There is no way I can even closely mention all the things you helped me with, all the times you helped me prevail and not go crazy, all the time you made so much better (well, that's actually all the time), so I just want to thank you so sooo so much for everything. You were there the whole time and endured everything and supported me unconditionally. I love you to the moon and back!

PS: I want to thank Maximilian Nöthe for the thesis template that I shamelessly stole (I guess I owe you a beer).